Structural, Thermal, and Electrochemical Studies of Manganese Dioxides for Alkaline and Lithium-Ion Cells

by

Oliver Schilling

M.Sc., Simon Fraser University, 1993

Thesis submitted in partial fulfillment of
the requirements for the degree of
Doctor of Philosophy
in the Department of Physics

Approval

Name:	Oliver Schilling
Degree:	Doctor of Philosophy
Title of Thesis:	Structural, Thermal, and Electrochemical Studies of Manganese Dioxides for Alkaline and Lithium-Ion Cells
Examining Committee:	Dr. E. Daryl Crozier (Chairperson)

Dr. Jeffrey R. Dahn, Senior Supervisor
Professor of Physics and Chemistry
Dalhousie University, Halifax, Nova Scotia

Dr. Albert E. Curzon

Dr. Michael Plischke

Dr. Robert F. Frindt, Internal Examiner

Dr. Peter G. Bruce, External Examiner
Professor of Chemistry
University of St. Andrews
St. Andrews, Fife, United Kingdom

Date Approved: 24 March 1997

PARTIAL COPYRIGHT LICENSE

I hereby grant to Simon Fraser University the right to lend my thesis, project or extended essay (the title of which is shown below) to users of the Simon Fraser University Library, and to make partial or single copies only for such users or in response to a request from the library of any other university, or other educational institution, on its own behalf or for one of its users. I further agree that permission for multiple copying of this work for scholarly purposes may be granted by me or the Dean of Graduate Studies. It is understood that copying or publication of this work for financial gain shall not be allowed without my written permission.

Title of Thesis/Project/Extended Essay

Structural, Thermal, and Electrochemical Studies of

Manganese Dioxides for Alkaline and Lithium-Ion Cells.

Author:
(signature)

Oliver Schilling
(name)

25 March 1997
(date)

Abstract

Manganese dioxides have been used in electrochemical cells for over a hundred years, starting with the Leclanché cell. Crystallographically, these manganese dioxides can appear in various modifications with varying suitability as cathodes in electrochemical cells. In order to be able to correlate the electrochemical behaviour with the crystal structure (as observed by powder X-ray diffraction), a programme has been developed that can fit experimental data with a calculation based on a model for a non-periodic intergrowth of pyrolusite faults in a ramsdellite matrix.

The mathematical formalism to express the scattered intensity for such a disordered system is reviewed and applied to the problem at hand. The intergrowth is described as a stochastic, parallel stacking of four different types of layers that possess two-dimensional periodicities perpendicular to the stacking direction. The final powder averaging of the intensity thus obtained has to be partly performed numerically.

The structures of electrolytically prepared manganese dioxides, which are widely used, especially in alkaline cells, are not well described by the model of ramsdellite/pyrolusite intergrowth. On the other hand, the structure of some chemically prepared manganese dioxides, as well as of electrolytically prepared ones that have been heat treated, can be fit by the model.

In recent years, a manganese dioxide with a spinel-type structure has found interest in the field of rechargeable lithium-ion cells. This modification is known to convert to the more stable pyrolusite form upon heating. The exothermic phase transition is followed by powder X-ray diffraction of samples heat treated at various temperatures. Most of the heat release occurs during the conversion of the cubic close packed

oxygen lattice of the spinel structure to the hexagonal close packed oxygen lattice of the pyrolusite structure. The arranging of the manganese atoms onto their final crystallographic positions lags behind and is not associated with a large heat release.

From the thermodynamic properties of the spinel manganese dioxide, it can be concluded that thermodynamic instability is not the origin of the capacity decrease observed when repeatedly charging and discharging this material. Other reasons for the fade are analyzed in the context of experimental data obtained.

Acknowledgement

Jeff Dahn' s constant enthusiasm for my work, his perpetual availability for discussions, his very generous financial support, as well as his personal interest in my career exceeded my expectations by far. Thank you.

My thanks extend to the members of my supervisory committee: Albert Curzon made his transmission electron microscope available to me, which proved very valuable in the preliminary phase of this project. Mike Plischke agreed without hesitation to take over committee responsibilities, after Daniel Loss left the university.

The numerous members of the Dahn-lab-group made the time enjoyable; thanks to all of them, but in particular to Monique Richard, who made some of her data available to me for incorporation into this thesis, and to Yuan Gao, who taught me a lot about lithium manganese spinels.

The many helpful discussion on X-ray diffraction with Alain Gibaud during his visit are much appreciated. None of the work on manganese dioxides for alkaline cells would have been possible without the many samples I was given. In particular, I wish to thank Jeff Wass (Chemetals, Inc.), Jean-Claude Rousche (Sedema), Dom Swinkels (Univ. of Newcastle), Rodney Williams (now BHP), and Michael Root (Rayovac Corp.).

I am much indebted to Darlene for her love and her support during all phases of this project. Andreas and Niklas always found a way to show me that there is life outside physics — thank you for that.

Contents

List of Tables

List of Figures

List of Selected Symbols

α_{12}, α_{23}, α_{31}	Angles between real space lattice vector
γ	Mixing parameter of Voigt function
$\delta(\vec{x})$	Dirac δ-function
η	Overall scale factor
2θ	Scattering angle, goniometer setting·
$\Delta(2\theta)$	Uncertainty in scattering angle
$2\theta_{\mathrm{m}}$	Scattering angle of the monochromator
$2\Delta\theta_{\mathrm{inc}}$	Opening angle of the divergence slit
θ_{min}	Minimum incident angle so that sample holder is not hit by beam
λ	Wavelength in general; in particular weighted average of CuKα_1 and CuKα_2 (1.5418 Å)
μ	Chemical potential; absorption coefficient; layer number
π	Twice the first zero of the cosine function
σ_1, σ_2, σ_3	Strain parameters for the three crystallographic directions
σ_{hl}	1/6 of the width of the hl-rod
ϕ_{ij}	Phase factor between two adjacent layers of types i and j
ϕ_s	Azimuthal angle of vector $\vec{s}$
χ	Label for the χ^{th} crystal in the sample
ψ_s	Polar angle of vector $\vec{s}$
$\Phi^{(0)}(\vec{s})$	Scattering amplitude of characteristic crystal
a_1, a_2, a_3	Lattice constants in real space
$b^{(1)}$, $b^{(2)}$, $b^{(3)}$	Lattice constants of the reciprocal space
c	Speed of light in vacuum
c_i	Coefficient for polynomial background ($i = -1, 0, 1, 2, 3, 4$)

$\vec{d}^{(\alpha)}$	Position of atom α in unit cell
e	Magnitude of the electronic charge
$f^{(\alpha)}(s)$	Atomic form factor of atom α
h	Miller index
i	Layer type; general summation index
j	Layer type
$i(\vec{s})$, $i(2\theta)$	Calculated intensities
$i^{(0)}(\vec{s})$	Intensity scattered by the characteristic crystal
$\overline{i^{(0)}}(\vec{s})$	Configuration-averaged intensity scattered by the characteristic crystal
k	Boltzmann constant, Miller index
l	Miller index
m	Active mass; mass in general; summation index
$\hat{n}_{\mathbf{inc}}$	Direction of incident beam
$\hat{n}_{\mathbf{scat}}$	Direction into which a scattering event is observed
p	Order parameter in ramsdellite/pyrolusite intergrowth model
p_{ij}	Probability that layer of type i is followed by layer of type j
q	Specific capacity of an electrode (Q/m)
$r_{\mathbf{g}}$	goniometer radius
r_{ij}	Distance between layers of type i and type j
$\vec{s}$	Scattering vector
s_1, s_2, s_3	Components of scattering vector along reciprocal unit vectors
$s = \|\vec{s}\|$	Length of the scattering vector
Δs	Uncertainty in the length of the scattering vector
t	Time
x	Fraction of lithium on (16d) in spinel
x, y, z	Cartesian coordinates with respect to the fixed lab frame
$\hat{x}$, $\hat{z}$	Unit vectors of Cartesian lab system
B	Temperature-dependent coefficient in the exponent of the Debye-Waller factor
$C(\vec{x})$	Electron density

ΔC	Difference between the heat capacities of sample and reference in DSC
E	Electrode potential
E^0	Standard electrode potential
$F_i(\vec{s})$	Fourier transform of unit cell of layer i, "layer structure factor"
G_1, G_3	Modulation functions in the 1- and 3-direction
I	Current
I_0	Energy flux density of incident X-ray beam
$I_{\mathrm{inc}}(z)$	Irradiance of the sample as a function of depth
$I_{\mathrm{integrated}}(hkl)$	Integrated intensity of Bragg peak due to hkl point in reciprocal space
N_1, N_2, N_3	Mean number of unit cell repetitions in the various direction
Q	Cell capacity, charge
R	Electric or thermal resistance
P	Power
T	Absolute temperature
U, V, W	Parameters describing peak breadth variation across the pattern in the Rietveld programme
V	Voltage, potential difference
$\mathcal{F}(\mu, \vec{s})$	Fourier transform of the electron density in layer μ
$\mathcal{L}$	Lorentz factor
$\mathcal{P}$	Polarization factor
$\mathsf{G}_2(\vec{s})$	Modulation function in 2-direction
Q	"average phase factor"
F	Column vector of F_i
i	imaginary unit: $\mathrm{i}^2 = -1$
A, B, C, D	Layer types in the ramsdellite/pyrolusite intergrowth model
X, Y, Z	Layer types in close-packed stackings
(1), (2), (3), (4)	Units in the unified ramsdellite-pyrolusite-intergrowth/microtwinning model

Chapter 1

Energy and Energy Storage

1.1 Energy

This thesis will be dealing with batteries and more specifically battery materials. These are topics one could categorize under the heading of "energy management" — a subject that gained a lot of attention since the so-called oil-crisis in 1973 and that is now so vast that this thesis can not deal with it in its entirety. It includes for instance environmental issues (overusage of energy, greenhouse effect due to burning of fossil fuels, etc.) and socio-economic issues (lack of available energy, poverty, North-South conflict, etc.). Energy as a colloquial term has therefore many connotations.

Scientifically, energy is one of the fundamental concepts of physics; it is therefore only fitting that it should be a physics thesis that deals with batteries and battery materials, although a lot of aspects would naturally fall into the field of electrochemistry. Two aspects of *energy* make it interesting and important to science and technology, and indeed everything that exists. One is the fact that nothing *works* without energy; the other is the postulate that energy is conserved.

One may argue, whether energy conservation is actually a postulate or merely a consequence of Noether's Theorem that associates the conservation of one variable describing a certain system with the invariance of this system under changes of its conjugate variable. Since energy generates time evolution, it is the invariance of the system under time transformation that one would need to investigate. But the

questions of, whether or not a system is invariant under time transformation, whether or not time itself is homogeneous, will be left to the realm of philosophy [1]. For the remainder of this thesis I will assume that energy is conserved.

Having established that, the next question arises: Where shall we take our energy from that we want to use in our daily life? The biggest energy converter in our vicinity is the sun. It fuses protons to alpha-particles. The mass loss (and therefore energy loss) that is encountered by this conversion is partly emitted in form of electromagnetic radiation which is incident on earth, where it can lead to an energy gain, if it is properly absorbed, for instance by plants or plankton or solar panels or solar cells. Whether or not such an energy gain is desirable is certainly worth discussing, but is beyond the scope of this thesis.

Solar cells are very interesting because they convert solar energy directly into electrical energy which can easily be transported, but not so easily be stored, especially in larger quantities. To store electrical energy in small quantities, an electrochemical cell is the ideal device, but only if it can be re-used many times. This immediately implies that a non-rechargeable, disposable, so-called primary battery[1] can not be the goal for energy management. The energy that goes into producing one battery is certainly much higher than the energy that it can deliver during one discharge. Only rechargeable or so-called secondary batteries can be efficient energy storage devices.

1.2 Electrochemical Cells

An electrochemical cell consists of two electrodes that are spatially separated by an ion-conductive electrolyte and can be connected by an electric lead, which conducts electrons (see figure 1.1). As a current flows through the electrical lead, one of the electrodes, called the anode, will be oxidized, the other, the cathode, will be reduced.

The cathode will receive electrons and (positively charged) ions such that charge neutrality is maintained, while the anode will give up electrons and ions. Of particular interest is the case where the ions received and given up by the two electrodes are actually the same. One can identify a chemical potential for this ion/electron pair in

[1] A battery is an array of cells, see section 1.7.1.

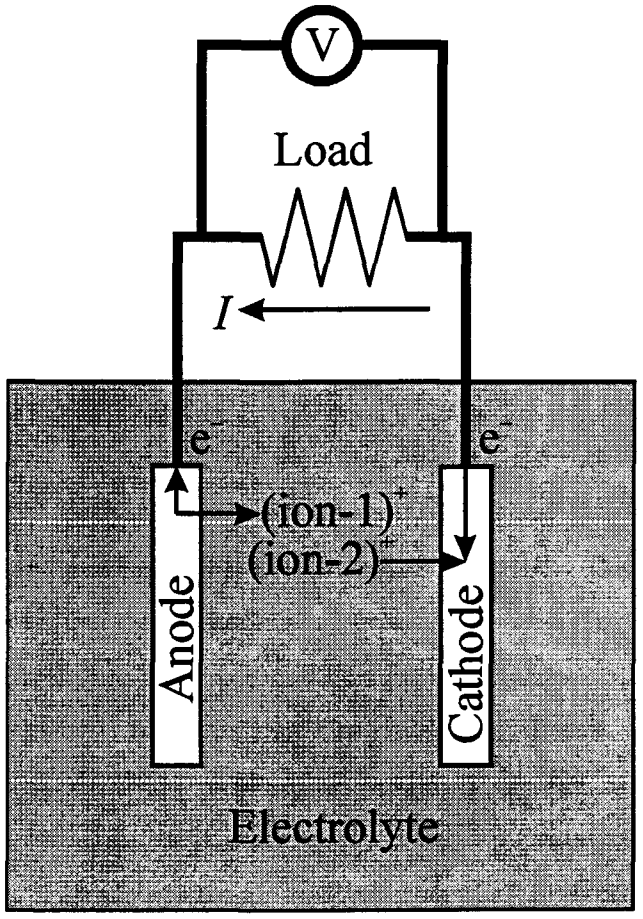

Figure 1.1: A typical electrochemical cell with two electrodes. The anode giving up electrons is the negative electrode, the cathode positive. In this schematic the anode and cathode are spatially separated to avoid an internal short. In real cells where space is limited, an electrically insulating, porous material (called a separator) is inserted between the electrodes instead. One problem that this figure shows is that the electric leads may be involved in chemical processes with the electrolyte as well, leading to unwanted side reactions that may affect the cell voltage or the life time of the cell. It is therefore important to choose the right material.

each of the electrodes. The pair, which can be an atom or a molecule, tends to stay where its chemical potential, μ, is lowest. For simplicity, I will be dealing with singly charged ions.

If the pair is already in its lowest energy state (within the system), one has to apply a current from an external source to force the electron through the electrical circuit out of its present state, *i.e.* the cell has to be charged. The ion will simultaneously move through the electrolyte to the other electrode such as to maintain charge neutrality. When the electric circuit is disconnected, the electron/ion pair is in a higher energy state than originally, but the electron can not go anywhere and therefore the ion has to stay as well. When re-connecting the electric circuit, the electron can then be utilized to do work on its way to the lower energy state, *i.e.* the cell is discharged.

As can be seen, whether an electrode is an anode or a cathode depends on whether the cell is charged or discharged. From now on, the electrode that is oxidized on discharge (*i.e.* the negative terminal) will be called the anode, the one that is reduced on discharge will be called the cathode.

The amount of reversible work the cell can do is the change in Gibbs free energy of the electron/ion system, which is just the change in chemical potential for each electron/ion pair. This decrease in chemical potential is seen by the electron as an increase in electric potential (electrons readily climb up potentials because they are negatively charged). The difference in electric potential between the two electrode leads, the so-called terminals, can be measured as an electromotive force, ΔE:

$$\Delta E = -\left(\left(\mu_{\text{cathode}}(\text{electron}) + \mu_{\text{cathode}}(\text{ion})\right) - \left(\mu_{\text{anode}}(\text{electron}) + \mu_{\text{anode}}(\text{ion})\right)\right)/e, \tag{1.1}$$

where e is the magnitude of the electronic charge.

One can assign individual electric potentials to each of the electrodes. These are either oxidation or reduction potentials, depending on whether an electron/ion pair is removed or added. These potentials are arbitrarily referenced with respect to a so-

Table 1.1: Standard electrode potential, E^0, for some reduction/oxidation (redox) processes. All influencing parameters must be in their standard form, that is a 1 molar concentration, atmospheric pressure, temperature of 298 K. All data taken from [2], except for †, which are taken from [3].

oxidized form		reduced form	E^0
$2\ H_3O^+ + e^-$	$\longrightarrow$	$H_2 + 2\ H_2O$	± 0.00 V
$O_2 + 4\ H_3O^+ + 4\ e^-$	$\longrightarrow$	$6\ H_2O$	$+1.23$ V
$Zn(OH)_2 + 2\ e^-$	$\longrightarrow$	$Zn + 2\ (OH)^-$	-1.25 V
$Zn(OH)_4^{2-} + 2\ e^-$	$\longrightarrow$	$Zn + 4\ (OH)^-$	-1.22 V†
γ-$MnO_2 + H_2O + e^-$	$\longrightarrow$	α-$MnOOH + OH^-$	$+0.30$ V
$Hg^{2+} + 2\ e^-$	$\longrightarrow$	Hg	$+0.85$ V†
$HgO + H_2O + 2\ e^-$	$\longrightarrow$	$Hg + 2\ OH^-$	$+0.10$ V
$Li^+ + e^-$	$\longrightarrow$	Li	-3.02 V

called standard hydrogen electrode.[2] The standard electrode potential, E^0, is chosen to be negative, if the electric potential of the electrode terminal is lower than that of the terminal of the standard hydrogen electrode. The standard electrode potentials are therefore effectively reduction potentials; some are listed in table 1.1 (oxidation potentials have the opposite sign).

In order to convert from these standard potentials to potentials under non-standard conditions, the so-called Nernst-Equation is useful. Given a chemical redox reaction

$$aA + bB \longrightarrow cC + dD, \tag{1.2}$$

where n electrons are transferred per formula unit, the potential is given by

$$E = E^0 + \frac{kT}{ne} \ln \frac{[C]^c[D]^d}{[A]^a[B]^b}, \tag{1.3}$$

where the square brackets indicate the activities of the different reactants. At sufficient dilution, which I will assume henceforth, the activities can be identified with the concentrations of the reactants. At room temperature this can be partially evaluated

[2]The standard hydrogen electrode is realized by bubbling hydrogen gas (H_2) at atmospheric pressure through a 1 molar H_3O^+-solution along a platinized platinum wire, that is a platinum which has finely dispersed platinum electroplated onto it. This high surface area platinum acts as a catalyst for the dissociation of the hydrogen molecule into two hydrogen atoms.

to give

$$E = E^0 + \frac{59\text{mV}}{n} \log_{10} \frac{[\text{C}]^c[\text{D}]^d}{[\text{A}]^a[\text{B}]^b}. \tag{1.4}$$

If, for instance, the hydrogen electrode was not operated in a 1 M H_3O^+-solution, that is at pH 0, but at pH 7, the potential of the electrode would decrease by $7 \times 0{:}059V = 0.42V$. For an electrode made from a mixture of Hg and HgO, it is the solubility of HgO that determines the Hg^{2+}-concentration and therefore the potential shifts away from the 0.85 V standard.

1.3 Electrochemical Characterization of Electrodes

For the purpose of determining the chemical potentials of cathode and anode individually, it can be useful to add a third electrode as a reference to the cell. Such a cell set-up is depicted in figure 1.2; it includes a working electrode (the one that is to be investigated), a counter electrode (in many cases just an inert piece of metal, platinum or stainless steel), and the reference electrode through which almost no current flows and which therefore changes little and has a (nearly) constant chemical potential. There are two distinct methods in characterization the working electrode.

1. As depicted in figure 1.2, one charges and discharged the cell galvanostatically, that is at a constant current, I, and monitors the voltage as charge is transferred from one electrode to the other. If the current is small enough, this technique measures the quasi-equilibrium behaviour of the working electrode and in the limit of zero current it would measure the so-called open-circuit voltage, V_{oc}. The amount of transferred charge, Q, is referred to as the capacity of the cell and is determined by the product of the time, t, for which the current has been flowing and the current itself: $Q = It$. Since Q is of course an extensive quantity, one typically quotes a specific capacity, that I will represent by $q = Q/m$ in this thesis . The mass, m, that is taken into consideration here is the so-called active mass of the electrode; what this is will become clearer when I will discuss real systems.

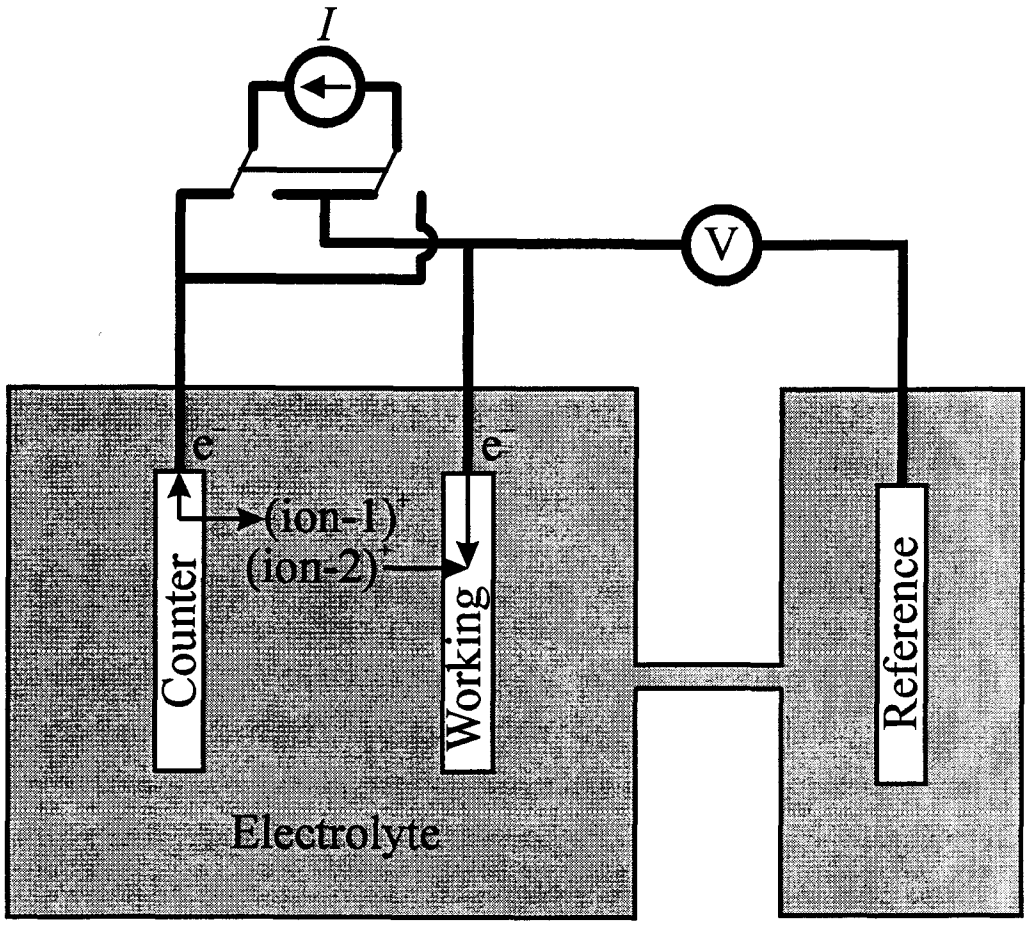

Figure 1.2: To characterize electrode materials, a three electrode design is typically favoured, since it involves a constant voltage reference. In order to minimize changes in the electrolyte in the vicinity of the reference electrode its chamber is often connected to the main chamber by a constriction to reduce ion diffusion.

2. In a potentiostatic measurement, one applies an external voltage to the electrodes which is slightly higher or lower than the electromotive force of the cell and therefore results in a current flow. One typically steps the applied voltage at constant rate and measures the current response leading to a so-called cyclic voltammogram. The measured current should of course decay with time, if the time between applied voltage steps is only large enough. Integrating the current over the time for which it decays should lead to a proper measurement of the capacity of the cell and its equilibrium characteristics (some people refer to this

as Step-Potential ElectroChemical Spectroscopy, SPECS [4]). Cyclic voltammetry itself, however, is an inherently non-equilibrium measurement and will not be pursued in this thesis.

In a cyclic voltammogram one obtains large currents at a certain voltage, V, if there are a lot of electron/ion pairs bound with the corresponding binding energy, $-eV$. In a galvanostatic voltage *vs.* time curve this would show up as plateau. Consequently, taking the derivative $\mathrm{d}t/\mathrm{d}V$ and plotting it *vs.* V gives the same feature as the cyclic voltammogram's I *vs.* V curve, except that the derivative curve can show properties closer to equilibrium, if the current is chosen small enough.

1.4 Crystal Structure and Chemical Potential

If one wants to utilize a certain electrochemical cell as an energy storage device, one needs to charge and discharge this cell repeatedly, that is cycle it. It is desirable that the cell voltage at a certain state of charge and the number of electron/ion pairs that can be transferred in each charge/discharge cycle not change with cycling. In order to improve an electrode material that does not fulfill these requirements, one has to understand what the origin of its deficiencies is. In order to understand the deficiencies, one has to understand the nature of the above mentioned quantities first.

As indicated above there are two contributions to the chemical potential of the electron/ion pair in an electrode: the chemical potential of the electron and the chemical potential of the ion. The chemical potential of the electron is directly related to the band structure and the density of states of the electrode material.[3]

The band structure is derived from the atomic energy levels of the atoms involved in the solid. Often the situation arises that the electronic states in the solid, whose

[3]In physics texts this quantity is frequently referred to as the Fermi energy, although a Fermi energy is properly defined only for a system that does not have any gaps in its density of states, such as a metal. The Fermi energy is defined (at zero temperature) as that energy up to which all energy levels are filled and the next available state has an infinitesimal higher energy. The chemical potential is generally defined as the energy taken up or released when the $(N+1)^{\mathrm{th}}$ particle is added to an N particle system.

energies are close to the chemical potential of the electron, are predominantly derived from one particular atom. Then it is this atom that determines the electronic chemical potential in the solid.

As new atoms are inserted into the structure and with it new electrons, the electronic chemical potential may stay relatively constant as long as states derived from the same particular atomic state are available. Once these are filled, states derived from a different state of the same atom or states from a different atom will be available. When this happens, one might suspect a more rapid change in the chemical potential, leading to a rapid change in the chemical potential of the electron/ion pair, which can be measured as a rapid change in of the electrode potential.

An example of this is the compound λ-MnO_2, whose voltage versus lithium metal for lithium insertion is around 4.0 V – 4.1 V. Substituting nickel for some of the manganese atoms, creates states with higher binding energy, leading to an initial cell voltage of 4.7 V, which drops to 4.0 V – 4.1 V after the nickel derived states are filled [5, 6].

As long as the electronic chemical potential is characterized by one type of atomic energy, the fine scale of the insertion voltage for an electron/ion pair is determined by the exact local environment that the ion will be found in after the electrode is reduced. It is then obvious that one does not want to change this local environment of the electrode, that is its crystal structure, from one charge/discharge cycle to another in order to maintain the same voltage profile during each discharge; better yet if it stays unchanged even during each of the cycles. It is for this reason that so-called intercalation materials are desirable for rechargeable cells. These materials (hosts) do not change their crystal structure significantly as the electron/ion pair (the intercalant) is inserted (intercalated) into and extracted (de-intercalated) from it.

The chemical potential of an intercalant in an intercalation material should then only change due to varying number of other intercalants in the host. A nice example for this phenomenon is set by lithium intercalation into molybdenum selenide, Mo_6Se_8. The variation in the chemical potential as measured by the voltage of an electrochemical cell utilizing $Li_xMo_6Se_8$ ($0 \leq x \leq 1$) as one electrode and lithium metal as the other (since the chemical potential of lithium in lithium metal is constant) can

be nicely fit by a lattice gas model of lithium atoms on a particular crystallographic site, while keeping the electronic contribution fixed by assuming a rigid band model [7]. Such a rigid band model, *i.e.* a model that assumes merely a change of the filling level, but not of the structure of the electronic bands during intercalation, can fail as recently demonstrated by Ouvrard and coworkers [8, 9].

Some intercalation compounds are prepared in their discharged state, for instance $LiCoO_2$ has all lithium atoms inserted. These lithium atoms may be extracted in an electrochemical cell and the crystal structure remains stable until about half the lithium atoms are removed. At this point the structure may change irreversibly rendering the material virtually useless as an electrode, see for instance reference [10] and references therein.

It is therefore essential to understand the crystal structure of the electrode in order to understand the chemical potential and its variation as electron/ion pairs are inserted into the material.

1.5 The Zn/MnO_2 System

1.5.1 Leclanché Cells

The Zn/MnO_2 system is one of the first cell chemistries that was commercialized. It was Leclanché in 1866 who invented a wet-cell using an ammonium chloride solution as the electrolyte. These cells have been improved since and are now marketed as dry-cells where the electrolyte is gelatinized to avoid leakage. Nowadays, cells are made with mixtures of ammonium chloride and zinc chloride solutions or zinc chloride alone. These types of cells are commonly called zinc-carbon cells because in the early days manganese dioxide was thought to be an inactive additive to the predominantly carbon cathode.

1.5.2 Manganese Alkaline Cells

In my thesis, I want to concentrate on the so-called alkaline cell that uses a concentrated KOH solution as the electrolyte (typically 9 molar in commercial cells). During

cell discharge the manganese dioxide is thought to initially reduce to the oxyhydroxide (MnOOH), whereas the zinc oxidizes to the soluble zincate ion ($[Zn(OH)_4]^{2-}$), which then precipitates as zinc hydroxide ($Zn(OH)_2$), dehydrating to ZnO. One can imagine that such a behaviour at the zinc anode limits the rechargeability strongly, but problems exist also with the cathode. If the cathode is discharged beyond one electron per manganese atom, the electrode material converts irreversibly to Mn_3O_4 [2]. These alkaline cells are therefore primary (non-rechargeable) cells. However in recent years, a rechargeable version that can cycle up to 30 times has been introduced on the market. These rechargeable versions contain a limited amount of zinc so as to avoid irreversible processes at the cathode during deep discharge.

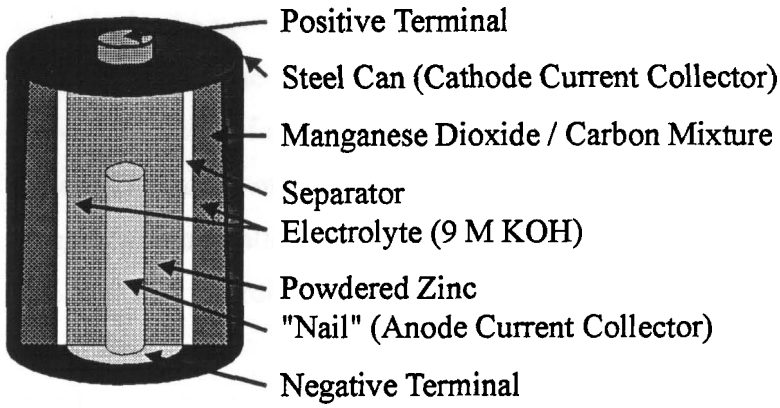

Figure 1.3: Schematic of the design of a real alkaline cell, adapted from reference [11].

A schematic of a cell design is shown in figure 1.3. Two things are obviously different from the ideal two-electrode cell shown in figure 1.1.

- In the ideal cell the two electrodes were spatially separated to avoid an electric short, whereas in the real cell one wants to utilize all the space available so that one avoids the short by placing a electrically insulating, porous membrane between the electrodes. The membrane, which is called a separator, allows electrolyte to flow through its pores and therefore does not impede the ionic current. In the aqueous alkaline cell, the separator is made of a cellulose based material

or of surface treated polyolefins (the surface treatment make the polyolefins hydrophilic).

- The manganese dioxide electrode consists of 10% (by weight) carbon, which is added to reduce the internal resistance of the cell originating from the low conductivity of the manganese dioxide. This internal resistance, R, leads to a drop of the terminal voltage by IR when a current, I, is drawn from the cell. At large currents this IR-drop would be large enough to render the cell useless, making it necessary to keep the internal resistance as small as possible.

The added carbon is electrochemically inactive, it does not have any capacity in the voltage range of interest. Other inactive ingredients may be added to the electrode as well, such as a binder to prevent a powdered electrode from falling apart, or may be present as impurities in the active material. For the purpose of characterizing electrode materials, it is therefore necessary to compare them on the basis of their active ingredients. The mass of the active ingredient of an electrode, also known as its active weight, will be called m. It should be pointed out, however, that this number is not so useful for producers of cells, who want to reduce the weight and volume of the complete cell (including parts such as electrolyte, separator, current collector, and can) while maintaining the same cell performance.

Figure 1.4 shows the discharge behaviour of two commercial AA-size alkaline cells, one from *Duracell* and the other a *no name* label. One observes a relatively steep initial drop down to 1.4 V or so, followed by a long sloping plateau, whose end coincides with the complete reduction of all MnO_2 to MnOOH. This end point may be reached at 1.15 V (or maybe 0.90 V, if the voltage drops at 1.15 V is associated with a change at the Zn anode). The remaining useful capacity down to 0.8 V or so is about 1/3 of the previous capacity, most likely associated with the reaction of 3 MnOOH to 1 Mn_3O_4 per transferred electron. It is the sloping nature of the overall discharge curve that enables Duracell to sell their cells with the "Copper Top Tester" or more recently with the "PowerCheck", which measures the state of charge of a cell based on the voltage at the terminals.

It is interesting to note that both AA-cells have very similar behaviour at 30 mA

discharge, although the capacity of *Duracell* (at 4 cells for cdn$ 4.29 plus tax) is slightly larger than the *no-name* label (at 2 cells for cdn$ 0.99 plus tax). A more significant advantage of the *Duracell* over the *no-name* label could possibly become apparent when discharging the two cells at higher currents so that it is worth paying the higher price of the *Duracell.*

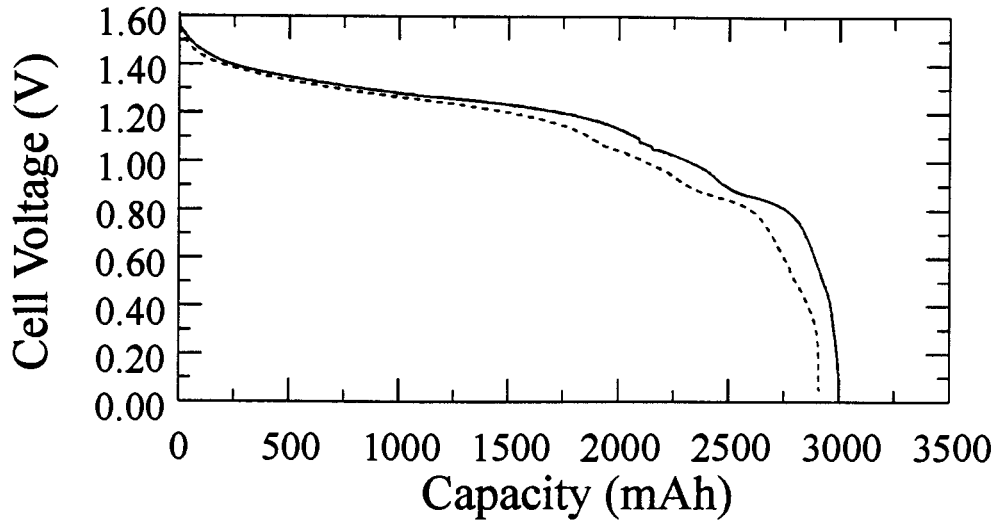

Figure 1.4: Comparison of the discharge behaviour of two commercial AA-size cells: *Duracell* (solid line) and a *no-name* (dashed line) label . During discharge at 30 mA the temperature was kept at 30 °C.

It is one goal of this thesis to add to the understanding of the discharge process of the manganese dioxide electrode, before MnO_2 has completely converted to MnOOH. As outlined before, a main part of this understanding is the understanding of the crystal structure of the partially reduced as well as the pristine material, which is commonly a manganese dioxide prepared electrolytically, a so-called EMD (see next section).

The usual method to determine crystal structures is the use of X-ray diffraction. This will be discussed in chapter 2 in greater detail. Figure 1.5 shows the change in the powder X-ray diffraction pattern as a particular manganese dioxide (International Common sample No. 14; IBA 14) is discharged. Two features can be noticed at a glance: (1) The X-ray diffraction pattern contains peaks that are not sharp, well

defined Bragg peaks, suggesting that the material is not well crystallized. (2) The pattern does not change much as the material is being lightly discharged, suggesting that the crystal structure does not change much. A more detailed analysis will follow in section 3.6.1.

Since in the Zn/MnO_2 system both electrodes change during discharge, it is necessary to utilize a reference electrode to separate the two contributions to the cell voltage. The best choice of reference electrode for this system is Hg/HgO because it is stable in these highly alkaline systems (see appendix A.1 for details). Figure 1.6 shows typical discharge curves for three manganese dioxides (TAD 1, Mitsui; CMD-R, Sedema; β-MnO_2, Fisher) in a 1 molar KOH-electrolyte solution.

I calculated the specific capacity based on the weight of the raw material; however, many manganese dioxides are not pure $Mn^{IV}O_2$, but contain other impurities such as water and manganese compounds of lower oxidation states. It is therefore necessary to determine the manganese(IV) content. This can be done, for instance, by chemical titration as described in reference [11].

If one assumes that the $Mn^{IV}O_2$ content of TAD 1 is similar to IBA 14, as their powder X-ray diffraction patterns are similar, the $Mn^{IV}O_2$ contents of TAD 1 and CMD-R are 92.7% and 95.8%, respectively [12]. Considering only the $Mn^{IV}O_2$ content as the active weight, then the specific discharge capacities for discharge down to -0.5 V *vs.* Hg/HgO of TAD 1 and CMD-R would increase from 274 mAh/g and 283 mAh/g to 298 mAh/g and 296 mAh/g, close to the theoretical limit of 308 mAh/g for a charge transfer of 1 e^- per formula unit MnO_2..

It is quite obvious that the discharge behaviour is different for different manganese dioxides — it would be interesting and important to understand these differences in order to eventually prepare manganese dioxide that can be recharged many times.

1.5.3 Manganese Dioxides — NMD, CMD, EMD

Natural Manganese Dioxide (NMD)

The cheapest way to produce a manganese dioxide is to dig it out of the ground and put it into a cell; this is a so-called natural manganese dioxide, NMD. X-ray diffraction

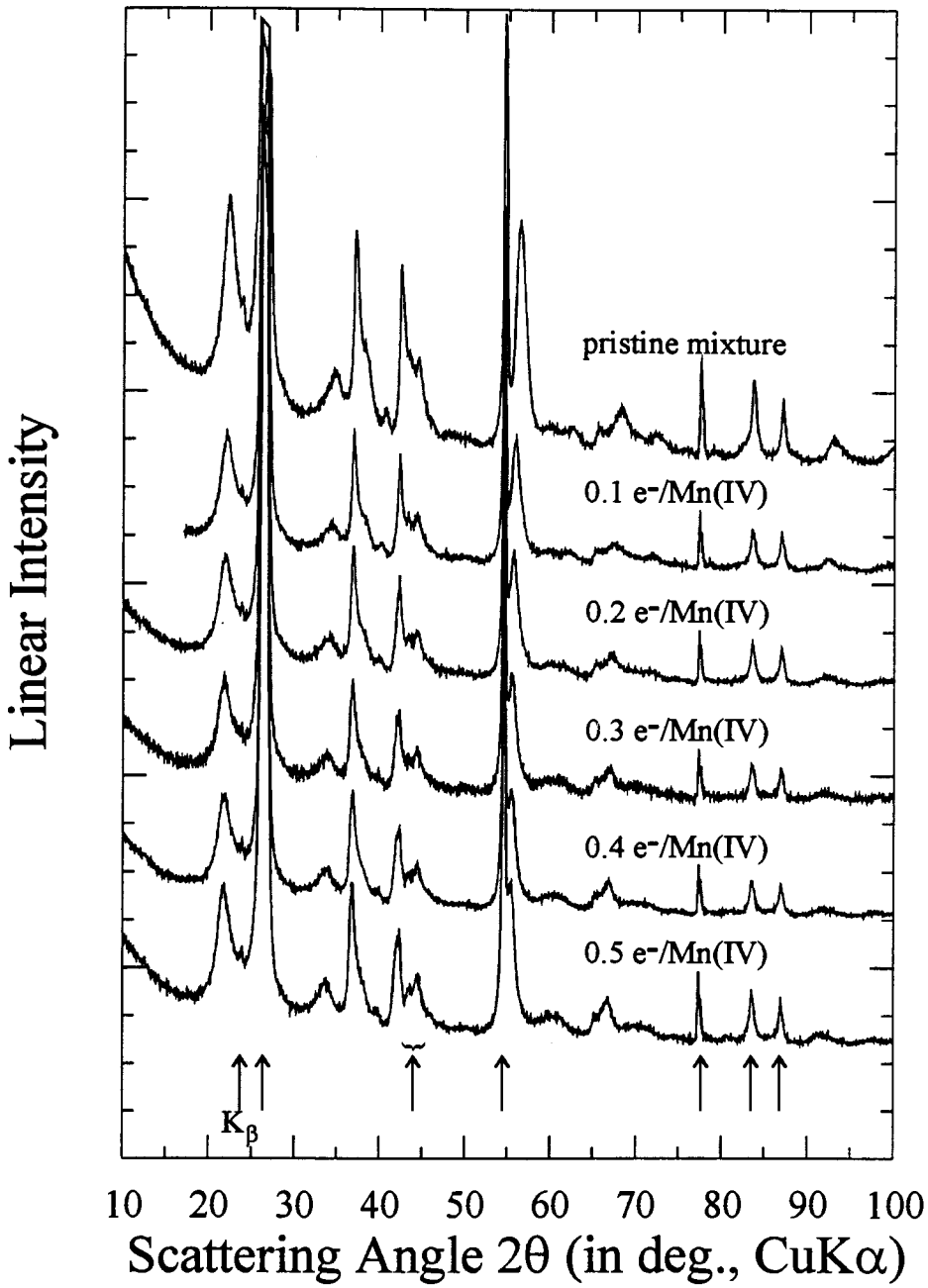

Figure 1.5: Powder X-ray diffraction patterns of the partially discharged EMD (IBA 14) mixed with graphite (Lonza KS-6), 50:50 by weight. The top curve is a pattern of the powder mixture before exposure to any electrolyte, the curves beneath show patterns from subsequently more deeply discharged materials. The electrodes were 1 g pellets of the mixture and discharged at a current of 1 mA. The arrows indicate peaks due to graphite; the leftmost arrow points to the CuKβ replica of the very strong peak at 26.5°.

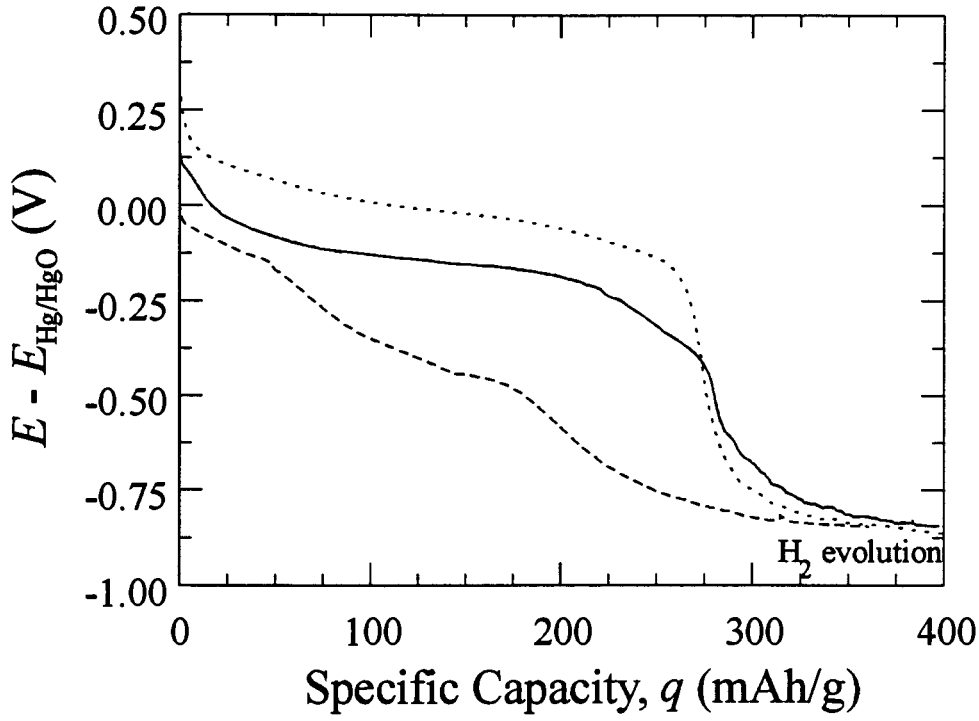

Figure 1.6: Discharge curves of three manganese dioxides. (a) TAD1 (dotted line). (b) CMD-R (solid line). (c) β-MnO_2 (dashed line). All materials were discharged at a rate of 3 mA/g. The specific capacities are based on the masses of the pristine, active materials. The cells were kept at constant temperature of 30 °C.

patterns of three NMD samples, kindly supplied by Chemetals Inc., Baltimore, MD, USA, are shown in figure 1.7. These NMDs may or may not be pure manganese dioxides, and if they are, they may not be single phase materials.

Chemical Manganese Dioxide (CMD)

A second method involves a chemical preparation. The details to obtain these so-called CMDs are usually proprietary and therefore not known to me. Generally, they involve two steps: (1) Partial oxidation of a Mn(II)-precursor to Mn(IV) by heating in air. (2) Densification by further oxidation at low temperatures in an aqueous environment. Each of these steps can be more or less extensive; in some cases only the first step is present, as in the Faradizer TR (Sedema, Tertre, Belgium), or only the second step, as in the IBA 11 (Kerr-McGee Corporation, Oklahoma City, OK,

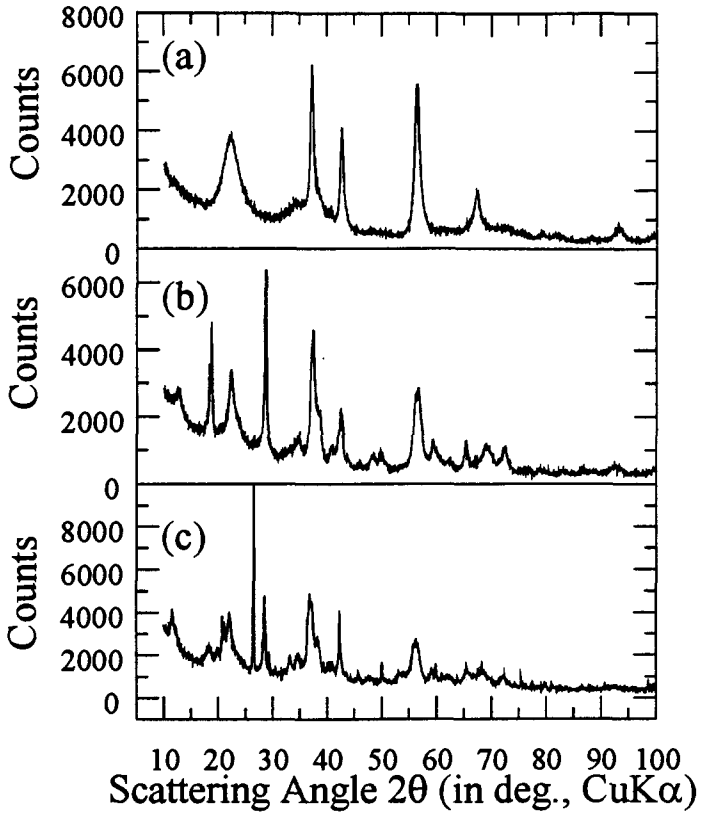

Figure 1.7: Powder X-ray diffraction patterns of three natural manganese dioxides: (a) Brazil Ore, (b) Moanda, (c) Buena Vista. Although these materials are referred to as manganese dioxides, they may contain other impurity cations so that the oxidation state of manganese may be lower than IV.

USA); see figure 1.8 for their powder X-ray diffraction patterns. A third CMD, a Sedema laboratory sample that I will refer to as CMD-R, is also shown. This CMD will be analyzed in more detail in chapter 3.

Electrolytic Manganese Dioxide (EMD)

The electrolytic method shall be discussed here in greater detail because it is the EMDs that are commonly used as electrode material in alkaline manganese dioxide cells. These EMDs are prepared by anodic (*i.e.* oxidative) deposition from an acidic Mn^{2+} solution, typically an $MnSO_4$ bath. Figure 1.9 shows a schematic of such a

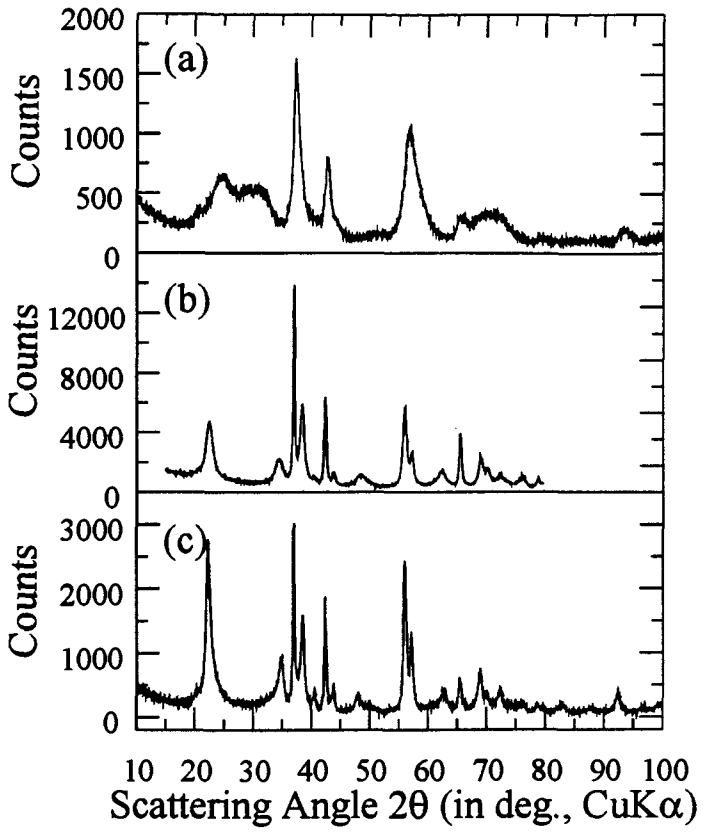

Figure 1.8: Powder X-ray diffraction patterns of three CMDs: (a) Faradizer TR, (b) IBA 11, and (c) CMD-R. As can be seen, the patterns and therefore the structures of these materials are very different from one another.

bath. The reactions at the two electrodes can be summarized as follows

$$Mn^{2+} + 2\,H_2O \longrightarrow MnO_2 + 2\,e^- + 4\,H^+ \quad \text{(anode)} \tag{1.5}$$

$$2\,H_2O + 2\,e^- \longrightarrow H_2 + 2\,OH^- \quad \text{(cathode)} \tag{1.6}$$

Parameters that affect the deposition are obviously the temperature of the bath, the size of the deposition current, the acidity, and the concentration of Mn^{2+}. But then there are less obvious ones, such as distance between the electrodes, type of material used for the current collectors at anode and cathode, and of course the possibility of dopants in the solution, which again would be proprietary information and is therefore unknown.

Three things are clear, however: (1) Preparation of EMD in an acidic aqueous

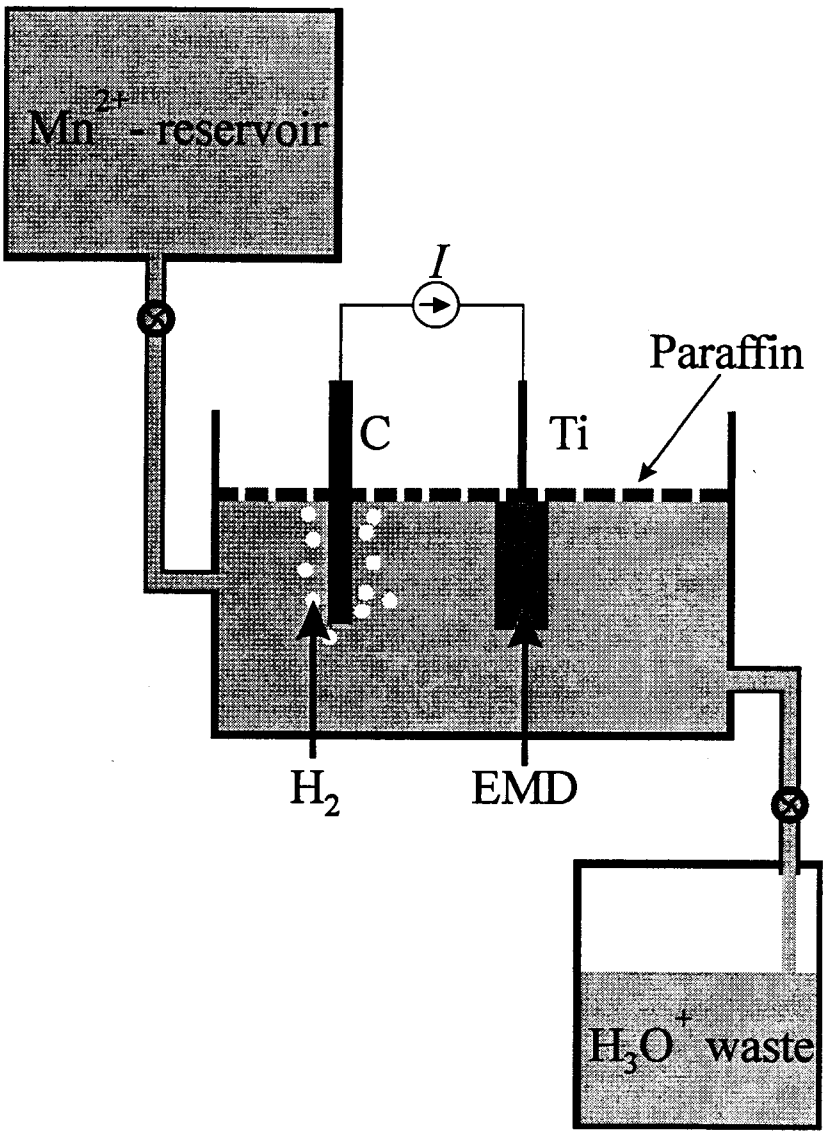

Figure 1.9: Schematic of a bath for anodic deposition of manganese dioxide (EMD-type)

solution will result in an incorporation of hydrogen and/or water in the structure. (2) Preparation of EMD in a sulfate-bath will lead to the incorporation of sulfate into the EMD (in fact, its concentration reaches up to 2% by weight). (3) It is likely that some Mn^{2+}-ions may get trapped inside the EMD without being oxidized.

There are many physical and chemical quantities by which these EMDs can be characterized. They include pore sizes, specific surface area, amount of incorporated water, average Mn oxidation state, and gravimetric density. The correlation between these quantities and the deposition conditions have recently been studied by Rodney Williams at the University of Newcastle, New South Wales, Australia [13]. The results are too vast as to be included into this thesis. One can see a qualitative trend between the evolution of some X-ray diffraction peaks and for instance bath temperature or deposition current, but the problem of correlating the structure of the deposited manganese dioxide with the deposition condition remains.

Figure 1.10 shows the powder X-ray diffraction pattern of some typical EMDs. They look similar to the EMD already seen in figure 1.6. There are, however, some subtle differences among them: The sample TAD 1 (Mitsui, Japan) shows a well defined peak at a scattering angle of 35°, whereas the same peak is broader and merges into the 37° peak for sample LSC 14/100 (Williams/Swinkels). On the other hand, sample LSC 23/40 (Williams/Swinkels) shows additional peaks at scattering angles of 12.55°, 17.90°, 28.60°. It is very desirable to understand the structural changes that lead to these changes in the X-ray diffraction pattern.

In Chapter 3, I will analyze the powder X-ray diffraction patterns in more detail and compare those of some manganese dioxides with calculated patterns based on a disorder model suggested by de Wolff in 1959 [14].

1.6 Non-Aqueous Lithium Systems

Disadvantages of the alkaline system are its poor cyclability as well as its low voltage (average 1.2 V per cell). This low voltage is of course due to the choice of the electrode materials, but can not be increased by very much due to the low voltage for water

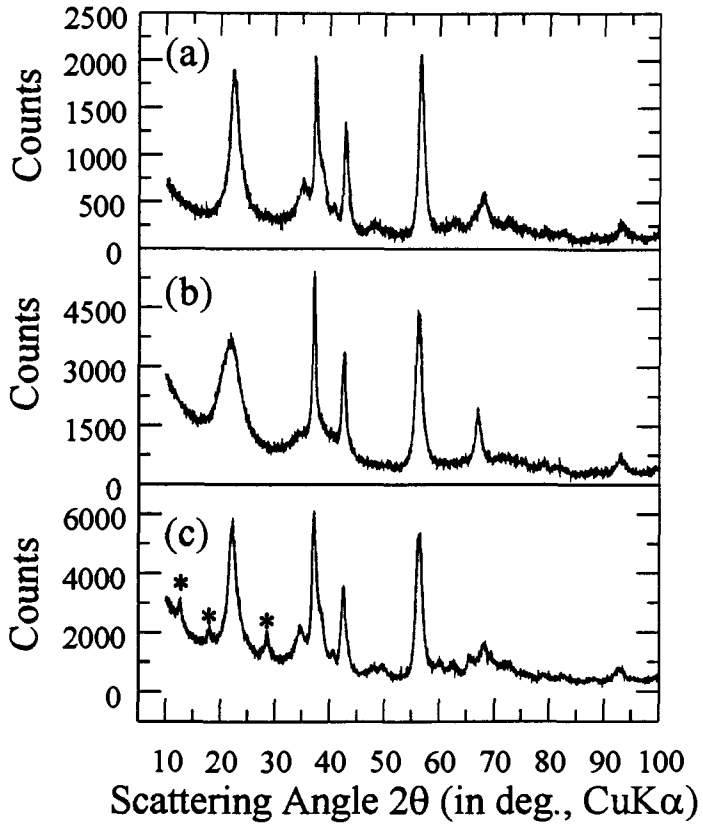

Figure 1.10: Powder X-ray diffraction patterns of some typical EMDs: (a) Mitsui TAD 1, (b) Williams/Swinkels LSC 14/100, and (c) Williams/Swinkels LSC 23/40. These EMDs were prepared under very different conditions, but their X-ray diffraction patterns look very similar. Pattern (c), however, shows additional peaks (marked with stars), which were already observed in some NMDs.

dissociation, 1.23 V.[4] If one wants to prepare cells with higher voltages one must utilize non-aqueous electrolytes.

[4]The actual voltage may be higher due to so-called overvoltages. These overvoltages can arise from impurities and surface films on the electrode, which may impede the diffusion of the electroactive species to the electrode surface. In contrast to such a kinetic barrier, films and impurities may also lead to a different chemistry (and therefore thermodynamics) at the electrolyte/electrode interface. A good examples for this latter phenomenon is the lead-acid cell with a terminal voltage of 2.1 V.

1.6.1 The Li/MnO_2 System

One such system is a non-rechargeable Li/MnO_2 cell that uses manganese dioxide similar to those in alkaline cells with an average operating voltage of about 3.0 V. These cells are rechargeable, in principle, especially before all lithium has been utilized in the discharge.[5] However, it is not desirable to recharge these Li/MnO_2 cells because lithium atoms do not plate smoothly onto the lithium metal, but form dendrites. Two things can happen:

1. The surface area of the lithium increases making the lithium metal more reactive towards the electrolyte.

2. Dendrites can penetrate the separator between anode and cathode, which can lead to lithium atoms on the cathode surface during charge. Once the charge stops, the dendrite tip is drawn back into the cathode. Such a transient internal short is typically associated with some heat release.

Although the exact circumstances are not completely understood, experience suggests that an internal short in connection with a high surface area lithium metal can lead to a thermal run-away ending with a so-called venting of the cell usually accompanied by flames.

The seriousness of such a situation is even more increased when charging a series of cells. At the moment when one cell is completely charged, while other ones are not and thus require a continuing charge current to flow through all cells, the current through the completely charged cell may lead to electrolyte decomposition and further heat generating reactions with the high surface area lithium metal.

1.6.2 The $C/LiMn_2O_4$-System

In order to avoid lithium metal in rechargeable cells, the so-called lithium-ion or rocking-chair cell was designed. Here the idea is that the anode, too, will be an insertion electrode with a potential close to that of metallic lithium. Typically the

[5] Frequently these cells are manufactured such that no lithium is left when the manganese dioxide is completely filled in order to avoid hazardous lithium metal in the discarded cell.

cell is assembled in its discharged state, that is the anode is void of lithium atoms which all reside in the cathode. One such anode would be graphite, but also non-graphitic carbons are being used and recently Fuji patented an anode based on a tin oxide.

Sony commercialized the first lithium-ion cell using $LiCoO_2$ as the cathode, and other manufacturers followed suit. Although this system shows large cyclability, 500-1000 cycles at an average open-circuit voltage of 3.7 V and a capacity of 500 mAh per AA cell, one must take care operating these cells, overcharge being a problem. Since the $LiCoO_2$ structure becomes unstable when too much lithium is extracted, the voltage during charge has to be limited to about 4.2 V, at which point about 0.5 lithium atoms per formula unit $LiCoO_2$ are left in the structure. Should one continue to charge, more lithium is extracted, but cannot be inserted into the carbon anode, as this one is completely filled (see below for determining the ratio of anode to cathode mass). The additional lithium then plates on the anode, forming metallic lithium associated with all its problems.

With the advent of the lithium-ion cells, a new technical aspect gained importance: balancing the cell. As pointed out already, in lithium-ion cells all available lithium is initially contained in one of the electrodes, whereas the other one is void of lithium. In order to determine how much of each electrode material should be used in a cell, one has to determine how much lithium one wants to take out of the initially lithium containing electrode (say, half a lithium per formula unit of $LiCoO_2$) and how much lithium can be inserted into the other electrode (for example, one lithium atom per six carbon atoms in graphite).

The ratio of the active weights of anode and cathode should be determined so that none (or as little as possible) of the material remains unused. Beside the commercial aspect of minimizing material cost, there is a performance advantage of calculating the ratio correctly: The more lithium is extracted from the cathode, the higher its potential becomes; and the more lithium is inserted into the anode, the lower its potential becomes. Therefore, one wants to empty the cathode and fill the anode as much as possible in order to obtain as large as possible a cell voltage in the charged state.

Since materials in use, typically behave differently from the theoretical expectation, one has to characterize each electrode individually in order to obtain the parameters for the balancing calculation. The proper reference electrode for these systems is lithium metal (more precisely, the redox couple Li/Li^+), typically in a 1 molar Li^+ solution, ideally in a three-electrode set-up, but the simpler two electrode system suffices. The coin cells used for this testing are described in appendix A.2.

In order to exemplify the balancing calculation, I chose a system with an $LiMn_2O_4$ cathode and a MCMB-graphite anode. $LiMn_2O_4$ is widely investigated as an alternate material for cathodes in lithium-ion cells and can be seen as a lithiated manganese dioxide, sometimes called λ-MnO_2 [15]. This material is (presently) lacking the cyclability of $LiCoO_2$, but has the advantage of lower toxicity and lower material cost. However, one can debate whether or not this is a relevant issue, as the cost of cobalt contributes only about 5% to cost of the final commercial $C/LiCoO_2$-cell. In chapter 4, I will discuss the properties of $LiMn_2O_4$ in more detail, in particular I will examine the thermodynamic stability of the charged electrode, λ-MnO_2.

The electrochemical data to characterize the electrode materials is taken from Monique Richard's M.Sc. thesis [16], which should also be consulted on further details of the cell design. Figures 1.11a and 1.11b show the first two half-cycles of $LiMn_2O_4$ and of MCMB. The fact that the second half-cycle has less capacity than the first one is an undesirable effect, and in the case of the $LiMn_2O_4$ not completely understood. In fact, the loss of the capacity of this electrode proceeds with continued cycling and is the focus of much research (see chapter 4).

In graphite, the capacity loss is limited to the first cycle. This so-called irreversible capacity is associated with side-reactions of the electrode such as the creation of a surface-electrolyte interface. Lithium atoms inside the graphite react with the solvent in the electrolyte to form compounds on the graphite surface, which hopefully will be ion-conductive, but prevent further reaction once a complete interface has been created. But also reaction of lithium with surface water on the graphite contribute to the irreversible capacity.

Although for application it is the reversible capacity of a cell that is important, for balancing the electrode weights, one needs to consider the first half-cycles. With

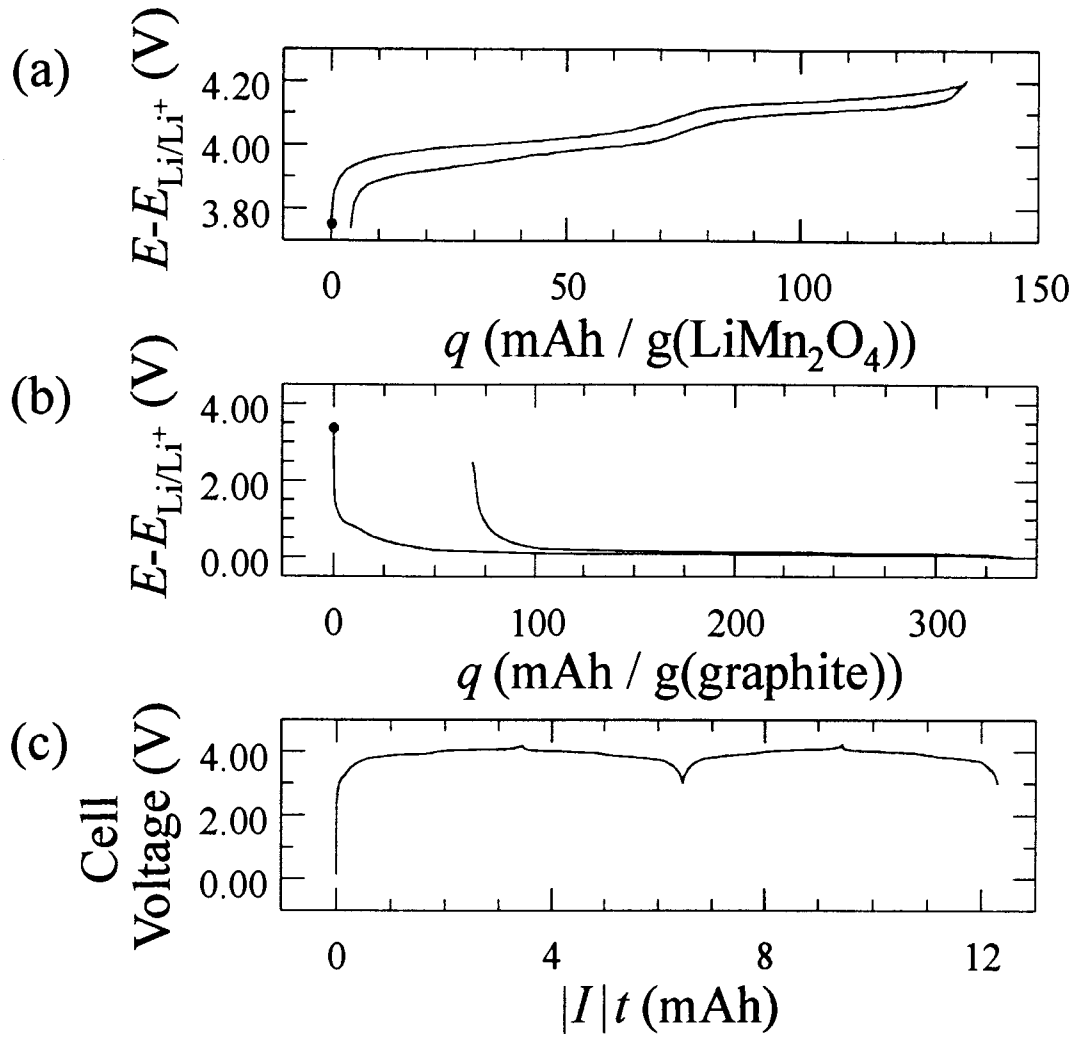

Figure 1.11: First two half-cycles of (a) $LiMn_2O_4$ against lithium and (b) graphite against lithium. The irreversible capacity of graphite in this cell is unusually high, about 80 mAh/g, instead of typically 30 mAh/g. (c) Two cycles of a lithium-ion cell with a $LiMn_2O_4$ cathode and a graphite anode.

a chosen upper voltage limit of 4.2 V for the $LiMn_2O_4$ electrode, one can extract about 135 mAh/g equivalent lithium, whereas 338 mAh/g equivalent lithium can be inserted into the graphite. Therefore, the cathode mass has to be a factor of about 2.5 larger than the graphite mass.

Since the electrode mass is typically controlled by the thickness of the films coated onto the current collector foils, it is desirable to know the packing density of the electrodes (including carbon black and binder). For $LiMn_2O_4$ it is typically 2.6 g/cm^3,[6] whereas for graphite is about 1.3 g/cm^3.

Figure 1.11 shows the first two cycles of the finished lithium-ion cell with graphite as the anode and $LiMn_2O_4$ as the cathode. An interesting feature is the fact that the initial voltages of both the Li/$LiMn_2O_4$ cell and the Li/graphite cell were about 3.5 V. Therefore the initial voltage of the graphite/ $LiMn_2O_4$-cell should be close to 0 V, as is observed.

1.7 Systems for Energy Storage

1.7.1 Batteries

The voltage of a certain cell design is fixed by its chemistry, its capacity determined by the size of the cell. In order to create an effective device to store electrical energy, one needs to be able to control the voltage of the storage device and its capacity. This can be done by connecting cells in series or in parallel, respectively, (or both) to make a so-called battery.

Since each cell shows highest capacity at small discharge currents (that is close to equilibrium), a design of parallel cells distributes a large current over several cells with smaller individual currents; the so-called rate capability increases.

A battery can therefore deliver an arbitrary amount of power ($P = \int I\,dV$) and store an arbitrary amount of energy ($W = \int P\,dt$) at a selectable voltage, V. The only limitation is the size and weight of the final battery — that is why the lead-acid system may not be a viable option for electric vehicles, unless good marketing

[6] $LiCoO_2$ wins here too. Its packing density is about 3.0 g/cm^3.

experts will be able to sell an electric vehicle with an operation range limited to 100 km before recharge is required. In fact, such an operation range may not be undesirable, considering that many cars are used to commute to and from work not further than 50 km away from home. A recent survey actually comes to the conclusion that there is a significant market for low-range electric vehicles in California [17].

When selecting a voltage for a particular application, one must keep in mind that bigger is not always better. Although a higher voltage may be seen as increasing the quality of the stored energy because a larger variety of applications could be serviced, one has to realize that some applications such as semiconductor TTL devices require a voltage range between 3.5 V and 5 V. In order to match voltages required by a certain application with those supplied by a battery, one typically needs additional, usually lossy, circuitry such as DC-DC converters. However, if a single cell can supply the voltage required by an application, then the additional circuitry as well as the complications associated with charging and discharging a battery can be avoided. In this sense, lithium-ion technology seems ideally suited for nowadays CMOS electronics.

If one needs to recharge a battery, it will be desirable to achieve this as quickly as possible. One would run a current (as large as possible) through it, until the "lost" energy is regained. For cells connected in parallel, the initial voltages and therefore states of charge are the same, if the voltage profiles are sloped (this may not be the case for NiCd-batteries, whose voltage curves are very flat, and cause problems). However, during charge the charging current may lead to different terminal voltages at each of the cells as the internal resistance of each of the cells may be different; in particular, one of the cells may have become overcharged and damaged. This problem becomes typically more serious towards the end of the battery's life as the capacity per charge/discharge cycle decreases at a different rate for the different cells within the battery pack. For a serial design, not all cells may have been discharged to the same extent, so that charging them at high rates may lead to overcharging of individual cells as well.

As was shown before, overcharged cells may become very reactive, several of them connected would be a safety hazard. The solution is to monitor each individual cell in the battery during charge and decrease the charging current as needed to

obtain a uniform state of charge. Motorola recently developed integrated circuits (*e.g.* MC33345 to MC33348) that perform these monitoring tasks for batteries of up to four cells.

1.7.2 Capacitors

As discussed above, one important drawback of an electrochemical cell, and therefore of a battery, is that their rate capabilities may be limited. The maximum current that can be drawn from a battery depends in part on the cell chemistry; for instance, the conductivity of aqueous electrolytes as in lead-acid batteries is one or two orders of magnitude higher than in non-aqueous lithium-ion system, but it is these latter system that are of particular interest as energy storage devices because of their high specific energy.

On the other hand, classical capacitors can be charged and discharged at currents that are limited by the load resistance, R_{L}, at least at times, t, small compared to $R_{\mathrm{L}}C$, where C is the capacitance of the capacitor. Since the load resistance is application dependent, the goal must be to design capacitor with as large a capacitance as possible.

So-called supercapacitors fulfill this requirement; for instance PolyStor's Aerocapacitor A-14500 (AA-size) has capacitance of 7 F. The principle behind supercapacitors is very simple; they utilize large-surface-area carbons as electrode materials in conjunction with non-aqueous, liquid electrolytes. Unlike solid dielectrics, which would only utilize the small geometric electrode area, the liquid "sees" the much larger surface of the carbons. Such a large surface will then lead to a large capacitance as is well known for parallel plate capacitors. Unfortunately, the internal resistance of these devices, arising from the finite time required to (re-)polarization the electrolyte, is not insignificant and effectively limits the current that can be drawn.

However, capacitors and supercapacitor do not retain their charges as long as batteries do; their self-discharge is comparatively high. Therefore, capacitors have to be used in conjunction with batteries, but that is exactly what they are needed for. Should the application demand more power for a short period of time, then

the capacitor can supply the necessary energy and is recharged by a parallel battery afterwards. The capacitor can act as a so-called load-levelling device for the battery as long as the internal resistance of the battery is substantially higher than that of the (super)capacitor. In fact, the capacitor can also aid during recharge, where it can take up current surges that may damage batteries. Such an energy storage solution that combines various energy storage devices is usually referred to as a hybrid system.

1.7.3 Fuel Cells

Another energy storage/delivery system that I should mention, if only very briefly, is the fuel cell. Here, the energy is not stored in form of electrical energy, but in form of chemical energy: Water is dissociated into hydrogen and oxygen, which are then stored. When these two gases are supplied to a fuel cell, they react catalytically and the decrease of the Gibbs free energy is directly converted into electrical energy; one electron per hydrogen atom at a voltage of 1.23 V. To increase the voltage, one combines several cells into a so-called fuel cell stack.

The power that such a stack can supply is largely dependent on how fast the two gases (oxygen and hydrogen) can react. If oxygen is taken from the air, instead of from a pressurized storage tank, a high power output involves the utilization of a compressor for the air intake, which can take up a large portion of the energy supplied by the fuel cell stack.

There are many more issues surrounding a fuel cell, such as the problems of hydrogen production, hydrogen storage, safety of hydrogen storage, and infrastructure of hydrogen supply. To discuss these issues is beyond the scope of this thesis, but were worth mentioning to bring batteries as energy storage devices into a better perspective.

1.7.4 Zero-Emission Vehicles

Before concluding this chapter, it must be pointed out that the main driving force behind the development of new energy storage solutions and the improvement of old

ones is the desire[7] or the necessity[8] or the mandate[9] for vehicles not to use combustion engines, but engines that do not have any exhausts except for possibly H_2O, so-called zero-emission vehicles.

At present, car manufacturers are very reluctant to promote zero-emission vehicles because with today's technology they will not have the same performance as cars with gasoline or diesel engines. However, with advances in the field of rechargeable batteries, supercapacitors and fuel cells, viable solutions should become available in the intermediate future. In order to be fruitful, the energy supply side must not be forgotten and the infra-structure to convert solar energy into electrical or chemical energy must be developed now in order to be available then.

When considering energy conversion/storage/delivery solutions, it will be important not to look at isolated options, but at integrated concepts to arrive at a useful and viable system.

[7]Of concerned users

[8]Fossil fuel are running out

[9]For example, resolution 90-58 adopted by the California Air Resources Board

Chapter 2

X-ray Diffraction of Powdered Materials

2.1 X-rays

In late 1895, Wilhelm Conrad Röntgen discovered that a fluorescent screen was illuminated when brought close to a vacuum tube, which was covered with thin, black cardboard while electrons were accelerated towards the anode. Members of the scientific community and (probably for the first time in history) ordinary citizens in all countries were grabbed by the fascination and the excitement that this discovery brought: One could see objects that were hidden to the naked eye. The news of these "Roentgen-rays" made it across the Atlantic Ocean [18] shortly after Röntgen had sent out preprints of his scientific paper on the subject [19] in late December 1895. Röntgen labelled the to-that-date unknown radiation that was responsible for the observed phenomenon as X-radiation. This discovery made Röntgen the first Physics Nobel Laureate in 1901.

It took 17 years, however, and Max von Laue at the Institute for Theoretical Physics at the University of Munich, led by Arnold Sommerfeld, to reason that if these X-rays were electromagnetic waves, one should be able to observe interference effects when diffracted by a periodic array whose equal spacings are comparable to the wavelength of the X-rays. Laue knew from density measurements and molecular

weights that crystals should have such a spacing and suggested to his experimental colleagues Walther Friedrich and Paul Knipping to build a set-up to test his hypothesis. The initial experiments were performed on a blue vitriol crystal ($CuSO_4 \cdot 5H_2O$), later on zinc blende (ZnS), rocksalt (NaCl), PbS, and diamond [20]. Laue's prediction of the diffraction of X-rays was successful and Laue was awarded the Nobel Prize in Physics in 1914.

Now we know that X-rays are electromagnetic waves, which can generally be produced by a dipole transition of electrons in an atom. If the energy difference, ΔE, between initial and final state is large enough, then the wavelength $\lambda = hc/\Delta E$ (h: Planck's constant, c: the speed of light) becomes small and one obtains X-rays for $\lambda \lesssim 100$ Å. If the final state is in the atom's K-shell, one obtains K-radiation, if the initial state was in the L-shell, the radiation is Kα.

The final states are created by bombarding the X-ray producing atoms with a flux of high-energy electrons that will excite core electrons into the vacuum. For a dipole transition the electron has to observe certain selection rules (change of orbital angular quantum number: ± 1; change of total angular momentum quantum number: $0, \pm 1$) so that there are two distinct Kα radiations for a copper atom. They are labelled as CuKα_1 and CuKα_2 with respective wavelengths of 1.540562(2) Å* and 1.544390(2) Å* [21]. The star at the Ångström unit indicates that these wavelengths were measured with respect to the tungsten X-ray standard, whose measured wavelength has some uncertainty. However, the difference between 1 Å* and 1Å is small so that I will ignore it in my thesis and set 1Å*=1Å.

The ratio of the two associated transition rates is exactly 2:1, leading to a weighted average for the wavelength of CuKα of $\lambda = 1.5418$ Å. This averaging appears unmotivated at this point, especially since the natural line width is $\Gamma \approx 0.9$ eV [22], but will become understandable later. The spread in energy is related to the life time τ of the L-states by $\Gamma\tau = \hbar$ [23]. Therefore the coherence length is

$$c\tau \approx 2200\text{Å}. \tag{2.1}$$

Additionally, there are weaker transitions from, for instance, the M- to the K-shell, so called Kβ-radiation (for copper the wavelength is 1.3926 Å), as well as a contin-

uous background due to the *bremsstrahlung* background created by the decelerating bombarding electrons.

2.2 The θ - θ Set-up for X-ray Diffraction

A diffractometer for powder diffraction consists of an X-ray tube and a detector that lie on the same circle of radius r_g, the so-called goniometer radius. More precisely, it is the focus of the tube and the receiving slit of the detector that lie on the circle, which defines the x, z-plane and whose centre lies at the origin of the coordinate system. The powder sample is placed at the origin in the x, y-plane.

For the measurements described in this thesis, two different diffractometers were used, a Siemens D5000, whose θ-θ set-up is depicted in figure 2.1, and a Philips PW 1730, whose θ-2θ set-up is slightly different. The X-ray tube of the PW 1730 is stationary with respect to the lab and both the sample plane as well as the detector are rotated by θ and 2θ, respectively. Further, the PW 1730 is not equipped with an antiscatter slit, which would prevent X-rays scattered by *e.g.* air molecules in the path of the incident beam from entering the receiving slit. The goniometer radius is 217.5 mm for the D5000, and is 173 mm for the PW 1730.

The X-rays are produced by electrons hitting the target at the focus F, typically a so-called line source with an extent of a centimeter or so in the y-direction. Each point on the line emits a spherical wave front that is restricted by an aperture, the divergence slit, to an opening angle $2\Delta\theta_{\text{inc}}$. The divergence in the y-direction is limited by a set of lamellae parallel to the x, z-plane, so-called Soller slits. This y-extent of the beam, the so-called height of the beam, must be considered in detail in Small-Angle-Scattering experiments (see for example reference [24]). For wide-angle measurements discussed here, it merely affects the width of diffraction peaks and becomes negligible, if other broadening mechanisms dominate. From now on, I will discuss the set-up as though it was two-dimensional in the x, z-plane.

The ray passing through the center of the slit intersects the origin at an angle θ with the negative x-axis. The width of the divergence slit is generally small enough compared to the goniometer radius, r_g, that the wave incident upon the sample can

be treated as a plane wave with a finite coherence length.

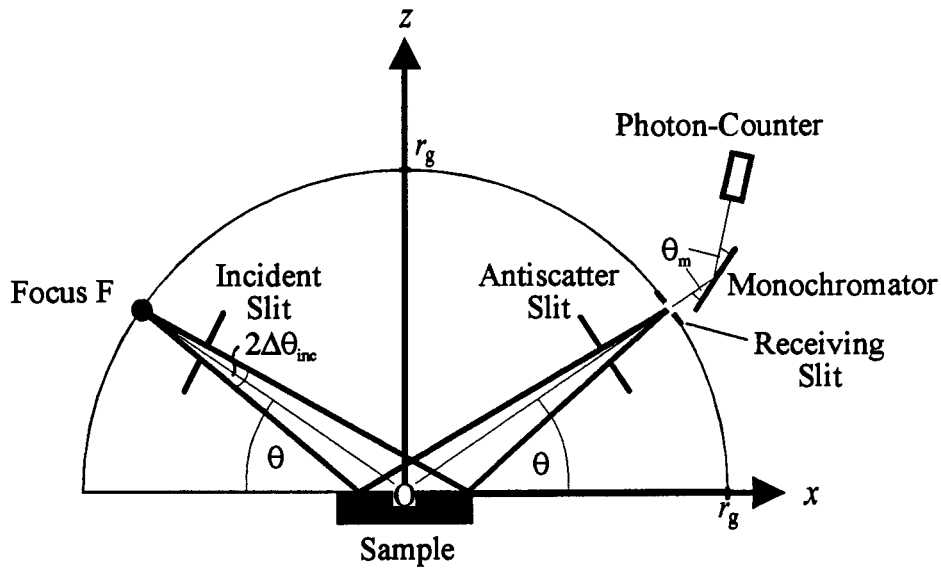

Figure 2.1: The θ-θ set-up. X-rays are emitted at the focus and are incident upon the sample placed at the centre of the goniometer circle, where they are scattered. Some of the scattered X-rays enter the receiving slit and are detected. In this set-up, the sample holder is stationary, whereas the focus (X-ray tube) and the receiving slit (detector) move on the goniometer circle. The monochromator selects a particular wavelength.

The main purpose of the divergence slit is to restrict the incident wave to a range on the x-axis that is actually covered with the sample. At angles $\theta < \theta_{\min}$ with $\sin\theta_{\min} = r_g\, 2\Delta\theta_{\text{inc}}/w_{\text{holder}}$, where w_{holder} is the width of the sample holder, the footprint of the beam ($\propto 1/\sin\theta$) becomes so large that only part of the beam irradiates the sample. For a uniform energy flux density, I_0, across the incident beam, the irradiance, I_{inc}, of the sample is given by

$$I_{\text{inc}} = I_0 \frac{\sin\theta}{\sin\theta_{\min}} \qquad \text{for } \theta < \theta_{\min}. \tag{2.2}$$

It is therefore desirable to choose the divergence slit such that features in the measured pattern occur at angles larger than $\theta_{\min}$. Table 2.1 summarizes various values of $\theta_{\min}$ for a holder width of 20 mm.

Some of the X-rays scattered by the sample will be collected by the so-called

Table 2.1: Some values of $2\theta_{\text{min}}$ for $w_{\text{holder}} = 20$ mm and $r_{\text{g}} = 217.5$ mm.

$2\Delta\theta_{\text{inc}}$	$2\theta_{\text{min}}$
0.25°	5.45°
0.50°	10.90°
0.75°	16.40°

receiving slit of width w_{rec}. The receiving slit is placed on the goniometer radius in such a way that a ray emitted at the origin in the x, z-plane makes an angle θ with the x-axis when it enters the centre of the receiving slit. The total deflection of the incident beam to the received beam is 2θ, the so-called scattering angle. A wider receiving slit increases the number of X-ray photons entering the photon-counter and therefore improves the signal-to-noise ratio, but decreases the angular resolution of the measurement. The scattering angle will have an uncertainty of $\pm\Delta(2\theta)$ due to the receiving slit, where

$$\Delta(2\theta) \approx \frac{w_{\text{rec}}}{2r_{\text{g}}}. \tag{2.3}$$

Other sources that decrease the resolution include the dichromatic nature of the CuKα-radiation, the natural line widths of α_1- and α_2-radiation, the width of the divergence slit and, as mentioned before, the finite gap between the lamellae of the Soller slits.

In the next section, I will use the so-called scattering vector, which is defined as

$$\vec{s} = \frac{1}{\lambda}\left(\hat{n}_{\text{scat}} - \hat{n}_{\text{inc}}\right), \tag{2.4}$$

where $\hat{n}_{\text{inc}}$ is the direction of the ray emitted by the focus and incident at a point $(x, 0, z)$ within the sample, and $\hat{n}_{\text{scat}}$ is the direction of the ray emitted at this point and incident at the receiving slit. For $x = z = 0$, one sees that $\hat{n}_{\text{inc}} = \hat{x}\cos\theta - \hat{z}\sin\theta$ and $\hat{n}_{\text{scat}} = \hat{x}\cos\theta + \hat{z}\sin\theta$ such that the length of the scattering vector, s, is given by $2(\sin\theta)/\lambda$. For a point $(x, 0, z)$ within the sample where $|x/r_{\text{g}}|$ is small enough, the length of the scattering vector can be evaluated as

$$s = \|\vec{s}\| = \frac{2\sin\theta}{\lambda}\left(1 - \frac{z}{r_{\text{g}}}\frac{\cos^2\theta}{\sin\theta}\right). \tag{2.5}$$

One sees that at a given goniometer setting of 2θ, there are contributions from scattering vectors with different lengths, if there are scatterers at various positions of z.

If $2\theta_{\text{theo}}$ is the scattering angle at which one would theoretically expect a certain scattering event, characterized by s, to be measured for $z = 0$, then the actual scattering angle of observation is

$$2\theta = 2\theta_{\text{theo}} + \frac{2z}{r_g}\cos\theta. \tag{2.6}$$

This effect is known as an off-axis shift.

In the beginning of the last section, it was pointed out that CuKα-radiation is di-chromatic so that a scattering event in the sample characterized by s would lead to observation at two different scattering angle, $2\theta_{\alpha_1}$ and $2\theta_{\alpha_2}$. The difference between these two angles of observation increases with increasing scattering angle so that one could resolve the two wavelengths, if the scattering event has a sufficiently small width about s. This will indeed be observed for highly crystalline samples and sufficiently narrow receiving slits. However, for disordered samples, whose scattering behaviour I consider in this chapter, the width Δs about s outweighs the peak splitting due to the two wavelengths. The use of the weighted average is therefore justified.

2.3 Interaction of X-rays with Matter

2.3.1 Plane Waves

As argued above, the X-rays incident upon the sample are considered to be a plane wave. In general, the propagation of electromagnetic waves in free space is described by Maxwell's equations, which imply that the direction of propagation $\hat{n}$, the electric field vector $\vec{E}$ and the magnetic field vector $\vec{B}$ are always mutually perpendicular: $\vec{B} = \hat{n} \times \vec{E}/c$, where c is the speed of light in vacuum.

Consequently, it suffices to describe electromagnetic waves by the electric field vector alone. A plane wave is given by:

$$\vec{E}(t,\vec{x}) = \vec{\epsilon}\|\vec{E}\| \exp\left\{\mathrm{i}\left(\frac{2\pi}{\lambda}\hat{n}\cdot\vec{x} - \omega t\right)\right\}, \tag{2.7}$$

where $\vec{\epsilon}$ gives the polarization of the wave. In free space the frequency, ω, and the wavelength, λ, are related by the speed of light in vacuum: $\omega = 2\pi c/\lambda$. The speed, v, of propagation in matter is generally different from c, while the frequency remains

the same, leading to a different wavelength. For X-rays under consideration here, $v/c = 1 - 7.6 \times 10^{-6} \approx 1$ [25] so that I will approximate the wavelength in matter to be the one in free space.

2.3.2 Scattering by Electrons

The electric field associated with an electromagnetic wave accelerates electrons, which happen to be in the path of the wave. The acceleration of the ν^{th} electron at the position $\vec{x}^{(\nu)}$ due to an incident plane wave can be described non-relativistically as long as the amplitude of the electric field is not too large. The acceleration is then given by

$$\vec{a}^{(\nu)}(t) = -\frac{e}{m}\vec{E}_{\text{inc}}(t, \vec{x}^{(\nu)}) = -\frac{e}{m}\vec{\epsilon}_{\text{inc}}\|\vec{E}_{\text{inc}}\| \exp\left\{\mathrm{i}\left(\frac{2\pi}{\lambda}\hat{n}\cdot\vec{x}^{(\nu)} - \omega t\right)\right\}, \tag{2.8}$$

where e is the magnitude of the electronic charge and m is the mass of the electron.

The electrons will re-emit a spherical electromagnetic wave of the same frequency as the incident wave. If the speed of these accelerated electrons is small compared with the speed of light, the scattered wave produced by the ν^{th} electron is given by [26]

$$\vec{E}^{(\nu)}_{\text{scat}}(t', \vec{x}') = -\frac{\mu_0 e}{4\pi}\left[\frac{\hat{n}_{\text{scat}} \times (\hat{n}_{\text{scat}} \times \vec{a}^{(\nu)}(t))}{\|\vec{x}' - \vec{x}^{(\nu)}\|}\right], \tag{2.9}$$

where $\vec{x}'$ is the position of the observer (*i.e.* the receiving slit), $t' = t + \|\vec{x}' - \vec{x}^{(\nu)}\|/c$ is the time of observation, and μ_0 is the permeability of free space, $\mu_0 = 4\pi \times 10^{-7}$ Vs/Am. The direction $\hat{n}_{\text{scat}}$ into which scattering must occur so that it is observed at $\vec{x}'$ is given by

$$\hat{n}_{\text{scat}} = \frac{\vec{x}' - \vec{x}^{(\nu)}}{\|\vec{x}' - \vec{x}^{(\nu)}\|}. \tag{2.10}$$

The energy flux density due to the scattering process, averaged over the period of oscillation, is given by the real part of the complex Poynting vector

$$\vec{S}_{\text{scat}}(t') = \vec{E} \times \frac{1}{\mu_0}\vec{B}^* = \frac{1}{\mu_0 c}\left\|\sum_{\nu}\vec{E}^{(\nu)}_{\text{scat}}(t')\right\|^2 \hat{n}_{\text{scat}}, \tag{2.11}$$

where I have added the amplitudes of the scattered waves, which is correct for scatterers within a volume of a linear dimension less than the coherence length. The

power $\mathrm{d}P$ scattered per unit solid angle $\mathrm{d}\Omega$ is then

$$\frac{\mathrm{d}P}{\mathrm{d}\Omega} = \|\vec{S}_{\mathrm{scat}}\| \, \|\vec{x}' - \vec{x}^{(\nu)}\|^2 \tag{2.12}$$

$$= I_{\mathrm{inc}} r_{\mathrm{e}}^2 \, \|\hat{n}_{\mathrm{scat}} \times (\hat{n}_{\mathrm{scat}} \times \vec{\epsilon}_{\mathrm{inc}})\|^2 \tag{2.13}$$

$$\left| \sum_{\nu} \exp\left\{ \mathrm{i} \left(\frac{2\pi}{\lambda} \hat{n}_{\mathrm{inc}} \cdot \vec{x}^{(\nu)} - \omega \left(t' - \frac{\|\vec{x}' - \vec{x}^{(\nu)}\|}{c} \right) \right) \right\} \right|^2 ,$$

where $r_{\mathrm{e}} = 2.818 \times 10^{-15}$ m is the classical electron radius and $I_{\mathrm{inc}} = \|\vec{E}_{\mathrm{inc}}\|^2 / \mu_0 c$ is the energy flux density of the incident beam . The argument of the exponential function can be simplified by using the approximation $\|\vec{x}' - \vec{x}^{(\nu)}\| \approx \|\vec{x}'\| - \hat{n}_{\mathrm{scat}} \cdot \vec{x}^{(\nu)}$ and using $\omega/c = 2\pi/\lambda$, so that one obtains

$$\exp\left\{ -\mathrm{i} \frac{2\pi}{\lambda} (\hat{n}_{\mathrm{scat}} - \hat{n}_{\mathrm{inc}}) \cdot \vec{x}^{(\nu)} \right\} \exp\left\{ \mathrm{i} 2\pi\omega \left(t' - \frac{\|\vec{x}'\|}{c} \right) \right\} , \tag{2.14}$$

where the second term is independent of ν and can be taken out of the summation so that its square modulus is 1; then $\frac{\mathrm{d}P}{\mathrm{d}\Omega}$ becomes independent of t', as it should for a time-averaged quantity.

Further, during the time of measurement at a certain observation point $\vec{x}'$, many different incident wavetrains are scattered by the electrons. One must therefore perform a second time-averaging, this time on a large time scale. This averaging leaves all terms unaffected, except for the so-called polarization factor, which in the case of unpolarized incident radiation becomes

$$\left\langle \|\hat{n}_{\mathrm{scat}} \times (\hat{n}_{\mathrm{scat}} \times \vec{\epsilon}_{\mathrm{inc}})\|^2 \right\rangle = \frac{1}{2} \left(1 + \cos^2 2\theta \right) . \tag{2.15}$$

The energy that is received over the time of measurement at the observation point $\vec{x}'$ is proportional to

$$i(\vec{s}) = (1 + \cos^2 2\theta) \left| \sum_{\nu} e^{-\mathrm{i} 2\pi \vec{s} \cdot \vec{x}^{(\nu)}} \right|^2 , \tag{2.16}$$

which I will call "intensity" for short.

So far, I have considered elastic scattering of the incident wave, but since an X-ray photon carries momentum that can be (partially) transferred to an electron, the photon may lose some of its energy to the increased kinetic energy of the electron. Some of the emitted X-rays have a therefore a larger wavelength (Compton scattering).

2.3.3 Scattering by Atoms

In case of a continuous charge distribution such as in an atom, the force equation that determines the acceleration of the electrons changes to

$$m\vec{a}(t,\vec{x}) = eC(\vec{x})\,\mathrm{d}^3x\,\vec{E}_{\mathrm{inc}}(t,\vec{x}), \tag{2.17}$$

where $eC(\vec{x})$ is the charge density due to electrons at point $\vec{x}$. Then the $\sum_\nu$ in equation (2.16) is to be replaced by $\int \mathrm{d}^3x$

$$\int \mathrm{d}^3x e^{-\mathrm{i}2\pi\vec{s}\cdot\vec{x}}\,C(\vec{x}), \tag{2.18}$$

which is effectively the Fourier transform of the electron density in the illuminated volume.

For an atom, the electron density is given by the square modulus of the electrons' wavefunction. The density is typically assumed to be spherically symmetric such that its Fourier transform, the so-called atomic form factor, $f(s)$, will only depend on the length of the scattering vector and not its direction:

$$f(s) = \int r^2\,\mathrm{d}r\,C(r) \oint \sin\psi\,\mathrm{d}\psi\,\mathrm{d}\phi\,e^{-\mathrm{i}2\pi sr\cos\theta} = \int \frac{C(r)\sin sr}{s}\,r\mathrm{d}r. \tag{2.19}$$

For $s = 0$, the form factor is just the number of electrons in the atom. Other values have been determined based on wavefunction calculations for the various atoms and the parameters for the following equation are tabulated in the *International Tables*[27],

$$f(s) = \sum_{j=1}^{4} a_j \exp\left(-b_j\left(\frac{s}{2}\right)^2\right) + c \tag{2.20}$$

The atomic form factor for the ion O^{2-} was obtained from reference [28]. Figure 2.2 shows the dependence of the form factor on the scattering angle for CuKα radiation.

Again, there are other processes that occur in addition to the elastic scattering. These additional scattering processes give rise to a small correction to the atomic form factor: the so-called anomalous scattering factor $\Delta f = \Delta f' + \mathrm{i}\Delta f''$ [29]. Compton scattering is one contributor, but not as prominently a one as with free, unbound electrons. In atoms, a new process, called fluorescence, arises where the incident X-ray photon is absorbed by exciting a core electron into the vacuum, then an X-ray

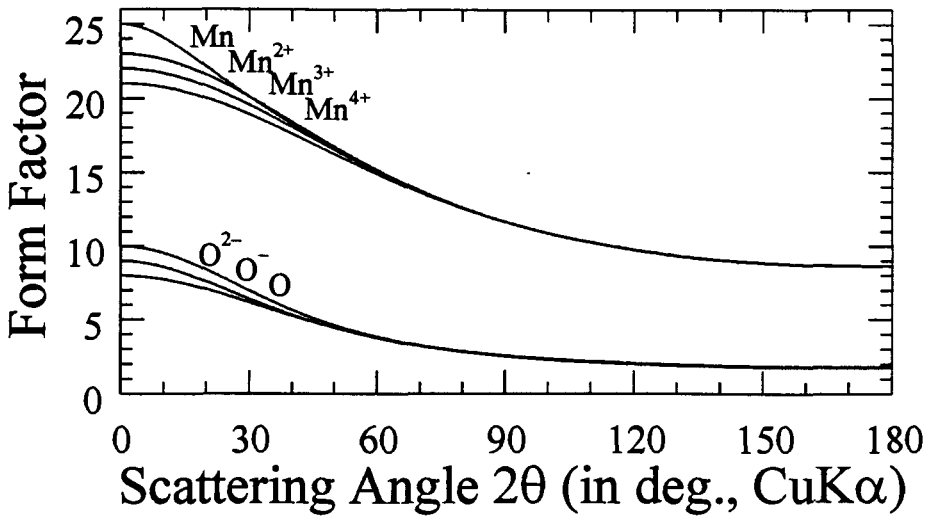

Figure 2.2: Variation of the atomic form factors of manganese and oxygen atoms and ions with scattering angle for CuKα radiation. From the top to the bottom, the curves are for the neutral Mn, Mn^{2+}, Mn^{3+}, Mn^{4+}, then for O^{2-}, O^{-}, and neutral O.

Table 2.2: Mass absorption coefficients of some elements for CuKα radiation as given in reference [30]

Element X	$\left(\frac{\mu}{\rho}\right)_X$ in cm^2/g
Mn	284
O	12.7
C	5.50
Li	0.68

photon characteristic of the scattering atom is emitted when an outer-shell electron decays into the core. The cross section for such an absorption process becomes large when the binding energy of the core electron is close to, but still smaller than or equal to the energy of the incident photon.

Due to the absorption process, the energy flux density of the incident X-ray beam decays exponentially as the beam enters matter, according to

$$I_{\text{inc}}(t) = I_{\text{inc}}(0)e^{-\mu z/\sin\theta}, \tag{2.21}$$

where $z/\sin\theta$ is the depth to which the X-rays penetrate the sample and μ is the so-called linear absorption coefficient. This coefficient for a mixture of atoms of

mass density ρ and mass m can be obtained from the tabulated mass absorption coefficients, $(\mu/\rho)_X$, by using

$$\mu = \frac{\rho}{m} \sum_X \left(\frac{\mu}{\rho}\right)_X m_X, \tag{2.22}$$

where m_X and $(\mu/\rho)_X$ are the mass and the mass absorption coefficients of element X in the material. In table 2.2, these coefficients are listed for some elements and CuKα radiation.

As can be seen from table 2.2, the absorption becomes large for manganese compounds when using CuKα-radiation. At the same time the fluorescence increases leading to an undesired radiation background. In order to cut this fluorescence background, it is necessary to employ a monochromator at the detector side of the set-up. Such a monochromator is selective for CuKα radiation and therefore removes the background arising from manganese atoms, for instance. The monochromator is a second scatterer whose incident radiation is partially polarized. One therefore has to re-calculate the polarization factor, which I will label $\mathcal{P}$, and finds that

$$\mathcal{P} = 1 + \cos^2 2\theta \cos^2 2\theta_{\mathrm{m}}, \tag{2.23}$$

where θ_{m} is defined in figure 2.1. The intensity given in equation (2.16) changes to

$$i(\vec{s}) = \mathcal{P} \left| \int_{V' \approx l_c^3; z' \approx z} \mathrm{d}^3x'\, e^{-\mathrm{i}2\pi \vec{s}\cdot\vec{x}'} C(\vec{x}') \right|^2 e^{-\mu z/\sin\theta}, \tag{2.24}$$

where V' is the volume that is integrated over and l_c is the coherence length of the X-rays. It is assumed that the absorption over the volume V' is small.

2.3.4 Scattering by Solids

In the experiment that I will describe, single-phase, powdered solids will be used. These single-phase powders consist of small crystals that are essentially identical, except that they may have different orientations in space. Within one crystal the scattered X-rays add coherently and the intensity from this one crystal is described by the square modulus of the Fourier transform of its electron density multiplied by the polarization factor. X-rays scattered from different crystals have a random phase

relation so that one has to add their intensities and not their amplitudes, even if they are less than the coherence length of the incident X-ray apart (see next section). In this thesis, the word "crystal" will not be used in the usual sense of a periodic arrangement of unit cells, but rather will refer to a connected arrangement of atoms in space that shows the same scattering characteristic throughout its volume.

When adding the intensities, one has to pay special attention to those arising from crystals deep in the sample holder. If the absorption is low, X-rays penetrating deeply into the solid still have an appreciable energy flux density, but a scattering event that one would expect at a certain scattering angle $2\theta_{\text{theo}}$ will be off-axis shifted. However, the intensity arising from the scattering process from deep inside the holder will have a smaller intensity than the same process at surface. This leads to a low-angle tail, for instance, in the very strong first peak in the graphite pattern.

Since I will be dealing with manganese compounds that have a large absorption coefficient no correction due to absorption (or the lack of the same) will be necessary. All scattering can be expected to arise from the $z = 0$-plane, assuming of course that the sample holder and the goniometer are properly aligned.

As I pointed out before, the incident energy flux density is independent of θ (as long as $\theta > \theta_{\text{min}}$) and therefore the scattered intensity will not need any correction due to change of the footprint of the beam onto the sample as long as one can assume that the crystals are sufficiently randomized.

2.4 Powder Averaging

As described in the previous section, one can find a crystal whose electron density is characteristic of all other crystals in a single-phase powder sample with the sole exception that those other crystals, χ, are shifted and/or rotated with respect to the characteristic one, $\chi = 0$:

$$C^{(\chi)}(\vec{x}) = C^{(0)}((\mathsf{R}^{(\chi)})^{-1}\vec{x} + \vec{t}^{(\chi)}), \tag{2.25}$$

where R is a rotation and $\vec{t}$ is a translation. The characteristic crystal has its coordinate system x', y', z' aligned with the lab coordinate system x, y, z. It is unlikely to

find two crystals that scatter strongly at same scattering angle 2θ separated by less than the coherence length (see the end of this section). Therefore, the intensities of the various crystals and not their amplitudes have to be added. The intensity then becomes

$$i(\vec{s}) = \mathcal{P} \sum_{\mathsf{x}} i^{(\mathsf{x})}(\vec{s}), \tag{2.26}$$

where

$$\begin{aligned} i^{(\mathsf{x})}(\vec{s}) &= \left| \int \mathrm{d}^3x e^{-\mathrm{i}2\pi\vec{s}\cdot\vec{x}} C^{(\mathsf{x})}(\vec{x}) \right|^2 && (2.27) \\ &= \left| \int \mathrm{d}^3x' \exp\left\{-\mathrm{i}2\pi\vec{s}\cdot\left(\mathsf{R}^{(\mathsf{x})}\vec{x}' - \vec{t}^{(\mathsf{x})}\right)\right\} C^{(0)}(\vec{x}') \right|^2 && (2.28) \\ &= \mathsf{R}^{(\mathsf{x})} \left|\Phi^{(0)}(\vec{s})\right|^2 && (2.29) \end{aligned}$$

with the scattering amplitude

$$\Phi^{(0)}(\vec{s}) = \int \mathrm{d}^3x e^{-\mathrm{i}2\pi\vec{s}\cdot\vec{x}} C^{(0)}(\vec{x}). \tag{2.30}$$

Since $i^{(0)}(\vec{s}) = \left|\Phi^{(0)}(\vec{s})\right|^2$, the intensity is given by

$$i(\vec{s}) = \mathcal{P} \oint \mathrm{d}\mathsf{R}\, n(\mathsf{R})\, \mathsf{R} i^{(0)}(\vec{s}), \tag{2.31}$$

where $n(\mathsf{R})$ is the fraction of crystals that are rotated by R.

The group of proper rotations is well known [31]. The rotation is described by Euler angles with respect to the fixed axes x, y, z as

$$\mathsf{R}(\alpha, \beta, \gamma) = \mathsf{R}_z(\alpha)\mathsf{R}_y(\beta)\mathsf{R}_z(\gamma) \tag{2.32}$$

Here γ distinguishes crystals which are oriented similarly except for rotations about their z'-axis. The angle β is the tilt of the crystal's z'-axis with respect to the sample normal and α is the polar angle of this axis with respect to the fixed coordinate system as shown in figure 2.3.

Rotations are generated by angular momentum operators; it is therefore desirable to introduce spherical harmonics, which are eigenfunctions of the angular momentum operator:

$$i^{(0)}(\vec{s}) = \sum_{lm} u_{lm}(s) Y_m^{(l)}(\psi_s, \phi_s), \tag{2.33}$$

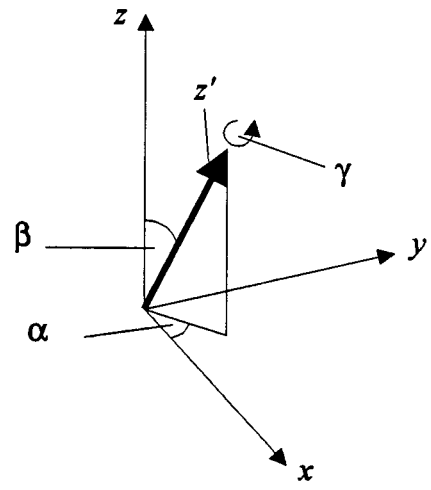

Figure 2.3: Angles used in defining the orientation of a crystal in the fixed lab reference frame.

where

$$u_{lm}(s) = \oint_{\|\vec{s}\,'\|=s} \mathrm{d}(\cos\psi'_s)\,\mathrm{d}\phi'_s\ \left(Y_m^{(l)}(\psi'_s,\phi'_s)\right)^*\ i^{(0)}(\vec{s}\,'). \tag{2.34}$$

Then the intensity becomes

$$i(\vec{s}) = \mathcal{P}\sum_{lmm'} u_{lm}(s) Y_m^{(l)}(\psi_s,\phi_s) \oint \mathrm{dR}\, n(\mathsf{R})\, \mathsf{D}^{(l)}_{mm'}(\mathsf{R}), \tag{2.35}$$

where $\mathrm{dR} = \mathrm{d}\alpha\,\mathrm{d}(\cos\beta)\,\mathrm{d}\gamma$ and $\mathsf{D}^{(l)}_{mm'}(\mathsf{R})$ are components of the rotation matrix.

Generally, the sample holder imposes a cylindrical symmetry such that $n(\mathsf{R})$ depends on β only, which implies

$$i(\vec{s}) = \mathcal{P}\sum_{l} u_{l0}(s) Y_0^{(l)}(\psi_s,\phi_s) \oint \sin\beta \mathrm{d}\beta\, n(\beta)\, P^{(l)}(\cos\beta), \tag{2.36}$$

where $P^{(l)}(\cos\beta)$ are Legendre polynomials. Expanding $n(\beta)$ into Legendre polynomials

$$n(\beta) = \sum_{l'=0}^{\infty} n_{l'} P^{(l')}(\cos\beta) \tag{2.37}$$

and utilizing the identity $Y_0^{(l)}(\psi_s,\phi_s) = \sqrt{(2l+1)/4\pi}\,P^{(l)}(\cos\psi_s)$ as well as the orthogonality relation $\oint \mathrm{d}(\cos\beta)\,P^{(l')}(\cos\beta)P^{(l)}(\cos\beta) = \delta_{ll'}2/(2l+1)$ one finds

$$i(\vec{s}) = \frac{\mathcal{P}}{4\pi}\oint_{\|\vec{s}\,'\|=s} \mathrm{d}(\cos\psi'_s)\,\mathrm{d}\phi'_s\, i^{(0)}(\vec{s}\,') \sum_{l=0}^{\infty} n_l P^{(l)}(\cos\psi') P^{(l)}(\cos\psi). \tag{2.38}$$

If there is no preferred orientation, $n(\beta)$ is independent of β and therefore $n_0 = \frac{1}{2}$ and $n_{l'} = 0$ for $l' > 0$. Then

$$i(\vec{s}) = \frac{\mathcal{P}}{4\pi} \oint \mathrm{d}(\cos\psi_s)\,\mathrm{d}\phi_s\, i^{(0)}(\vec{s}). \tag{2.39}$$

becomes independent of the direction $\vec{s}$ and depends on its length only, in other words

$$i(s) = i(\vec{s}), \tag{2.40}$$

and one can measure the intensity scattered by a powder on a circle at scattering angles, 2θ, and does not have to measure at all points in space.

Each point on the surface of the sphere of radius s corresponds to a differently oriented crystal within the powder. As will be seen at the end of this chapter, there are only a few regions on this surface where the scattering is strong. Consequently, only a small fraction of crystals in the powder contribute to the intensity measured at 2θ. As I assumed a randomly mixed powder, the probability for two of these few crystals to be closer to each other than the coherence length of the incident X-rays is negligible. This justifies the addition of the intensities of the various crystals instead of their scattering amplitudes, retroactively.

2.5 Real and Reciprocal Space

In order to evaluate the scattering amplitude for a crystal, one needs some knowledge of the arrangement of the atoms inside. This section gives the necessary tools to describe this structure. The Fourier transform involves a dot-product of two vectors. Here, basis vectors will be introduced such that the product will have a simple form. For that purpose one defines unit vectors $\hat{e}_1, \hat{e}_2, \hat{e}_3$ that span a three dimensional space. Generally, the direction of these unit vectors do not coincide with the x', y', z' axes introduced earlier. The angles between two such vectors are:

$$\hat{e}_1 \cdot \hat{e}_2 = \cos\alpha_{12} \qquad \hat{e}_2 \cdot \hat{e}_3 = \cos\alpha_{23} \qquad \hat{e}_3 \cdot \hat{e}_1 = \cos\alpha_{31}. \tag{2.41}$$

A vector $\vec{x}$ is then given by

$$\vec{x} = x^{(1)}\hat{e}_1 + x^{(2)}\hat{e}_2 + x^{(3)}\hat{e}_3, \tag{2.42}$$

where $x^{(1)}, x^{(2)}, x^{(3)}$ are the contravariant coordinates of $\vec{x}$.

One can define reciprocal space unit vectors $\hat{e}^{(1)}, \hat{e}^{(2)}, \hat{e}^{(3)}$ by

$$\hat{e}^{(1)} = \frac{\hat{e}_2 \times \hat{e}_3}{\sin \alpha_{23}} \qquad \hat{e}^{(2)} = \frac{\hat{e}_3 \times \hat{e}_1}{\sin \alpha_{31}} \qquad \hat{e}^{(3)} = \frac{\hat{e}_1 \times \hat{e}_2}{\sin \alpha_{12}}, \tag{2.43}$$

implying $\hat{e}_i \cdot \hat{e}^{(j)} = 0$ for $i \neq j$. The covariant coordinates of a vector $\vec{s}$ with respect to the reciprocal unit vectors are obtained from the expansion

$$\vec{s} = s_1 \hat{e}^{(1)} + s_2 \hat{e}^{(2)} + s_3 \hat{e}^{(3)}. \tag{2.44}$$

The dot-product between $\vec{x}$ and $\vec{s}$ involves the triple product

$$v_e = \hat{e}_1 \cdot (\hat{e}_2 \times \hat{e}_3) = \begin{vmatrix} \hat{e}_1 \cdot \hat{e}_1 & \hat{e}_1 \cdot \hat{e}_2 & \hat{e}_1 \cdot \hat{e}_3 \\ \hat{e}_2 \cdot \hat{e}_1 & \hat{e}_2 \cdot \hat{e}_2 & \hat{e}_2 \cdot \hat{e}_3 \\ \hat{e}_3 \cdot \hat{e}_1 & \hat{e}_3 \cdot \hat{e}_2 & \hat{e}_3 \cdot \hat{e}_3 \end{vmatrix}^{\frac{1}{2}} \tag{2.45}$$

$$= \left(1 + 2\cos\alpha_{23}\cos\alpha_{31}\cos\alpha_{12} - \cos^2\alpha_{23} - \cos^2\alpha_{31} - \cos^2\alpha_{12}\right)^{1/2} \tag{2.46}$$

Thus

$$\vec{x} \cdot \vec{s} = v_e \left(\frac{x^{(1)} s_1}{\sin \alpha_{23}} + \frac{x^{(2)} s_2}{\sin \alpha_{31}} + \frac{x^{(3)} s_3}{\sin \alpha_{12}} \right) \tag{2.47}$$

If one encounters an object that has a spatial periodicity along, say, the $\hat{e}_1$- and $\hat{e}_3$-direction with the respective repeat distances a_1 and a_3, as will be the case in the next section, it is convenient to express distances in units of these repeat distances and define basis vectors $\vec{a}_1 = a_1 \hat{e}_1$ and $\vec{a}_3 = a_3 \hat{e}_3$. Linear combination of these real space basis vectors with integer coefficients define points in space that are referred to as a (real space) lattice.

Additionally, one can introduce lengths $b^{(1)}$ and $b^{(3)}$ of reciprocal space basis vectors $\vec{b}^{(1)} = b^{(1)} \hat{e}^{(1)}$ and $\vec{b}^{(3)} = b^{(3)} \hat{e}^{(3)}$, which define the reciprocal lattice, as[1]

$$b^{(1)} = \frac{\sin \alpha_{23}}{a_1 v_e} \qquad \text{and} \qquad b^{(3)} = \frac{\sin \alpha_{12}}{a_3 v_e}. \tag{2.48}$$

[1]In crystallography, one usually labels the real space basis vectors as $\vec{a}$, $\vec{b}$, and $\vec{c}$, and the reciprocal space basis vectors are $\vec{a}^*$, $\vec{b}^*$, and $\vec{c}^*$. I wanted to avoid the star, '*', as it denotes the complex conjugate in this thesis; further, this notation is awkward when writing sums. On the other hand, the notation common in physics texts, $\vec{a}_i$ with $i = 1, 2, 3$ for real space basis vectors and $\vec{b}_i$ for reciprocal space basis vectors, contains an additional factor of 2π in the definition of $\vec{b}_i$ in order to avoid the explicit 2π in the exponent of the Fourier transform. The latter reason also leads to the introduction of the momentum transfer $\vec{q} = 2\pi\vec{s}$.

Then

$$\vec{x} \cdot \vec{s} = \frac{x^{(1)}}{a_1} \frac{s_1}{b^{(1)}} + \frac{x^{(2)} s_2 v_e}{\sin \alpha_{31}} + \frac{x^{(3)}}{a_3} \frac{s_3}{b^{(3)}} \tag{2.49}$$

2.6 Scattered Intensity

This section aims at deriving an expression for the intensity, $i^{(0)}(\vec{s})$, of the characteristic crystal $\chi = 0$. The electron density of this crystal can generally be written as the sum of the electron densities of individual layers in the crystal:

$$C^{(0)}(\vec{x}) = \sum_{\mu=1}^{N_2} \varrho(\mu, \vec{x}) * \delta(\vec{x} - \vec{r}(\mu)), \tag{2.50}$$

where $\varrho(\mu, \vec{x})$ is the electron density in the μ^{th} layer, $\vec{r}(\mu)$ is its position within the stack, δ is the Dirac delta-function, and N_2 is the number of layers stacked. The star indicates a convolution. To facilitate the applicability of this theory to de-Wolff-disordered manganese dioxides in chapter 3, the direction in which layers are stacked is chosen to be the 2-direction, $\hat{e}_2$, perpendicular to the layers, all of which are assumed to be based on the same two-dimensional lattice spanned by the vectors $\vec{a}_1$ and $\vec{a}_3$. The layer size is given by $\|N_1\vec{a}_1 \times N_3\vec{a}_3\|$.

The Fourier transform of this electron density then gives the scattering amplitude $\Phi^{(0)}(\vec{s})$:

$$\Phi^{(0)}(\vec{s}) = \int \mathrm{d}^3x e^{-\mathrm{i}2\pi\vec{s}\cdot\vec{x}} C^{(0)}(\vec{x}) = \sum_{\mu=1}^{N_2} \mathcal{F}(\mu, \vec{s}) e^{-\mathrm{i}2\pi\vec{s}\cdot\vec{r}(\mu)}, \tag{2.51}$$

where $\mathcal{F}(\mu, \vec{s})$ is the Fourier transform of the of electron density in layer μ. The square modulus of the scattering amplitude will give the intensity of one particular crystal that follows the construction prescribed by particular values for $\mathcal{F}(\mu, \vec{s})$ and $\vec{r}(\mu)$ for the μ^{th} layer. In many cases, all crystals in the powder follow the same construction. However, there are examples where (ideally infinitely) many crystals with the same orientation in the powder that have different realizations of the possible stackings. One therefore has to add the intensities for different possible stackings, weighted by the probability, P, that such a stacking configuration can occur.

The derivation given here is based on work by Hendricks and Teller [32] and Drits and Tchoubar [33]. Treacy, Newsam, and Deem [34] have recently given another,

equivalent description with many references to earlier work. Schematically, one can write the stacking averaged intensity as

$$\overline{i^{(0)}}(\vec{s}) = \frac{1}{N_1 N_2 N_3} \sum_{\text{configurations}} P(\text{configuration}) |\Phi^{(0)}(\vec{s}, \text{configuration})|^2. \qquad (2.52)$$

At this point, one has to make an assumption about how the crystals are formed. One can reasonably assume that the number of different types of layers is small and one type of layer may occur many times in one stack. The probability for the μ^{th} layer to be of type j_μ ($1 \leq j_\mu \leq$ number of different types of layers) will typically depend on the type of the preceding layer, $j_{\mu-1}$. This probability will be called $p_{j_{\mu-1},j_\mu}$. For the first layer I will assign a probability, $w_{j_1}^{(1)}$, for it to be of type j_1. The probability for a given stack is then:

$$P = w_{j_1}^{(1)} p_{j_1,j_2} \cdots p_{j_{N_2-1},j_{N_2}} \qquad (2.53)$$

Some useful relations in obtaining the intensity are:

$$\sum_{j_\mu}^{\text{all types}} p_{j_{\mu-1},j_\mu} = 1 \qquad (2.54)$$

and

$$\sum_{j_{\mu-1}}^{\text{all types}} w_{j_{\mu-1}}^{(\mu-1)} p_{j_{\mu-1},j_\mu} = w_{j_\mu}^{(\mu)}, \qquad (2.55)$$

which gives the probability for the μ^{th} layer to be of type j_μ. The intensity of the X-rays scattered by a stacking averaged crystal can then be written as

$$\begin{aligned} \overline{i^{(0)}}(\vec{s}) &= \frac{1}{N_1 N_2 N_3} \sum_{\mu=1}^{N_2} \sum_{j_\mu}^{\text{all types}} w_{j_\mu}^{(\mu)} |\mathcal{F}_{j_\mu}(\vec{s})|^2 \\ &+ \frac{2}{N_1 N_2 N_3} \text{Re} \sum_{\mu=1}^{N_2-1} \sum_{j_\mu}^{\text{all types}} w_{j_\mu}^{(\mu)} \mathcal{F}_{j_\mu}^*(\vec{s}) \sum_{m=1}^{N_2-\mu} [\mathsf{Q}^m]_{j_\mu,j_{\mu+m}} \mathcal{F}_{j_{\mu+m}}(\vec{s}), \qquad (2.56) \end{aligned}$$

where the quantities $\mathcal{F}$ now depend on j_μ — the type of layer μ. Q is a square matrix with components

$$[\mathsf{Q}]_{ij} = p_{ij} \phi_{ij} \qquad (2.57)$$

with $\phi_{ij} = \exp(-\text{i}2\pi \vec{s} \cdot \vec{r}_{ij})$, where $\vec{r}_{ij}$ is the displacement of a layer of type j with respect to a layer of type i. Next we assume that a layer of type i occurs with the

same probability anywhere in the stacking sequence. This defines a diagonal square matrix W:

$$[\mathsf{W}]_{ii} = w_i^{(\mu)} = w_i^{(\nu)}, \tag{2.58}$$

for all $\mu, \nu \in \{1, \ldots, N_2\}$. The intensity can then be brought into a simple form:

$$\overline{i^{(0)}}(\vec{s}) = \frac{1}{N_1 N_3} \mathrm{Re} \mathcal{F}^\dagger \mathsf{WT} \mathcal{F} = \frac{1}{N_1 N_3} \mathcal{F}^\dagger \frac{(\mathsf{WT}) + (\mathsf{WT})^\dagger}{2} \mathcal{F}, \tag{2.59}$$

where $\mathcal{F}$ is a column vector containing the Fourier transforms of the electron density of the various types of layers ($\mathcal{F}^\dagger$ is the corresponding complex conjugated row vector):

$$\mathcal{F} = \begin{bmatrix} \mathcal{F}_1(\vec{s}) \\ \vdots \\ \mathcal{F}_i(\vec{s}) \\ \vdots \end{bmatrix}. \tag{2.60}$$

The matrix T is given by

$$\mathsf{T} = \mathsf{I} + \frac{2}{N_2} \sum_{m=1}^{N_2 - 1} (N_2 - m) \mathsf{Q}^m, \tag{2.61}$$

where I is the identity matrix. One can define a matrix

$$\mathsf{G}_2(\vec{s}) = \frac{1}{2} \left((\mathsf{WT}) + (\mathsf{WT})^\dagger \right), \tag{2.62}$$

which will turn out to be a function that depends strongly on s_2; it governs the variation of the intensity along the 2-direction and is therefore called the modulation function (or interference function) in the 2-direction.

2.7 Inter-layer Structure

2.7.1 Spatial Fluctuations

The previous treatment assumes that there is a definite phase relation, ϕ_{ij}, between two adjacent layers of type i and type j. However, this is never rigorously true; for instance, there are always motions of atoms about their mean position — even at 0 K.

These spatial fluctuations of atoms (or layers) imply that, after averaging over sufficient time[2], the rms deviation of the n^{th} neighbour is $\sqrt{\langle\delta^2\rangle}$, independent of n. This leads to the so-called Debye-Waller factor $\exp(-Bs^2/2)$ [29], where $B = 8\pi^2\langle\delta^2\rangle$, in every term Q^m in equation 2.61. Figure 2.4 shows the effect of these fluctuation for one-dimensional crystal, a diffraction grating.

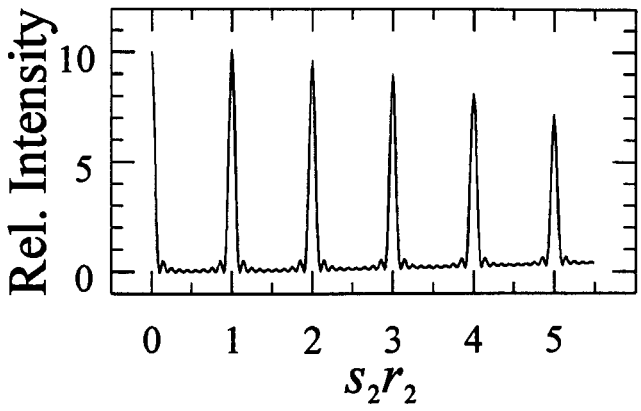

Figure 2.4: Effect of the spatial fluctuation of the lines of a diffraction grating on the relative intensities of the diffraction peaks. The mean spacing of the 10 lines is r_2, its rms deviation $\sqrt{\langle\delta^2\rangle} = 0.02r_2$.

2.7.2 Strain[3]

In addition to spatial fluctuations, the phase relation between adjacent layers of types i and j may vary across the crystal, if layers are permanently frozen into positions such that their nearest neighbour distances vary about a mean value by an rms deviation of σ. This eliminates long-range order. Figure 2.5a shows one realization for a one-dimensional strained crystal, while other crystals in the ensemble may have their layers in different places. Figure 2.5b shows for comparison a one-dimensional crystal subject to fluctuations. The ensemble of all strained crystals defines a probability

[2]Spatial fluctuations originating from ensemble averaging over different crystals with frozen-in displacements lead to the same expression, provided that long-range order is preserved.

[3]The type of strain introduced here must be contrasted with strain as experienced due to applied stress within the elastic limit. In this usual case the lattice expands or contracts uniformly, leading to well defined increased or decreased lattice constants.

distribution for nearest neighbour deviations. I will assume that such a distribution is Gaussian and independent from one layer to the next; then the rms deviation of the n^{th} neighbour is given by $\sqrt{n}\sigma$ (Moivre principle of statistics). Averaging over all possible realizations, one obtains an additional factor for the nearest neighbour phase factor ϕ_{ij} [35]

$$\phi_{ij} \longrightarrow \phi_{ij} \exp\left(-2\pi^2 s_2^2 \sigma_2^2\right). \tag{2.63}$$

The solid lines in figure 2.6 show the effect of strain on the diffraction pattern of an ensemble of diffraction gratings; the dashed lines will be explained in the next section.

2.7.3 Random Faults

After introducing strain and giving up long-range order, one can ask how meaningful is N_2, the number of layers in a stack. One could overextend Ergun's interpretation of a lattice with random faults [36, 35] and replace $(N_2 - m)/N_2$ by ${U_2}^m$ in equation (2.61) with $U_2 = \exp(-2/N_2)$, where N_2 is now the average number of layers stacked without encountering a random fault.

It should be pointed out that diffraction patterns of individual crystals within the ensemble of crystals with random faults are not identical to the diffraction pattern obtained from the ensemble as a whole. Even though it is this ensemble diffraction pattern that I am interested in, I will refer to a hypothetical crystal that produces the same diffraction pattern as the ensemble as an Ergun crystal or, in the one-dimensional case, an Ergun grating.

The total stack can then be assumed to be infinitely large (the upper limit of the sum in equation (2.61) is replaced by ∞) so that the modulation function simplifies to

$$\mathsf{G}_2 = \frac{1}{2}\mathsf{W}\frac{\mathsf{I} + U_2\mathsf{Q}}{\mathsf{I} - U_2\mathsf{Q}} + \text{h.c.}, \tag{2.64}$$

where h.c. means the hermitian conjugate.

A comparison between the modulation functions for a one-dimensional crystal of definite extent N_2 and an Ergun grating with a mean extent of N_2 is shown in figure 2.6 for $N_2 = 10$. In panel (a), the two peak shapes are contrasted: The peak

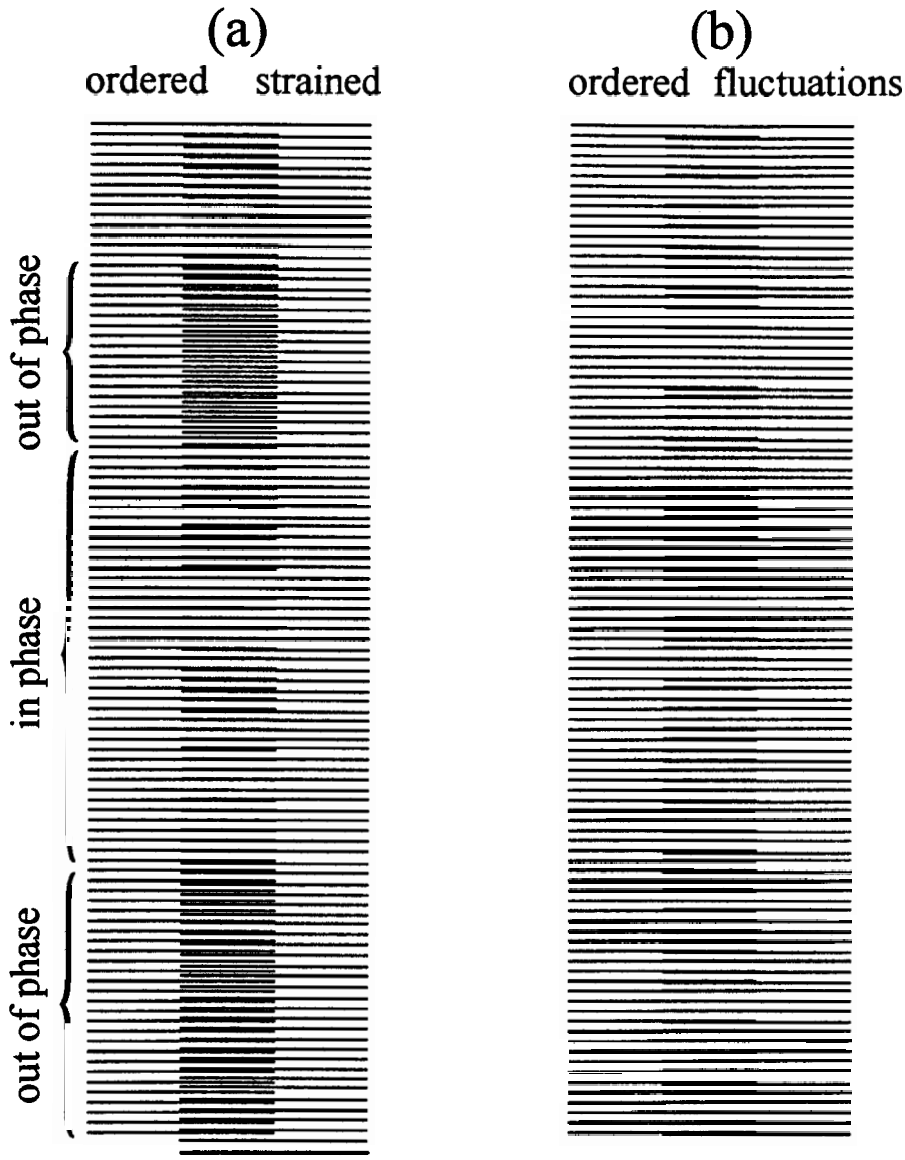

Figure 2.5: Comparison between an ordered grating and (a) a strained one and (b) one with spatial fluctuations. All gratings are made with 100 lines. One can see that in panel (b) the spatial fluctuations about a mean position preserve long-range order, whereas in (a) one sees regions where the strained grating is in phase with the ordered grating and other regions where they are out of phase.

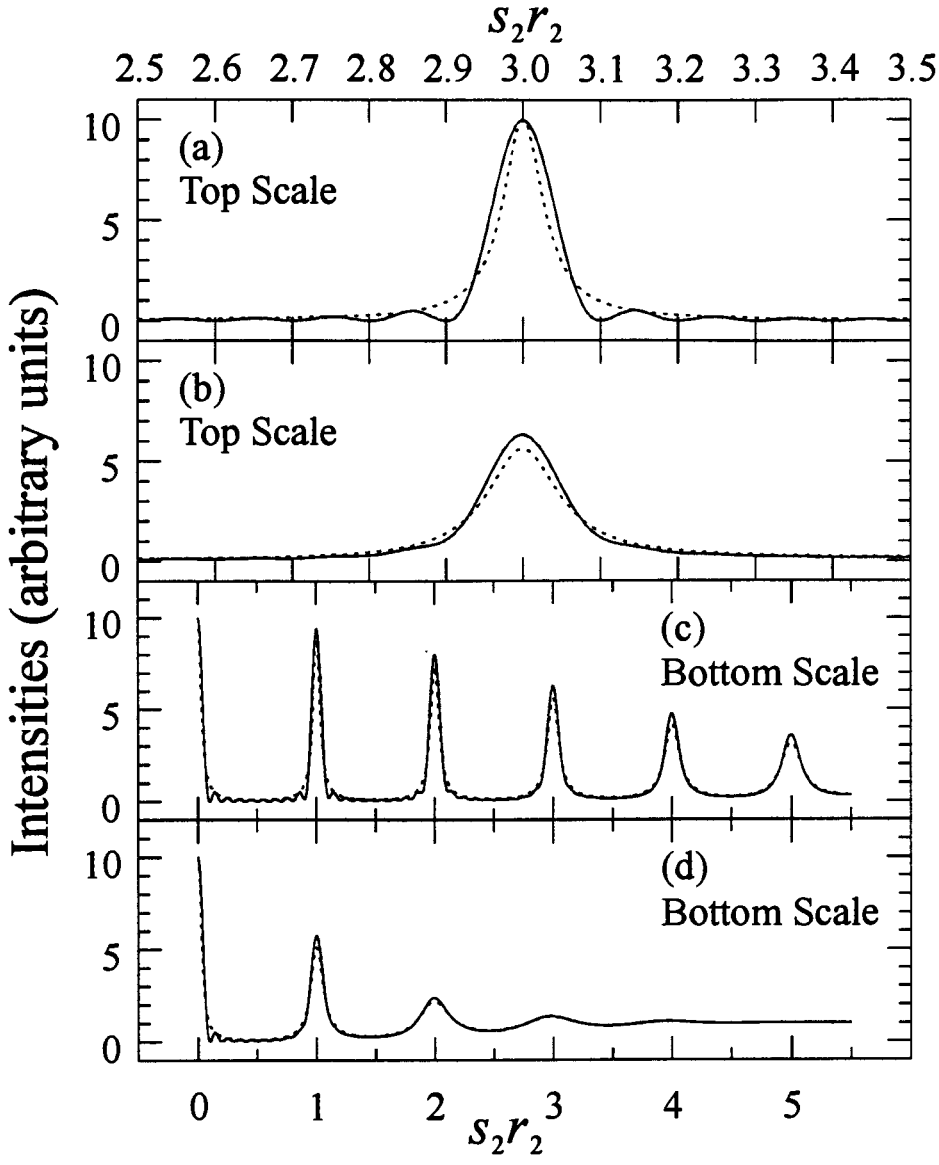

Figure 2.6: Effect of strain and random faults on the diffracted intensity of an ensemble of diffraction gratings. In all cases, the individual gratings have 10 lines separated by a mean spacing of r_2. The diffraction patterns of the unstrained and of the ensemble-averaged strained diffraction gratings (solid lines) are compared to an Ergun-grating (dashed lines). In the unstrained case, all peaks within the pattern of a given grating have the same shape and size. Panel (a) shows a representative peak that demonstrates that the Ergun pattern does not exhibit the oscillation obtained in the ordinary case. As the strain increases, the shapes become more similar, as can be seen in panel (b), which shows the third order peak for a strain parameter of $\sigma_2 r_2 = 0.03$. Panel (c) shows the complete diffraction pattern for $\sigma_2 r_2 = 0.03$, and panel (d) for $\sigma_2 r_2 = 0.10$.

from the grating with definite extent shows the oscillations well known for diffraction from multiple slits. In the Ergun case these oscillations are washed out; however, the overall peak shape is changed as well. If one considers strained cases of the two lattices, the resulting peaks become more and more similar as one goes to higher order peaks (panel (b)). Panels (c) and (d) show how higher order peaks broaden and decrease in integrated intensity along with an increased background.

For sufficiently narrow peaks ($U_2 \approx 1$), the positions of the maxima are given by the roots of the square modulus of the determinant of $\mathsf{I} - \mathsf{Q}$.

2.8 Intra-layer Structure

The electron density within layer μ is determined by the electron density within the layer unit cell at the origin of the layer, $\varrho(0, \mu, 0; \vec{x})$:

$$\varrho(\mu, \vec{x}) = \varrho(0, \mu, 0; \vec{x}) * \left[\sum_{m_1=0}^{N_1-1} \delta(\vec{x} - m_1 \vec{a}_1) \sum_{m_3=0}^{N_3-1} \delta(\vec{x} - m_3 \vec{a}_3) \right]. \tag{2.65}$$

Let layer μ be of type i; then the Fourier transform becomes

$$\mathcal{F}_i(\vec{s}) = F_i(\vec{s}) \frac{1 - e^{-\mathrm{i}2\pi N_1 s_1 / b^{(1)}}}{1 - e^{-\mathrm{i}2\pi s_1 / b^{(1)}}} \frac{1 - e^{-\mathrm{i}2\pi N_3 s_3 / b^{(3)}}}{1 - e^{-\mathrm{i}2\pi s_3 / b^{(3)}}}, \tag{2.66}$$

where we have utilized $\vec{s} = s_1 \vec{b}^{(1)}/b^{(1)} + s_2 \hat{e}^{(2)} + s_3 \vec{b}^{(3)}/b^{(3)}$. Here $\vec{b}^{(1)}, \hat{e}^{(2)}, \vec{b}^{(3)}$ are the reciprocal space basis vectors corresponding to $\vec{a}_1, \hat{e}_2, \vec{a}_3$, the real space basis vectors.

The functions $F_i(\vec{s})$ are ordinary geometric structure factors associated with the unit cell in the layer of type i:

$$F_i(\vec{s}) = \sum_{\alpha_i} f^{(\alpha_i)}(s) \exp(-\mathrm{i}2\pi \vec{s} \cdot \vec{d}^{\,(\alpha_i)}), \tag{2.67}$$

where the sum is over all atoms, α_i, in the unit cell of layer i. The position of the atom in the unit cell is given by $\vec{d}^{\,(\alpha_i)}$ and its atomic form factor is $f^{(\alpha_i)}(s)$.

In the expression for the intensity, equation (2.59), an $\mathcal{F}_i$ multiplies an $\mathcal{F}_j^*$ leading to G_1, the modulation function in the 1-direction,

$$G_1(s_1/b^{(1)}) = \frac{1}{N_1} \left(\frac{\sin \pi N_1 s_1/b^{(1)}}{\sin \pi s_1/b^{(1)}} \right)^2, \tag{2.68}$$

and an analogous expression for G_3, the modulation function in the 3-direction. These modulation functions are sharply peaked about integers:

$$h = \mathrm{ent}(s_1/b^{(1)} + 0.5) \tag{2.69}$$

$$l = \mathrm{ent}(s_3/b^{(3)} + 0.5), \tag{2.70}$$

where ent denotes the largest integer less than or equal to the argument. Compared to G_1 and G_3, the functions G_2 and F_i vary slowly with s_1 and s_3. In these latter functions, one can therefore approximate $s_1 \approx hb^{(1)}$ and $s_3 \approx lb^{(3)}$.

The intensity can then be written as

$$\overline{i^{(0)}}(\vec{s}) = \sum_{hl} G_1(s_1/b^{(1)} - h)G_3(s_3/b^{(3)} - l)\overline{i^{(0)}}(h, l, s_2) \tag{2.71}$$

with

$$\overline{i^{(0)}}(h, l, s_2) = \mathsf{F}^\dagger(h, l, s_2)\mathsf{G}_2(h, l, s_2)\mathsf{F}(h, l, s_2), \tag{2.72}$$

where F is a column vector of the various structure factors.

In order to facilitate the powder-averaging, which I will discuss in the next section, it is useful to approximate the modulation functions G_1 and G_3 by equal-area Gaussians. Before introducing this approximation, I will change the model of the intra-layer structure by replacing the well-defined, constant layer size by a mean size in the sense of Ergun's random faults. With a mean extent in the 1-direction, N_1, the modulation function becomes

$$G_1 = \frac{1 - {U_1}^2}{1 + {U_1}^2 - 2U_1 \cos 2\pi s_1/b^{(1)}}, \tag{2.73}$$

where $U_1 = \exp(-2/N_1)$. If one allows for strain as well, one finds

$$U_1 = \exp\left\{-2\left(\frac{1}{N_1} + \pi^2 \left(s_1/b^{(1)}\right)^2 \sigma_1^2\right)\right\} \tag{2.74}$$

$$\approx \exp\left\{-2\left(\frac{1}{N_1} + \pi^2 h^2 \sigma_1^2\right)\right\}, \tag{2.75}$$

where σ_1 is a dimensionless strain parameter. Defining an effective layer size, $N_1^{\mathrm{eff}} := (1 + U_1)/(1 - U_1)$, one can finally introduce the Gaussian approximation, needed in the next section:

$$G_1 \approx \left(N_1^{\mathrm{eff}} - \frac{1}{N_1^{\mathrm{eff}}}\right) \exp\left\{-\pi \left(N_1^{\mathrm{eff}}\right)^2 \left(s_1/b^{(1)} - h\right)^2\right\} + \frac{1}{N_1^{\mathrm{eff}}} \tag{2.76}$$

$$\approx N_1^{\mathrm{eff}} \exp\left\{-\pi \left(N_1^{\mathrm{eff}}\right)^2 \left(s_1/b^{(1)} - h\right)^2\right\}. \tag{2.77}$$

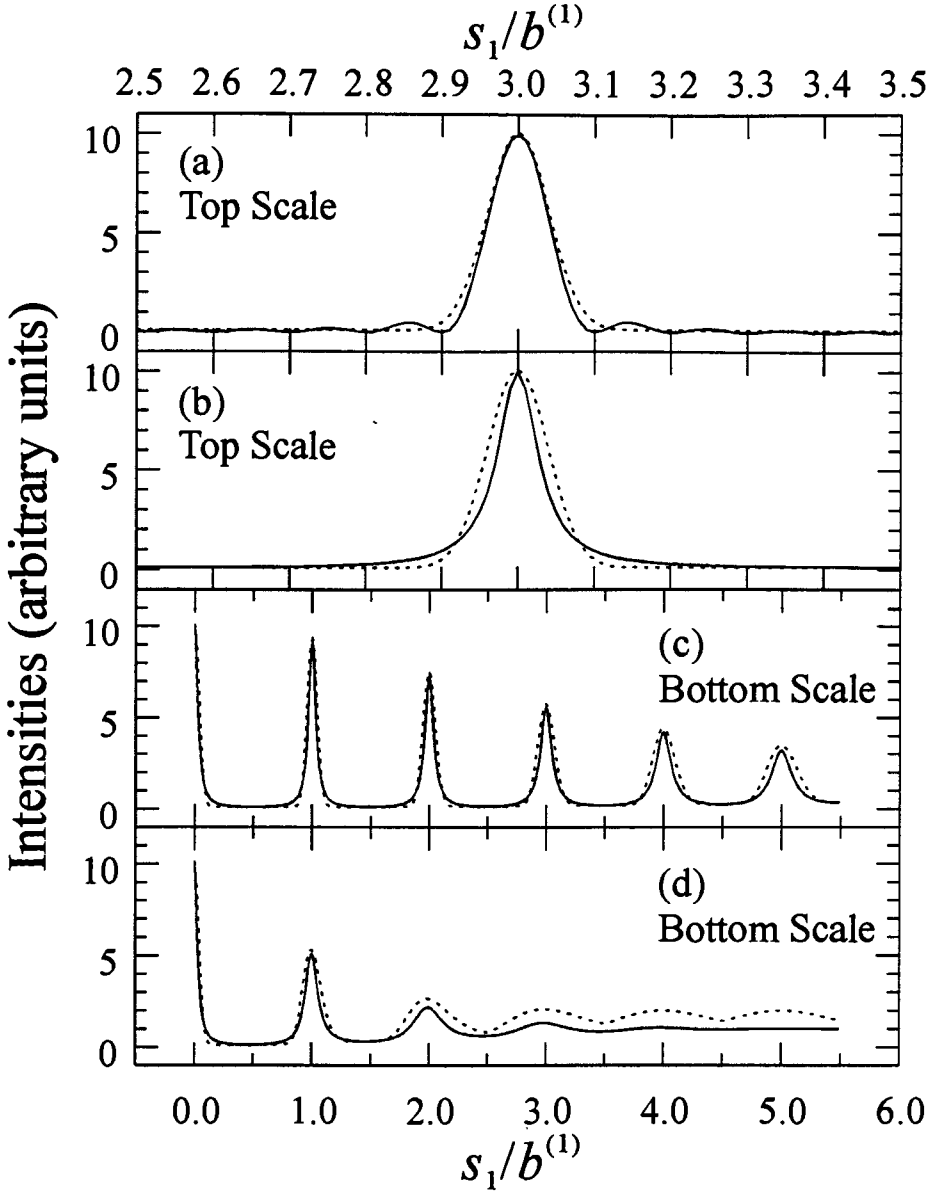

Figure 2.7: Gaussian approximants for diffraction peaks of various gratings with 10 lines spaced either exactly or on average by $1/b^{(1)}$. Panel (a) shows a comparisons between a diffraction peak of an unstrained grating (solid line) and an equal-area Gaussian (dashed line). Panel (b) shows a similar comparison between a diffraction peak of an Ergun grating (solid line) and its equal-area Gaussian approximant (dashed line). Panels (c) and (d) show complete diffraction patterns of strained Ergun gratings (solid lines) as well as Gaussian approximant for the individual diffraction peaks (dashed lines). In (c) the dimensionless strain parameter is $\sigma_1 = 0.03$, and in (d) it is $\sigma_1 = 0.10$. The Gaussian approximation appears to be good until the peak height drops below 5.

This approximation works well for $N_1^{\text{eff}} \gtrsim 5$, as can be seen in figure 2.7. The 3-direction can be treated analogously.

2.9 Tangent Cylinder Approximation

The intensity given by equation (2.39) involves an integral over all angles ψ_s and ϕ_s. Utilizing $s^2 \mathrm{d}(\cos\psi_s)\mathrm{d}\phi_s = \mathrm{d}S$, a surface element of the sphere of radius s, one can write

$$i(s) = \frac{\mathcal{P}}{4\pi s^2} \oint_{\|\vec{s}\|=s} \overline{i^{(0)}}(\vec{s})\,\mathrm{d}S \tag{2.78}$$

$$= \sum_{hl} \frac{\mathcal{P}}{4\pi s^2} \oint_{\|\vec{s}\|=s} \overline{i^{(0)}}(h,l,s_2) G_1(s_1 a_1 - h) G_3(s_3 a_3 - l)\,\mathrm{d}S. \tag{2.79}$$

The only factors in $\overline{i^{(0)}}(\vec{s})$ that depends on s_1 and s_3 are the modulation functions G_1 and G_3. The product of these functions is constant on the surface of rods of elliptical cross section in reciprocal space, whose centres intersect the $s_2 = 0$ plane at a $\vec{s}_0 = h\vec{b}^{(1)} + l\vec{b}^{(3)}$. The magnitude of the product is largest on the surface of rods with vanishing cross section, decreases as the elliptical cross section becomes larger and becomes vanishingly small when the rod is wider than a rod that I will call the hl-rod. I will define later what I consider vanishingly small — certainly a subjective choice.

For the following, it will be assumed that these hl-rods are perpendicular to the $s_2 = 0$ plane, which in turn requires a crystal structure that is monoclinic or of higher symmetry; the angles both α_{23} and α_{12} must be 90°. If the width of the hl-rods is small compared to the length of the scattering vector $\vec{s}$, then, for a particular hl-rod, the integration over the spherical surface of radius $\|\vec{s}\|$ can be replaced by an integration over a cylindrical surface of radius $\|\vec{s}\|$, whose symmetry axis is perpendicular to both the vector $\vec{s}_0$ and the hl-rod itself.

In this so-called tangent cylinder approximation [37] the scattering vector

$$\vec{s} = s_1\vec{b}^{(1)}/b^{(1)} + s_2\hat{e}^{(2)} + s_3\vec{b}^{(3)}/b^{(3)} \tag{2.80}$$

is approximated by

$$\vec{s} \approx \vec{c}_1 s\cos\phi + \vec{c}_2 s\sin\phi + \vec{c}_3\zeta \tag{2.81}$$

where

$$\vec{c}_1 = \begin{cases} \vec{b}^{(1)}/b^{(1)} & \text{if } h = l = 0 \\ \vec{s}_0/s_0 & \text{otherwise} \end{cases} \tag{2.82}$$

$$\vec{c}_2 = \hat{e}^{(2)} \tag{2.83}$$

$$\vec{c}_3 = \begin{cases} \vec{b}^{(1)} \times (\vec{b}^{(3)} \times \vec{b}^{(1)})/b^{(1)2} b^{(3)} \sin\alpha_{31} & \text{if } h = l = 0 \\ \vec{s}_0 \times (\vec{b}^{(3)} \times \vec{b}^{(1)})/s_0 b^{(1)} b^{(3)} \sin\alpha_{31} & \text{otherwise} \end{cases} . \tag{2.84}$$

Comparing the expansion coefficients in equations (2.80) and (2.81), one obtains

$$s_1 = \begin{cases} s\cos\phi - \zeta\cot\alpha_{31} & \text{if } h = l = 0 \\ \frac{hb^{(1)}}{s_0} s\cos\phi - \frac{\vec{s}_0\cdot\vec{b}^{(3)}}{s_0 b^{(3)}\sin\alpha_{31}}\zeta & \text{otherwise} \end{cases} \tag{2.85}$$

$$s_2 = s\sin\phi \tag{2.86}$$

$$s_3 = \begin{cases} \zeta/\sin\alpha_{31} & \text{if } h = l = 0 \\ \frac{lb^{(3)}}{s_0} s\cos\phi + \frac{\vec{s}_0\cdot\vec{b}^{(1)}}{s_0 b^{(1)}\sin\alpha_{31}}\zeta & \text{otherwise} \end{cases} . \tag{2.87}$$

For a cylinder, the surface element $\mathrm{d}S$ is given by $\mathrm{d}S = s\mathrm{d}\phi\mathrm{d}\zeta$ such that powder averaging now involves

$$i(s) = \sum_{hl} \frac{\mathcal{P}}{4\pi s^2} \int \mathrm{d}\phi\, i(h,l,s_2(\phi)) \int \mathrm{d}\zeta\, G_1(s_1(\zeta,\phi)a_1 - h)\, G_3(s_3(\zeta,\phi)a_3 - l) \tag{2.88}$$

If the modulation functions G_1 and G_2 are Gaussian, the ζ-integral can be done analytically. It was for this reason that I introduced the Gaussian approximants in the last section. One obtains:

$$\int_{-\infty}^{\infty} \mathrm{d}\zeta\, G_1(s_1(\zeta,\phi))a_1 - h)\, G_3(s_3(\zeta,\phi)a_3 - l) \tag{2.89}$$

$$= b^{(1)}b^{(3)}\sin\alpha_{31} \begin{cases} \frac{1}{\sqrt{2\pi}\sigma_{00}} \exp\left[-(s\cos\phi)^2/(2\sigma_{00}^2)\right] & \text{if } h = l = 0 \\ \frac{1}{\sqrt{2\pi}\sigma_{hl}} \exp\left[-(s\cos\phi - s_0)^2/(2\sigma_{hl}^2)\right] & \text{otherwise} \end{cases}$$

where

$$\sigma_{00} = \frac{1}{\sqrt{2\pi}} \frac{b^{(1)}b^{(3)}}{N_1^{\text{eff}} N_3^{\text{eff}}} \sqrt{\left(\frac{N_1^{\text{eff}}\cos\alpha_{31}}{b^{(1)}}\right)^2 + \left(\frac{N_3^{\text{eff}}}{b^{(3)}}\right)^2} \tag{2.90}$$

and

$$\sigma_{hl} = \frac{1}{\sqrt{2\pi}} \sqrt{\left(\frac{\vec{s}_0/s_0\cdot\vec{b}^{(1)}}{N_1^{\text{eff}}}\right)^2 + \left(\frac{\vec{s}_0/s_0\cdot\vec{b}^{(3)}}{N_3^{\text{eff}}}\right)^2} . \tag{2.91}$$

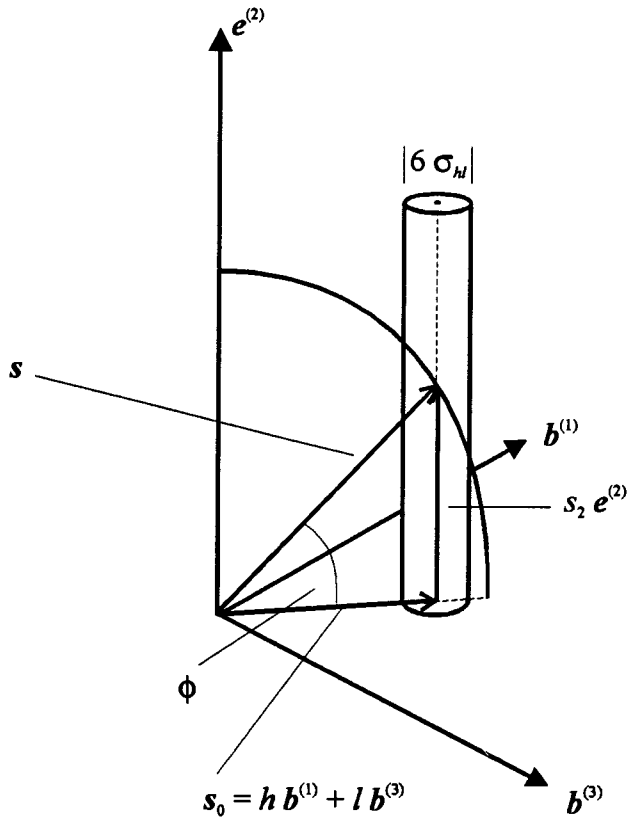

Figure 2.8: Reciprocal space with hl-rod

An hl-rod in reciprocal space is depicted in figure 2.8, which also shows the arc described by ϕ. Substituting the integration variable ϕ by s_2, one obtains if $h \neq 0$ or $l \neq 0$, after dropping the $\vec{s}$-independent factor $b^{(1)}b^{(3)} \sin \alpha_{31}/(4\pi\sqrt{2\pi})$

$$i_{hl}(s) = \frac{\mathcal{P}}{s^2\sigma_{hl}} \int_{s_2^{\min}}^{s_2^{\max}} \mathrm{d}s_2 \, \frac{\overline{i^{(0)}}(h,l,s_2) + \overline{i^{(0)}}(h,l,-s_2)}{\sqrt{1-(s_2/s)^2}} \exp\left\{ -\frac{(\sqrt{s^2 - {s_2}^2} - s_0)^2}{2\sigma_{hl}^2} \right\}. \tag{2.92}$$

The integration limits are to be determined by the width of the hl-rod. As indicated above, the choice of this width is certainly arbitrary. Since about 99% of the area under a Gaussian peak, given by $\exp(-x^2/2\sigma^2)/\sqrt{2\pi\sigma^2}$, is within a range of $\pm 3\sigma$ about the peak mean, I chose the width of the hl-rod to be $6\sigma_{hl}$, leading to the integration limits $s_2^{\min} = \sqrt{s^2 - [\min(s, s_0 + 3\sigma_{hl})]^2}$ and $s_2^{\max} = \sqrt{s^2 - (s_0 - 3\sigma_{hl})^2}$.

If $h = l = 0$, one substitutes $s_{hl} = s\cos\phi$ and utilizes the fact that s_2 varies little along an arc cutting through the 00-rod, so that one approximates $s_2 \approx s$. After

integrating over s_{hl} and dropping the same factor as above, one arrives at

$$i_{00}(s) = \frac{\mathcal{P}}{s^2}\left[\overline{i^{(0)}}(0,0,s) + \overline{i^{(0)}}(0,0,-s)\right] \tag{2.93}$$

In order to obtain the powder average intensity, one has to add the contribution from the various hl-rods:

$$i(s) = \sum_{hl} i_{hl}(s). \tag{2.94}$$

2.10 Measured Intensity

So far, I calculated the energy per unit solid angle scattered to the observation point $\vec{x}'$ during the time of measurement. In an experimental set-up the receiving slit has a finite width and finite height in the y-direction. One therefore has to integrate the calculated intensity over this range of solid angle. However, the variation of the intensity over the range in solid angle is typically negligible and the integration would merely lead to an additional, constant multiplicative factor. Since some of the multiplicative constants are known, but others are unknown, I combine all into a common scale factor, η.

There may also be X-ray photons entering the receiving slit from other sources and/or processes in the sample other than the one of interest giving rise to a background, which can be accounted for by a polynomial background function. The measured intensity can then be written as

$$I_{\text{meas}}(2\theta) = \eta i(2\theta) + c_0 + c_1 2\theta + c_2(2\theta)^2 + c_3(2\theta)^3 + c_4(2\theta)^4 + c_{-1}(2\theta)^{-1}, \tag{2.95}$$

where

$$\begin{aligned} i(2\theta) \;=\; & \frac{1+\cos^2 2\theta\cos^2 2\theta_{\text{m}}}{\sin^2\theta} \times \exp\left(-2B\frac{\sin^2\theta}{\lambda^2}\right) \times \\ & \left\{ \overline{i^{(0)}}(0,0,\frac{2\sin\theta}{\lambda}) + \overline{i^{(0)}}(0,0,-\frac{2\sin\theta}{\lambda}) + \right. \\ & \left. \sum_{h,l;\ \text{not } h=l=0} \frac{1}{\sigma_{hl}} \int_{s_2^{\min}}^{s_2^{\max}} \frac{\mathrm{d}x\,\left(\overline{i^{(0)}}(h,l,x) + \overline{i^{(0)}}(h,l,-x)\right)}{\sqrt{1-(x\lambda/2\sin\theta)^2}} G_{hl}(x,\theta) \right\}, \end{aligned} \tag{2.96}$$

where

$$G_{hl}(x,\theta) = \exp\left[-\frac{\left(\sqrt{\left(\frac{2\sin\theta}{\lambda}\right)^2 - x^2} - \|h\vec{b}^{(1)} + l\vec{b}^{(3)}\|\right)^2}{2\sigma_{hl}^2}\right] \tag{2.97}$$

and B in the exponent of the Debye-Waller factor reflects the fluctuations of the atoms about their mean lattice positions. The quantities $\overline{i^{(0)}}(h,l,x)$ can only be evaluated, if one considers a particular crystal, as I will do in the next chapter.

2.11 Periodic Crystals and the Rietveld Method

Before closing this chapter, I want to tie the previously developed formalism in with the common text book examples of so-called crystalline powders, in my terminology: powders of crystals with three-dimensional translational periodicity. The modulation functions associated with all three crystallographic directions are now scalars, and a Miller index k can be defined similar to h and l. The number of repetitions of a unit cell is typically large, so that the modulation function are all strongly peaked about certain points in reciprocal space, leading to relatively sharp peaks in the diffraction pattern, labelled as hkl peaks (sometimes this label includes crystallographically equivalent peaks).

If one wants to fit the diffraction pattern to extract information about atom positions, say, it is desirable to approximate the shape of the diffraction peaks as closely as possible. Instead of varying the shape of the various modulation functions, one prefers to vary the shape of the diffraction peak directly, while maintaining the same area of the calculated peak as in the measured one. The measured hkl peak is integrated across the range in scattering angle, 2θ, after subtracting the background. To compare the calculated intensity, one has to perform the same integration over 2θ leading to a volume integration about the hkl-point in reciprocal space

$$I_{\text{integrated}}(hkl) = \int \mathrm{d}(2\theta)\, i(2\theta) = \int \frac{\lambda\,\mathrm{d}s}{\cos\theta} i(s) \tag{2.98}$$

$$\propto \frac{\mathcal{P}}{\sin^2\theta\,\cos\theta} \int_{V_{hkl}} \mathrm{d}^3 s\, G_1(s_1) G_2(s_2) G_3(s_3)\, |F_{hkl}|^2, \tag{2.99}$$

where $\mathcal{L} = 1/\sin^2\theta\cos\theta$ is referred to as the Lorentz factor. The variation of the structure factor across the integration volume is small so that it can be taken out of the integral. The integral over the modulation functions then evaluates to a constant. If the measured peak contains contributions from various hkl-points, then the integrated intensities from these points have to be added up, of course.

One ends up with the well known result that the integrated intensity is proportional to the product of the Lorentz-Polarization factor, $\mathcal{LP}$, and the square modulus of the structure factor of the unit cell.

$$I_{\text{integrated}}(hkl) = \frac{1+\cos^2 2\theta\cos^2 2\theta_{\text{m}}}{\sin^2\theta\,\cos\theta}|F_{hkl}|^2 \tag{2.100}$$

I prefer not to emphasize a multiplicity factor, which arises from the number of terms in the sum over crystallographically equivalent hkl-points that contribute to the measured intensity at the same scattering angle, because there may be other, non-equivalent hkl-points that contribute to the measured intensity as they lie on the surface of the sphere of radius $2(\sin\theta)/\lambda$ accidentally.

As pointed out above, one tries to fit a calculated diffraction pattern to the measured one by assuming a certain (refineable) peak shape. A common peak shape is a mixture of a Gaussian and a Lorentzian peak, a so-called pseudo-Voigt peak. It tries to mimic contributions from instrumental broadening (assumed to be Gaussian) and from finite crystal size (assumed to be Lorentzian). The mixing parameter, γ, is 1 for a purely Lorentzian peak and 0 for a purely Gaussian peak. Sensible mixing parameters are therefore in the interval between 0 and 1.

Further, the widths of these pseudo-Voigt peaks is allowed to vary smoothly across the pattern, with the full width at half maximum given by $(U\tan^2\theta + V\tan\theta + W)^{1/2}$, where U, V, and W are refineable parameters. Such a variation in peak width is necessary as an increase in peak width is expected for increasing scattering angle: Each of the three modulation functions contains peaks of constant widths in s_1, s_2, and s_3 so that the diffraction pattern plotted as a function of s contains peaks of constant widths as well. However, when transforming intervals, $[s, s+\Delta s]$, of fixed widths, Δs, into intervals in scattering angle, 2θ with $s = 2(\sin\theta)/\lambda$, one observes broader widths for larger scattering angles: $[2\theta, 2\theta + \lambda\Delta s/\cos\theta]$. This is the result

of the well-known Scherrer equation.

Although the Rietveld method employs a fit of the whole pattern so as to minimize the sum of the differences at each data point between the measured and calculated pattern, it is still important to evaluate the so-called Bragg-R factor, R_B. This factor is the normalized sum of the relative differences between the measured and calculated integrated intensities for each of the diffraction peaks:

$$R_B = \frac{\sum_{\text{all peaks}} |I_{\text{integrated,observed}} - I_{\text{integrated,calculated}}|}{\sum_{\text{all peaks}} I_{\text{integrated,observed}}}. \tag{2.101}$$

More details on the Rietveld method can be found in reference [38].

At this point, one has tools available that describe ordered crystals as well as crystals with stacking-fault and/or strain disorder. In the investigation of materials for electrodes of batteries, as to be carried out in the next two chapters, both tools will be needed.

Chapter 3

Manganese Dioxides for Alkaline Cells

3.1 Structural Elements

Many transition metal oxides have structures that are based on hexagonal or cubic close packed oxygen lattices with cations (*i.e.* the oxidized ions) on so-called octahedral or tetrahedral sites. This section aims at explaining these terms. Both hexagonal and cubic close packed lattices are constructed from two-dimensional hexagonal[1] lattices, forming so-called layers, that are stacked into the third dimension. Such a hexagonal lattice is depicted in figure 3.1.

In the ideal case, each site on the hexagonal lattice has a 6-fold rotational symmetry, although in many compounds only a 3-fold symmetry is realized, as in $LiCoO_2$ or $LiNiO_2$. The real space lattice vectors, $\vec{a}_1^{\text{hex}}$ and $\vec{a}_2^{\text{hex}}$, are therefore chosen to be non-Cartesian with an angle of 120° between them. Other compounds, in particular the manganese oxides discussed in the next section, are based on a distorted variation of the hexagonal lattice. These lattices are therefore more conveniently described by orthogonal axes.

There are two distinct stacking possibilities that lead to a so-called close packing, in which the void space is minimized. These two stacking possibilities, which are

[1] A hexagonal lattice is also known as a triangular lattice

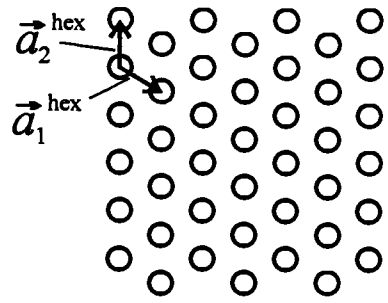

Figure 3.1: A two-dimensional hexagonal lattice with a particular choice of lattice vectors.

depicted in figure 3.2, lead to three distinct positions for the hexagonal lattice, which I will call X, Y, and Z. With respect to layer X, layer Y is shifted by $\vec{r}_{\mathrm{XY}} = \frac{1}{3}\vec{a}_1^{\,\mathrm{hex}} + \frac{2}{3}\vec{a}_2^{\,\mathrm{hex}}$, whereas layer Z is shifted by $\vec{r}_{\mathrm{XZ}} = -\vec{r}_{\mathrm{XY}}$. A hexagonal close packed lattice is then built by stacking ...XYXYXY..., and the cubic close packed lattice has the form ...XYZXYZXYZ...

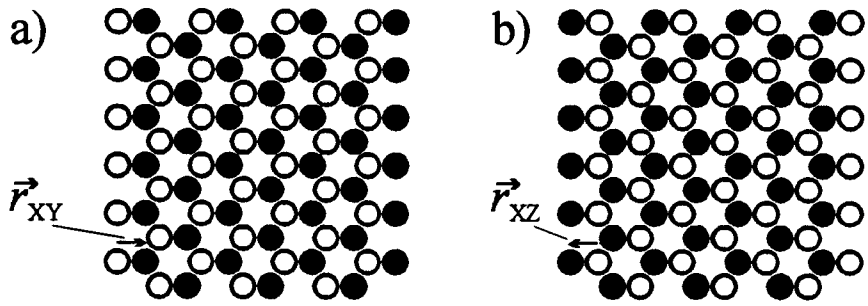

Figure 3.2: Distinct stackings of hexagonal lattices.

In a transition metal oxide that is based on such an oxygen lattice, the transition metal atoms, M, are typically organized on hexagonal layers as well; these layers interlace the oxygen layers, leading to a sequence of, for instance, ...$\mathrm{X_O Z}_M \mathrm{Y_O}$... The local environment of the M-atom is depicted in figure 3.3; one sees that M is surrounded by six O-atoms leading to an MO_6-octahedron. Such a site for the M atom is therefore referred to as an octahedral site. In some cases, for instance the lithium in $LiMn_2O_4$, a metal atom is not positioned on the hexagonal layer, but

halfway between the hexagonal cation and oxygen layers, leading to a tetrahedral coordination Such tetrahedral sites can be filled adjacent to unfilled octahedral sites, shown in figure 3.3 as well.

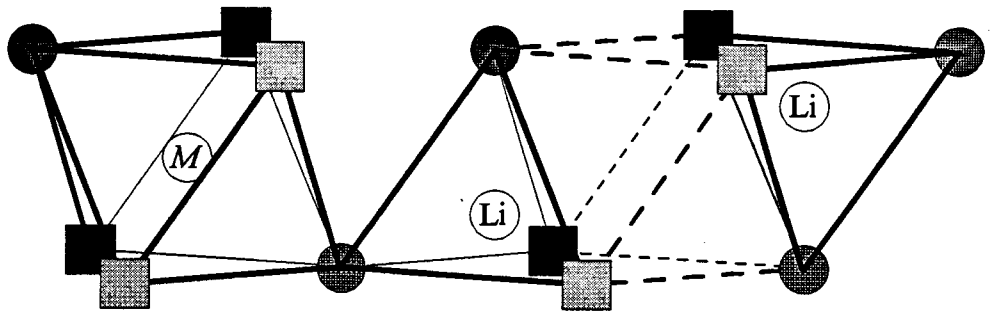

Figure 3.3: Octahedral and tetrahedral sites between hexagonal oxygen layers. The oxygen atoms are symbolized by shaded squares and circles, which are out of the plane of the paper and in it, respectively. The octahedrally coordinated M atom can be one of many choices, in particular it can be Mn(III) or Mn(IV), whereas the tetrahedral site is occupied by only a few atoms, among them Li in $Li[Mn_2]O_4$, but also Mn(II) in hausmannite $Mn[Mn_2]O_4$.

3.2 Manganese Dioxide Polymorphs

3.2.1 Ramsdellite

Ramsdellite is a very rare mineral whose crystal structure was determined by Byström [39]. Some authors have claimed to have prepared this material synthetically [40, 41, 42], but it is questionable if it is purely ramsdellite that was prepared or rather a γ-MnO_2 with a high content of ramsdellitic domains. The ramsdellite structure is shown in figure 3.4a. It is characterized by double chains or ribbons of edge-sharing octahedra that extend in the 3-direction. Adjacent ribbons have octahedral corners in common. This leads to the creation of so-called 2×1 tunnels (2 octahedra wide and 1 octahedron high).

In the 1-direction, the structure is based on a distorted hexagonal close packed oxygen lattice with oxygen atoms in layers X and Y, and manganese atoms on half

the available sites of layer Z, leading to a stacking

$$\ldots \mathrm{X_O Z_{1/2Mn} Y_O}\ \mathrm{Z'_{1/2Mn}}\ \mathrm{X_O Z_{1/2Mn} Y_O}\ \mathrm{Z'_{1/2Mn} X_O} \ldots$$

Figure 3.5 shows the manganese layer Z, in which the black sites are filled with manganese atoms and the white sites are empty. In layer Z', the black sites are unfilled, the white ones are filled.

According to Byström the ramsdellite structure is based on space group Pbnm (No. 62) with all atoms in Wyckoff position (4c): $(u, v, \frac{1}{4})$, $(\frac{1}{2}+u, \frac{1}{2}-v, \frac{3}{4})$, $(\frac{1}{2}-u, \frac{1}{2}+v, \frac{1}{4})$, $(-u, -v, \frac{3}{4})$, where (u, v) is (0.022,0.136) for Mn, (0.333,0.275) for O(1), and (-0.211,-0.033) for O(2). The lattice constants are $a_1 = 4.533$ Å, $a_2 = 9.27$ Å, $a_3 = 2.866$ Å. The unit cell is depicted in figure 3.6. The combining of atoms into the layers A, B, C, and D shown in figure 3.6 will be important when defining the model for γ-MnO_2.

3.2.2 Pyrolusite or β-MnO_2

The mineral pyrolusite and its synthetic analogue, β-MnO_2, have structures that are very similar to the one of ramsdellite, the main difference being the way in which the manganese atoms are arranged on their hexagonal layers. Instead of the ramsdellitic ribbons of manganese atoms, one finds single chains or strings, as depicted in figure 3.7. This leads to a structure with one-dimensional 1×1 tunnels (figure 3.4b).

Pyrolusite is based on the tetragonal space group $P4_2/mnm$ (No. 136) [43] with manganese in Wyckoff position (2a): $(0,0,0)$ and $(\frac{1}{2},\frac{1}{2},\frac{1}{2})$, and oxygen in (4f): $(u,u,0)$, $(\frac{1}{2}+u, \frac{1}{2}-u, \frac{1}{2})$, $(-u,-u,0)$, and $(\frac{1}{2}-u, \frac{1}{2}+u, \frac{1}{2})$ with $u = 0.302$. The lattice parameters are $a_1 = a_2 = 4.396$ Å, $a_3 = 2.871$ Å. The unit cell is depicted in figure 3.8. The combining of atoms into layers B, and D', shown in figure 3.8, will be important when defining the model for γ-MnO_2.

3.2.3 γ-MnO_2

Initially, manganese dioxides were classified as γ-MnO_2 because of certain features of their X-ray diffraction pattern, which is characterized by some broad peaks and

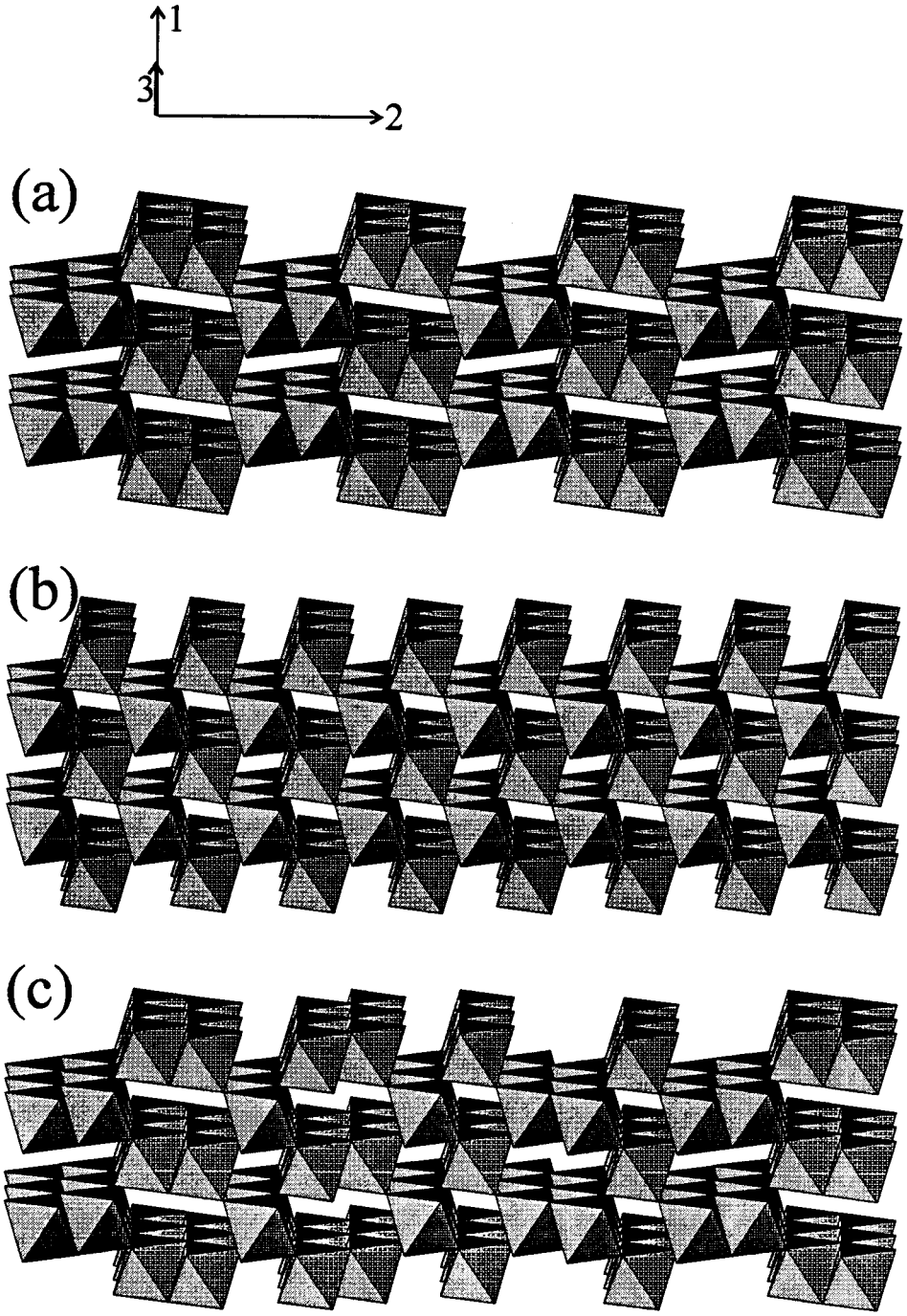

Figure 3.4: Depiction of idealized structures of some MnO_2 polymorphs: (a) ramsdellite, (b) pyrolusite, and (c) γ-MnO_2. The octahedra shown have oxygen atoms at the 6 corners and a manganese atom in the centre. The figure ignores distortions of the octahedra and shows a hexagonal close packing of oxygen atoms.

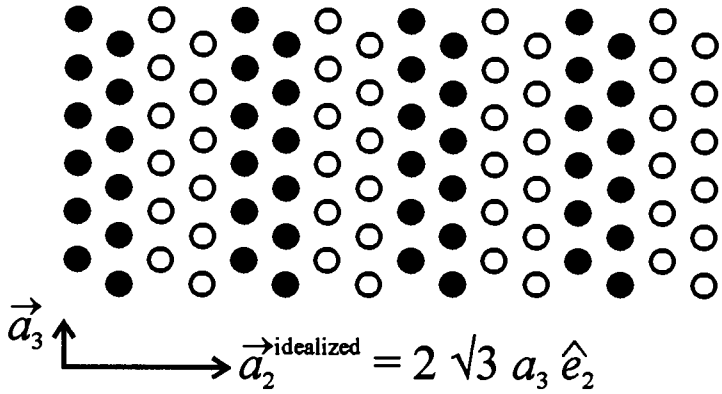

Figure 3.5: Idealized hexagonal manganese layer of ramsdellite. The black and white sites are either filled and unfilled, or unfilled and filled, depending on the position of this layer in stack.

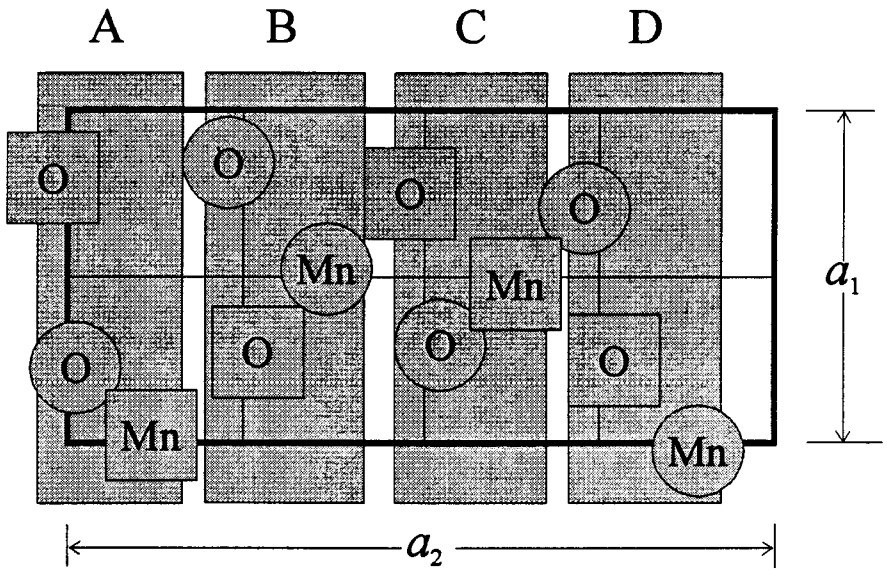

Figure 3.6: Unit cells of ramsdellite viewed along the 3-direction. Circles indicate atoms in the plane of the paper, squares indicate atoms $a_3/2$ above the plane. The shaded regions of the ramsdellite unit cell define the layers A, B, C, and D.

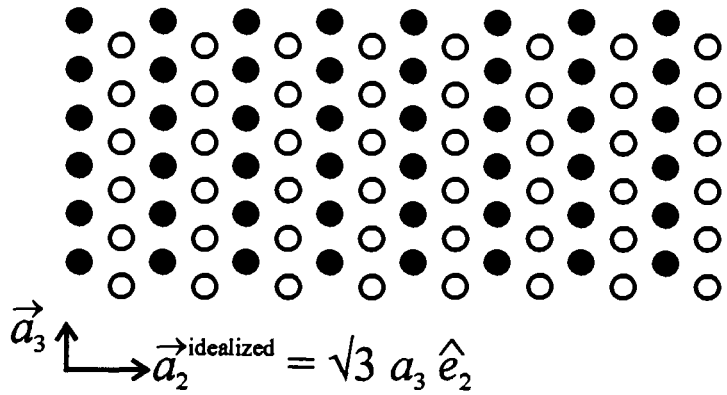

Figure 3.7: Idealized hexagonal manganese layer of pyrolusite. The black and white sites are either filled and unfilled, or unfilled and filled, depending on the position of this layer in stack.

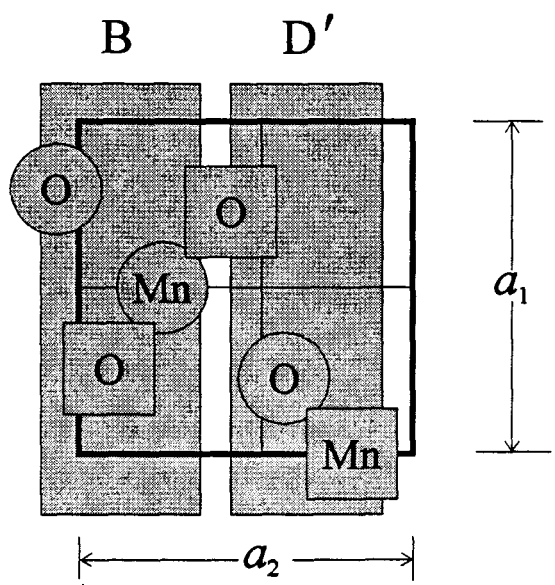

Figure 3.8: Unit cells of pyrolusite viewed along the 3-direction. Circles indicate atoms in the plane of the paper, squares indicate atoms $a_3/2$ above the plane. Ramsdellite layers B and D′ are also present in the pyrolusite unit cell, where D′ is a D layer shifted by $a_3/2$ in the 3-direction.

some sharp peaks. In 1959 de Wolff [14] devised a model that can account for such a pattern, which is indicative of a non-periodic structure . In this thesis, I define the structure of γ-MnO_2 by this model of de Wolff, which describes the structure as an intergrowth of ramsdellitic and pyrolusitic domains.

Again, it is the way the manganese atoms are arranged on their hexagonal layers that distinguishes γ-MnO_2 from the previous modifications . Here one finds a random succession of ribbons and strings, instead of just ribbons (as in ramsdellite) or just strings (as in pyrolusite). An example for such an intergrowth of ribbons and strings is depicted in figure 3.9 leading to an mixture of 2×1 and 1×1 tunnels in the three-dimensional structure (figure 3.4c).

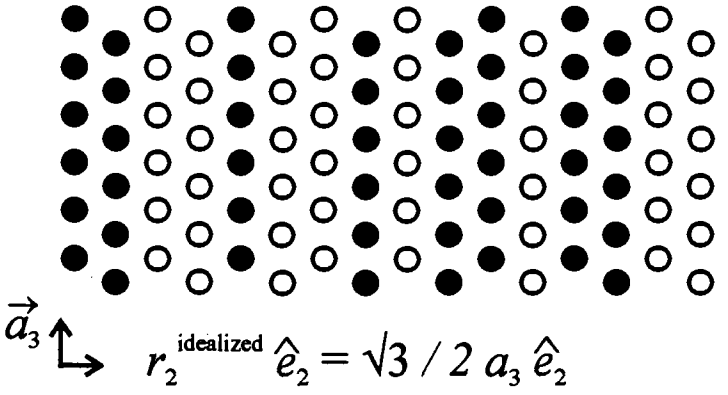

Figure 3.9: Idealized hexagonal manganese layer of γ-MnO_2. The black and white sites are either filled and unfilled, or unfilled and filled, depending on the position of this layer in stack.

In order to formalize this statement of intergrowth, one needs to take a closer look at the unit cells of ramsdellite and pyrolusite, shown in figures 3.6 and 3.8. Here certain manganese atoms and oxygen atoms have been combined into layers, as indicated by the gray shadings. For the pyrolusite case, it is not immediately obvious, why the right-hand layer should be labelled D', instead of A, but a look at the constraints imposed by the respective space groups shows that D' (*i.e.* a D layer shifted by half a unit cell in the a_3-direction) is the correct assignment.

Ramsdellite is created by an ordinary stacking of ...ABCDABCD... If a pyro-

lusite fault was to be introduced in this stacking sequence, then a B layer should be followed by a D layer (with an appropriate phase shift, *i.e.* D′) or a D layer should be followed by a B layer (again with an appropriate phase shift, *i.e.* B′).

Based on this model, the positions of the atoms in the layers A, B, C, and D can be described by seven parameters as shown in table 3.1. Parameters for the atom positions in the 1- and 3-directions are given as fractions of the lattice constants, whereas parameters for the 2-direction are given in Ångström because γ-MnO_2 does not have a well defined lattice constant a_2.

Table 3.1: Use of the seven parameters to define the atom positions in layers A, B, C, and D.

Layer	Atom	d_1/a_1	d_2/Å	d_3/a_3
A	O	$1 - \mathrm{d}x_{\mathrm{Ol}}$	$-\mathrm{d}y_{\mathrm{Ol}}$	0
	O	$0 + \mathrm{d}x_{\mathrm{Ol}}$	$\mathrm{d}y_{\mathrm{Ol}}$	0.5
	Mn	$0 + \mathrm{d}x_{\mathrm{Mn}}$	$\mathrm{d}y_{\mathrm{Mnl}}$	0
B	O	$0.5 + \mathrm{d}x_{\mathrm{Os}}$	$-\mathrm{d}y_{\mathrm{Os}}$	0.5
	O	$0 + \mathrm{d}x_{\mathrm{Os}}$	$\mathrm{d}y_{\mathrm{Os}}$	0
	Mn	$0.5 + \mathrm{d}x_{\mathrm{Mn}}$	$\mathrm{d}y_{\mathrm{Mns}}$	0.5
C	O	$0.5 + \mathrm{d}x_{\mathrm{Ol}}$	$-\mathrm{d}y_{\mathrm{Ol}}$	0
	O	$0.5 - \mathrm{d}x_{\mathrm{Ol}}$	$\mathrm{d}y_{\mathrm{Ol}}$	0.5
	Mn	$0.5 - \mathrm{d}x_{\mathrm{Mn}}$	$\mathrm{d}y_{\mathrm{Mnl}}$	0
D	O	$1 - \mathrm{d}x_{\mathrm{Os}}$	$-\mathrm{d}y_{\mathrm{Os}}$	0.5
	O	$0.5 - \mathrm{d}x_{\mathrm{Os}}$	$\mathrm{d}y_{\mathrm{Os}}$	0
	Mn	$0 - \mathrm{d}x_{\mathrm{Mn}}$	$\mathrm{d}y_{\mathrm{Mns}}$	0.5

In ramsdellite, these parameters would take the following values

$$\begin{aligned} \mathrm{d}x_{\mathrm{Ol}} &= 0.211 \quad \mathrm{d}y_{\mathrm{Ol}} = 0.31 \\ \mathrm{d}x_{\mathrm{Os}} &= 0.333 \quad \mathrm{d}y_{\mathrm{Os}} = 0.23 \\ \mathrm{d}x_{\mathrm{Mn}} &= 0.022 \quad \mathrm{d}y_{\mathrm{Mnl}} = 1.26 \\ & \qquad\quad \mathrm{d}y_{\mathrm{Mns}} = 1.06. \end{aligned} \tag{3.1}$$

Layers B and D′ would create the pyrolusite structure, if

$$\begin{aligned} \mathrm{d}x_{\mathrm{Os}} &= 0.302 \quad \mathrm{d}y_{\mathrm{Os}} = 0.22 \\ \mathrm{d}x_{\mathrm{Mn}} &= 0.000 \quad \mathrm{d}y_{\mathrm{Mns}} = 1.10 \end{aligned} \tag{3.2}$$

These values are not too different from the corresponding ramsdellite values, certainly within the limits of distortion that one could expect in an intergrowth structure.

3.2.4 ε-MnO_2

As with γ-MnO_2, this modification was initially characterized by the appearance of its X-ray diffraction pattern, which consists of only three or four strong, well defined, though broad, peaks. Again, it was de Wolff (this time with co-workers) [44] who proposed a structure for these materials, which consists of a hexagonal close packed oxygen lattice with a random arrangement of manganese atoms on half the octahedral sites of their hexagonal layers. In the direction perpendicular to the layers, which corresponds to the a_1-direction of γ-MnO_2, filled and unfilled octahedra alternate periodically.

3.2.5 δ-MnO_2, Pyrochroite, Birnessite, Buserite

A δ-MnO_2 is actually not a true manganese dioxide, but rather a layered oxide of the form A_xMnO_2 (A = Na, K, NH_4, Cs, H_2O ...) [45, 46, 47] and is structurally related to pyrochroite, $Mn(OH)_2$. Pyrochroite itself is, again, based on a hexagonal close packed oxygen lattice, but with cation layers alternatingly completely occupied with and free of manganese atoms. Such a description ignores the presence of hydrogen next to the oxygen atoms, which are important as they balance the charge and stabilize the structure. However, their presence cannot be observed directly by X-ray diffraction as their atomic form factor is small, if not zero (in case the charge transfer from hydrogen to oxygen is complete).

Figure 3.10 shows a powder X-ray diffraction pattern of $Mn(OH)_2$[2] including a fit obtained by Rietveld refinement. The space group for this compound is $P\bar{3}m1$ (No. 164) with manganese atoms in Wyckoff position (1a): $(0,0,0)$, and oxygen

[2] $Mn(OH)_2$ can be prepared by mixing a de-aerated Mn^{2+}-solution (*e.g.* $MnSO_4$) with a de-aerated hydroxide solution (*e.g.* LiOH). The white precipitate has to be filtered off and dried under oxygen-free conditions, as to avoid oxidation of $Mn(OH)_2$ to β–MnOOH and Mn_3O_4. This can be achieved, for instance, by rinsing with anhydrous acetone.

atoms in (2d): $(\frac{1}{3}, \frac{2}{3}, u)$, $(\frac{2}{3}, \frac{1}{3}, \bar{u})$. From refinement, I obtained lattice parameters $a_1 \equiv a_2 = 3.3199(3)$ Å and $a_3 = 4.7367(7)$ Å. The structural parameter, u, refined to $u = 0.249(2)$; the Bragg-R factor of 2.66 is not too large so that one can have confidence in the refined values.

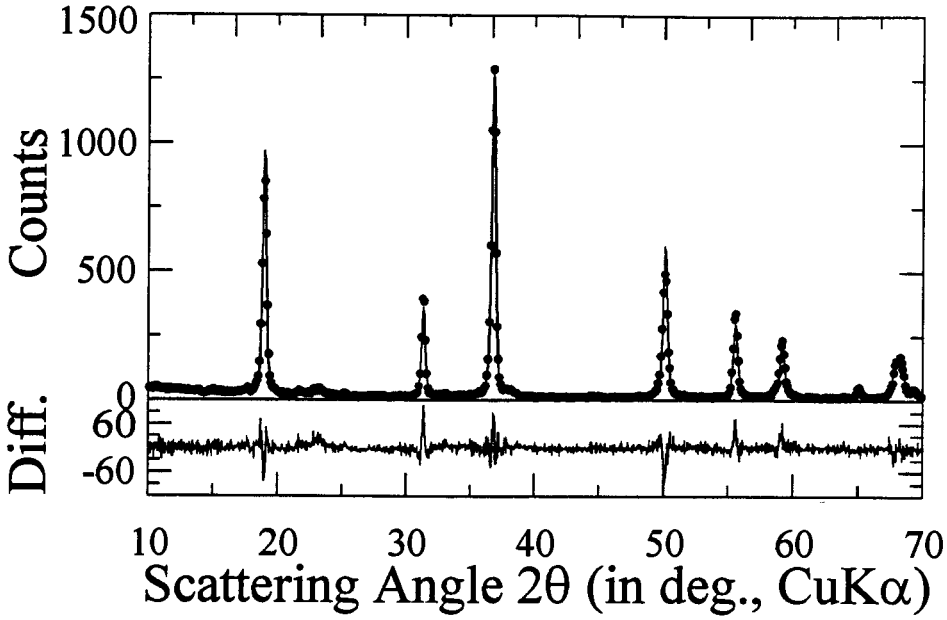

Figure 3.10: Powder X-ray diffraction pattern of $Mn(OH)_2$ (dots) and refinement fit (solid line). The quality of the fit suggests that the obtained parameters are reliable.

In birnessite (after Birnes, Scotland, where it was first found), the "unoccupied" layers typically contain cations, such as potassium, sodium, or magnesium, as well as water, which increases the lattice parameter a_3 from 4.7 Å in pyrolusite to 7 Å in birnessite. This value gave rise to the alternate name of 7Å-manganite for these compounds, while compounds with even more interstitial water are 10Å-manganites or buserites (after W. Buser, who was the first to isolate the mineral and then to synthesize it — see footnote in [48]).

The space group of birnessite was only recently determined by Post and Veblen [49] as monoclinic C 2/m (No. 12). The lattice parameters depend on the dopant cation, for potassium they found: $a_1 = 5.149$ Å, $a_2 = 2.843$ Å, $a_3 = 7.176$ Å, and

$\alpha_2 = 100.76°$. The manganese atoms are in (2a): $(0,0,0)$ and $(\frac{1}{2},\frac{1}{2},0)$; the oxygen are in (4i): $(u,0,v)$, $(\frac{1}{2}+u,\frac{1}{2},v)$, $(\bar{u},0,\bar{v})$, and $(\frac{1}{2}-u,\frac{1}{2},\bar{v})$ with $u = 0.365$ and $v = 0.136$, and potassium in (4i) with $u = 0.723$ and $v = 0.522$, and 1.3 potassium atoms for every 2 oxygen atoms and every manganese atom. Additionally they propose to have 0.3 water at (2c): $(0,0,\frac{1}{2})$ and $(\frac{1}{2},\frac{1}{2},\frac{1}{2})$. The structure of these birnessites is similar to those of the layered $LiMnO_2$ compound recently synthesized by Armstrong and Bruce [50].

I prepared a similar material by reacting MnO_2 (CMD-R from Sedema) and KOH at 470 °C in argon, following [51]. However, I washed the product with water instead of ethanol. The powder X-ray diffraction pattern including a Rietveld refinement is shown in figure 3.11. The lattice parameters are close to those in reference [49], but the refinement of the structural parameters is not completely reliable, since the Bragg R factor remains high (approximately 5). The resulting crystal structure is depicted in figure 3.12.

3.2.6 λ-MnO_2

Unlike the previous modifications, λ-MnO_2, is based on a cubic close packed oxygen lattice. Since it is obtained by de-lithiating $LiMn_2O_4$ [15], which has the same structure as the spinel $MgAl_2O_4$, λ-MnO_2 contains many apparent voids in the cation lattice. These voids are connected to form a three-dimensional network of channels along which lithium atoms can be re-inserted, making λ-MnO_2 an attractive material for rechargeable lithium cells (this will be the subject of the next chapter).

The space group of these spinel structures is Fd3m (recently renamed as $Fd\bar{3}m$); the Bravais lattice face-centred cubic with a lattice constant of 8.03 Å for λ-MnO_2 and 8.24 Å for the lithiated compound $LiMn_2O_4$.

Using the origin choice 2 with the origin at the centre ($\bar{3}m$), the oxygen atoms are in (32e) (u,u,u), $(\frac{1}{4}-u,\frac{1}{2}+u,\frac{3}{4}-u)$, $(\frac{3}{4}+u,\frac{1}{4}+u,\frac{1}{2}-u)$, $(\frac{1}{4}+u,\frac{1}{2}-u,\frac{3}{4}+u)$, $(\frac{3}{4}-u,\frac{1}{4}-u,\frac{1}{2}+u)$, $(\frac{1}{2}+u,\frac{3}{4}-u,\frac{1}{4}-u)$, $(\frac{1}{2}-u,\frac{3}{4}+u,\frac{1}{4}+u)$, and $(\bar{u},\bar{u},\bar{u})$ + face-centring with $u \approx 0.26$; manganese atoms are in (16d): $(\frac{1}{2},\frac{1}{2},\frac{1}{2})$, $(\frac{1}{4},\frac{3}{4},0)$, $(\frac{3}{4},0,\frac{1}{4})$, and $(0,\frac{1}{4},\frac{3}{4})$, + face-centring; lithium atoms in $LiMn_2O_4$ are in (8a): $(\frac{1}{8},\frac{1}{8},\frac{1}{8})$, $(\frac{7}{8},\frac{3}{8},\frac{3}{8})$, +

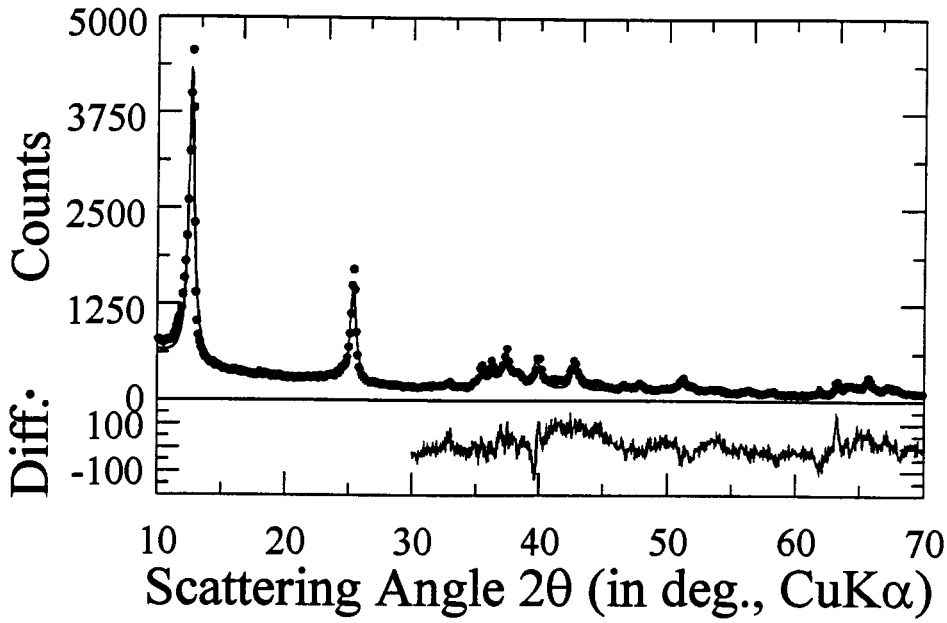

Figure 3.11: Powder X-ray diffraction pattern of a potassium-based δ-MnO_2 (dots) and a refinement fit (solid line). The difference plot starts at 30° because lower angle differences are off-scale. The lattice parameters are close to those in reference [49], the refinement of the structural parameters is not completely reliable, since the Bragg R factor remains high (approximately 5).

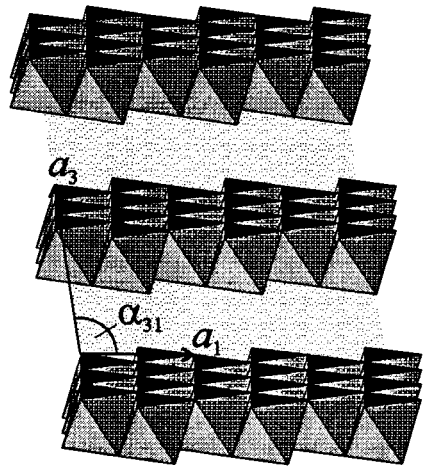

Figure 3.12: Structure of δ-MnO_2. The shaded interstitial space is typically filled with water and/or cations. In general, $\alpha_{31} \neq 90°$ — the crystal system is monoclinic.

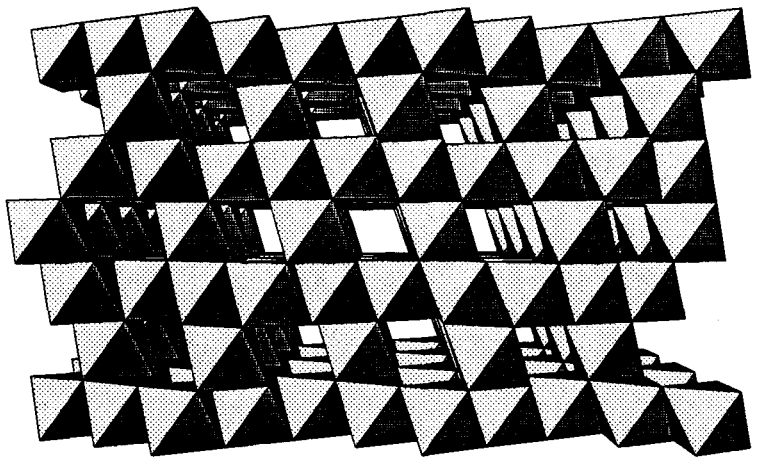

Figure 3.13: Structure of λ-MnO_2. 3/4-filled manganese layers alternate with 1/4-filled ones along the [111]-direction (up on the page), leading to a three-dimensional network of channels. The view is down the 1×1-tunnels that extend along the $[10\bar{1}]$-direction.

face-centring.

Since λ-MnO_2 is face-centred cubic, there are four equivalent directions (the cubic [111], $[\bar{1}11]$, $[1\bar{1}1]$, and $[11\bar{1}]$ directions) perpendicular to which there are hexagonal layers. The stacking along the [111] direction is depicted in figure 3.13, which shows the alternating 3/4- and 1/4-filling of the cation layers with manganese atoms. Crystallographically, these octahedral sites have the Wyckoff label (16d), the vacant ones are (16c). The filled and unfilled sites are more visibly depicted in figure 3.14 which shows a 3/4- and a 1/4-filled manganese layer, including the positions of the lithium atoms about the 1/4-filled layer in $Li[Mn_2]O_4$ (the square brackets indicate the atom or the atoms that occupy the (16d) site).

3.2.7 Hollandite, Cryptomelane, α-MnO_2

Materials in this category are not based on close-packed oxygen lattices, but contain large voids (one-dimensional 2×2 tunnels as shown in figure 3.15) that are usually stabilized by cations, such as potassium, barium or lead [52]. Naturally occurring materials of this structure are minerals such as cryptomelane, hollandite, and coro-

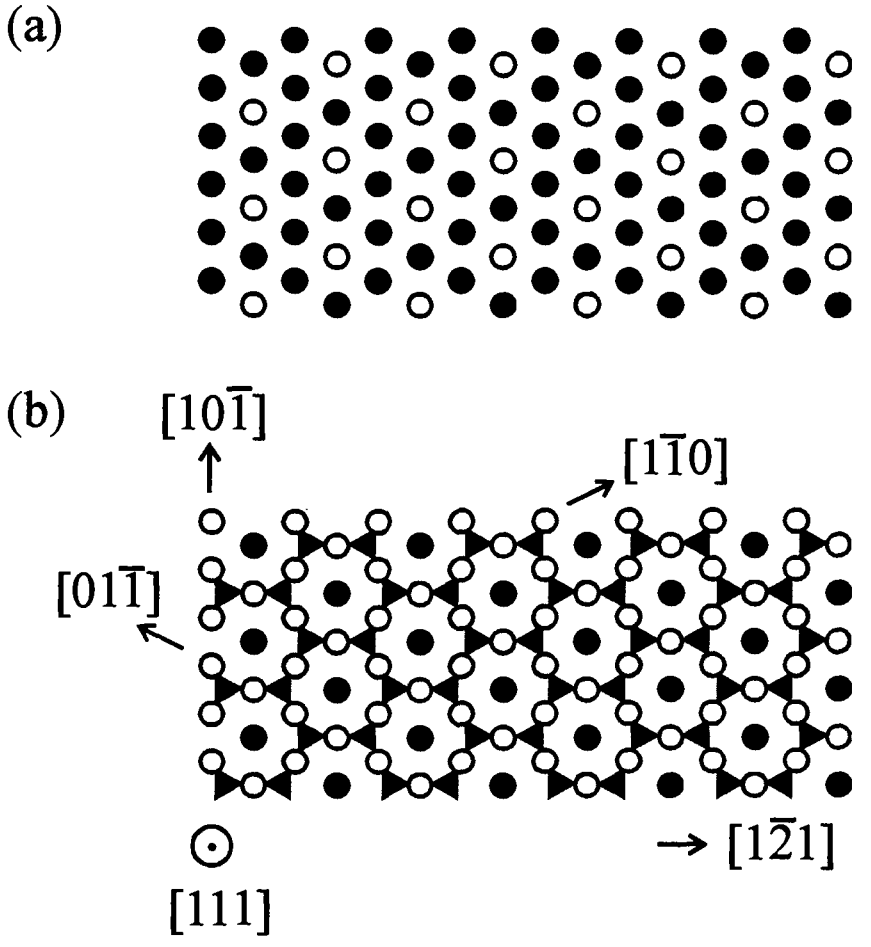

Figure 3.14: Hexagonal manganese layer of λ-MnO_2. The black circles represent (16d) sites filled with manganese atoms, and the white circles represent unfilled (16c) sites. Panel (a) shows a 3/4-filled layer and (b) a 1/4-filled layer. The stacking along the [111]-direction positions the 1/4-filled layer on top of the 3/4-filled layer such that the left-pointing triangles in (b) are above the white circles in (a). The next 3/4-filled layer is placed such that the white circles in (a) are above the right-pointing triangles in (b).
The triangles in (b) indicate the tetrahedral (8a) sites, filled with lithium atoms in $LiMn_2O_4$. The distance of the lithium atoms to the 1/4-filled manganese layer is half the distance between this manganese layers and the adjacent oxygen layers. Right-pointing triangles are above the plane of the manganese atoms, left-pointing triangles are below.

nadite. However, Rossouw and co-workers [53] recently reported that they prepared this polymorph without any stabilizing atoms in the tunnels, but a small amount of water in the tunnel sites leading to an overall composition of $MnO_2{\cdot}0.3H_2O$.

The space group of these materials was determined by Byström and Byström [52] to be the body centred tetragonal I4/m (No. 87). The lattice parameter depend on the number of cations present in the structure; for $MnO_2{\cdot}0.3H_2O$ they are $a_1 = a_2 = 9.7799$ Å and $a_3 = 2.8534$ Å [53]. The manganese atoms are in(8h): $(u, v, 0)$, $(\frac{1}{2}+u, \frac{1}{2}+v, \frac{1}{2})$, $(\bar{u}, \bar{v}, 0)$, $(\frac{1}{2}-u, \frac{1}{2}-v, \frac{1}{2})$, $(\bar{v}, u, 0)$, $(\frac{1}{2}-v, \frac{1}{2}+u, \frac{1}{2})$, $(v, \bar{u}, 0)$, $(\frac{1}{2}+v, \frac{1}{2}-u, \frac{1}{2})$ with $u = 0.348$ and $v = 0.167$; oxygen atoms of type 1, O(1), are in (8h) with $u = 0.153$ and $v = 0.180$; oxygen atoms of type 2, O(2), are in (8h) with $u = 0.542$ and $v = 0.167$; and the cations are in(2b): $(0, 0, \frac{1}{2})$ and $(\frac{1}{2}, \frac{1}{2}, 0)$. A more recent refinement [54] found a small monoclinic distortion in hollandite and cryptomelane ($\alpha_{31} \approx 91°$), which I will ignore.

3.3 Model for γ-MnO_2

3.3.1 Modulation Function for the Ramsdellite/Pyrolusite Intergrowth

The first step in finding the modulation function in the 2-direction, G_2, is to obtain the matrix Q, which is determined by the products $p_{ij}\phi_{ij}$. There are four types of layers in the de-Wolff model (A, B, C, D); thus Q will be a 4×4-matrix.

In order to find the correct spacings for the inter-layer phase factors, one can consider the spacings in ramsdellite and pyrolusite. With the lattice constant of ramsdellite ($a_2 = 9.27$ Å) a little more than twice that of pyrolusite ($a_1 = a_2 = 4.40$ Å), the difference between the two inter-layer spacings is not too big ($r_P = 2.20$ Å *vs.* $r_R = 2.32$ Å). Since it is not obvious how the inter-layer spacing would be affected in a fault-containing stacking sequence, I introduced a mean spacing together with a strain factor, leading to a strained phase factor,

$$\phi = \exp\left(-i2\pi s_2 r_2 - 2\pi^2 {s_2}^2 {\sigma_2}^2\right), \tag{3.3}$$

where r_2 is the mean inter-layer distance and σ_2 is the rms deviation.

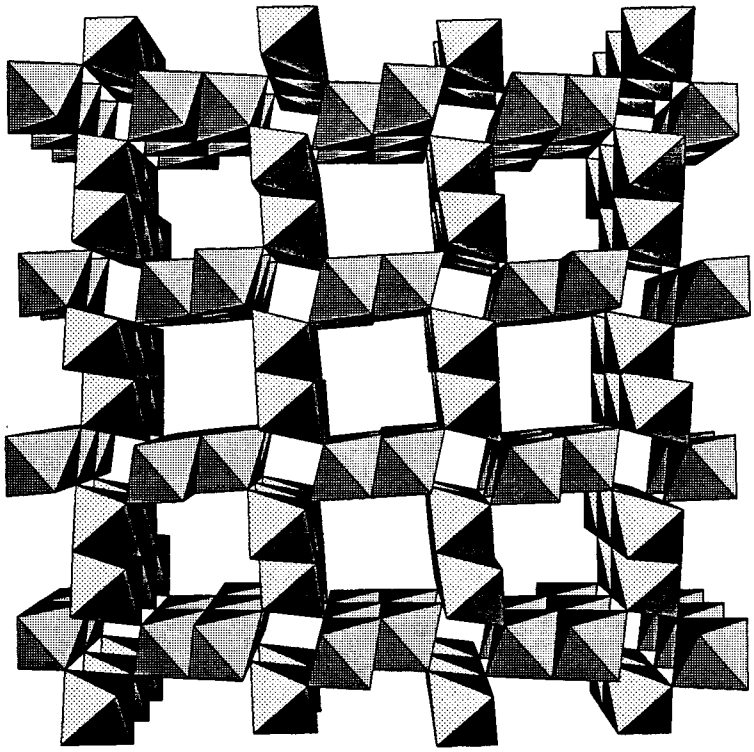

Figure 3.15: The structure of α-MnO_2 is characterized by the presence of both 1×1- and 2×2-tunnels along the crystallographic 3-direction. The 2×2-tunnel typically contain cations and/or water.

After defining an order parameter p, the probability that a B layer is followed by a D′ layer instead of a C layer, one can write down the matrix Q:

$$\mathsf{Q} = \begin{bmatrix} 0 & 1 & 0 & 0 \\ 0 & 0 & 1-p & p(-1)^l \\ 0 & 0 & 0 & 1 \\ 1-p & p(-1)^l & 0 & 0 \end{bmatrix} \phi, \tag{3.4}$$

where the phase factor $(-1)^l$ accounts for the shifts of layers B and D by half a unit cell in the 3-direction to obtain layers B′ and D′, respectively. At this point there are two ways to proceed: (1) One can do the sum (equation 2.61) used in the expression for the modulation function (equation 2.62) first, which leads to the problem of inverting I-Q. (2) One can diagonalize Q and do the sum afterwards. If both problems needed to be tackled numerically, it would not be obvious which option

to choose. Fortunately, one can block-diagonalize Q algebraically, since Q is of the form

$$\mathsf{Q} = \begin{bmatrix} \mathsf{Q}' & \mathsf{Q}'' \\ \mathsf{Q}'' & \mathsf{Q}' \end{bmatrix}. \tag{3.5}$$

One finds

$$i(h,l,s_2) = \mathsf{F}^{(+)\dagger}\mathsf{G}_2^{(+)}\mathsf{F}^{(+)} + \mathsf{F}^{(-)\dagger}\mathsf{G}_2^{(-)}\mathsf{F}^{(-)}, \tag{3.6}$$

with

$$\mathsf{F}^{(\pm)} = \begin{bmatrix} F_\mathrm{A} \pm F_\mathrm{C} \\ F_\mathrm{B} \pm F_\mathrm{D} \end{bmatrix} \tag{3.7}$$

and

$$\mathsf{G}_2^{(\pm)} = \mathsf{W}^{(\pm)} \left(\mathsf{I} + \frac{2}{N_2} \sum_{m=1}^{N_2-1} (N_2 - m)(\mathsf{Q}^{(\pm)})^m \right) + \text{h.c.}, \tag{3.8}$$

where

$$\mathsf{W}^{(+)} = \mathsf{W}^{(-)} = \begin{bmatrix} 1-p & 0 \\ 0 & 1 \end{bmatrix} \text{ and } \mathsf{Q}^{(\pm)} = \mathsf{Q}' \pm \mathsf{Q}'', \tag{3.9}$$

and h.c. is the hermitian conjugate. The remaining diagonalization of the 2×2-matrix $\mathsf{Q}^{(\pm)}$ is straightforward.

3.3.2 Position of the Diffraction Peaks

Following the discussion of random faults in section 2.7.3, the term $(N_2 - m)/N_2$ in equation (3.8) can be replaced by ${U_2}^m$, where $U_2 = \exp(-2/N_2)$ and N_2 is now the average number of layers stacked without encountering a random fault. The total stack can then be assumed to be infinitely large (the upper limit of the sum in equation (3.8) is replaced by ∞) so that the modulation function simplifies to

$$\mathsf{G}_2^{(\pm)} = \mathsf{W}^{(\pm)} \frac{\mathsf{I} + U_2\mathsf{Q}^{(\pm)}}{\mathsf{I} - U_2\mathsf{Q}^{(\pm)}} + \text{h.c.} \tag{3.10}$$

$$= \left\{ \frac{2}{1 \mp (pU_2\phi_\mathrm{P}e^{i\pi l} + (1-p)(U_2\phi_\mathrm{R})^2)} \begin{bmatrix} \pm[(1-p)U_2\phi_\mathrm{R}]^2 & (1-p)U_2\phi_\mathrm{R} \\ (1-p)U_2\phi_\mathrm{R} & 1 \end{bmatrix} + \begin{bmatrix} 1-p & 0 \\ 0 & -1 \end{bmatrix} \right\} + \text{h.c.} \tag{3.11}$$

For sufficiently narrow peaks ($U_2 \approx 1$), the positions of the maxima are given by the roots of the square modulus of the determinant of $\mathsf{I} - \mathsf{Q}^{(\pm)}$. If one assumes that the mean inter-layer distance, r_2, is the weighted average of the ramsdellite and pyrolusite spacing, $r_2 = ((1-p)2r_R + pr_P)/(2-p)$, one can plot the position of the diffraction peaks for various values of the order parameter, p.

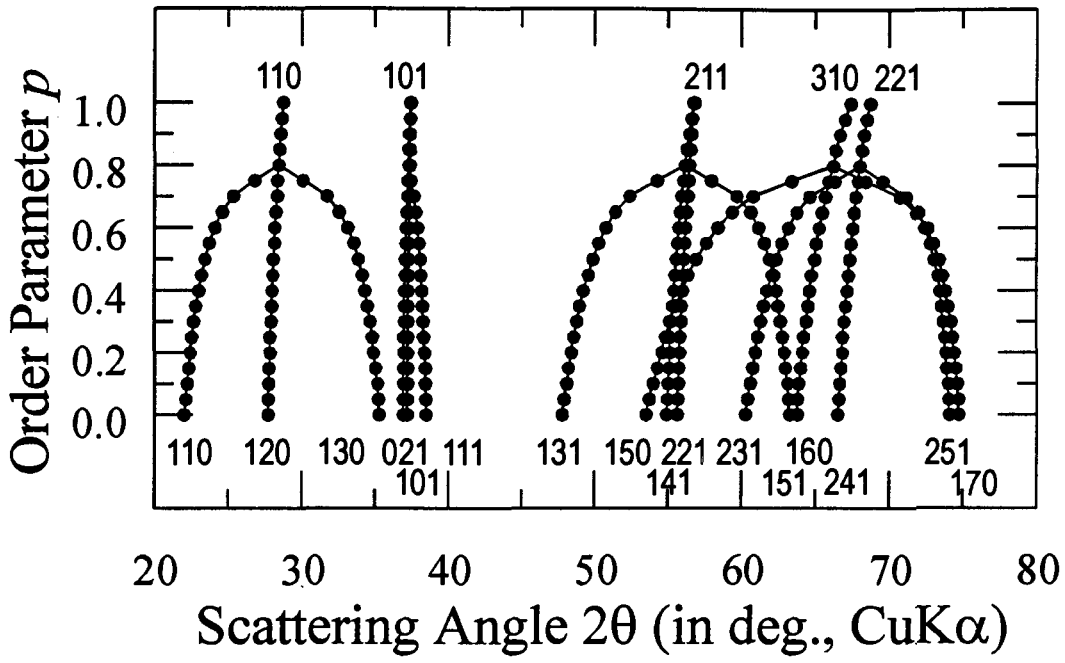

Figure 3.16: Shifts of the positions of selected powder X-ray diffraction peaks of γ-MnO_2 with increasing order parameter, p. Some of the lattice parameters are also adjusted: $a_1 = 4.40$ Å $+ (1-p)\ 0.13$ Å, $r_2 = ((1-p)\,2\times 2.32$ Å $+p\,2.20$ Å $)/(2-p)$, whereas $a_3 = 2.87$ Å is kept constant. The Miller indices at the bottom correspond to a ramsdellite unit cell, those at the top to a pyrolusite unit cell.

This has been done for selected peaks in figure 3.16. One can see how certain peaks of the ramsdellite pattern ($p = 0$) move and eventually merge to make up the peaks of the pyrolusite pattern ($p = 1$). However care must be taken in drawing conclusions from this figure: It only shows peak positions and does not give any information regarding the intensities or breadths of the peaks that one would obtain by taking the full expression for $\mathsf{G}_2^{(\pm)}$ as well as the structure factors into consideration. Nonetheless, this figure shows that one expects the ramsdellite 110 peak to move to

higher angle whereas the 130 and 111 peaks should move to lower angles. Also the 131 and 151 peaks will be of interest later.

On the first glance, it may seem surprising that major positional shifts of the diffraction peaks occur for p in the range between 0.6 and 0.8, or so, instead of around 0.5. However, one has to realize that p gives the ratio of the number of 1×1-tunnels to the total number of tunnels. If one takes the larger size of the 2×1-tunnels into consideration and calculates the volume fraction, $v_{1\times1} = p/(2-p)$, of 1×1-tunnels in the structure, one finds that the transition indeed occurs for $v_{1\times1} \approx 0.5$.

3.3.3 Fitting Programme

In order to perform the non-linear fit to the measured X-ray diffraction pattern, I utilize a routine given in *Numerical Recipes* [55]. It aims at minimizing

$$\chi^2 = \sum_{n=1}^{N_{\text{data}}} \frac{\left(i_n^{\text{meas}} - i_n^{\text{calc}}\right)^2}{\left(\sigma_n^{\text{meas}}\right)^2}, \tag{3.12}$$

where N_{data} is the number of data points to be fit, $i_n^{\text{meas}} - i_n^{\text{calc}}$ is the difference between the measured and calculated intensity at the n^{th} data point, and σ_n^{meas} is the uncertainty in the measured intensity. I assume that the main contributing factor to the uncertainty in the measurement was the temporal randomness with which X-ray photons enter the detector, leading to a Poisson distribution with the uncertainty in the measured number of photons being equal to the square root of that number.

Parameters included in the programme are: an overall scale factor, η; a background function $\sum_{n=-1}^{4} c_n(2\theta)^n$; an overall temperature factor, B; for the 1- and 3-direction, lattice constants, mean numbers of unit cell repetitions, strain parameters; for the 2-direction, inter-layer spacing, mean number of layers, strain parameter, order parameter p; atomic positions, 3 manganese coordinates, 4 oxygen coordinates.

The programme is currently implemented on a Pentium-90 PC and each iteration step during refinement typically takes less than a minute, depending on number and range of data points as well as the precision in the numerical integration.

In order to test the fitting programme with a known structure for $p = 1$, I employed commercial β-MnO_2 (99.5%, Fisher). For comparison purposes, the X-ray

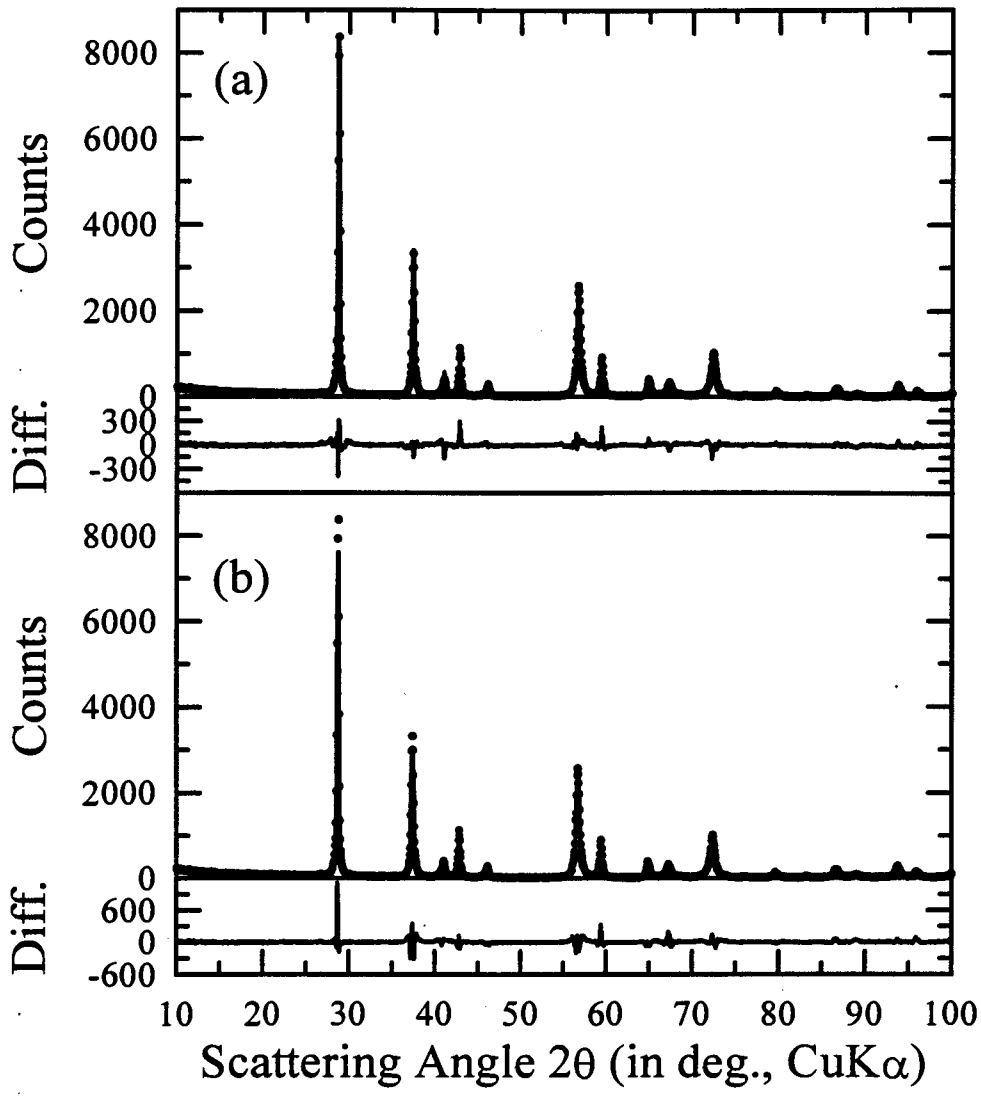

Figure 3.17: Fit to the X-ray diffraction pattern of commercial β-MnO_2 with (a) a Rietveld programme and (b) the programme developed in this thesis.

diffraction pattern of this β-MnO_2 was also fit by a Rietveld programme [56, 57] (see figure 3.17). The fit of the Rietveld programme is better, mainly because of a better match to the peak shapes by utilizing pseudo-Voigt peaks, whereas my extensive manipulation of the modulation functions G_1, G_2, and G_3 may not result in a peak shape function that fits as nicely. All parameters are summarized in table 3.2.

The parameters of the Rietveld fit are within the expected range, only the overall temperature factor remains negative. Repeated grinding of the sample led to increased improvement of the fit as the crystal size of the powder continuously decreased and the randomization of crystal orientation increased. The origin of the anomalous temperature factor of the pattern shown in figure 3.17 may still lie in prevalent preferred orientation effects or already in the damage to the crystal structure due to extensive grinding. Whatever the origin, a different temperature factor does not affect the lattice parameters or the one parameter for the oxygen position significantly. The pattern suffices to test my fitting programme.

Looking at the parameters obtained from my fitting programme, one sees that all average repeat distances, N_1, N_2, and N_3, are large and that the corresponding strain factors are small. This is consistent with the high crystallinity of the measured material. The lattice parameter a_3 is almost identical to the Rietveld one, whereas parameters a_1 and $2r_2$ are larger and smaller than the Rietveld parameters, a_1 and a_2, as no space group constraints are imposed.

The positional parameters of the manganese atom are reasonable, although they do not correspond exactly to the expected parameters, as described in section 3.2.3. From this comparison, one can see that the statistical uncertainties obtained from the numerical analysis of the fitting process and given in table 3.2 are of no relevance because other errors dominate. Nonetheless, they were included in the table so as to indicated which parameter were varied during the fitting process.

It would have been most desirable to have a ramsdellite sample available in order to test the $p = 0$ limit. Unfortunately, this was not the case and I instead fit an X-ray diffraction pattern that was calculated with the Rietveld programme based on the structure proposed by Byström [39] (figure 3.18). I used a Gaussian/Lorentzian mixing parameter $\gamma = 0.3$ and a peak width variation that resembles the expected

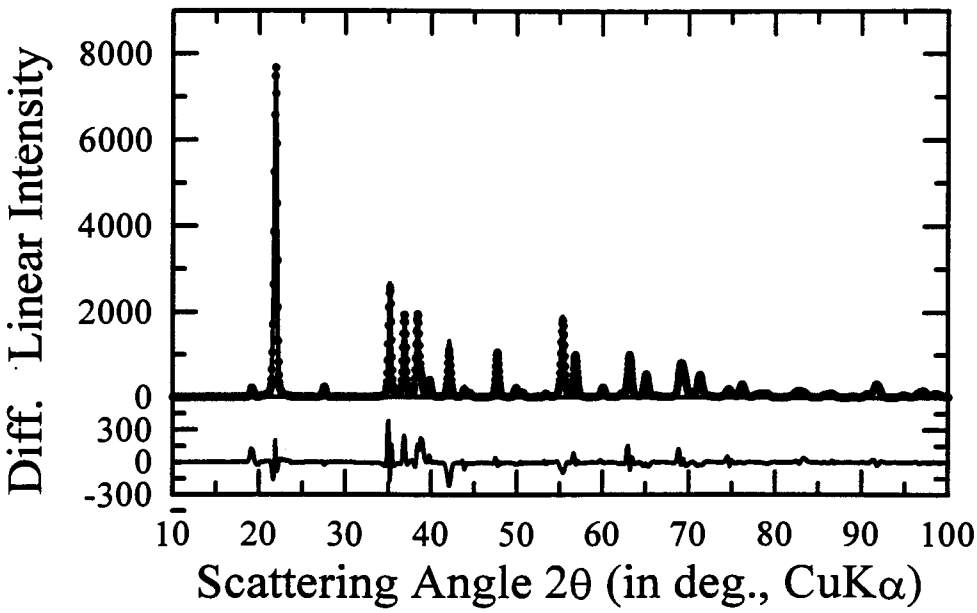

Figure 3.18: Fit to a calculated X-ray diffraction pattern of ramsdellite, generated by a Rietveld programme, with the programme developed in this thesis.

$1/\cos\theta$ broadening closely when calculating the ramsdellite pattern.

Again the fit is not perfect, but very encouraging. All lattice parameters obtained from the fit are almost identical to the values used to calculated the pattern. Again, the mean number of unit cell repetitions as well as the strain factors are of reasonable size. Even the positional parameter of the oxygen atoms are almost exactly as expected (see section 3.2.3) as is dx_{Mn}. Only the parameter for the position of the manganese atoms in the 2-direction are both larger than expected.

After having gained confidence that the programme calculates powder X-ray diffraction patterns point by point for the limiting structures, one can now continue and calculate a series of patterns for different order parameters, p. The evolution of the pattern is shown in figure 3.19. One can clearly see the change in the positions of the 110, 130, and 111 peaks as already shown in figure 3.16, but now one also sees the associated broadening, even more important for the 131 and 151 peaks.

Table 3.2: Parameters of my programme used to fit the measured β-MnO_2 and the calculated ramsdellite patterns as well as parameters obtained from the Rietveld programme, which was used to fit the β-MnO_2 pattern and to calculate the ramsdellite pattern. Quantities in parentheses are statistical uncertainties, obtained from the numerical fitting process, and indicate those parameter that were varied.

My programme			Rietveld programme		
Parameter	β-MnO_2	Ramsdellite	Parameter	β-MnO_2	Ramsdellite
$\eta \times 10^4$	4.45(2)	3.00(1)	$\eta \times 10^3$	17.1(1)	5.7
$c_{-1} \times 10^{-3}$	2.43(2)	0	$c_{-1} \times 10^{-3}$	2.30	0
c_0	−42(1)	6.9(1)	c_0	−26(2)	10
c_1	0.42(1)	0	c_1	0.20(3)	0
c_2	0	0	c_2	0	0
c_3	0	0	c_3	0	0
c_4	0	0	c_4	0	0
B	0.22(2)	0.03(2)	B	−0.35(5)	0
a_1	4.4100(2)	4.5303(1)	a_1	4.4012(3)	4.5300
N_1	250(10)	50(0)			
σ_1	0.0095(2)	0.0054(2)			
a_3	2.87442(8)	2.86604(6)	a_3	2.8741(2)	2.8660
N_3	86(1)	75(1)			
σ_3	0.0101(3)	0.0063(4)			
r_2	2.19658(8)	2.31629(6)	a_2	$\equiv a_1$	9.270
N_2	142(2)	143(2)			
σ_2	0.0353(7)	0.014(1)			
p	1	0			
dx_{Mn}	0.000(6)	0.0220(2)	u_{Mn}		0.022
dy_{Mnl}	1.26	1.364(8)	v_{Mn}		0.136
dy_{Mns}	1.12(4)	1.159(8)	$u_{O(1)}$	0.3036(5)	0.333
dx_{Ol}	0.211	0.2097(5)	$v_{O(1)}$		0.275
dy_{Ol}	0.31	0.310(3)	$u_{O(2)}$		−0.211
dx_{Os}	03222(9)	0.3327(6)	$v_{O(2)}$		−0.033
dy_{Os}	0.179(4)	0.227(3)			
			γ	1.03(2)	0.3
			U	0.26(5)	0.46
			V	0.19(5)	−0.15
			W	-0.037(9)	0.15

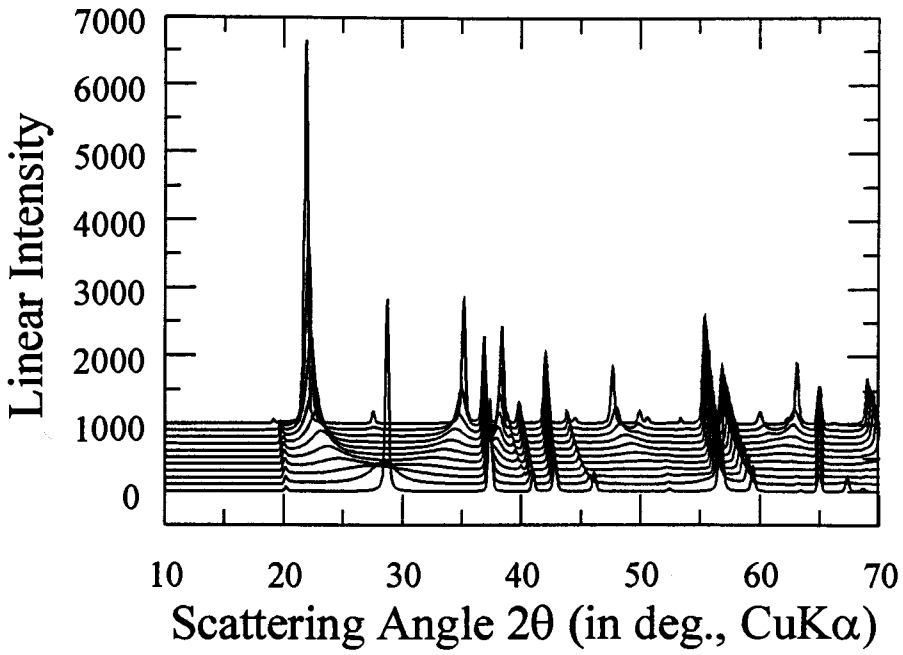

Figure 3.19: Evolution of the X-ray diffraction pattern of a γ-MnO_2 with changing order parameter p. The front pattern is that of pyrolusite ($p = 1$); subsequent patterns have order parameters 0.1 smaller and are offset by 100 on the intensity axis. The lattice parameter changes are as in figure 3.16. The small 100 peak at $2\theta \approx 20°$ in the $p = 1$ calculation appears because the atomic positions were not adjusted such that the two half-cells would have equal scattering strength leading to destructive interference.

3.3.4 Fits to a Ramsdellitic CMD and an EMD

I prepared a series of samples by heating two precursors in air overnight: TAD 1 and CMD-R. A few grams of each precursor were heated at the following temperatures: 110 °C, 250 °C, 300 °C, 350 °C, and 425 °C. Heating at higher temperature leads to oxygen loss and conversion to Mn_2O_3 (see section 3.5). Powder X-ray diffraction patterns were obtained on a Siemens D5000 diffractometer with a copper target tube and a diffracted beam monochromator selective for CuKα radiation. In order to obtain good counting statistics, a wide receiving slit (0.6 mm) at a goniometer radius of 217.5 mm and long count times (15s or 30s per 0.05° step) were chosen. Since the diffraction peaks were expected to be broad, the wide receiving slit would not add significant instrumental broadening.

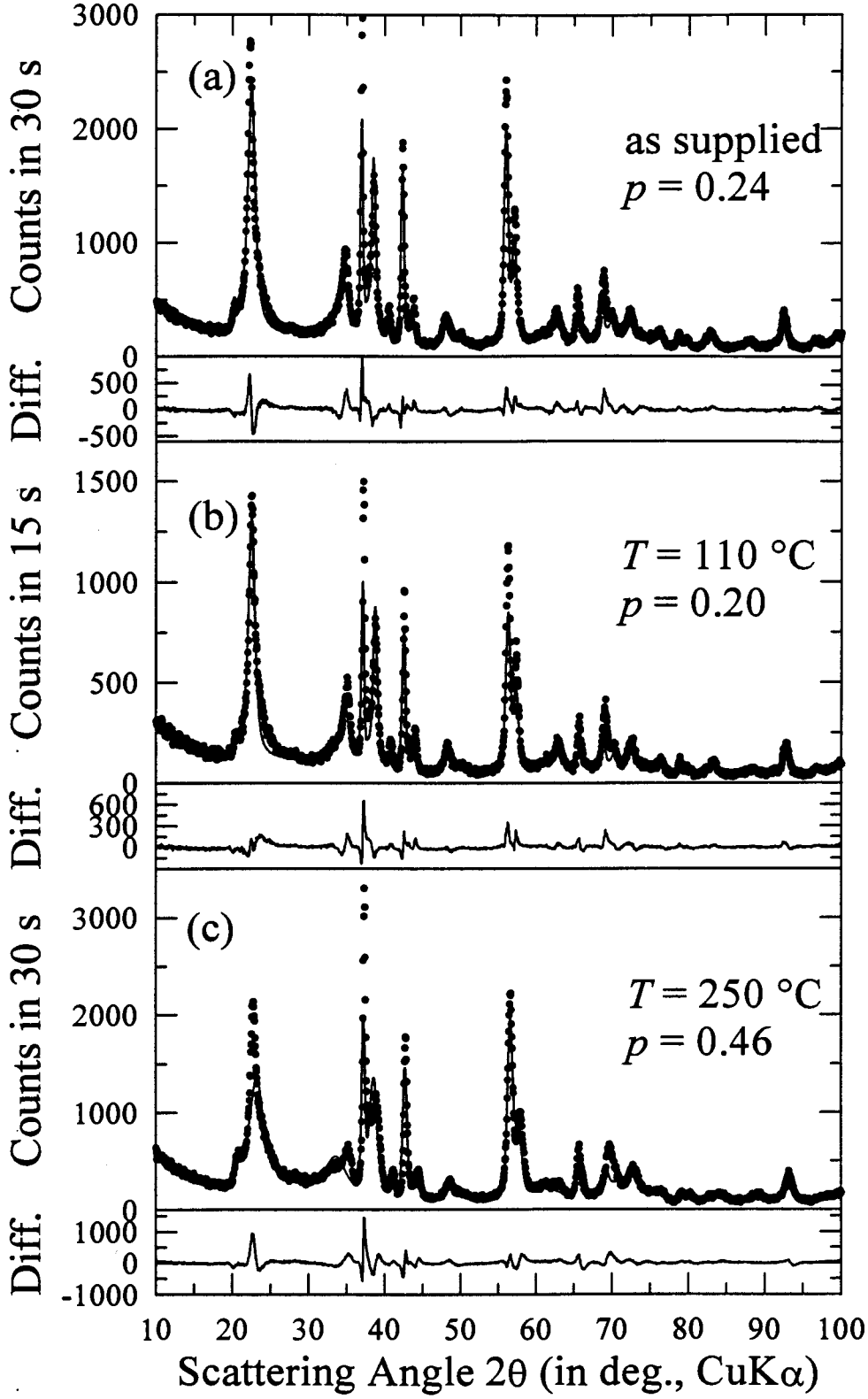

Figure 3.20: Measured X-ray diffraction patterns of CMD-R: (a) as supplied, (b) 110 °C, and (c) 250 °C (filled circles) together with best fits (solid lines).

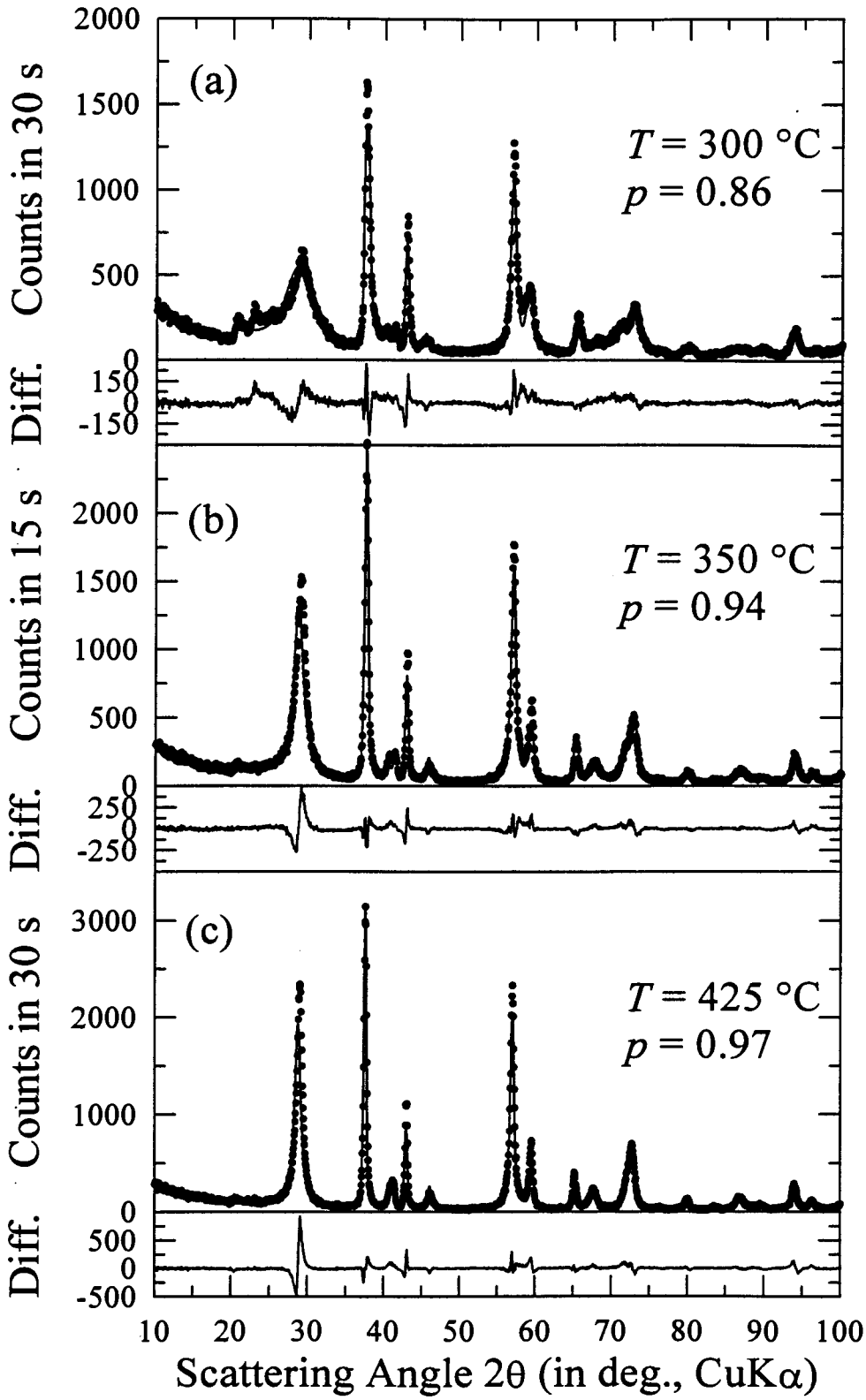

Figure 3.21: Measured X-ray diffraction patterns of CMD-R: (a) 300 °C, (b) 350 °C, and (c) 425 °C (filled circles) together with best fits (solid lines).

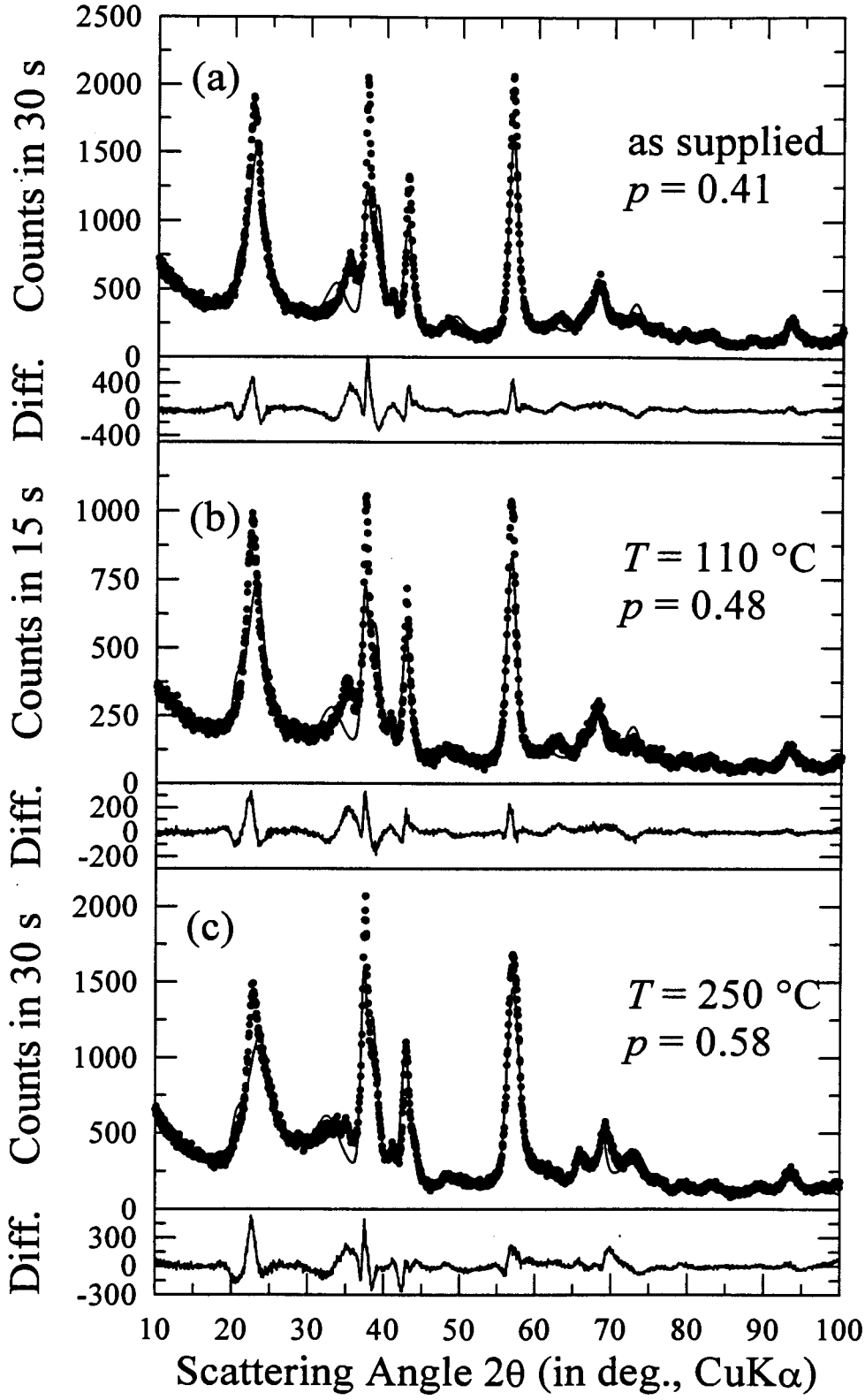

Figure 3.22: Measured X-ray diffraction patterns of TAD 1: (a) as supplied, (b) 110 °C, and (c) 250 °C (filled circles) together with best fits (solid lines).

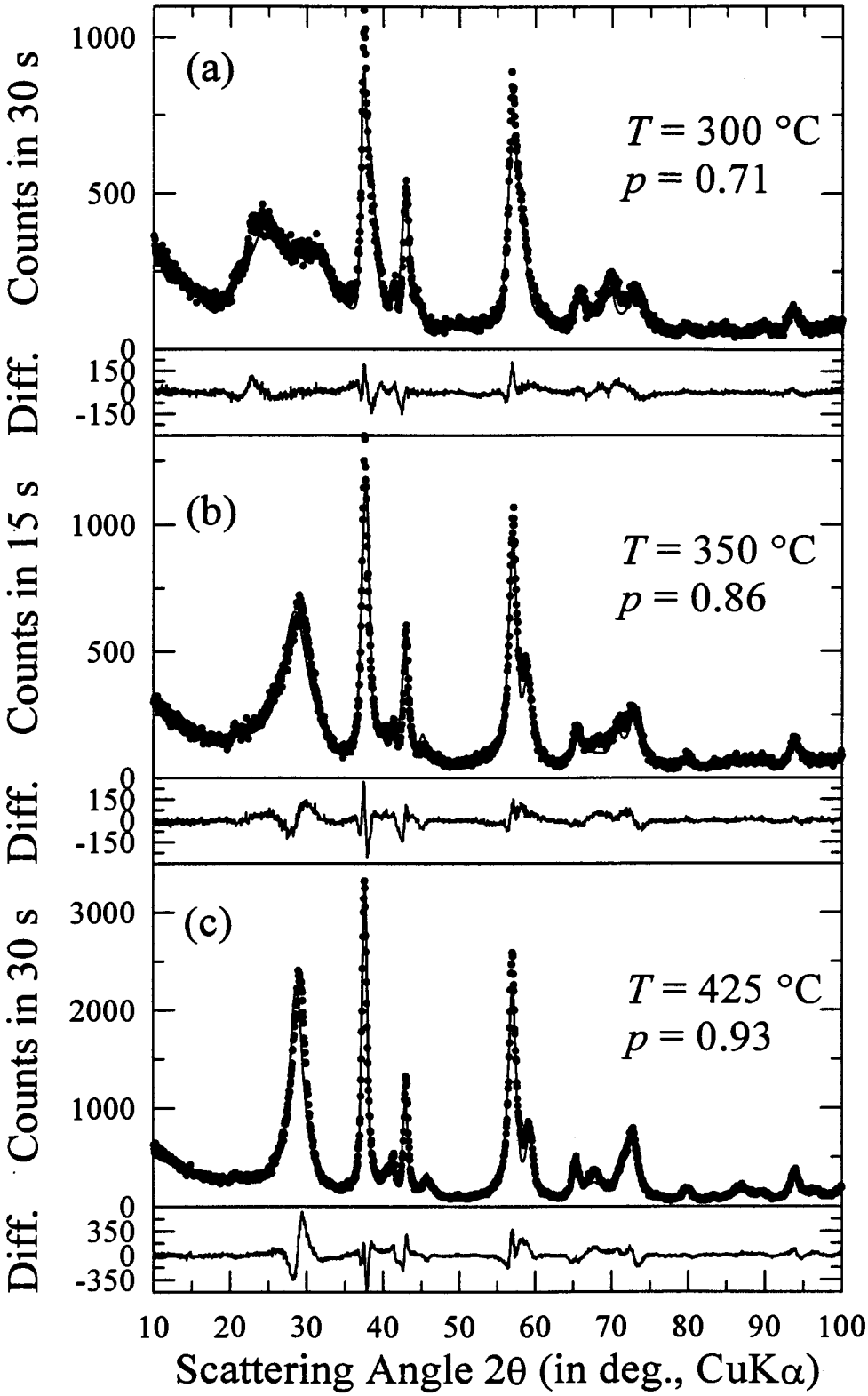

Figure 3.23: Measured X-ray diffraction patterns of TAD 1: (a) 300 °C, (b) 350 °C, and (c) 425 °C (filled circles) together with best fits (solid lines).

Table 3.3: Summary of the parameters that gave best fits for the X-ray diffraction patterns of CMD-R derived samples. Parameters without statistical uncertainty were not varied during the fitting process.

		CMD-R heated at				
Parameter	as supplied	110 °C	250 °C	300 °C	350 °C	425 °C
$\eta \times 10^4$	4.75(2)	2.23(2)	6.16(3)	4.09(3)	5.08(3)	5.11(3)
$c_{-1} \times 10^{-3}$	4.08(1)	2.74(2)	5.86(1)	3.53(3)	3.47(3)	3.33(3)
c_0	17(1)	7.6(7)	−63(4)	−55(2)	−69(2)	−72(2)
c_1	0	0	0.56(4)	0.36(3)	0.52(2)	0.58(2)
c_2	0	0	0	0	0	0
c_3	0	0	0	0	0	0
c_4	0	0	0	0	0	0
B	0.37(3)	0.79(5)	0.17(4)	0.00(4)	0.13(3)	0.14(3)
a_1	4.4510(2)	4.4280(5)	4.3984(3)	4.3678(4)	4.3586(3)	4.3664(3)
N_1	36(1)	38(1)	25(0)	26(1)	58(3)	77(3)
σ_1	0.0130(3)	0.0172(6)	0.0128(6)	0.0133(6)	0.0184(4)	0.0157(3)
a_3	2.8479(1)	2.8347(2)	2.8290(2)	2.8541(2)	2.8584(1)	2.8598(1)
N_3	116(5)	120(7)	80(2)	160(20)	96(4)	113(3)
σ_3	0.0199(3)	0.0202(5)	0.0226(3)	0.0226(5)	0.0165(4)	0.0157(3)
r_2	2.3430(1)	2.3354(3)	2.3240(2)	2.2473(3)	2.2213(2)	2.2054(2)
N_2	73(2)	77(3)	161(8)	67(3)	61(2)	57(1)
σ_2	0.057(2)	0.047(2)	0.094(1)	0.091(2)	0.060(1)	0.043(2)
p	0.2416(8)	0.198(1)	0.461(1)	0.8632(9)	0.9444(5)	0.9696(4)
dx_{Mn}	0.011(1)	0.010(2)	0.000(1)	0.000(2)	0.001(2)	0.001(1)
dy_{Mnl}	1.33(3)	1.33(4)	1.35(3)	1.41(7)	1.56(3)	1.26
dy_{Mns}	1.12(3)	1.12(4)	1.13(3)	1.08(7)	1.18(1)	0.983(9)
dx_{Ol}	0.2243(7)	0.224(1)	0.2330(9)	.243(3)	0.296(6)	0.211
dy_{Ol}	0.28(1)	0.28(2)	0.19(1)	0.02(4)	−0.50(5)	0.31
dx_{Os}	0.2840(7)	0.283(1)	0.2882(7)	0.2805(8)	0.2799(7)	0.2769(7)
dy_{Os}	0.261(9)	0.27(1)	0.358(8)	0.353(6)	0.379(4)	0.372(4)

Figures 3.20, 3.21, 3.22, and 3.23 show the powder X-ray diffraction patterns of the samples together with their fits. As can be seen, the fits to the data of the two materials heated at 425 °C are very good. The parameters (summarized in tables 3.3 and 3.4) suggest that the fraction of 1×1 tunnels in these materials is about 95% . The lattice constants are close to those of β-MnO_2. The parameters for the atomic positions are probably not reliable; especially, the small value for dy_{Mns} is questionable, although it may indicate that heating at this temperature already leads to possibly oxygen vacancies in the structure. Thermogravimetric data, shown

Table 3.4: Summary of the parameters that gave best fits for the X-ray diffraction patterns of TAD 1 derived samples. Parameters without statistical uncertainty were not varied during the fitting process.

		TAD 1 heated at				
Parameter	as supplied	110 °C	250 °C	300 °C	350 °C	425 °C
$\eta \times 10^4$	5.78(4)	3.37(4)	7.92(5)	4.39(4)	5.12(4)	11.00(4)
$c_{-1} \times 10^{-3}$	6.95(6)	3.74(5)	6.02(6)	3.47(4)	3.58(4)	6.59(5)
c_0	−22(5)	−28(3)	−39(5)	−48(4)	−58(3)	−104(3)
c_1	0.13(5)	0.27(4)	0.41(5)	0.44(4)	0.46(3)	0.85(3)
c_2	0	0	0	0	0	0
c_3	0	0	0	0	0	0
c_4	0	0	0	0	0	0
B	0.13(4)	0.42(6)	0.50(4)	0.65(6)	0.33(4)	0.30(3)
a_1	4.4180(6)	4.4210(9)	4.3796(7)	4.367(1)	4.3510(7)	4.356(4)
N_1	19(0)	17(0)	14(0)	13(0)	26(1)	29(1)
σ_1	0.0148(8)	0.015(1)	0.0189(8)	0.013(1)	0.0206(8)	0.0190(5)
a_3	2.7993(5)	2.8027(6)	2.8081(4)	2.8247(5)	2.8503(4)	2.8590(1)
N_3	55(3)	59(4)	64(3)	91(9)	45(2)	65(2)
σ_3	0.0384(7)	0.0355(9)	0.0376(6)	0.0380(8)	0.0262(7)	0.0235(4)
r_2	2.3726(6)	2.3663(7)	2.3369(4)	2.3072(6)	2.2612(4)	2.2293(2)
N_2	33(1)	38(2)	67(4)	74(6)	41(2)	33(1)
σ_2	0.061(3)	0.054(5)	0.070(2)	0.085(2)	0.086(2)	0.056(2)
p	0.413(1)	0.478(2)	0.575(2)	0.711(1)	0.8647(9)	0.9336(5)
dx_{Mn}	−0.011(1)	−0.002(2)	−0.005(1)	0.003(2)	0.001(3)	0.001(2)
dy_{Mnl}	1.24(2)	1.24(3)	1.27(2)	1.33(3)	1.33(4)	1.44(3)
dy_{Mns}	1.06(2)	1.02(3)	0.99(1)	1.03(3)	1.07(4)	1.07(2)
dx_{Ol}	0.213(1)	0.210(1)	0.228(1)	0.239(1)	0.285(3)	0.330(5)
dy_{Ol}	0.20(1)	0.22(3)	0.11(1)	0.16(3)	0.00(4)	−0.44(4)
dx_{Os}	0.2859(9)	0.293(1)	0.3028(9)	0.301(1)	0.2880(8)	0.2863(5)
dy_{Os}	0.231(9)	0.22(1)	0.354(6)	0.35(1)	0.381(6)	0.387(3)

in section 3.5, is not completely conclusive in this respect.

The structural parameters that are associated with 2×1-tunnels, dy_{Mnl}, dx_{Ol}, and dy_{Ol}, become unreliable as the order parameter, p, becomes large and the fraction of 2×1-tunnels becomes small. For the unheated CMD-R sample, all structural parameters correspond roughly to those expected in section 3.2.3, but it is not clear whether the deviation from those expected parameters is significant or whether the deviation is within the uncertainty to be expected from a non-perfect fit.

Comparing the two fits to the X-ray diffraction patterns taken of the samples

heated at 300 °C, one sees that at this temperature more 1×1 tunnels have been created in the case of CMD-R ($p = 0.86$) than in TAD 1. TAD 1 ($p = 0.71$) appears to be more resistant to the conversion. It should be noted, however, that the X-ray diffraction pattern of CMD-R heated at 300 °C shows an additional, weak peak at $2\theta \approx 22°$, which suggests that a small part of the sample has a lower fraction of 1×1 tunnels ($p \approx 0.75$) — the sample is not single-phase in p.

A spread in p can already be inferred from the X-ray diffraction pattern of the unheated CMD-R: Here, the measured peaks at $2\theta \approx 22°$ and $2\theta \approx 35°$ are broader than the calculated ones and, moreover, show some asymmetry, suggesting $0.1 \leq p \leq 0.3$.

The conversion of the unheated CMD-R to β-MnO_2 is characterized well by an intergrowth of ramsdellitic ribbons and pyrolusitic strings with increasing pyrolusite fraction. This behaviour is summarized in figure 3.24. For the EMD sample TAD 1, this conversion model is only satisfactory near the pyrolusite limit. At lower heating temperatures, and particularly for the unheated sample, the γ-MnO_2 model does not seem to describe the structure well.

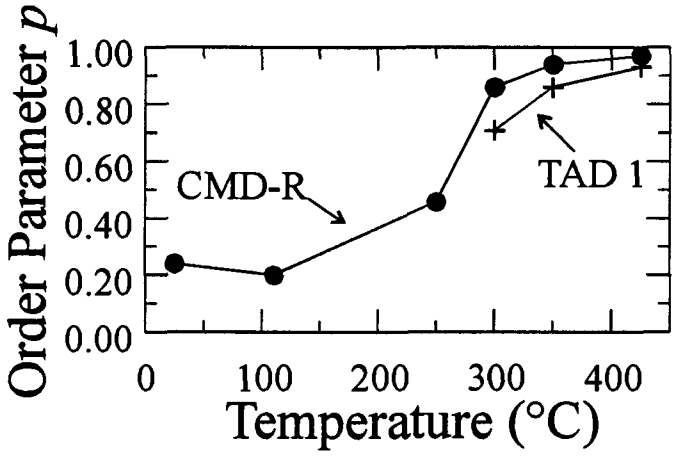

Figure 3.24: Variation of order parameter, p, with heating temperature. The values obtained for the unheated TAD 1 and TAD 1 heated at 110 °C and 250 °C are not included because they are deemed to not represent the true structure.

The large discrepancies between the measured data and the calculated fit for

unheated TAD 1 are shown in figure 3.25. In order to decrease the misfit between the calculated 111 peak and the measured data, the programme increased p in order to move this peak to smaller angles. At the same time, however, the 110 and 131 peaks are moved to larger angles, whereas the 130 and 151 peaks are moved to smaller angles, increasing the misfit of these peaks. Also, in order to match the broadness of many $1kl$ peaks, the programme refined N_1 the mean extent in the 1-direction to a relatively small number; this however led to too strong a broadening of the 200 peak.

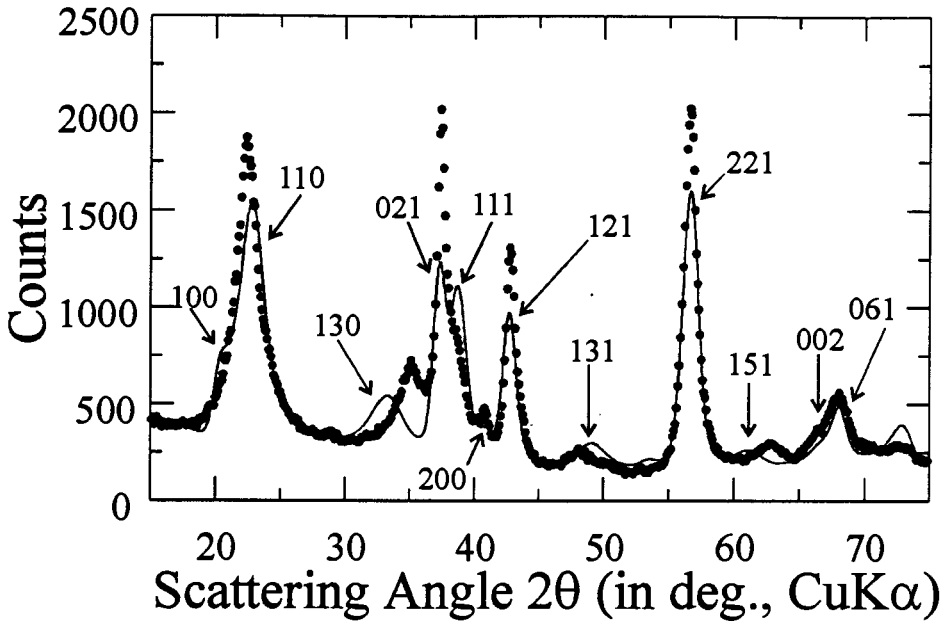

Figure 3.25: This closer look at the powder X-ray diffraction pattern of the EMD sample TAD 1 (as supplied) shows the regions where the fit deviates significantly from the measured pattern. The peak indices are based on a ramsdellite unit cell.

The one reliable result obtained by the fit is the match to the 002 peak which is very broad in the measured pattern. Such broadness can have its origin in small particle sizes, *i.e.* small N_3. This cause was excluded, however, as it would have led to a broadening of all peaks with non-zero Miller index l, including the relatively sharp 021 peak at $2\theta \approx 37°$. The programme therefore calculated a strain parameter ($\sigma_3 = 0.04$) much larger than in the CMD-R samples or the limit testing fits of ramsdellite and pyrolusite, where the programme ended up with parameters of 0.02

in order to match the peak shape better. Although the strain parameter decreases for the heated TAD 1 progressively with heating temperature, the 002 peak does not become as sharp as in the heated CMD-R samples.

Further, both CMD-R and TAD 1 show a large background at angles below $2\theta = 20°$. The origin of this background is not purely instrumental, but the powder samples seem to have some scattering strength in this region. In the materials investigated so far this scattering is diffuse, which may be caused by a disordered stacking of larger entities, possibly in the a_1-direction, as I will discuss in the next section.

3.4 Other Models

3.4.1 Potential Influence of Impurities

The last section showed that, in particular for EMDs, de-Wolff's model of ramsdellite/pyrolusite intergrowth can not generate the X-ray diffraction pattern observed. One main element of EMDs that has not been explicitly incorporated into that model is the presence of structural water. This water could, at least in principle be present in various forms: physisorbed and chemisorbed water at the surface, as part of a reduced manganese dioxide (MnOOH), as hydrogen that replaces manganese cations ("Ruetschi hydrogen" [58, 59, 60]), or as water in interstitial sites (as in δ-MnO_2). Additionally, the effect of sulfate on the structure has to my knowledge not been considered at all.

Water that is physisorbed (typically by weak van-der-Waals interactions) at the surface can typically be removed by heating materials to 110 °C, whereas chemisorbed water is bound more strongly and typically needs heating in excess of 200 °C to be removed. Both species certainly play a role in EMDs as can be seen from the weight loss during heating, discussed in the next section, as well as the fact that they have a very large specific surface area of typically 25-40 m^2/g [61] and large porosity of typically 8-12 % [13]. However, surface water does not affect the bulk structure and it is this bulk structure that is measured by X-ray diffraction.

From chemical titration [11], one finds that the average oxidation state of man-

ganese is slightly less than IV so that one infers a presence of some MnOOH in the material. However, the amount of oxyhydroxide it is not large enough to account for all the water in the material.

Ruetschi's model can account for all the water in the material because 4 protons replace one Mn(IV) so that there is no limit to the number of hydrogen atoms present. Additionally, these hydrogen-filled manganese vacancies provide a nice path for hydrogen motion from one tunnel to an adjacent one during the discharge process. A lot of Ruetschi hydrogen should therefore enhance the kinetics and improve the rate capability of the cell. However, such a local replacement of manganese atoms with hydrogen atoms will not lead to structural changes that would be obvious in an X-ray diffraction experiment, although a careful analysis may find that the average scattering power of scatterers on the manganese site is actually smaller than the Mn or the Mn^{4+} form factor would account for. Such an effect is small and can not account for the strong discrepancies between measured and calculated X-ray diffraction pattern seen above.

For completeness, I should mention that the scattering factor of hydrogen in a neutron diffraction experiment is high, even more so when looking at inelastically scattered neutrons (strong Compton effect for quasi-free protons and absorption lines for bound protons) so that such experiments can give some insight into the way hydrogen is arranged in the structure. Over the last years, a group in France led by Fillaux performed a series of experiments that seem to confirm the presence of both hydrogen in tunnels (partial reduction) and on manganese sites (Ruetschi model) [62, 63, 64, 65, 66].

The possibility of interstitial water has not been investigated yet, probably because the ramsdellite and pyrolusite structure do not have obvious space for water molecules. On the other hand, the layered δ-MnO_2 has the perfect structure for such water. I will consider a model for an intergrowth of ramsdellite and birnessite in section 3.4.3. Quite possibly, the water-containing galleries of such a structure could also accommodate sulfate ions and/or manganese(II)-ions, which are thought to be too large for the octahedral sites in ramsdellite and pyrolusite.

3.4.2 Microtwinning

Before getting to some new models, I should point out that Pannetier[67, 68, 69, 4] proposed — what he calls — a microtwinning model when I started my investigation. Two possible types of twinning[3] are depicted in the top of figure 3.26 for ramsdellite: The ribbons that extend along one of the hexagonal axes, $[010]^{\text{hex}}$, take a turn and continue to propagate at (a) a 60° angle along $[1\bar{1}0]^{\text{hex}}$ (twinning about the $(021)^{\text{ortho}}$-plane), or (b) a 120° angle along $[\bar{1}00]^{\text{hex}}$ (twinning about the $(061)^{\text{ortho}}$-plane). "Micro"twinning then describes the possibility that such twinning can occur frequently, but randomly anywhere in the crystals.

Microtwinning can be described with a single type of layer, whose layer structure factor $\mathcal{F}$ is a number, leading to the 1×1-matrix Q_3 with

$$\mathsf{Q}_3 = [(1-p_+)\exp(-\mathrm{i}2\pi(-k/8)) + p_+ \exp(-\mathrm{i}2\pi(k/8))]\exp(-\mathrm{i}2\pi s_3 r_3), \qquad (3.13)$$

where I have chosen the 1-direction as before (perpendicular to the hexagonal layers), and, depending on whether the twinning plane is $(021)^{\text{ortho}}$ or $(061)^{\text{ortho}}$, the 2-direction as $[\bar{1}10]^{\text{hex}}$ or $[100]^{\text{hex}}$ and the 3-direction as the stacking direction along $[120]^{\text{hex}}$ or $[110]^{\text{hex}}$. Pannetier then limits p_+ to $0 \leq p_+ \leq 0.5$ and defines the percentage of microtwinning as $200p_+$.

Unfortunately, Pannetier does not show any direct comparison between measured powder X-ray diffraction patterns and calculations based on this model, partly because the fit would not be good either, since no ramsdellite/pyrolusite-intergrowth is considered simultaneously. I, too, will leave such a comparison for future work, but will outline how one could achieve a calculation based on disorder in two(!) non-collinear directions.

From the layering in the 1-direction, one can obtain a simple modulation function of the form $(\sin^2 N_1\pi s_1/b^{(1)})/(\sin^2 \pi s_1/b^{(1)})$ for which one can introduce a Gaussian approximation. Secondly, it should be possible to obtain (at least numerically) a Gaussian approximation for the modulation function in the 3-direction, whose width

[3]Twinning refers to a fault in a crystals that leads to two parts that are mirror-images of each other.

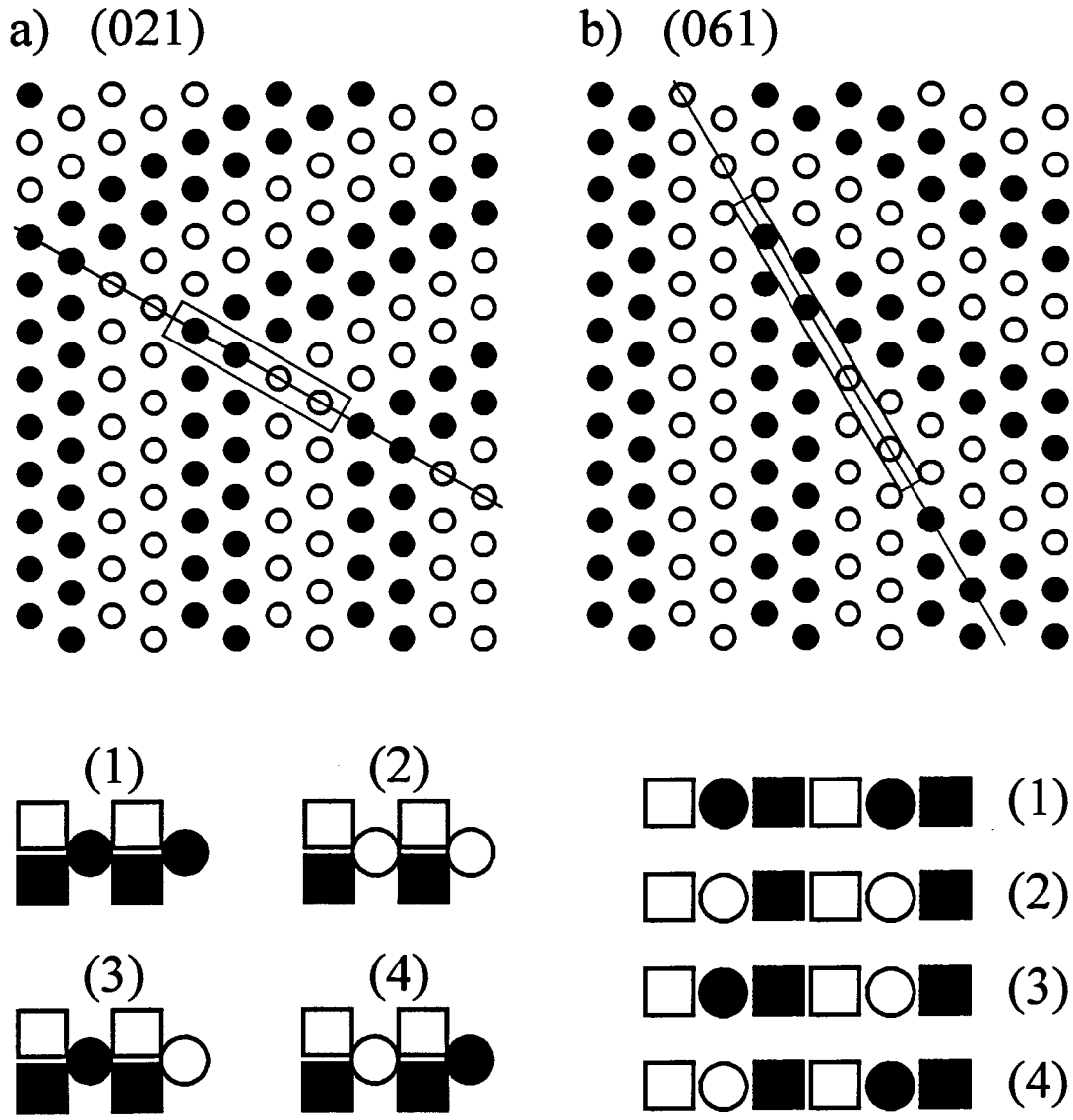

Figure 3.26: Twinning planes for ramsdellite about (a) the $(021)^{\text{ortho}}$-plane and (b) the $(061)^{\text{ortho}}$-plane. The rectangles indicate the repeating units, the long side is $4r_2$, the short side is r_3. These repeating units consist of units (1) and (2) depicted at the bottom of each case, where the oxygen atom have been added: Given that manganese atoms (circles) are in layers of type Z, then the oxygen atoms are in layers X (black squares) and Y (open squares). Units (3) and (4) have to be introduced in order to create twinned pyrolusite or twinned γ-MnO_2.

will certainly depend on $k = \mathrm{ent}(s_2\, 4r_2 + 0.5)$ as well:

$$G_3(k, s_3) = 2N_3\ \mathrm{Re}\left(1 + \frac{2}{N_3}\sum_{m=1}^{N_3-1}(N_3 - m)\mathrm{Q}_3^m\right). \tag{3.14}$$

To obtain the most general modulation function in the 2-direction based on the units (1), (2), (3), and (4) that are depicted in the bottom of 3.26, one can write down a 4×4-matrix Q_2:

$$\mathrm{Q}_2 = \begin{bmatrix} p_8 & p_1 & p_2 & p_3 \\ p_1 & p_8 & p_3 & p_2 \\ p_4 & p_5 & p_6 & p_7 \\ p_5 & p_4 & p_7 & p_6 \end{bmatrix} \phi_2, \tag{3.15}$$

where $\phi_2 = \exp(-\mathrm{i}2\pi s_2 r_2)$ and the quantities p_i $(i = 1, 2, \ldots, 8)$ describe the probabilities for certain sequences in the stacking of the four units; for instance, unit (1) follows itself with a probability of p_8, and follows unit (2) with a probability p_1, etc. The matrix, Q, is of course much too complex to deal with.

I want to point out one special case of the 4×4-matrix, which only utilizes units (3) and (4). It suffices to use these units in order to build ramsdellite or pyrolusite, but the model for γ-MnO_2 will be slightly different form before. The 2×2-matrix Q_2' is then

$$\mathrm{Q}_2' = \begin{bmatrix} p & 1-p \\ 1-p & p \end{bmatrix} \phi_2 \tag{3.16}$$

and ramsdellite is formed for $p = 0$ and pyrolusite for $p = 1$. In this model, γ-MnO_2 cannot contain a 1×1-tunnel that is both preceded and succeeded by 2×1-tunnels; 1×1-tunnels will always occur in pairs. The intensity variation along the hl-rod then turns out to be

$$\begin{aligned} \overline{i^{(0)}}(h, l, s_2) \;=\; & |F_3 + F_4|^2 \left(1 + \frac{2}{N_2}\sum_{m=1}^{N_2-1}(N_2 - m)\phi_2^m\right) + \\ & |F_3 - F_4|^2 \left(1 + \frac{2}{N_2}\sum_{m=1}^{N_2-1}(N_2 - m)(2p-1)^m\phi_2^m\right) + \text{ c.c,} \end{aligned} \tag{3.17}$$

where F_3 and F_4 are the structure factors associated with units (3) and (4), and c.c. is the complex conjugate.

The quantity $\overline{i^{(0)}}(h,l,s_2)$ describes two types of peaks, those that remain sharp are associated with the sum F_3+F_4, whereas those that are broadened are associated with F_3-F_4. The sum, F_3+F_4, places manganese atoms on all octahedral sites and doubly occupies all oxygen positions. Since manganese atoms in unit (4) are just shifted by half a unit cell distance in the 1-direction, $F_3+F_4 = 2F_3^{(O)}+F_3^{(Mn)}(1+\exp\{-i\pi h\})$. All peaks with even h remain sharp. On the other hand, $F_3-F_4 = F_3^{(Mn)}(1-\exp\{-i\pi h\})$ and peaks with odd h will be broadened, unless they are predominantly derived from oxygen atoms. An example for such an 'oxygen-peak' is the 121 peak in ramsdellite, which corresponds to 111 peak in pyrolusite (see section 3.4.5). A broadening of $1kl$ peaks, except for the 121^{rams} peak, is exactly what is desired for EMDs.

At this point it may be easier to approximate the unbroadened and the broadened modulation functions in the 2-direction with Gaussians so that one would create hk-rods. The advantage of this procedure is that the modulation functions in the 2-direction do not depend on s_3, but the modulation function in the 3-direction makes explicit reference to k because of the transverse shift during stacking. It would be interesting to see, if this very simple model can create the desired peak shifts.

3.4.3 Ramsdellite/Birnessite Intergrowth

Unlike the previous disorder model, this one considers the 1-direction perpendicular to the hexagonal layers. The stacking in the 1-direction is very simple: Ordinarily, ramsdellite layers would be stacked at a spacing of $a_1^{\text{R}} \approx 4.4$ Å; a birnessite fault is introduced by having a spacing of $a_1^{(\delta)} \approx 7$ Å instead. Whereas the ramsdellite/pyrolusite intergrowth affected the structure factor of the stacked layers (A, B, C, D), this intergrowth merely involves changes in the spacings between identical layers.

In addition to the increased spacing that is encountered when a birnessite fault is present, one can allow for a transverse shift, Δr_2, in order to account for the monoclinic distortion that is observed in birnessite. However, the re-arrangement of the atoms on the hexagonal layers, which will certainly occur in the real crystal, will not be considered because its effect on the X-ray diffraction pattern is small, as was

already discussed in context with hydrogen replacing manganese atoms.

Based on this model, one could write down the modulation function in the 1-direction which would be governed by the 1×1-matrix

$$\mathsf{Q}_1 = (1 - p_\delta) \exp\left(-\mathrm{i}2\pi s_1 a_1^{\mathrm{R}}\right) + p_\delta \exp\left(-\mathrm{i}2\pi\left(s_1 a_1^{(\delta)} + k\Delta r_2 / a_2^{\mathrm{R}}\right)\right) \qquad (3.18)$$

Calculating an interference pattern based on this expression for Q_1, one finds that some higher order peaks can become very sharp (at values of s_1 where both $s_1 a_1^{\mathrm{R}}$ and $s_1 a_1^{(\delta)} + k\Delta r_2 / a_2^{\mathrm{R}}$ are close to integers). Such a phenomenon was already presented by Hendricks and Teller [32] in their figure 1. It is questionable how realistic this result is; it is more likely that due to slight displacements of the layers, long-range order is not preserved so that one would have to introduce an additional strain factor.

It is, therefore, more sensible to interpret these birnessite faults in the structure as a random fault in the sense of Ergun [35], which I already incorporated in my expression for the modulation function in the 1-direction, G_1. The number of layers that are stacked in the 1-direction can then be large, while the mean number of faultlessly stacked layers remains small leading to a broad 200-peak consistent with measured X-ray diffraction patterns of EMDs.

As pointed out before, such a birnessite fault can then account for some of the structural water as well as allow for sites which can be occupied by sulfate-ions.

3.4.4 Cryptomelane-Intergrowth

Another contender for the disorder in the 1-direction is the α-MnO_2 structure. However, an intergrowth of an α-MnO_2 structure with a ramsdellite structure does not appear very likely because these two structures are not quite commensurate. It is more feasible that, if the conditions during crystal growth are such that an α-MnO_2-growth is probable, a phase separation rather than an intergrowth will result. This is actually observed when purposely doping the EMD-bath with potassium ions [70]. Other EMD samples show α-MnO_2-type impurities, although no potassium was added to the bath. An example is the EMD shown in figure 3.27, which was prepared by the Chemetals laboratory (Baltimore, MD, USA). This sample shows small Bragg

peaks in the low angle range, associated with a cryptomelane- or α-MnO_2-like phase. Similar features were also seen with sample LSC 23/40 in figure 1.10.

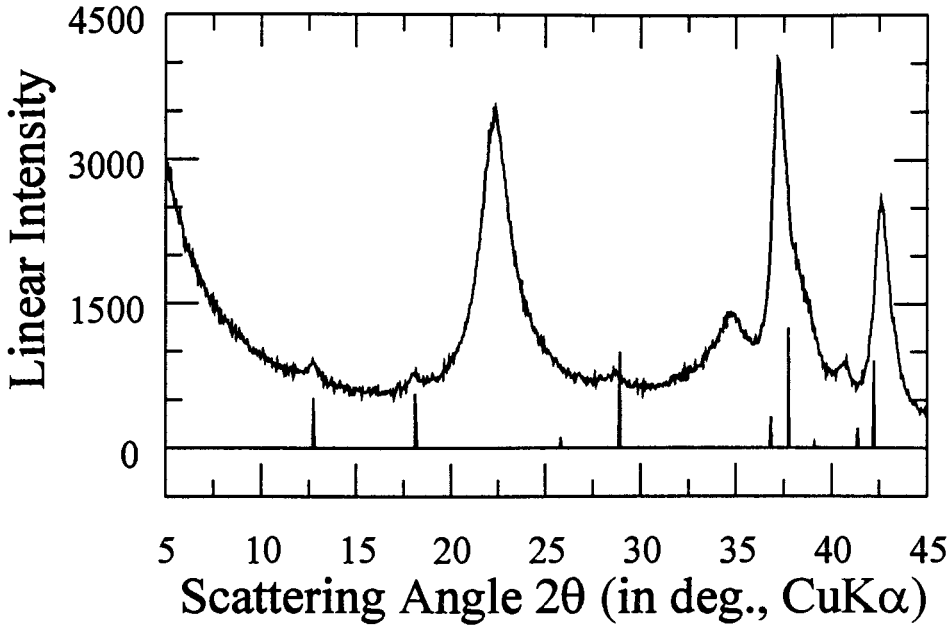

Figure 3.27: Low angle part of the X-ray diffraction pattern of an experimental EMD prepared by the Chemetals laboratory. The preparation conditions were such that a cryptomelane-like phase appears, as evidenced by comparison with the JC-PDS data base (No. 42-1348), shown as sharp peaks at the bottom of the figure.

3.4.5 Reverse-Monte-Carlo Calculations

So far it has been established that EMDs are most likely based on a hexagonal[4] close packed oxygen lattice with manganese atoms in a more or less disordered arrangement on half of the available octahedral sites. A Reverse-Monte-Carlo-type programme [71, 72] then seems to be ideally suited for this problem.

One takes a fixed oxygen lattice and seeds manganese atoms on half of the octahedral sites. Then one utilizes a Monte-Carlo step by moving one of the manganese atoms from its present site to an unfilled octahedron and checks whether or not this

[4]A cubic close packed manganese dioxide is thermodynamically unstable and converts to hexagonal close packing with moderate heat treatment ($\sim$ 200 °C) — see next chapter for details.

new arrangement improved the difference between the measured X-ray diffraction pattern and the one based on the model structure. If the fit is better than before, the new structure is accepted, if is worse it is accepted with a certain probability that decreases with increasing misfit.

One continues this process until the calculated and measured patterns match closely. In practice, one would have to move several atoms before comparing calculated and measured patterns because the change of two sites in a crystal would not affect its X-ray diffraction pattern much. Also, one still has to consider the necessity of ensemble-averaging over a large number of calculated configurations and patterns because in the measured sample not all crystals are built exactly the same, but are disordered in a similar fashion. The goal of this numerical investigation is then to define an order parameter that can describe the disorder in EMDs.

In order to calculate the X-ray diffraction patterns based on the occupations of well-defined sites, one employs the so-called Debye-formula, which gives an exact description for the intensity of a powder-averaged X-ray diffraction pattern:[5]

$$i(s) = (1 + \cos^2 2\theta \cos^2 2\theta_{\mathrm{m}}) \sum_{\alpha=1}^{N} \sum_{\beta=1}^{N} f^{(\alpha)} f^{(\beta)} \frac{\sin 2\pi s \|\vec{d}^{(\alpha)} - \vec{d}^{(\beta)}\|}{2\pi s \|\vec{d}^{(\alpha)} - \vec{d}^{(\beta)}\|}, \tag{3.19}$$

where N is the number of atoms in the crystal and $\vec{d}^{(\alpha)}$ are their positions. This expression can be modified to cut the calculation time in half, but it still goes as N^2 and for a pyrolusite crystal with $15 \times 15 \times 15$ unit cells (*i.e.* about 20000 atoms) it took over 24 hours to calculate a pattern for $10° \leq 2\theta \leq 45°$ at intervals of $0.1°$ on a Sun Ultra 1 workstation.

Before discussing a remedy for the long calculation times, I would like to comment on the result of this (exact) calculation as shown in the top of figure 3.28. The top panel shows various curves derived from contribution that involve two oxygen atoms ("O-O"), one manganese and one oxygen atom ("Mn-O"), and two manganese atoms ("Mn-Mn") as well as the curve of the sum of these contributions. It is interesting to note that scattering from manganese atoms contributes to most peaks, whereas the O-O-contribution is generally very weak, except for the 111 peak at 43°, which does

[5]One merely has to write down the square modulus of the crystal structure factor and integrate over all direction of the scattering vector $\vec{s}$

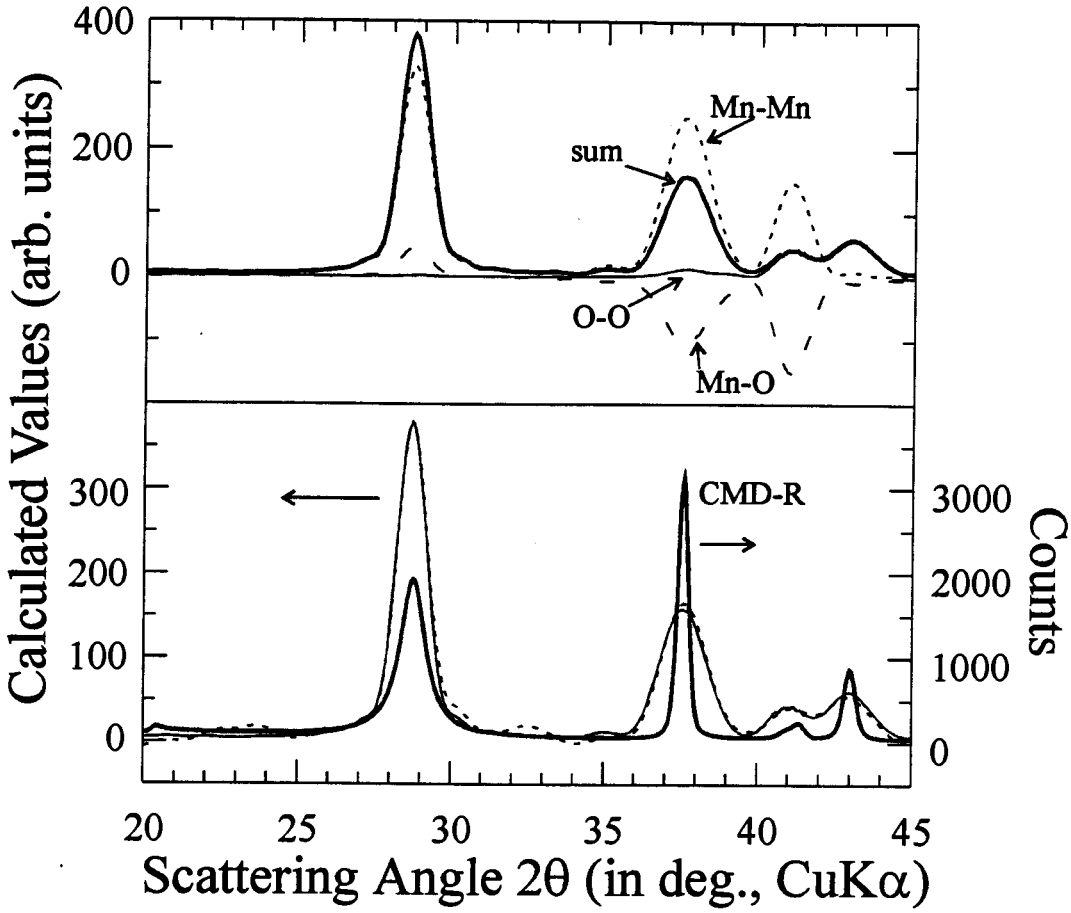

Figure 3.28: Debye-calculation for β-MnO_2 (top panel) and comparison of its peak width to the measured pattern of CMD-R heated at 425 °C bottom panel). The top panel also shows the contribution of Mn-Mn (dotted line), O-O (thin solid line), and Mn-O (dashed line) containing terms to the total intensity (thick solid line). The bottom panel shows in addition to the measured pattern (thick solid line) and the exact Debye calculation (thin solid line), a Debye calculation based on the histogram method (dotted line).

not contain any substantial contribution involving manganese atoms — any disorder on the manganese sublattice will leave this peak unaffected.

The lower panel shows the total intensity of the calculation and compares it to the measured X-ray diffraction pattern of CMD-R heated at 425 °C. One sees that the peak width of the measured 101 peak at 37.5 ° is maybe a third of the calculated one. This implies that the 15 × 15 × 15-unit-cell crystal was not large enough. Increasing each linear dimension by a factor of three would lead to a 729(!)-fold increase in calculation steps — completely out of the question for the exact calculation.

Fortunately, the so-called histogram method [73] reduces the calculation time dramatically by binning the atomic distances into intervals of a given width. By choosing a width of 0.05 Å, I calculated the dashed pattern in the lower panel in only 10 minutes. Because of its approximating nature, the calculation based on the histogram method shows deviations from the exact calculation and calculated even (slightly) negative intensities, but these deviations may become less important for larger crystals. Also by choosing exact distances for short ranges (in a crystal with periodic lattice sites there are only a finite number of these), instead of distance intervals, one may decrease these "long-wavelength" oscillations in the pattern.

Although the time for the initial calculation of the increased crystal would be of the order of 5 days, it is still acceptable, especially since the re-calculation of the intensity after an atom is moved only goes as N and not N^2. Based on these estimates, an EMD "synthesized" on a computer, may not be too far from reach.

3.5 Thermal Analysis of Some Manganese Dioxides

Many powerful tools for analyzing and characterizing materials are available in the field of thermal analysis. Such tools include: following structural changes due to heat treatment by (powder) X-ray diffraction of materials heated at various temperatures (as was already presented)[6], weighing the sample during heating in air, in oxygen-

[6]Better yet, measure diffraction patterns as the material is heated

poor or even reducing atmosphere — so-called thermogravimetric analysis (TGA), measuring the specific heat of the material as it is heated by means of a differential scanning calorimeter (DSC).

3.5.1 Thermogravimetric Analysis

To obtain TGA data, one places a small amount of material (20–40 mg) on a balance inside a tube, which in turn is positioned inside a furnace. The atmosphere around the sample can be controlled by flowing gases through the tube. Especially when flowing gases other than air, one has to ensure that all air, which entered the tube when loading the sample, has been exchanged for the purge gas. However, this waiting can lead to errors because surface water may already desorb unnoticed at room temperature.

Figure 3.29 shows TGA data for TAD 1 and CMD-R in extra-dry[7] air (Praxair) and ultra-high purity argon (Praxair). After heating to 600 °C or so, all samples have converted to α-Mn_2O_3 (bixbyite) as evidenced by powder X-ray diffraction after cooling. I therefore present the weight loss with the final common product as having a weight of 100.

The low temperature part of all curves can be easily understood.; it is characterized by the desorption of physisorbed water, which continues up to about 170 °C[8]. The gap for TAD 1 between the air and the argon heated curves is most likely related to the fact that the argon sample was losing weight, while I waited for argon to fill the tube. For the air-heated sample, one observes a rapid initial drop as water is taken up by the moisture free air.

In the temperature range from 170 °C to 210 °C, the EMD loses weight quite rapidly, in argon this continues up to 270 °C. It is very likely that the water desorbed in this range was chemisorbed on the surface, *i.e.* a species such as OH^-, which involves a partial charge transfer with the bulk. Removing 2 OH^- in form of H_2O, leaves an O^{2-} and, possibly, dangling bonds on the surface. When the heating pro-

[7]This air has been passed through a cold trap so as to remove all water and all carbon dioxide

[8]This temperature is higher than the 110 °C given before because of kinetic reasons. The heating rate was 10 °C/min.

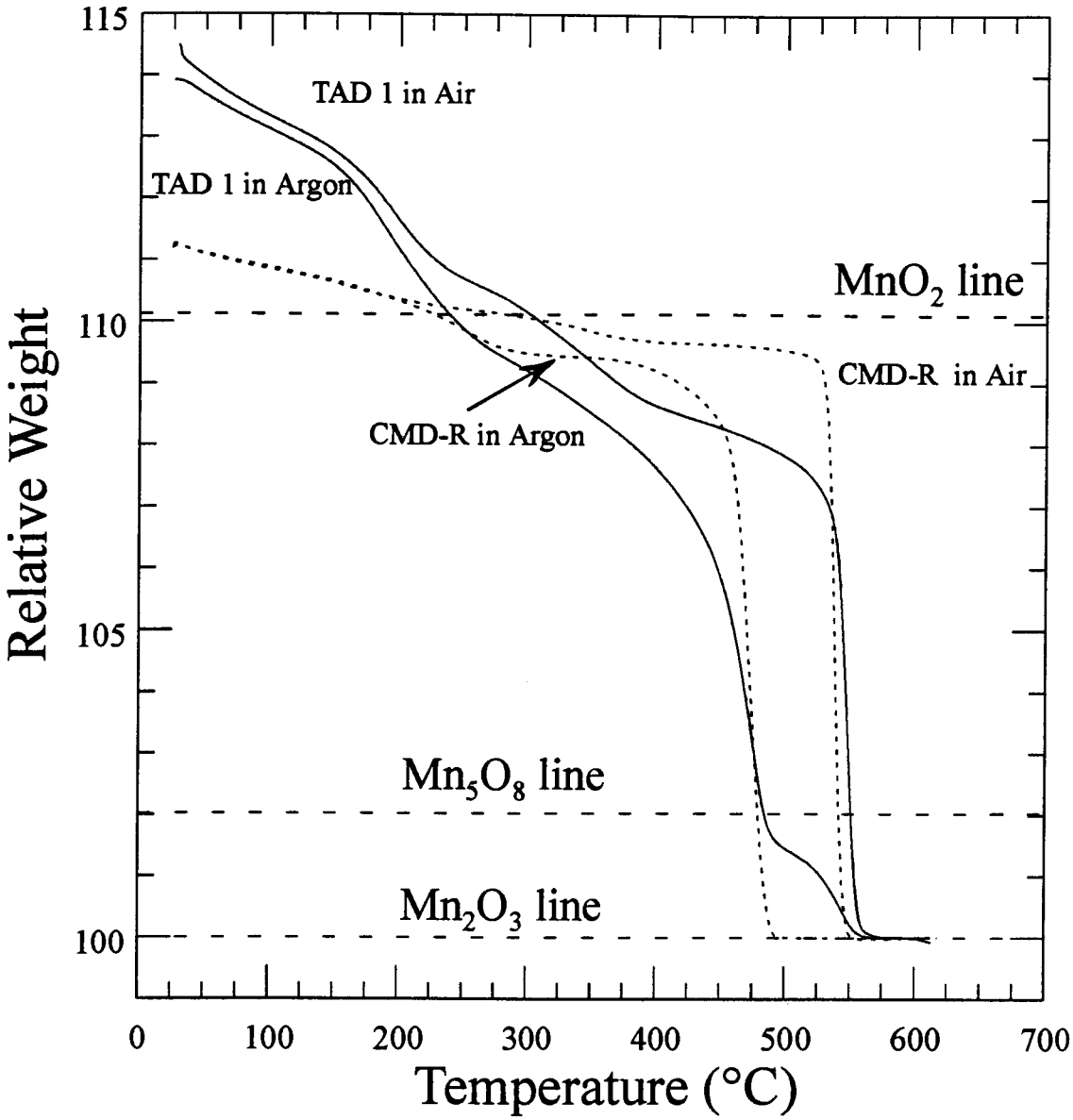

Figure 3.29: Weight loss of CMD-R and TAD 1 as they are heated in air and in argon.

ceeds in air, these dangling bonds can be satisfied by oxygen resulting in a less rapid weight loss.

Eventually, the decomposition of manganese dioxide according to

$$MnO_2 \longrightarrow \frac{1}{2} Mn_2O_3 + \frac{1}{4} O_2 \tag{3.20}$$

starts to take place in air at about 525 °C. Since the change in enthalpy, ΔH, of the reaction is positive (see next section on calorimetry) and the change in entropy, ΔS, is positive as well because a gas is produced, the temperature has to be large enough so that the change in Gibbs free energy of the reaction is just negative:

$$T_{\min} = \frac{\Delta H}{\Delta S}, \tag{3.21}$$

where $T_{\min}$ is the minimum temperature at which an endothermic reaction can occur, provided that the entropy increases due to the reaction. Since the change in entropy per oxygen molecule is larger, if the created oxygen molecules are very diluted as in a flowing argon gas, than for the case where the flowing gas already contains a significant amount of oxygen, as in air, the onset temperature for the reaction, $T_{\min}$, is smaller in argon flow.

Several things can be seen from these data: (1) The overall weight loss of TAD 1 is much larger than for CMD-R — TAD 1 contains much more water. (2) Neither of the two materials becomes stoichiometric MnO_2, although CMD-R is close. (3) TAD 1 accommodates a significant amount of chemisorbed water.

It is the third point that leads to the unanswered question: Where is this chemisorbed water in the material? I suggest that it is at least partly contained in δ-MnO_2-type galleries.

3.5.2 Differential Scanning Calorimetry

A DSC, described in more detail in appendix A.3, is a useful tool for determining whether a chemical reaction or a phase transition of a certain material releases heat (exothermic behaviour) or takes up heat (endothermic bahaviour). The result from the DSC measurement will be presented as the difference of the heat capacities between the sample of interest and a reference, normalized with respect to the weight

of the sample. Since the heat capacity of the reference is essentially featureless, although it may change smoothly over the temperature range of interest, any peaks that appear in the presented data can be attributed to the sample.

Figure 3.30 shows DSC curves of various manganese dioxides. The top panel, (a), shows the manganese dioxides that were investigated thermogravimetrically as well: TAD 1 and CMD-R. On the scale shown, their curves are essentially featureless until the materials decompose by releasing oxygen. This decomposition is associated with a negative (endothermic) peak, as already pointed out in the previous section.

It is remarkable that the re-arrangement of the manganese atoms within the material that was observed by X-ray diffraction measurement (*e.g.* for CMD-R the order parameter, p, changed from 0.2 to near 1 over temperature range from 20 °C to 425 °C) is not associated with any large heat, either released or taken up. In fact, the features that one observes in the low temperature region are strongly influenced by the deformation of the sample container due to pressure build-up during the evaporation of water, in particular for the EMD, TAD1. The unexpectedly different areas associated with the decomposition endotherm is likely related to the deformation of EMD container.

In subsequent measurement such a build-up of pressure was avoided by puncturing a hole in the lid of the sample container (and the reference container as well, for symmetry reasons). This led to signals in the low temperature region that were more trustworthy, as those seen in panel (c). Here, the DSC curves of three different EMDs are shown. The X-ray diffraction patterns of these EMDs are similar to the three representative cases, shown in figure 1.10. It is striking that the DSC curves of these three, relatively different, materials are quite similar. The offset along the vertical axis stems from the fact that the sample sizes were different so that in $\Delta C/m_s$ the subtracted amount C_r/m_s varied.

Finally, I would like to draw the attention to the decomposition of two CMDs, Faradizer TR and β-MnO_2, shown in panel (b). Unlike the other samples investigated, the endothermic peak between 500 °C and 600 °C splits into a doublet. In the β-MnO_2 case the transition is not complete before the maximum temperature of the calorimeter is reached. It would certainly be interesting to investigate the nature of

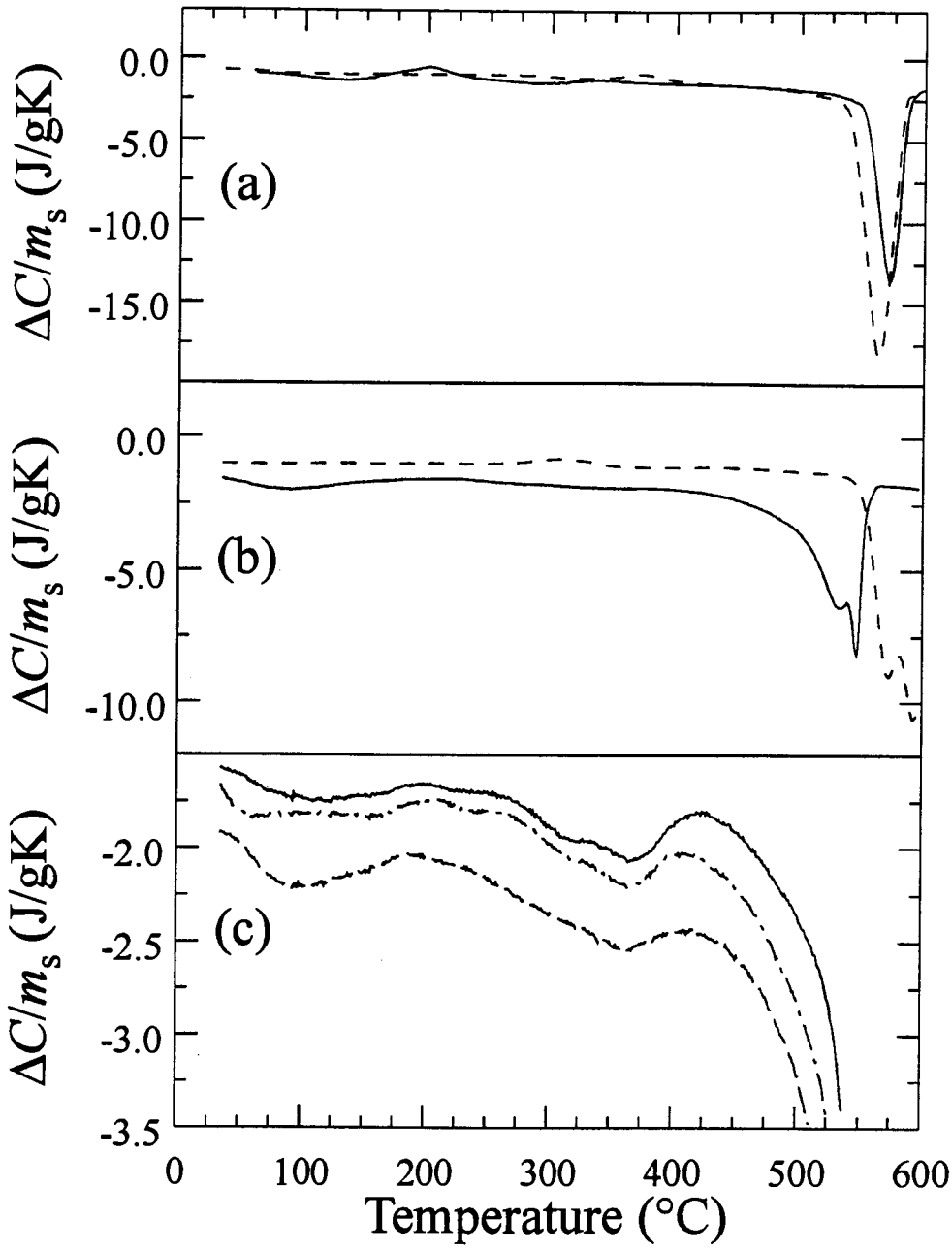

Figure 3.30: Differential scanning calorimetry data of various manganese dioxides. All curves were recorded at a scan rate of 10 °C/min in air. Panel (a) shows data for TAD-1 (solid line) and CMD-R (dashed line). (b) Faradizer TR (solid line) and Fisher β-MnO_2 (dashed line). (c) Three EMDs from Williams and Swinkels: LSC 18/20 (solid), LSC 23/40 (dash-dot), LSC 10/100 (dashes).

this doublet, which is, however, beyond the scope of this thesis.

3.6 Discharge Behaviour of Manganese Dioxides in Alkaline Electrolytes

3.6.1 Structural Changes of EMD During Discharge in 9 M KOH

As I pointed out in chapter 1, the discharge behaviour of an electrode material is inherently coupled to its crystal structure or rather the change of its crystal structure. The purpose of the fitting programme developed in this thesis was to have a tool available to describe the structural changes during discharge. Unfortunately, this tool will not find its desired purpose with regards to EMDs as these are not well described by the ramsdellite/pyrolusite-intergrowth model on which the fitting programme is based.

Nonetheless, it may be instructive to study the changes in the powder X-ray diffraction patterns of EMDs by conventional means, *i.e.* identification of diffraction peaks, measurement of their positions by fitting individual peaks with a pseudo-Voigt peak, and plot of positional shift as a function of depth of discharge. From Michael J. Root at Rayovac Corporation, I obtained a series of discharged EMDs whose powder X-ray diffraction I measured carefully (long count times for good statistics).

Samples were prepared from a mixture of an EMD, IBA 14 (Japan Metals and Chemicals), or of CMD-R with 50 % w/w Lonza KS-6 graphite, which was added to improve the electronic conduction of the electrode during discharge. Since graphite does not participate in the discharge process, some of its diffraction peaks (004, 200 from $K\alpha_1$, and 200 from $K\alpha_2$) were utilized as internal standards to calibrate the scattering angle for each pattern.

Figure 3.31 shows the shift of the diffraction peaks with regards to the undischarged electrode as a function of depth of discharge, which is expressed as the

number of electrons transferred per Mn(IV) atom in the working electrode[9]. The overall trend is towards more negative shifts indicating the expected expansion of the lattice as hydrogen is incorporated in the structure.

It is worth noting that the change in the position of the 002 peak is very small, indicating that the reduction does not affect the oxygen-oxygen distance along the ribbons and strings (regarding the labelling of manganese dioxide peaks, see figure 3.25). This finding must be contrasted with results by Gabano and co-workers [74], the Tye-group[75, *e.g.*], and more recently by Mondoloni and co-workers [76] who apparently identified the 061 peak as the 002 peak. It is therefore not a question of *in-situ vs. ex-situ* X-ray diffraction studies, as Pannetier suggested [4].

Some small deviation from this trend may be related to fact that most diffraction peaks were relatively broad and sometimes merged into one another. Since no structure factor information was used that could impose constraints on the relative intensities of merging peaks, the peak fitting programme chose peak positions, integrated peak intensities, and peak widths so as to obtain a best fit, although a poorer fit may have had more physical meaning. It is for this reason that fits to individual peaks are not desirable, unless no alternative is available, and the attempt to create a programme that would fit the manganese dioxide diffraction pattern as a whole was undertaken in this thesis.

One observation that is certainly related to some anomalous shifts, such as the increase in the peak position of the 111 peak in the 0.80 e^-/Mn(IV) sample, is the appearance of an additional diffraction peak at 12.35° and a hint of a peak in the low-angle shoulder of the graphite 002 peak in the sample discharged to 0.8 e^-/Mn(IV) (see figure 3.32a). The position of these peaks is already familiar from the potassium-based δ-MnO_2 that I describe in the beginning of this chapter. These peaks occur in the discharged CMD-R already at 0.5 e^-/Mn(IV) (figure 3.32b) and maybe even at 0.2 e^-/Mn(IV).

The appearance of the δ-MnO_2 peaks is likely related to the high potassium concentration in the electrolyte, which was an aqueous 9 molar KOH solution. In fact, discharge of CMD-R to 0.5 e^-/Mn(IV) in a 1 molar KOH solution did not lead

[9]See reference [11] for details on how the Mn(IV) content can be obtained.

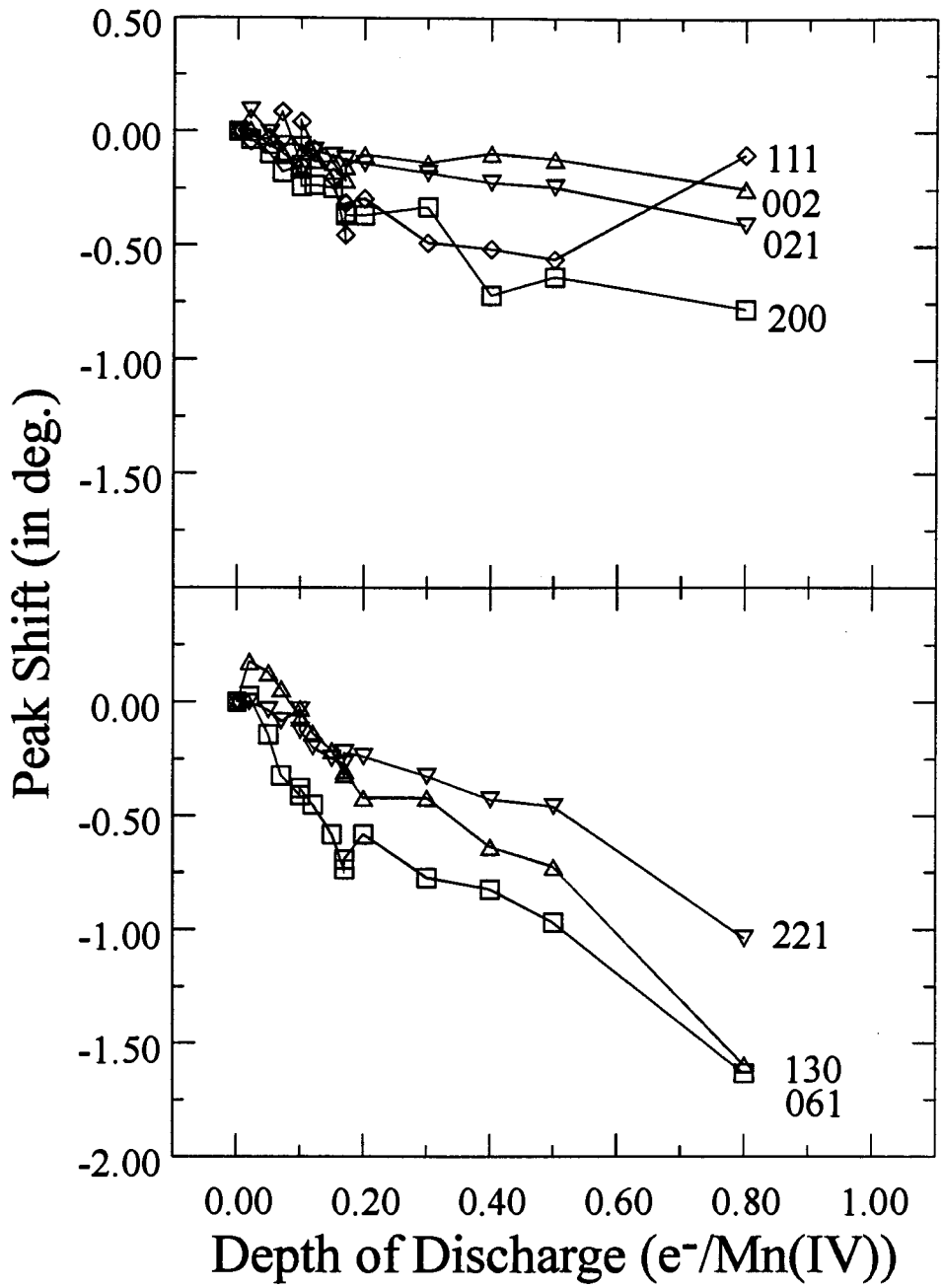

Figure 3.31: Shifts of X-ray diffraction peak positions as a function of the depth of discharge

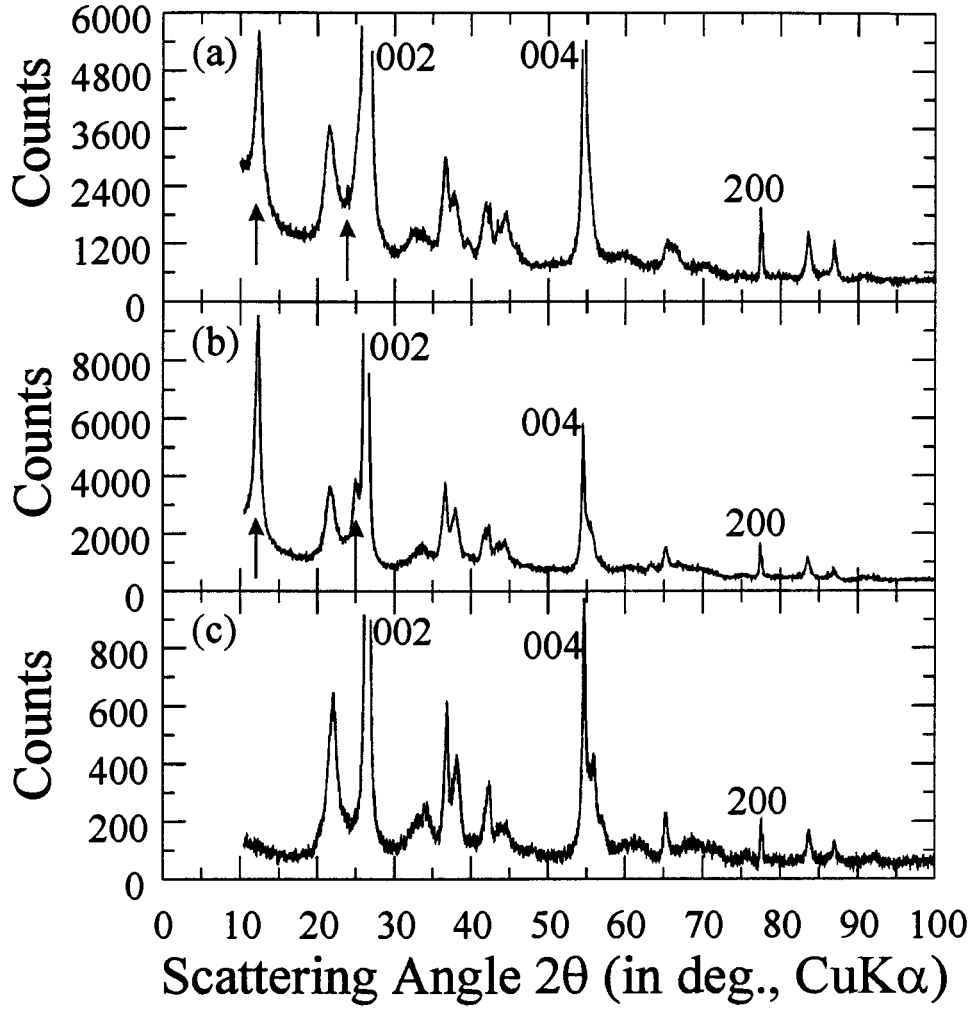

Figure 3.32: New diffraction peaks (arrows) appear, when manganese dioxides are discharged in a 9 M KOH solution: (a) EMD IBA 14 at 0.8 e^-/Mn(IV) and (b) CMD-R at 0.5 e^-/Mn(IV). However, discharging in a 1 M KOH solution does not lead to the formation of these addition peaks: (c) CMD-R at 0.5 e^-/Mn(IV) in 1 M KOH. The additional diffraction peaks are indicative of a δ-MnO_2 structure. Graphite peaks are labelled in this figure, the manganese dioxide labels are given in figure 3.25.

to the additional peaks (figure 3.32c).

One must conclude that the structural changes observed with the EMD discharged to various degrees are affected by the presence of a high[10] concentration of potassium in the electrolyte. At later stages in the discharge, the shift in the diffraction peaks is not simply based on hydrogen insertion into the structure, whether or not a co-insertion of potassium or potassium hydroxide occurs in the early stages of the EMD discharge in a 9 molar KOH solution is not clear.

3.6.2 Electrochemical Behaviour in 1 M KOH

Encouraged by the more easily understandable discharge behaviour in a 1 molar KOH solution, I discharged some samples myself. In particular, I was interested in the discharge product of CMD-R after 1 electron transfer. Theoretically, one expects the discharge product of ramsdellite to be groutite (α-MnOOH), which has the same crystal structure and space group as ramsdellite [77].

For these experiments, I did not use graphite as a conductor, but used a highly disordered carbon. Details of the cell assembly and electrode preparation can be found in appendix A.1.

Figure 3.33 shows the discharge curves of CMD-R at various discharge currents. One sees that the length of the plateau, corresponding to the specific capacity of the material, shrinks with increasing current — the kinetics of the reduction process is very slow, which is not desirable in practical cells. In fact, Sedema, the makers of CMD-R, state that it is electrochemically inactive for alkaline cells. On the other hand, one can observe an increased noise level in the data as time progresses when looking at the derivative $\mathrm{d}q/\mathrm{d}V$ (not shown). The increase in noise may be related to processes at the working electrode or at the reference electrode. The latter is not very likely because the same reference electrode was reused with a different working electrode, which did not show any noise initially. Also, the same noise is observed in the data of the voltage between the stainless steel counter electrode and the working electrode.

[10]A 9 molar KOH solution is almost saturated

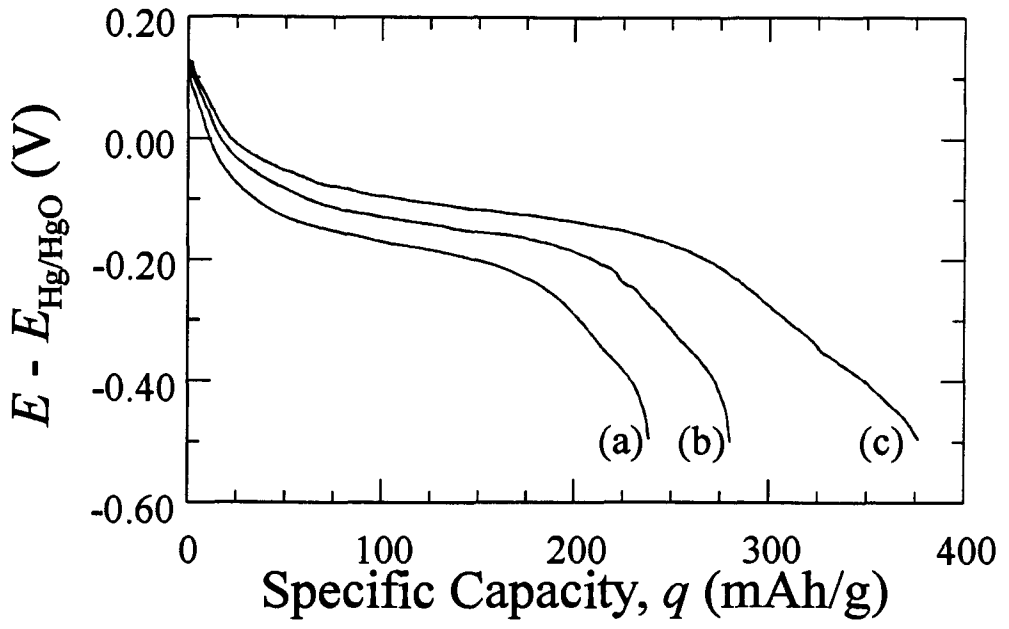

Figure 3.33: Discharge of CMD-R at various specific currents (a) 10 mA/g, (b) 3 mA/g, and (c) 1 mA/g in 1 molar KOH and 30 °C.

Whatever the origin of the noise, it makes the differential capacity curve, obtained by differentiation of the specific capacity with respect to voltage, virtually useless. Even averaging of data did not lead to a clean derivative curve. But it is this differential capacity that one must use to compare the discharge behaviour of various materials. To obtain reasonable derivatives, I utilized larger discharge currents, well aware of the fact that this leads to data farther away from equilibrium.

Figure 3.34 shows the differential capacity as a function of the electrode potential, referenced with respect to Hg/HgO, for three manganese dioxides (TAD 1, CMD-R, and β-MnO_2) whose discharge curves at smaller specific currents were already shown in figure 1.6. It is surprising that the main reduction peak of TAD 1 is centred at a higher voltage than the one of CMD-R. The origin of this may be either intrinsic (that is due to different binding energies of hydrogen in the two structures) or kinetic (larger ohmic resistance in CMD-R leading to a significant IR-drop). Kinetics certainly plays a role as was shown before, but it is not clear if it can account for the entire voltage gap. Structural differences may be an additional contributor to the different voltage

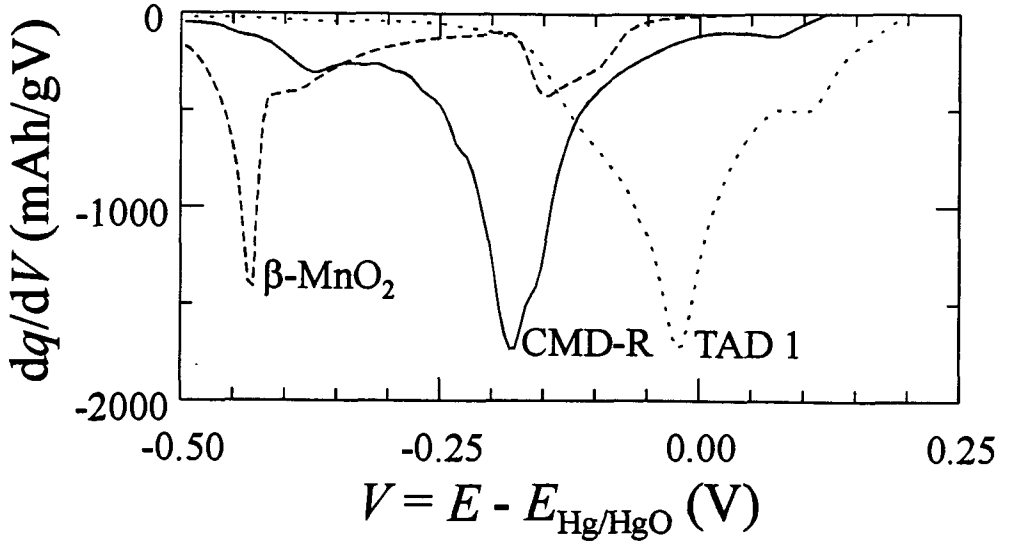

Figure 3.34: Comparison of the differential capacities of CMD-R (solid line) , TAD 1 (dotted line) and β-MnO_2 (dashed line), discharged at 10 mA/g and 30 °C.

profiles.

A way to test whether or not kinetics is the only contributor would be to re-charge the working electrodes after partial discharge, observe the voltage profile, and confirm that the re-charged material is the same as the starting material.

β-MnO_2, on the other hand, shows hardly any capacity at high voltages, and it is not clear whether it is merely the difficulty of inserting hydrogen into the 1×1-tunnels or whether there are other issues involved.

These types of investigation can certainly be continued, and they will surely show some interesting results,[11] but I would like to leave them for future work. However, one interesting aspect should be mentioned: Due to the composition of the working electrode (Super S instead of graphite), powder X-ray diffraction patterns show predominantly peaks from the discharged manganese dioxide.

Since my fitting programme works well for CMD-R and certainly for β-MnO_2, it could be fruitful to follow the discharge of these materials by (*ex situ*) powder X-ray diffraction and try to fit the data with the ramsdellite/pyrolusite-intergrowth model.

[11]Of particular interest is the origin of the reduction peak at 0.1 V, which was ascribed to surface effects by Chabre [4]. Again the question is, which surface is involved? Could it be internal surfaces?

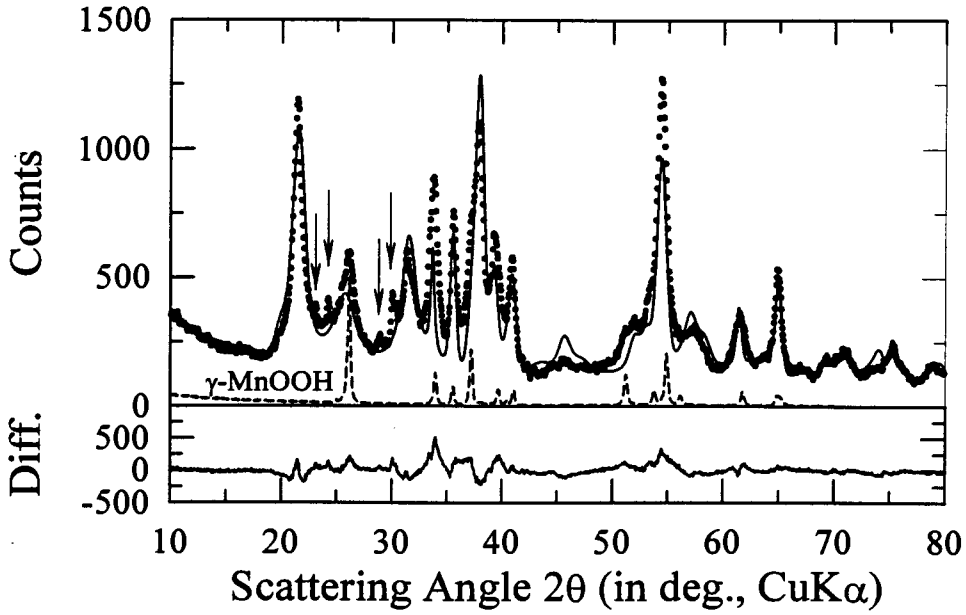

Figure 3.35: Powder X-ray diffraction of CMD-R discharged down to −0.8 V *vs* Hg/HgO and fit to this groutitic material. Due to the presence of γ-MnOOH and another impurity, whose peaks are indicated by arrows, the fit is only partially reliable.

Figure 3.35 shows the powder X-ray diffraction pattern of CMD-R after discharge down to −0.8 V *vs.* Hg/HgO (1 M KOH). It is very satisfactory that this discharge product could be fit fairly well with the intergrowth model of 2×1- and 1×1-tunnels, although some manganite[12] as well as a third, as yet unidentified, phase appear to be present. In particular, both the undischarged and the fully discharged material contain the same fraction of faults; in the undischarged CMD these are pyrolusite faults in a ramsdellite matrix, in the discharged product they may be manganite faults in a groutite matrix.

Since the impurity peaks influence intensities of adjacent peaks due to overlap, the refined atomic positions are not reliable. However, the lattice constants should be trustworthy: $a_1 = 4.524$ Å, $4r_2 = 10.564$ Å, and $a_3 = 2.871$ Å. These values are close to the ones of groutite, which are 4.560 Å, 10.700 Å, and 2.8700 Å, respectively [77]. The value for the 2-direction, however, is different, which is not surprising because

[12]Manganite (γ-MnOOH) is the hydrogenated form of pyrolusite (β-MnO_2)

the discharged CMD-R contains 1 × 1-tunnel faults that shorten the average lattice parameter. Whether these 1 × 1-tunnels contain hydrogen (and are therefore manganite faults) or not, is not clear. Nonetheless, I will talk about a groutite/manganite intergrowth.

The order parameter, p, was eventually fixed at 0.20 for best visual correspondence between the measured and the calculated pattern; when left to be refined, it increased to about 0.35 because of the low-angle shoulder of the 130 peak at 32°, which was caused by the unidentified impurity.

It is encouring that a fit to a manganese dioxide discharged in an alkaline electrolyte could be achieved. Ideally, one would like to have a series of samples discharged to various degrees and fit their powder X-ray diffraction pattern. One thing appears to be clear from the one pattern obtained. Manganese dioxides that can be described with the ramsdellite/pyrolusite intergrowth model do not change their structure when discharged in 1 M KOH. They merely seem to expand the lattice to obtain a groutite/manganite intergrowth.

It would be of interest to have a fitting programme available that can deal with EMDs so that one can obtain insight into their discharge behaviour as well. Hopefully, one of the possible modelling methods that I described in this chapter will work for EMD. In a second step, it will be important to analyze, whether the discharge behaviour of EMDs in 9 M KOH is similar to the discharge in 1 M KOH or whether the discharge of manganese dioxides in almost saturated KOH solution is dominated by the presence of potassium ions that may (co-)intercalate into the cathode materials.

Chapter 4

Manganese Dioxides for Lithium-Ion Cells

4.1 The Lithium-Manganese-Oxygen Gibbs Triangle

In chapter 1, I pointed out that lithium metal is discriminated against as a choice for anodes in rechargeable lithium cells because of the large specific surface area that develops upon cycling. To avoid this problem, manufacturers switched to alternate anode materials, which to date do not contain any lithium atoms. Consequently, it has to be the cathode that contains lithium atoms in the initial assembly. For this reason, the manganese dioxides discussed in the last section are not useful for rechargeable lithium-ion cells — that is at present.

There are certainly researchers who want to make a lithium-metal cell work as a safe rechargeable cell, for instance by designing new liquid electrolytes that reduce or even prevent dendrite growth during recharge [78] or by using solid electrolytes that form a physical barrier against dendrites. It is also feasible, that other anode

materials could be found that already contain extractable lithium atoms[1]. In these cases, the 3 V manganese dioxides could see a revival because they are less reactive than the 4 V material currently used and therefore make potentially safer cathodes.

At present, however, the only useful manganese dioxide for lithium-ion cells is λ-MnO_2 that is prepared in its lithiated form, the stoichiometric spinel $LiMn_2O_4$[2].

On the other hand, there is no reason why one should be restricted to lithiated manganese *di*oxides. It is certainly worth while to investigate other lithiated manganese oxides. Figure 4.1 shows the Gibbs triangle for materials composed of lithium, manganese, and oxygen. In this triangle, the relative abundance of an atom within the compound is one at the apex identified with that atom and decreases linearly to the opposite side, where the abundance is zero. The relative abundance is therefore constant along lines parallel to this opposite side. The triangle contains many compounds, but only a few are shown for clarity.

Compounds with the spinel structure can be found along the "spinel-line"; at the manganese-rich side, both (16d) and (8a) sites are occupied by manganese atoms. Following the line to higher lithium content, manganese atoms on (8a) are exchanged for lithium atoms. This exchange is complete at the $LiMn_2O_4$ point. When the lithium content is further increased, manganese on (16d) is replaced with lithium until the $Li[Li_{1/3}Mn_{5/3}]O_4$ point is reached (the square brackets indicate atoms on the (16d) site). At this point all manganese atoms are in oxidation state IV and spinel compounds with a higher average oxidation state are unknown.

In the shaded region to the right of the spinel line, one can find so-called defect spinels, compounds with cation vacancies in the spinel-structure, such as λ-MnO_2. Of course, not all compounds in the shaded region have to have a spinel structure; for

[1]The drawback of lithiated low voltage material (that is, the voltage versus lithium metal is small, below about 3.3 V) is that they are unstable in air: The lithium atoms inside will react with moisture from the ambient to form LiOH or with carbon dioxide to form Li_2CO_3. This problem is a lot worse for powder with large specific surface areas than for lithium metal foil.

[2]Spinel as a mineral is $MgAl_2O_4$. However, in the context of lithium manganese oxides for lithium-ion cells, the compound $LiMn_2O_4$ is commonly referred to as manganese-spinel or simply spinel. To distinguish it from materials with the same structure, but contain other cations mixed on the manganese sites, one adds the word 'stoichiometric'.

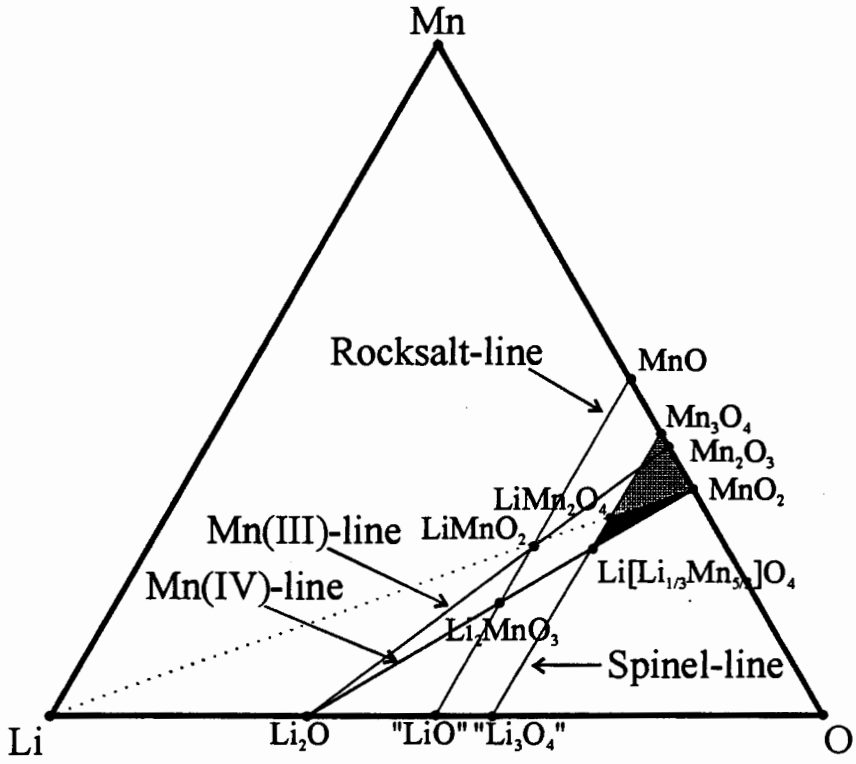

Figure 4.1: Some Lithium-Manganese-Oxides in the Li-Mn-O Gibbs triangle

instance β-MnO_2 does not. Two phases exist for Mn_2O_3, namely an orthorhombic α-phase [79, 80] and a defect spinel γ-phase [81].

The "spinel-line" is distinguished from the "rocksalt-line" by the fact that atoms can both be inserted (into unfilled (16d) octahedra) and extracted from the spinel phase, whereas in "rocksalt" materials, all octahedral sites are filled and only extraction is possible.

Lithium extraction follows the extrapolated tie-line between the Li vertex and the compound point towards smaller lithium content. In the case of $LiMnO_2$, this is indicated by the dotted line. The de-lithiation starts at $LiMnO_2$, continues via the $LiMn_2O_4$ point, which is of course identical to the $Li_{0.5}MnO_2$ point, towards the MnO_2 composition point. The Gibbs triangle cannot given any information about the crystal structures that are encountered during the de-lithiation process. In fact, it cannot even assert if every point on the tie-line is realized or if there are regions that are not accessed due to discontinuous phase separations. The tie-line therefore

gives only an average composition of the de-lithiated product.

The darkly shaded region will be discussed in greater detail in section 4.2. Here I want to restrict myself to the following, apparently useful, compounds: Li_2MnO_3, $LiMnO_2$, and $Li_{3/7}MnO_2$ (not shown, but also to be found on the Li–MnO_2 tie-line).

4.1.1 Li_2MnO_3

This material contains a lot of lithium per unit mass and could therefore have a large specific capacity. Additionally, its crystal structure is very similar to layered materials such as $LiCoO_2$ and $LiNiO_2$, which are commercialized as or considered as cathode materials for lithium-ion cells. The correspondence becomes evident, if one writes Li_2MnO_3 as $Li(Li_{1/3}Mn_{2/3})O_2$: Alternate cation layers are filled with only lithium atoms and with $\frac{1}{3}$ lithium/$\frac{2}{3}$ manganese atoms. Unfortunately, all manganese atoms are in oxidation state IV; removing lithium would lead to an increase in oxidation, which is not achievable with present electrolytes. This compound has no capacity below 5 V versus lithium metal and it is therefore undesirable to have Li_2MnO_3 as an impurity phase in the cathode material.

As a general rule, one could postulate that lithium can only be removed practically from compounds until the extrapolated Li–compound tie-line intersects the "Mn(IV)-line" [82, *e.g.*].

4.1.2 $LiMnO_2$ and $Li_2Mn_2O_4$

These materials do not suffer from the drawback of manganese in oxidation state IV and they still have one lithium atom per manganese atom available for removal. The orthorhombic $LiMnO_2$ phase can be synthesized by reacting stoichiometric[3] ratios of, for instance, lithium carbonate and manganese dioxide at 800 °C in argon. And indeed, lithium can be removed, but at a price: Charging $LiMnO_2$ to 4.2 V *vs.* lithium metal and thereby removing most of the lithium leaves a structure that appears to convert to a disordered spinel [83]. During the subsequent discharge, a poorly

[3]A slight excess of lithium may be desirable to account for possible lithium losses due to evaporation of lithia, Li_2O, during synthesis.

crystallized $LiMn_2O_4$-phase is formed and further cycling shows a voltage profile indicative of a spinel.

In the $LiMn_2O_4$ spinel, all lithium atoms have filled the (8a) octahedral site. Further lithium insertion therefore must lead to a rearrangement of the lithium atoms to fill the octahedral (16c) sites and one obtains a new phase, $Li_2Mn_2O_4$, which does not exhibit cubic symmetry, but shows a tetragonal distortion. During lithium insertion one therefore observes a phase separation

$$x\mathrm{Li} + \mathrm{LiMn_2O_4} \longrightarrow (1-x)\mathrm{LiMn_2O_4} + x\mathrm{Li_2Mn_2O_4}, \tag{4.1}$$

leading to a two-phase coexistence along a 3 V plateau[4].

Unfortunately, cells do not cycle well over this 3 V plateau, apparently due to the cubic-to-tetragonal transformation that the material would have to undergo, repeatedly. Such repeated toggling between the cubic and the tetragonal structures is thought to fracture the initial crystallites such that electronic contact is lost. These fractured particles are then electrochemically inactive — the cell has lost capacity. Further details will appear in Immo Koetschau's M.Sc. thesis [84].

Recently, Armstrong and Bruce [50] prepared a layered $LiMnO_2$ compound with a δ-MnO_2 structure. This compound may become interesting, although it is still in its infancy at the moment.

4.1.3 $Li_{3/7}MnO_2$ — CDMO

This material is prepared by reacting EMD with, for instance, LiOH in the appropriate ratio at 350 °C in air. The presence of lithium appears to stabilize the EMD structure so that it does not convert to β-MnO_2. The powder X-ray diffraction pattern is similar to the one of the initial EMD, but with larger interatomic distances due to the additional lithium. Some researchers believe that the crystal structure is a mixture of one-dimensional 1×1- or 2×1-tunnels and a three-dimensional network of 1×1-tunnels, as in the spinel. Sanyo labelled this compound therefore CDMO, composite dimensional manganese oxide.

[4]This is an example for the aforementioned inaccessibility of certain regions of the triangle.

Unfortunately, the specific capacity on first charge up to 4.2 V is only about 50 mAh/g [85] compared to a theoretical value of 128 mAh/g, if all the lithium could be removed. This suggest that 60% of the initial lithium remains in the material, nominally $Li_{0.25}MnO_2$.

When cycling materials against lithium metal, one can fill them with more lithium than they initially contained. In this case, one can insert lithium beyond the initial content equivalent to a specific capacity of approximately 160 mAh/g, corresponding to a discharged compound of "γ-$LiMnO_2$". This material can then be cycled between 2.5 V and 4.2 V with a total capacity of about 0.70 e^-/Mn, corresponding to about 200 mAh/g based on the weight of the fully lithiated compound.

Ideally, one would like to prepare the fully lithiated compound in a chemical synthesis. This would have to be done at low temperatures to avoid the formation of the spinel $LiMn_2O_4$ or orthorhombic $LiMnO_2$. One idea that was pursued in our lab was to reduce EMD chemically by cinnamyl alcohol to form an MnOOH phase and to exchange the hydrogen for lithium in a 4 molar LiOH solution at 50 °C. Unfortunately, instead of the lithiated EMD, a disordered rocksalt phase $[Li_xMn_{1-x}]O$ was formed [85].

In view of the predominance of non-lithiated anode materials, it is still desirable to find a good synthesis method for a fully lithiated manganese dioxide with the EMD structure.

4.2 $Li[Li_xMn_{2-x}]O_4$ and Capacity Fade

As can be seen, there are many lithium manganese oxide compounds available, which can be potentially useful for lithium-ion cells. The ones closest to commercialization are, since electrolytes that are stable above 4 V (even at 55 °C) have become available [86], the spinels of the general composition $Li[Li_xMn_{2-x}]O_4$ with $0 \leq x \leq 1/3$. In these materials a fraction of x lithium atoms per formula unit replaces manganese atoms on the (16d) sites.

The upper limit of x, 1/3, is set by the average oxidation state of manganese reaching IV. Again this compound should not have any useful capacity. However, if

one exposes this manganese(IV) compound to a reducing gas at elevated temperature, one could expect some oxygen to be removed from the compound and the average oxidation state of manganese to be lowered so that lithium can be removed during electrochemical charging. The feasibility of such a process was demonstrated by Richard and coworkers [87]; however, the practically achievable specific capacity of the stoichiometric spinel, about 125-130 mAh/g, could not be reached.

If this post-synthesis reduction is to be avoided, then, during charge, manganese can only be oxidized to manganese(IV), and therefore only remove $1 - 3x$ lithium atoms can be removed per formula unit from $Li[Li_xMn_{2-x}]O_4$ leaving a compound of the composition $Li_{4x}Mn_{2-x}O_4$. In other words, the highest theoretical capacity is achieved by the stoichiometric spinel.

Consequently, the goal must be to make stoichiometric spinels work and find their optimum synthesis process. The conditions that a good cathode material must fulfill include good cyclability, low specific surface area[5], as large a specific capacity as possible and easy synthesis to limit manufacturing costs.

In order to obtain a low specific surface area, usually high synthesis temperatures are required (for the spinels up to 900 °C). Since the cyclability of the stoichiometric spinels is not very good, especially at temperatures above room temperature (*e.g.* 55 °C) [88], one likes to improve upon it by adding a little excess lithium [82], but not too much so that the specific capacity does not decrease by more than is gained by the improved cycling behaviour. Unfortunately, spinels with or without excess lithium tend to phase separate into spinels with a lesser lithium content[6] and (the electrochemically inactive) Li_2MnO_3 above a certain temperature that decreases with increasing lithium content [89].

For an excess lithium content of $x \approx 0.2$, the temperature of phase separation is as low as approximately 600 °C [89]. In order to avoid a multiphase product after heating to 900 °C, one would need to cool very slowly to reverse the phase separation; the patent literature suggests a preferred cooling rate of 2–3 °C/h from the heating

[5]A specific surface area of 1 m^2/g or less is desired to limit side reactions between the electrolyte and the electrode.

[6]Gao and Dahn propose a compound that is on the "spinel-line" close to the Mn_3O_4 point.

temperature down to at least 500 °C [90]. Such a manufacturing process is certainly highly uneconomical and therefore undesirable. Alternatively, one can add the excess lithium in a second heating step below or at 600 °C [91].

The questions that needs to be answered is: Why does excess lithium improve the cycle life of the spinels? Among the possible reasons for the fading capacity are:

1. The de-lithiated product $Li_0Mn_2O_4$ may react with the electrolyte, leading to passivating, structural changes of the active material [92]. It is not clear, however, why excess-lithium spinels should be less reactive, when their voltages in the charged states and therefore their oxidation strengths are the same.

2. A possible reason for different reactivity of stoichiometric and excess-lithium spinels towards the electrolyte may lie in their surface properties. An excess lithium spinel may form a surface-electrolyte-interface that is more stable than the one of stoichiometric spinel. Recent results of improved cycling after the coating of stoichiometric spinel with an ion-conductive, glassy Li_2O:B_2O_3-film suggest that the reactivity of the spinel surface towards the electrolyte is certainly one factor in the capacity fade problem [93].

3. Since the excess-lithium spinels contain lithium on the (8a) sites even in the charged state, they may be more stable against structural changes. It is known that the de-lithiated stoichiometric spinel, λ-MnO_2, converts to β-MnO_2 upon heating [15, 94].

4. Manganese in the fully lithiated stoichiometric spinel has the lowest average oxidation state among $Li[Li_xMn_{2-x}]O_4$ compounds, 50% Mn(III) and 50% Mn(IV). Since Mn^{3+} is a Jahn-Teller ion, that is its electron density is not spherically symmetric, a large amount of manganese(III) leads to a distortion of the cubic structure, as observed in the tetragonal $Li_2Mn_2O_4$. However, this compound is only formed when the discharge voltage drops to the 3 V plateau. Consequently, one would not expect any Jahn-Teller effect when cycling down to 3.5 V; nonetheless, a capacity loss upon cycling is observed with this lower limit. Also, *in-situ* powder X-ray diffraction shows no evidence of a tetragonal

distortion in the discharged state at 3.5 V.

5. The 4-V-plateau of the $Li_{1-x}Mn_2O_4$ is actually split into two levels, separated by about 0.1 V. *In-situ* powder X-ray diffraction shows that during cycling over the higher voltage level, two phases with different lattice constants are present [95, 16]. In the case of the cubic-to-tetragonal distortion during discharge of $LiMn_2O_4$, such a two-phase regime was thought to be responsible for the fade of the 3-V-plateau. Contrary to the two phases of the 3-V-plateau, which have different symmetries, the two phases of the upper level of the 4-V-plateau are both spinels — or so it appears: Powder X-ray diffraction can, of course, give no evidence for or against certain symmetries other than the fact that the peak intensities calculated on the basis of a certain space group match those observed by the experiment reasonably well.

In the next section, I will try to resolve some issues regarding the third point above.

4.3 Stability of Acid-treated Spinel

4.3.1 Mechanism of Acid-treatment

If the reason for the capacity fade of $LiMn_2O_4$ was the thermodynamic instability of $Li_0Mn_2O_4$, then materials obtained by de-lithiating $Li[Li_xMn_{2-x}]O_4$ with $x > 0$ should be thermodynamically more stable than materials with x=0. Such a difference in the thermodynamic properties should be evident in the behaviour of these materials during heating.

Hunter [15] invented a method to chemically de-lithiate spinels by treating them with diluted acid at room temperature. The de-lithiation is thought to proceed by a disproportionation reaction of 2 Mn(III) into Mn(II), which dissolves, and Mn(IV):

$$4Li[Mn^{III}Mn^{IV}]O_4 + 8H^+ \longrightarrow 3[Mn_2^{IV}]O_4 + 4Li^+ + 2Mn^{2+} + 4H_2O. \qquad (4.2)$$

A possible competing reaction could, of course, be the simple ion-exchange of Li^+-ions in the spinel structure for protons, as is discussed by Feng and co-workers [96].

An incorporation of protons certainly takes place, but one has to observe the water stability window. A de-lithiated spinel has an electrochemical potential of approximately 4.0–4.2 V *vs.* Li/Li^+, and consequently a standard electrode potential of about 1.2 V in a 1 molar Li^+-solution, and even more positive if the concentration of Li^+ is smaller. At a pH of 0, oxidation of water according to

$$2H_2O \longrightarrow O_2 + 4H^+ + 4e^- \tag{4.3}$$

occurs at a standard electrode potential of about 1.23 V, at pH 1 the potential decreases (at 298 K) by 59 mV to 1.18 V. Consequently, a direct hydrogen insertion may be favoured, if the potential of the de-lithiated spinel is higher than the potential of water oxidation, similar to the $CoO_2/CoOOH$-system investigated by Amatucci and co-workers [10]. Since the de-lithiation of the spinel is achieved in an aqueous environment, a disproportionation according to equation 4.2, followed by hydrogen insertion due to equation 4.3, is therefore equivalent to an ion-exchange of lithium-ions for protons.

4.3.2 Materials Preparation

For a preliminary sample, I prepared a precursor batch of $LiMn_2O_4$ by mixing 50.00 g of EMD (TAD 1, Mitsui) with 10.09 g Li_2CO_3 (FMC, Bessemer City, NC, USA) and heating the mixtures at 900 °C for 12 hours in air, then cooling it at 50 °C/h. The weight ratio was based on the assumption that TAD 1 is 59.6% manganese by weight.[7]

15 g of this precursor were immersed in diluted H_2SO_4 and stirred. More acid was added until the pH stabilized at 2. After a further 45 minutes of stirring, the suspension was decanted, then washed and filtered in a sintered glass filter. The final product was dried in air at 110 °C for several hours. This material will be referred to as sample P.

In order to determine whether or not the thermodynamic stability of the de-lithiated compounds plays a role in the capacity fade process, I prepared three more

[7]Yuan Gao, private communication

precursor materials $Li[Li_xMn_{2-x}]O_4$ with $x = 0.0$, 0.1, and 0.2, following the synthesis procedure given in [91]. Three batches of $LiMn_2O_4$ were prepared as before. LiCl, dried at 110 °C for several hours, was added to 45 g of two of the batches, 1.668 g and 3.522 g, respectively. All three batches were then heated a second time at 600 °C for 18 hours in air and allowed to cool down to 100 °C over a period of 10 hours, after which they were taken out of the furnace. These three batches will be referred to as 00a, 10a, and 20a, depending on the nominal value of x.

5 g portions of precursor material were then immersed in 100 ml of diluted H_2SO_4 of definite initial pH to obtain de-lithiated samples. The suspension was stirred for 2 hours then filtered through a sintered glass filter and the pH of the filtrate was recorded, which will subsequently be reported as "final pH". The cake was repeatedly washed and filtered and finally dried under vacuum down to 100-200 milli torr at room temperature. This drying procedure does not remove all water from the powder, but it suffices for further handling. However, moisture is not desirable in *non*-aqueous lithium cells and it may affect the electrochemical behaviour of electrodes made from these acid-treated samples.

4.3.3 Characterization by Powder X-ray Diffraction

Powder X-ray diffraction data of all samples were obtained using a Siemens D 5000 or a Philips PW 1730 (for sample P) diffractometer equipped with copper target X-ray tubes and diffracted beam monochromators selective for CuKα-radiation. To minimize, if not avoid, effects of preferred orientation, which may arise when pressing highly crystalline powders into deep-well holders, the powders were manually ground and then lightly packed into the holders.

Typical measuring parameters on the D5000 were a range of 10°–120° in scattering angle, a step size of 0.05° and a count time of 20 s per step. Divergence and anti-scatter slits were 0.5°, the receiving slit was 0.2 mm at a goniometer radius of 217.5 mm. For sample P, I used a 0.5° divergence slit and a receiving slit of typically 0.6 mm width at various count times. The patterns of crystalline materials were then analyzed by the Rietveld method [56, 57]. The respective lattice constants are given

in table 4.1

Table 4.1: Parameters of chemically de-lithiated spinel samples. The first column is the sample label, the second the final pH of the filtrate in the acid-treatment process, the third the lattice parameter of the cubic unit cell, the fourth and fifth columns are the occupancies of the two crystallographic lattice sites of the spinel structure with lithium and manganese, respectively, the last column is a reliability factor of the previous crystallographic data. Samples 00a, 10a, and 20a are the precursor materials $Li[Li_xMn_{2-x}]O_4$ with $x = 0.0$, 0.10 (0.06), and 0.20 (0.16), respectively.

sample	final pH	a/Å	(8a)	(16d)	R_B
P	2	8.035	–	0.49	4.52
00a	–	8.245	0.24	0.52	2.88
00b	4.0	8.231	0.25	0.51	2.32
00c	3.9	8.191	0.24	0.50	3.35
00d	3.7	8.156	0.18	0.50	2.99
00f	1.3	8.037	0.07	0.49	2.70
10a	–	8.223	0.28	0.51	3.15
10b	4.3	8.208	0.25	0.49	3.45
10c	3.2	8.155	0.17	0.49	1.99
10e	2.3	8.070	0.11	0.47	5.05
20a	–	8.191	0.25	0.46	2.80
20c	3.2	8.147	0.14	0.48	5.21
20e	2.2	8.091	0.10	0.47	3.44

The nominally stoichiometric spinel, 00a (a=8.245 Å), showed small α-Mn_2O_3 impurities because, as it turned out afterwards, the Li_2CO_3 precursor was only 98% pure and the total manganese content of TAD 1 may be larger than the 59.6% assumed for synthesis[8]. The Mn_2O_3 phase may make up 4–5% of the final material. Consequently, the spinels with excess lithium, nominally $x = 0.1$ and 0.2, have actually true values of $x \approx 0.06$ and 0.16, respectively. To be consistent with data obtained by Gao and Dahn [97, 92, 91, 89], I will keep the nominal values with the approximately true value in parentheses.

When refining the structures of the 00-series, a second phase of Ia3 symmetry was incorporated to account for the Mn_2O_3 impurity. This space group is not rigorously

[8]Data obtained from Moli Energy (1990) Ltd. show a total manganese content of about 60.5% by weight.

correct as Mn_2O_3 shows a slight orthorhombic distortion [80, 79], but the error is negligible and the simpler space group reduces the number of parameters to be varied, which is appropriate as Mn_2O_3 is present only as an impurity.

Also, all acid-treated samples could be indexed using the cubic spinel structure. The lattice constants and final pH values are summarized in table 4.1. Samples P and 00f have lattice constants of $a = 8.035$ Å and $a = 8.037$ Å, respectively, the same as the λ-MnO_2 prepared by Hunter who reported $a = 8.03$ Å. It is evident that within each series a lower final pH implied a smaller lattice constant suggesting that more lithium was leached out and more manganese(III) was converted to the smaller manganese(IV).

During Rietveld refinement, the individual temperature factors associated with the various crystallographic sites were kept fixed at zero and only an overall temperature factor was allowed to vary so that the occupancies of the various crystallographic sites may have meaningful interpretations. The occupancies of O on the (32e) sites was fixed at 1, the refined occupancies of Li on (8a) and Mn on (16d) are listed in table 4.1. One can debate whether or not ionic form factors, *e.g.* Mn^{4+} and O^{-2}, should be used instead of those of the neutral atom. Since a choice had to be made and the nature of the Mn–O bond is not clear, I chose those of the neutral atoms.

Theoretically, one expects the occupancy of (8a) to drop from 0.25 to $0.25 \times 3x$, *i.e.* 0, 0.08 (0.05), and 0.15 (0.12) for $x = 0.0$, 0.1 (0.06), and 0.2 (0.16), if one assumes that lithium is removed from the (8a) site only, and not from (16d). On the other hand, the occupancies of the (16d) site should stay constant within each series at

$$\text{(16d) occupancy} = 0.5 \times \frac{(2-x)\, f^{\mathrm{Mn}}(s) + x f^{\mathrm{Li}}(s)}{2 f^{\mathrm{Mn}}(s)} \approx \frac{2-x}{4}, \qquad (4.4)$$

which yields 0.5, 0.475 (0.486), and 0.450 (0.464) for $x = 0.0$, 0.1 (0.06), and 0.2 (0.16). It is very encouraging that the values of the refined (8a) occupancies decrease with decreasing pH, suggesting that lithium is removed from the tetrahedral sites (see table 4.1).

On the other hand, it is not clear how reliable the variation of the refined (16d) occupancies within each series is, since the Bragg-R factor remained poor in some cases (larger than 3.0), partly due to preferred orientation effects that were not com-

pletely eliminated despite careful handling. Allowing for a preferred orientation in the [111]-direction, the Bragg-R factor for samples 20c and 20e decreased to 2.19 and 1.60, respectively, and in both cases the (16d) occupancies refine to 0.46 as in the precursor material.

Since the refinement of the occupancies was only reliable in the trend of decreasing occupation of the (8a) site and not in the absolute value of the occupancies of any of the crystallographic sites, powder X-ray diffraction could not determine whether the removed lithium originated solely from (8a) sites or from (16d) sites as well. The electrochemical investigation may give some suggestions (see section 4.4).

4.3.4 Thermal Stability of λ-MnO_2

Thermodynamic stability of a material is easily tested using of a differential scanning calorimeter (DSC) (see appendix A.3 for a description); we used a DuPont 910 DSC in connection with TA Instruments Thermal Analyst 2000 software. At a heating rate of 10 °C/min and a static, but constant pressure, air ambient, sample P undergoes an exothermic transition at 270 °C followed by an endothermic decomposition at 550 °C (see figure 4.2). The exothermic peak is associated with the transition from λ-MnO_2 to β-MnO_2 as observed by X-ray diffraction, whereas the endothermic peak is associated with the decomposition of β-MnO_2 to α-Mn_2O_3.

Figure 4.3 shows the evolution of the X-ray diffraction pattern of sample P with increased temperatures to which the sample was exposed during overnight heating. The X-ray diffraction patterns of the 350 °C sample shows predominantly peaks associated with β-MnO_2. Samples heated at lower temperatures show patterns of disordered structures (referred to as ε-MnO_2 in reference [94]). Even the as-made sample P, which was dried at 110 °C, as well as the X-ray diffraction pattern of the λ-MnO_2 shown by Hunter, contain peaks that do not correspond to the spinel λ-MnO_2 phase.

The patterns of the materials heated at 160 °C and 200 °C show, in addition to the emerging β-MnO_2 peaks and vanishing spinel peaks, features that are similar to those of some chemically prepared manganese dioxides, such as Faradizer M (Sedema,

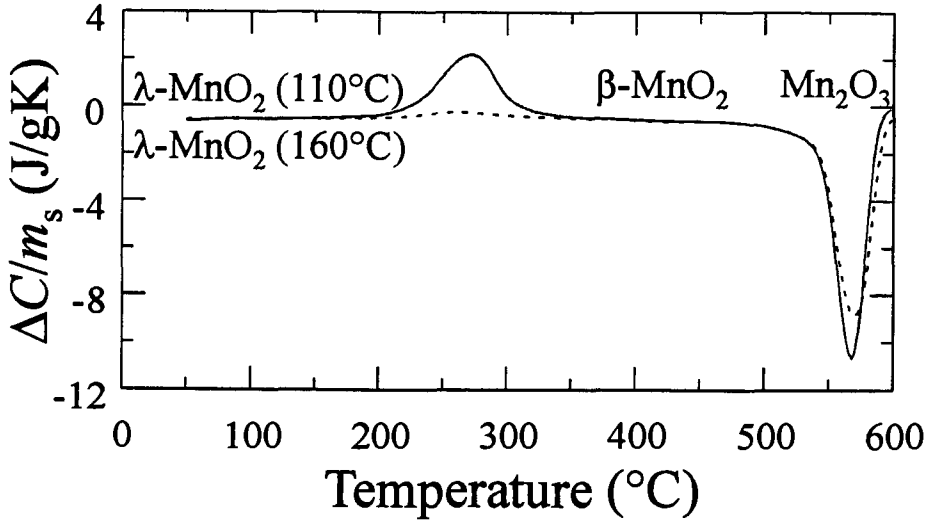

Figure 4.2: Differential scanning calorimetry data of λ-MnO_2 (sample P; solid line) and sample P preheated at 160 °C (dashed line). The heating rate was 10 °C/min. The preheated sample shows only weak exothermic behaviour where λ-MnO_2 has a strong signature - the heat releasing transition has already occurred.

Belgium), as shown in figure 4.4a . The X-ray diffraction pattern of the latter material can be fit with a calculation based on the γ-MnO_2-structure described in chapter 3. Figure 4.4b shows a fit with $p = 0.70$, *i.e.* 70% 1 × 1- and 30% 2 × 1- tunnels . The essential point here is that the γ-MnO_2 structure is based on a hexagonal close packed oxygen lattice, and therefore the structure of Faradizer M is, too.

Based on the parameters obtained from the Faradizer M fit, I calculated a pattern that matches in particular the broad peak at 24° of the 200 °C pattern reasonably well (shown in figure 4.4d) — a true fit could not be obtained because of the multiphase nature that this pattern exhibits. Nonetheless, when adding the contributions of this manual "fit", of Faradizer M, and of β-MnO_2, one could recover the 200 °C pattern (and by similarity the 160 °C pattern), which must therefore be on a hexagonal close packed oxygen lattice.

The origin of the two peaks below 20° scattering angle is unclear. The respective *d*-spacings are 4.84 Å and 4.56 Å. The smaller 4.84 Å peak may be associated with a disordered defect spinel structure with manganese atoms occupying some tetrahedral sites, similar to Mn_3O_4 or its manganese deficient correspondent, γ-Mn_2O_3. Such

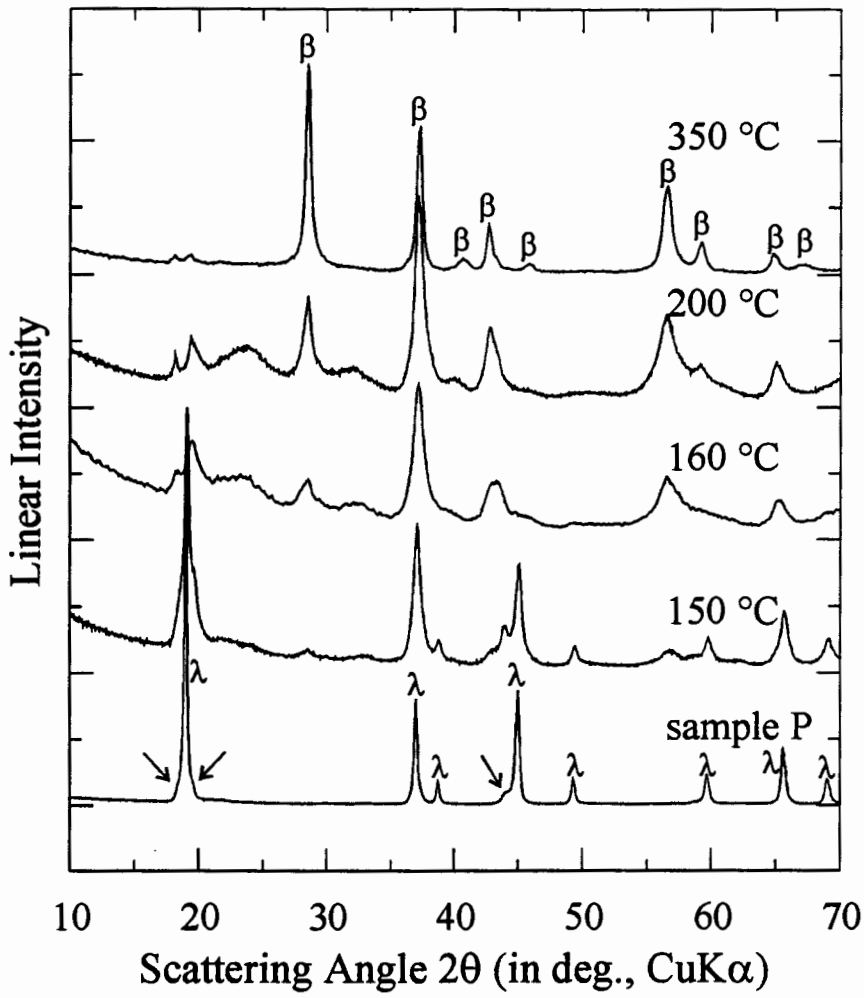

Figure 4.3: Powder X-ray diffraction patterns of sample P (predominantly λ-MnO_2) and sample P heated at various temperatures overnight in air. The initial material, which was dried at 110 °C, shows some impurity peaks (indicated with arrows), which become more noticeable as the λ-MnO_2 peaks decrease in intensity with increased heating temperature. Samples heated at 160 °C and 200 °C show some degree of disorder in addition to the emerging β-MnO_2 peaks. At 350 °C, the transition to β-MnO_2 is complete, except for the low-angle impurities.

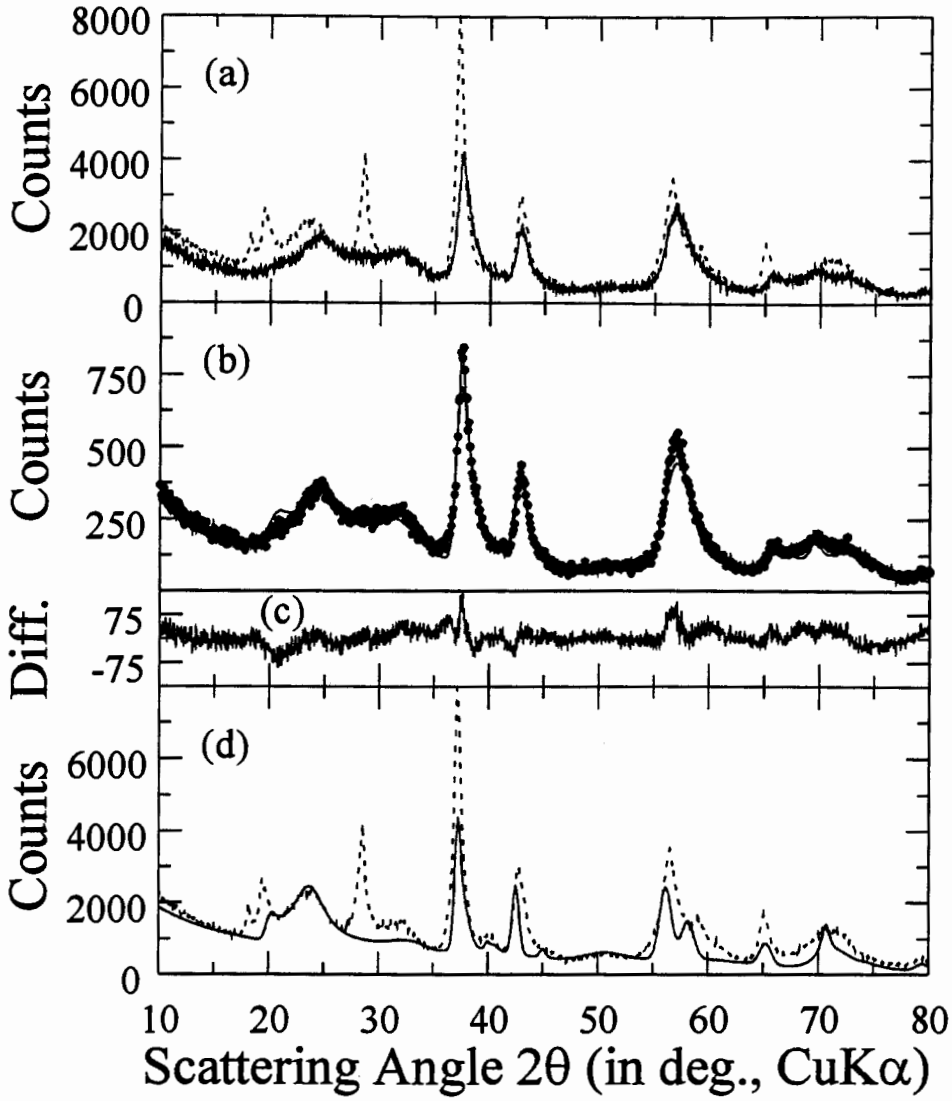

Figure 4.4: (a) Comparison of λ-MnO_2 heated at 200 °C (dashed line) and Faradizer M (solid line, scaled by a factor of 2). (b) Powder X-ray diffraction pattern of Faradizer M (dots) fit with the γ-MnO_2-model (solid line, $p = 0.70$). (c) Difference between measured and calculated intensities in (b). The relatively good fit suggests that Faradizer M is based on a hexagonal close packed oxygen lattice and therefore the heated λ-MnO_2 with features similar to Faradizer M is based on it as well. (d) Comparison of λ-MnO_2 heated at 200 °C (dashed line) and γ-MnO_2 (solid line, $p = 0.60$). This graph shows that λ-MnO_2 heated at 200 °C consists of a β-MnO_2 phase and a range of γ-MnO_2 phases with p varying between 0.6 and 0.7. The structure of λ-MnO_2 heated at 200 °C is therefore based on a hexagonal close packed oxygen lattice.

a defect spinel may or may not contain any lithium The 4.56 Å peak, which seems to decrease in relative intensity as heating progresses, may be associated with a hydrogenated and/or lithiated manganese dioxide with an α-MnOOH or γ-MnOOH structure, both of which have lattice parameters close to this value.

I demonstrated that the material heated at 160 °C is essentially a mixture of manganese dioxides with hexagonal close packed oxygen lattices and with ordered or disordered manganese atoms. The subsequent ordering of the manganese atoms in part of the sample is not associated with a large release of energy as can be seen from the DSC curve of sample P heated at 160 °C overnight in air (see figure 4.2). One must conclude that most of the heat of the λ-MnO_2 to β-MnO_2 transition is associated with the change from cubic to hexagonal close packing of the oxygen sublattice.

This justifies retroactively the statement made in the last chapter that the EMD structure was based on a hexagonal close packed oxygen lattice. DSC curves of EMDs did not show significant heat release during the EMD to β-MnO_2 conversion as one would have expected, if the EMDs had contained oxygen in a cubic close packed arrangement.

4.3.5 Thermodynamics of De-lithiated $Li[Li_xMn_{2-x}]O_4$

The DSC data of sample P show an exothermic peak at elevated temperature that is associated with the λ-MnO_2 to β-MnO_2 transition, *i.e.* the change in enthalpy $\Delta H = H(\beta\text{-}MnO_2) - H(\lambda\text{-}MnO_2)$ is negative. λ-MnO_2 is therefore metastable; its transition to β-MnO_2 is an activated process and is governed by an energy barrier, E_a, that needs to be overcome. The rate, R, at which this transition occurs is proportional to a Boltzmann factor

$$R = \nu \exp(-E_a/kT) \tag{4.5}$$

and is thus smaller at lower temperatures, T, but not zero (k is the Boltzmann constant, ν is the attempt frequency).

This means that the cathode in a fully charged electrochemical cell made with $LiMn_2O_4$ as the active material will eventually become inactive as λ-MnO_2 converts to β-MnO_2.

The question arises whether or not it is this metastability of λ-MnO_2 that is responsible for the poor cyclability of the stoichiometric spinel $LiMn_2O_4$. To investigate this, I took DSC data of de-lithiated spinels, obtained from the $Li[Li_xMn_{2-x}]O_4$ ($x = 0.0, 0.1, 0.2$) precursors.

In particular, I compared the behaviour of samples 00f, 10e, and 20e, whose compositions should ideally be given by $Li_{4x}Mn_{2-x}O_4$ such that all manganese atoms are in oxidation state IV. The X-ray diffraction patterns of these materials show very sharp peaks (see figure 4.5) because the samples were not exposed to any heat treatment — the oxygen sublattice remained cubic close packed. Sample 00f retained the Mn_2O_3-impurity of its precursor, at an increased concentration of about 8-10%, since about 50% of the initial $LiMn_2O_4$ were dissolved during the acid treatment.[9]

All three samples show strong exothermic peaks during heating just as sample P does. Figure 4.6 summarizes the exothermic transitions for samples 00f, 10e, and 20e. The energy released during the exotherm is lower for samples 10e and 20e, since these materials contain remaining lithium atoms so that only part of the material should convert to β-MnO_2. One would expect a disproportionation of $Li_{4x}Mn_{2-x}O_4$ into MnO_2 and a lithium containing manganese(IV) oxide, a compound that lies on the tie-line between MnO_2 and Li_2MnO_3 in the Li-Mn-O Gibbs triangle.

Figure 4.7 shows powder X-ray diffraction patterns of samples 10e and 20e heated at 350 °C overnight. In both cases a mixture of phases is present, one of which is β-MnO_2, but a complete separation into two phases did not take place, presumably because the heat generated by the conversion to β-MnO_2 is not large enough to drive the disproportionation. Heating at a higher temperature may increase the disproportionation, although one soon reaches the regime where β-MnO_2 loses oxygen and decomposes to Mn_2O_3, and manganese in the lithium-containing manganese(IV) oxide is partly reduced to manganese(III) so that $LiMn_2O_4$ is formed.

I showed that the de-lithiated excess-lithium spinels have an exothermic transition in the same temperature range and of the same order of magnitude as de-

[9]It is not clear why the Mn_2O_3 peaks did not vanish as was the case for sample P. Maybe it is related to the different nature of the acid-treatments or the fact that the precursor of sample P was not exposed to a prolonged second heat treatment.

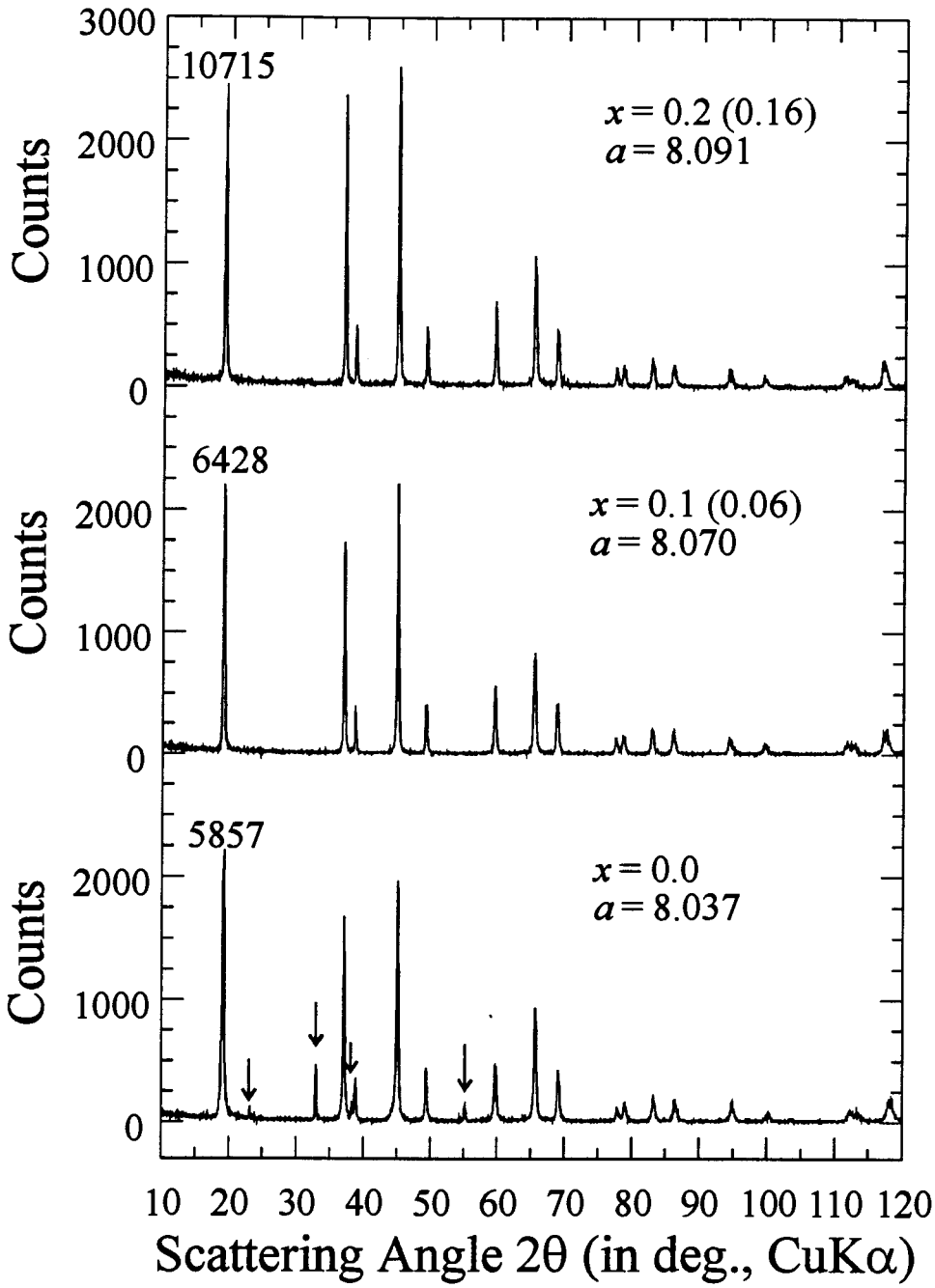

Figure 4.5: Powder X-ray diffraction patterns of samples 00f, 10e, and 20e. The delithiated $x = 0$ sample retained the α-Mn_2O_3 impurities (indicated by arrows). Since these materials were not dried at elevated temperature, but at room temperature under vacuum, the Bragg peaks remain sharp. The numbers above the first peaks give the maximum number of counts of these peaks.

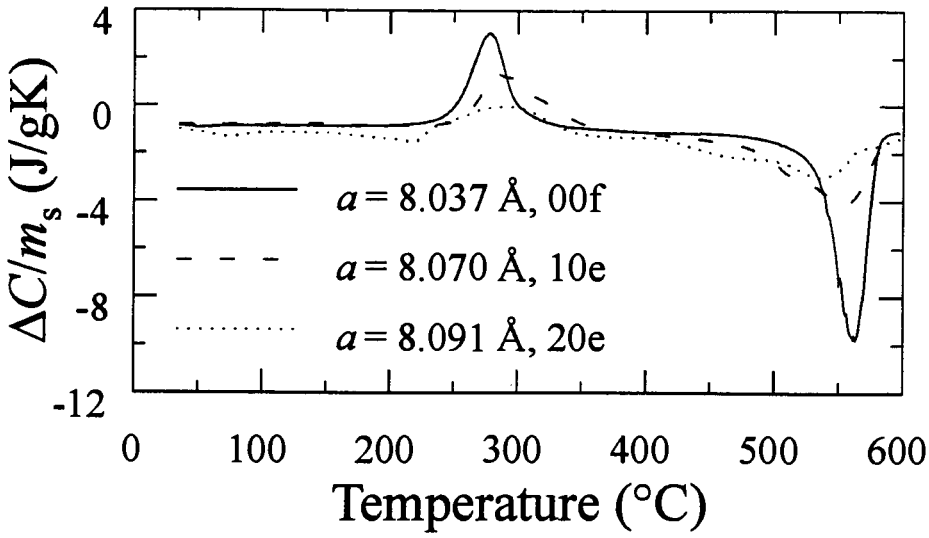

Figure 4.6: Differential scanning calorimetry data for samples 00f, 10e, and 20e. One observes exothermic peaks for all three samples, somewhat smaller and broader for the samples with remaining lithium content. The latter is also responsible for the broadened endothermic peak, which is associated with the phase separation into $LiMn_2O_4$ and α-Mn_2O_3.

lithiated stoichiometric spinels. In all cases, the exotherms are associated with the re-arrangements of the oxygen sublattices. This finding suggests that it is not the metastability of $Li_0Mn_2O_4$ that leads to a rapid capacity fade in electrochemical cells using stoichiometric spinel as a cathode. If this was the case, then the metastability of $Li_{4x}Mn_{2-x}O_4$ with $x > 0$ should make cells using spinels with excess lithium fade fast as well, but this is not observed.

The irrelevance of the λ-MnO_2 to β-MnO_2 transition for the capacity fading is further supported by the slow kinetics of this transition. I heated sample 00f at three different rates in the DSC (10 °C/min, 1 °C/min, 0.1 °C/min) as shown in figure 4.8. As expected, the peak shifts to lower temperatures with smaller heating rates.

The time a transition takes is reflected in the width of the exothermic peak. From the peak widths one can therefore obtain a rough estimate of the transition times,

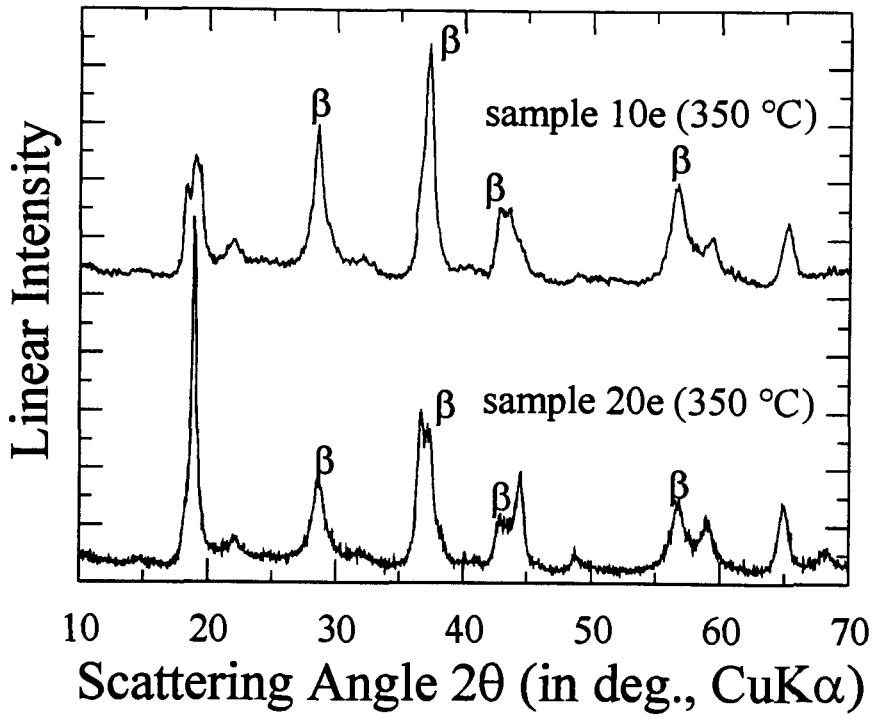

Figure 4.7: Powder X-ray diffraction patterns of samples 10e and 20e heated at 350 °C in air overnight. Each pattern shows a mixture of phases, one being β-MnO_2.

ignoring other effects that can lead to peak broadening, such as large sample sizes[10]. However, I believe that such effects play a secondary role.

At 278 °C the transition takes 4.8 min, at 238 °C 38 min, at 202 °C 180 min. Figure 4.9 shows the three data points from which one can extract the height of the energy barrier, $E_a = 1.07$ eV, and the attempt frequency, $\nu = 2.1 \times 10^7$ s^{-1}. Extrapolating to lower temperatures, one finds that at room temperature the complete transition should take about 6000 years, at 55 °C about 100 years.

[10]The effect of sample size can be seen, for instance, in the different peak widths of the β-MnO_2 to Mn_2O_3 transition for samples P (4.3 mg) and sample P preheated at 160 °C (8.1 mg), shown in figure 4.2.

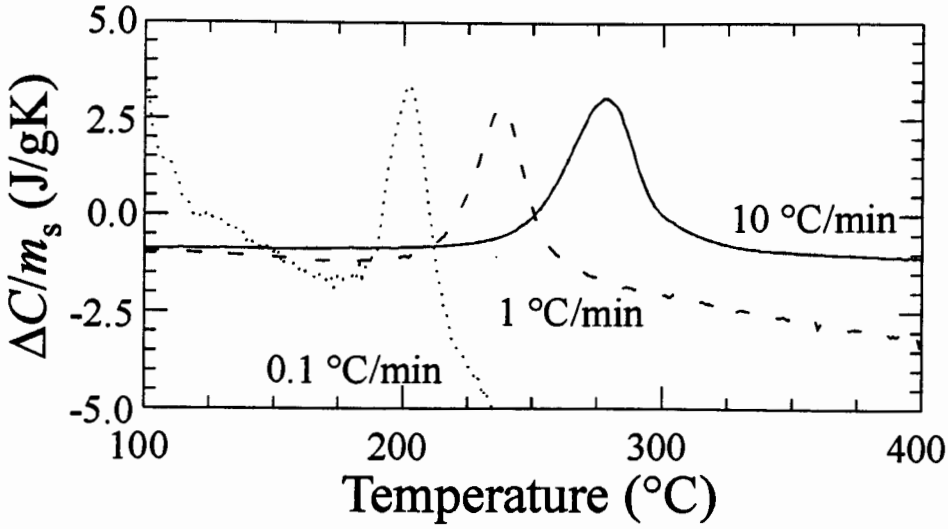

Figure 4.8: Kinetic investigation of the λ-MnO_2 to β-MnO_2 transition. The exothermic peak shifts to lower temperatures as the heating rate decreases.

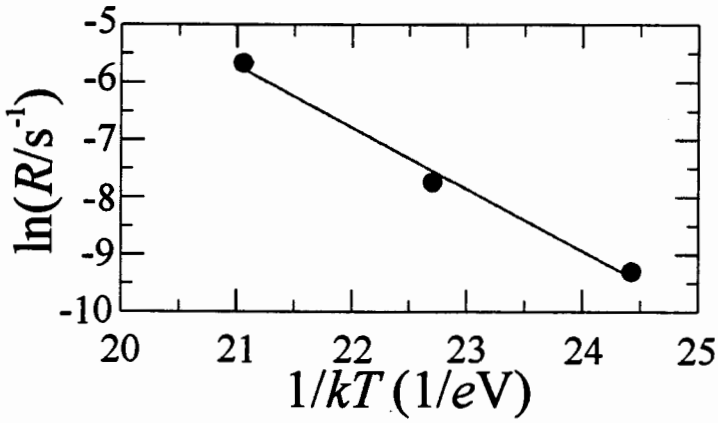

Figure 4.9: Arrhenius plot of the kinetics of λ-MnO_2 to β-MnO_2 transition based on the time that the transitions took at various heating rates and the temperatures of the transitions. The resultant activation energy is $E_a \approx 1.07$ eV and the attempt frequency is $\nu \approx 2.1 \times 10^7$ s^{-1}.

4.4 Electrochemical Data of Spinels

4.4.1 Cycling of $Li[Li_xMn_{2-x}]O_4$ Electrodes

Cells for electrochemical testing of the spinels were prepared and assembled as described in appendix A.2. These cells were then cycled (*i.e.* repeatedly charged and discharged) galvanostatically, typically at a specific current of 29.6 mA/g[11] and, in order to accelerate the fading, at elevated temperature (55 °C). Figure 4.10 shows the derivatives of the specific capacity with respect to voltage as a function of voltage for the three precursor materials $Li[Li_xMn_{2-x}]O_4$ with $x = 0.0$, 0.1 (0.06), and 0.2 (0.16), *i.e.* samples 00a, 10a, and 20a. Peaks of these curves correspond to plateaus in voltage vs. time curves.

The stoichiometric spinel shows well-defined peaks, separated by about 0.1 V, which corresponds to the well-known splitting of the 4-volt plateau. These two peaks merge as the amount of excess lithium is increased. A model for this merging was proposed by Gao and co-workers [98]. Important to notice is the decrease in the peak heights (corresponding to decreased plateau length) for the stoichiometric spinel as the material is being cycled. To a slightly lesser degree this holds true for the $x = 0.1$ (0.06) sample as well. On the other hand, the $x = 0.2$ (0.16) sample shows no fading.

After 20 cycles the cell of the $x = 0.0$ sample was opened on charge and X-ray diffraction data was taken of the working electrode. From figure 4.11, which shows the X-ray diffraction patterns of (a) a fresh electrode and (b) the electrode after 20 cycles on charge, one must conclude that the active material has fallen apart. However, this charged electrode still contains a significant amount of lithium, probably in form of a lithium-manganese-oxide, as demonstrated in panel (c), which shows the electrode after heat-treatment at 600 °C in air. Comparing the strongest peaks of the $LiMn_2O_4$- and the Mn_2O_3-phases, one can estimate a mixing ratio of approximately 0.4:0.6. On the other hand, the $x = 0.2$ (0.16) sample shows nice crystallinity after 20 cycles on charge (figure 4.12).

Gao and Dahn showed [92] that a discharge peak in the derivative curves at

[11]This corresponds to a 5 hour charge rate for the 148 mAh/g theoretical capacity of stoichiometric spinel.

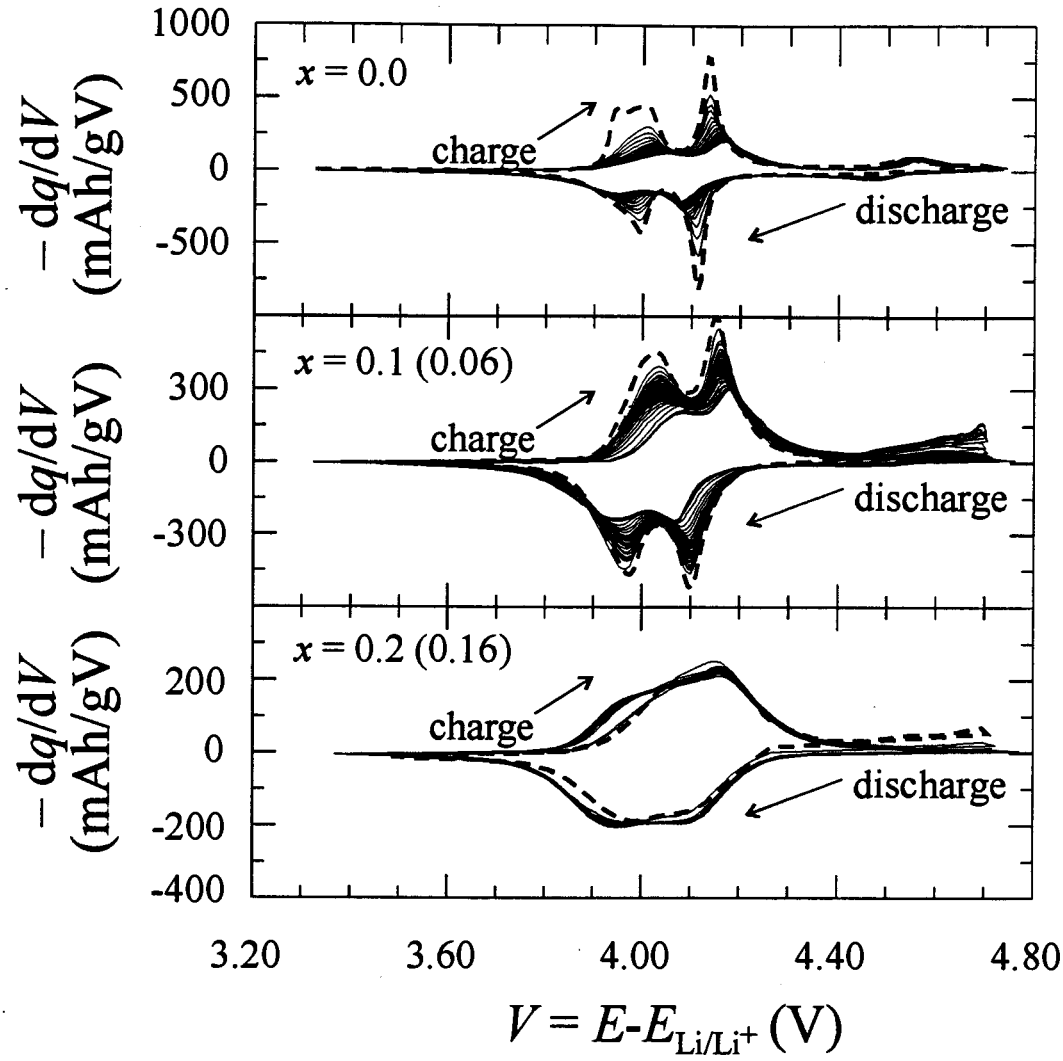

Figure 4.10: Differential capacity of samples 00a, 10a, and 20a cycled between 3.5 V and 4.7 V at 29.6 mA/g and 55 °C. The dashed line shows the first charge/discharge cycle. Subsequent cycles are drawn in a finer, solid line. One sees that the area under the curves decreases for the $x = 0.0$ and $x = 0.1(0.06)$ samples, indicating a decrease in capacity upon cycling. The $x = 0.2(0.16)$ sample does not show such a capacity fade.

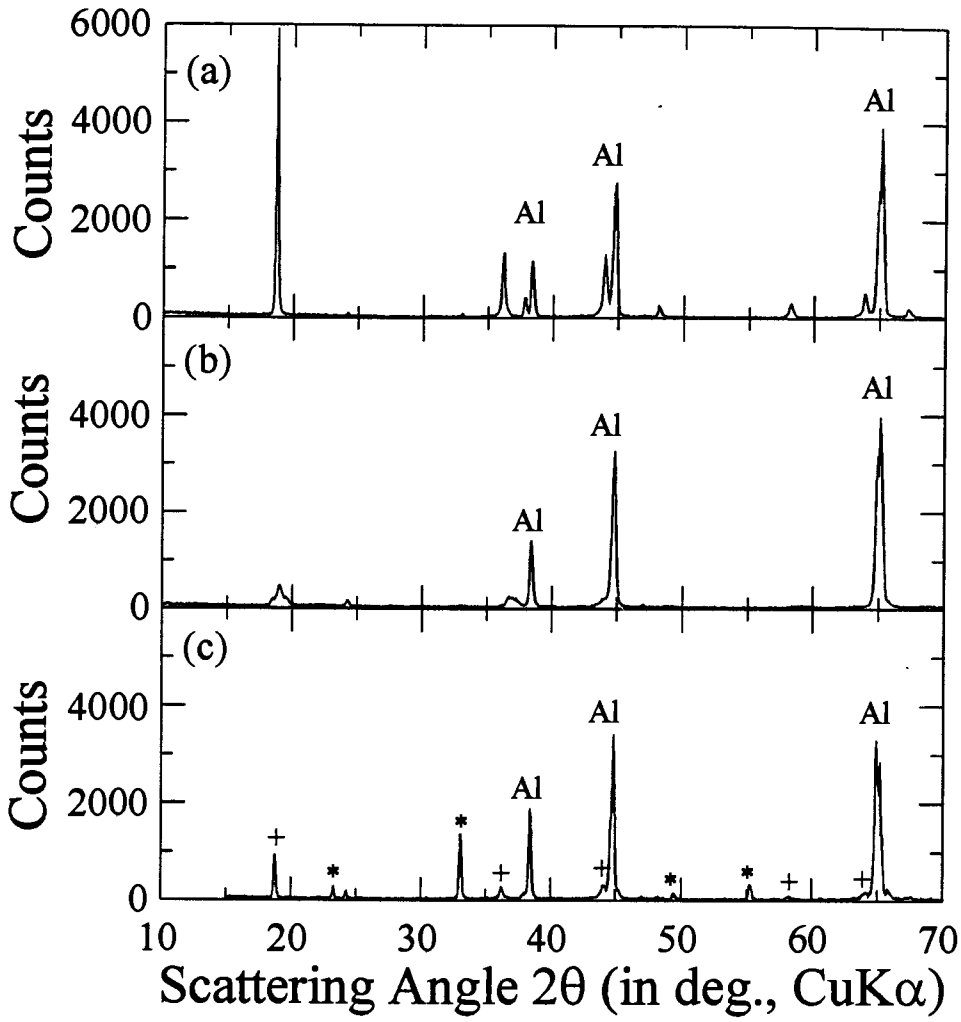

Figure 4.11: Powder X-ray diffraction patterns of (a) a fresh $Li[Li_xMn_{2-x}]O_4$ ($x = 0.0$) electrode and (b) a charged $Li[Li_xMn_{2-x}]O_4$ ($x = 0.0$) electrode after 20 cycles between 3.5 V and 4.7 V at 29.6 mA/g and 55 °C. One sees that the spinel structure decayed, but no β-MnO2 peaks appeared. Panel (c) shows electrode (b) heat-treated at 600 °C; one observes a lithium-containing spinel phase (+) in addition to the Mn_2O_3-peaks (*). The peaks from the aluminum substrate set a reference scale for the peak intensities.

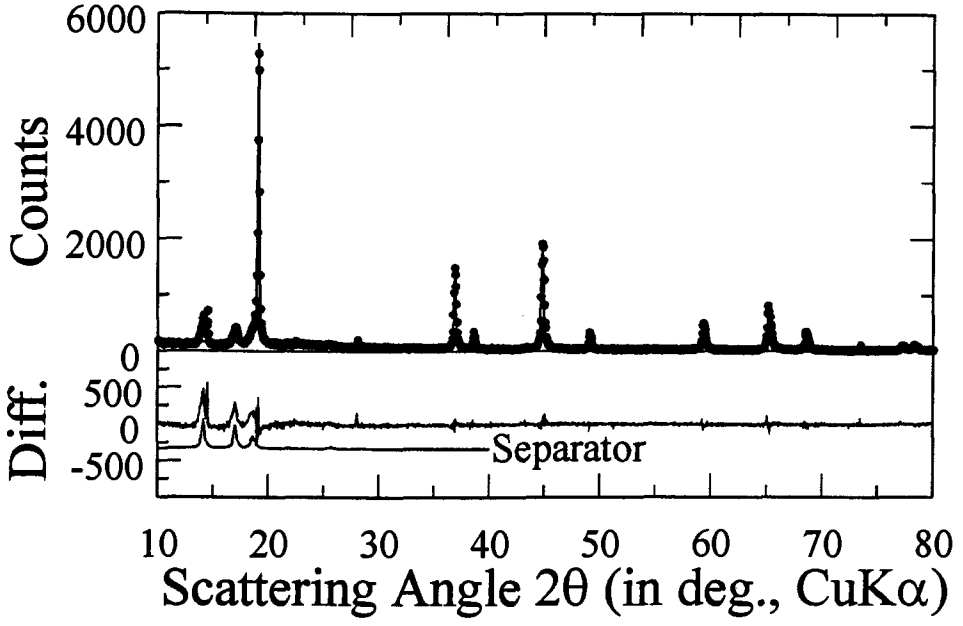

Figure 4.12: Powder X-ray diffraction pattern of a charged $Li[Li_xMn_{2-x}]O_4$ (x = 0.2) electrode showing high crystallinity after 20 cycles between 3.5 V and 4.7 V at 29.6 mA/g and 55 °C. When disassembling the cell the electrode was stuck to the separator.

about 3.3 V is indicative of a material that is susceptible to capacity fade. I therefore decreased the lower cut-off voltage of cells with $x = 0.0$ and $x = 0.2$ (0.16) after cycling twenty times between 3.5 V and 4.7 V. Figure 4.13 shows the last cycles between 3.5 V and 4.7 V, as well as the first few cycles after the lower voltage limit was changed to 3.0 V.

Whereas the $x = 0.2$ (0.16) material continues to cycle apparently unaffected by the change in voltage cut-off, the $x = 0.0$ material shows a very strong peak on first discharge at 3.25 V. Even more noteworthy is the fact that, on subsequent charge, the 4.0 V and 4.1 V peaks are increased. This indicated that after 20 cycles part of the lost capacity can be re-covered. This would not have been possible, if the decrease in capacity had been entirely due to the electrical disconnection of the active material.

Gao and Dahn did not observe this phenomenon because they used a cut-off voltage of 3.0 V starting with the first discharge cycle. Also, their 3.3 V peak never appeared as prominent, which is understandable considering that the 3.3 V peaks

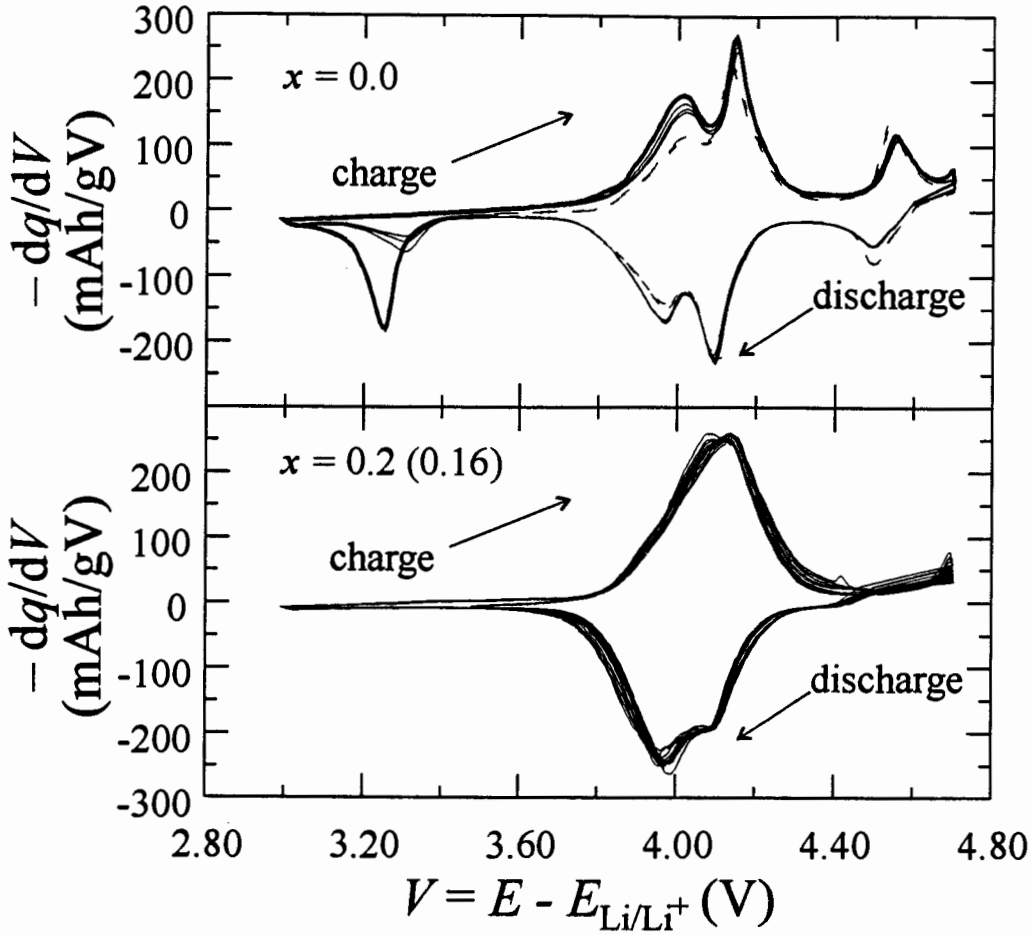

Figure 4.13: Differential capacity of $Li[Li_xMn_{2-x}]O_4$ with $x = 0.0$, and 0.2 (0.16), cycled between 3.5 V and 4.7 V for twenty cycles, then between 3.0 V and 4.7 V, at 29.6 mA/g and 55 °C. In order to distinguish cycles before and after the change of the cut-off voltage for the $x = 0.0$ sample, the last few cycles before the voltage limit was decreased are shown with dashed thin lines, the first cycle with new cut-off is shown with a heavy solid line, and subsequent cycles are shown with thin solid lines.

observed on continued cycling down to 3.0 V decreased in my investigation as well. The observed behaviour suggests that repeated cycling can build up a latent capacity at 3.3 V. Finally, it is not clear whether or not the shift of the first discharge peak from 3.3 V to 3.25 V bears any significance.

4.4.2 Cycling of Acid-Treated Samples

Since powder X-ray diffraction could not give a definite answer, the question of stoichiometry of the acid-treated samples needs to be addressed electrochemically. Figure 4.14 shows the derivative curves of cycling samples 00f and 20e. In both cases the first or the first few cycles do not show the same features as the subsequent ones. This suggests that the acid-treatment did not merely de-lithiate the samples as would have happened in an electrochemical cell. Since the powder X-ray diffraction patterns show sharp Bragg peaks, the spinel framework remained unaltered. The acid treatment may have left vacancies on any of the crystallographic sites and/or introduced hydrogen so as to change the local environment of the lithium insertion site. Alternatively or additionally, the surface of the particle may have been altered, maybe due to moisture, so as to impede the lithium insertion/extraction mechanism.

Whatever the cause of different initial derivative curves, the differences are eventually removed on further cycling. In particular, the 3.3 V peak associated with fading was not observed for the 20e sample when the discharge voltage was lowered to 3.0 V. The shape of the final derivative curve is intermediate to those of spinels with an excess-lithium value of $x = 0.1(0.06)$ and 0.2 (0.16). They can be compared to derivative curves given in reference [98] so that one can conclude that the active electrode material can be assigned an excess-lithium content of $x = 0.15$ (0.11) — the acid treatment must have affected the occupation of the (16d) sites.

4.4.3 Cycling between 4.05 and 4.3 V

I have demonstrated that electrical disconnection of the active material is not the entire reason for the capacity fade. In this section, I want to investigate to what extent it does play a role. For that purpose, I cycled sample 00a ($x = 0.0$), after

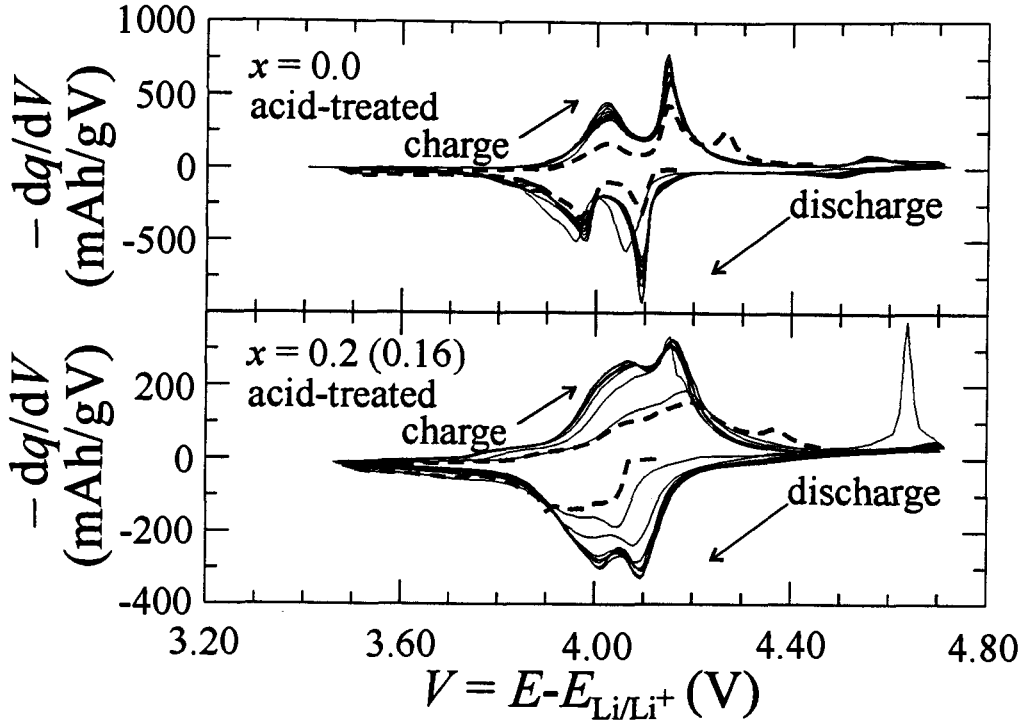

Figure 4.14: Differential capacity of de-lithiated $Li[Li_xMn_{2-x}]O_4$ with $x = 0.0$, and 0.2, cycled between 3.5 V and 4.7 V at 29.6 mA/g and 55 °C. After an initial cycle (dashed line), the $x = 0$ sample shows cycling behaviour similar to its precursor, including the capacity fade. On the other hand, the $x = 0.2$ (0.16) sample finally cycles similar to a hypothetical $x = 0.15$ (0.11) precursor, suggesting that the acid treatment did affect lithium on (16d) sites. It is not clear, whether or not the difference between the initial open circuit voltages of the two cells (4.162 V *vs.* 4.125 V) is related to the different pH of the acid-treatment (1.3 *vs.* 2.2).

charging to 4.3 V, between 4.05 V (the trough between the two peak in the derivative curve) and 4.3 V. The derivative curve of this cycling is shown in figure 4.15, where it is compared to the cycling of the acid-treated sample, 00f.

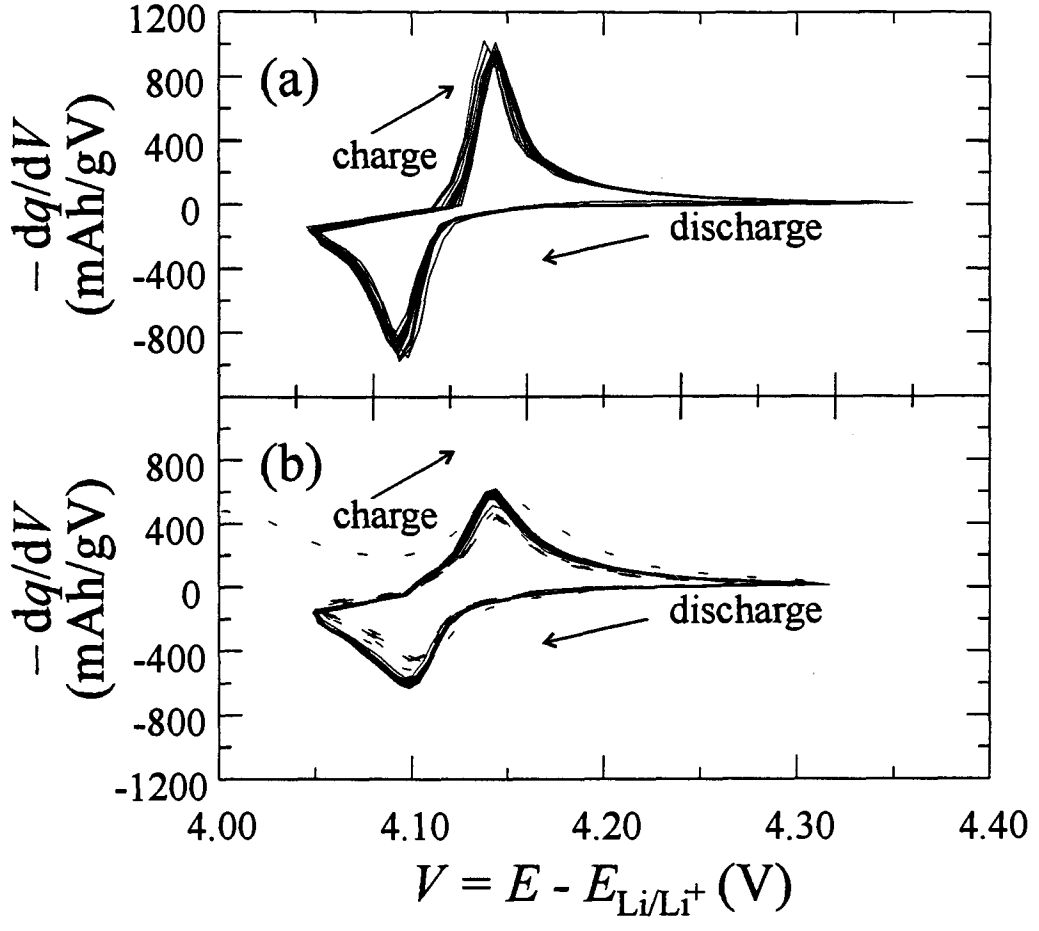

Figure 4.15: (a) Differential capacity of sample 00f, an acid-treated $Li[Li_xMn_{2-x}]O_4$ with $x = 0.0$. It was cycled between 4.05 V and 4.3 V at 29.6 mA/g and 55 °C. The initial charge to 4.3 V is not visible as the initial, room-temperature open-circuit voltage was 4.17 V. The voltage shift between charge and discharge peaks is likely related to the IR-drop associated with the internal resistance of the cell.
(b) Differential capacity of sample 00a, $Li[Li_xMn_{2-x}]O_4$ with $x = 0.0$. Here, the first charge to 4.3 V from the initial, room-temperature open-circuit voltage of 3.50 V is visible. Subsequent cycling between 4.05 V and 4.3 V was carried out at a smaller specific current of 14.8 mA/g, but also at 55 °C. The dashed lines represent cycles 1 to 10, the solid line represents cycles 10 to 40. It is not clear, why the cell gained capacity at cycle 10, but important in this context is that it did not lose any.

The acid-treated sample shows very stable cycling between 4.05 V and 4.3 V, although the capacity of about 37 mAh/g is very low. One would have expected about half the total capacity of stoichiometric spinel for the upper level of the split 4 V-plateau instead of just a quarter. This stable cycling is very different from the cycling of the acid-treated sample over the voltage range from 3.5 V to 4.7 V, shown in figure 4.14, where the capacity in the 4.05–4.3 V range first grew, but then steadily decreased.

For sample 00a, the stoichiometric spinel, one observes a similar result. When cycled of the full voltage range from 3.5 V to 4.7 V, the overall capacity decreased, but the capacity also decreased continuously in the 4.05–4.3 V range. However, when cycling is limited to this range, the capacity does not decrease. Why, in fact, it increases from about 18% to 23% of the theoretical capacity of stoichiometric spinel over the range of a two or three cycles is not clear, but important is that before and after this jump a stable capacity is observed.

This investigation demonstrates that stoichiometric spinel can be cycled over the voltage range of the two-phase region without capacity loss. Although the capacity is surprisingly low, repeated cycling that would lead to fractures of the crystallites of the active material should have lowered it even more. The presence of the two-phase region does not contribute to the capacity fade, at least not substantially.

4.5 Remarks on the Origin of Capacity Fade

In section 4.2, I discussed various points that could be possible reasons for the capacity fade of the stoichiometric spinel electrode. So far, I found that points 3 and 5 describe processes that are of little relevance to the capacity fade of stoichiometric spinels. As discussed, these may contribute to the capacity fade, but at a different time scale as the, now, dominant processes. Point 4 was already characterized as unlikely.

Point 1, proposed by Gao and Dahn [92], involves oxygen loss of the spinel due to electrolyte oxidation with a subsequent restructuring of the surface region of the crystallites. It is suggested that this restructuring may lead to an electrochemically inactive rocksalt structure, similar to Li_2MnO_3. As pointed out in section 4.2, it is

not clear why oxygen loss should occur for stoichiometric spinels, but not for spinels with excess lithium, unless the surfaces of these compound are of different reactivity, as suggested by point 2. Also, point 1 on its own does not explain the appearance of the 3.3 V peak.

If the surfaces of stoichiometric and excess-lithium spinels do indeed show different reactivity towards the electrolyte, one can still invoke the oxygen loss reaction proposed in [92]. However, it may not be the oxygen loss *per se* that is responsible for the capacity loss. I suggest that the oxygen loss leaves manganese atoms in a lower oxidation state making them more likely to dissolve in the electrolyte, either directly, if Mn(II) is formed, or via a disproportionation reaction, 2 Mn(III) become Mn(II) and Mn(IV). This loss of manganese implies that on subsequent discharge fewer lithium atoms can be inserted in the electrode

The presence of manganese in the electrolyte after cycling is well known. For instance, Yoshio and Xia [99] showed that substantial amounts of manganese can be found in the electrolyte after cycling between 3.5 V and 4.5 V at 50 °C (about 7 mg/ml), whereas spinels stored in electrolyte at 50 °C led to only 0.3 mg/ml. This suggests that either the high voltage during cycling aids in the dissolution of manganese (due to oxygen loss) or the current flowing into the spinel leads to the extraction of manganese atoms. The charged electrode would then contain, in part, a lithium-containing manganese(IV)-oxide, consistent with figure 4.11. One would have to investigate this further by storing charged spinel electrodes in electrolyte at elevated temperature and measuring the dissolved manganese.

Finally, I would like to speculate about origin of the 3.3 V peak. With manganese ions present in the electrolyte in addition to lithium ions, it is likely that manganese atoms can be inserted into the spinel as well. This insertion can not take place into the tetrahedral (8a) sites because these should already be filled with lithium atoms when the discharge voltage drops down to 3.3 V *vs.* Li/Li^+. However, the initial dissolution of manganese atoms from the spinel may have left (16d) sites vacant, into which manganese from the electrolyte can be re-inserted. Having manganese back on (16d) allows more lithium to be removed on subsequent charge, as was observed. Of course, this hypothesis needs further investigation.

Before concluding this chapter, I should point out that the cyclability of the stoichiometric spinel investigated here, sample 00a, is worse than typical. This may be related to the high temperature of the first heating step. Even subsequent soaking in air at 600 °C for 18 hours can apparently not cure the damages (likely lost oxygen) incurred at 900 °C. It is therefore essential to heat spinels always below the onset temperature of the oxygen loss (about 825 °C for stoichiometric spinels) in order to obtain best cycling performance. However, for a scientific investigation, it may not have been bad to prepare a particularly poor sample, a method that Amatucci and co-workers purposely chose [100] by substituting fluorine for oxygen in spinels.

Chapter 5

Conclusion

If this thesis had attempted to undertake a comprehensive study of manganese dioxides as battery materials for two different electrochemical systems, it would never have seen its completion. A comprehensive investigation of each system alone would probably amount to more than one person's life-time research. Nonetheless, this thesis shows how diverse research in an application-oriented field is (or at least can be). I believe that an understanding of, if not proficiency in, in very different areas is important to find new solutions to (possibly old) problems.

Led by this credo, this thesis gives an account of my research performed on very different aspects of the same problem: how can manganese dioxides as battery materials be improved? This pursuit involves not so much the development of new scientific tools (they are usually available in the literature), but the application of these tools to the problem, which then governs the choice of tools to be used. Due to the diversity of the problem, these tools necessarily come from very different areas of science, such as crystallography, diffraction theory, preparative and analytical chemistry, electrochemistry, and certainly common sense (common scientific sense that is).

Consequently, this thesis investigated many aspects of manganese dioxides in alkaline and lithium-ion cells, but could not see these aspects to their completion. It is for this reason that this thesis may read like a story of "what I did not do". However, the fact that I suggest further research in many sections of this thesis only indicates

how important it is to look at the various aspects. It is then this thesis that sets the basis for that further research.

While chapter 1 motivated the necessity for the research presented in chapters 3 and 4, it was chapter 2 that developed the necessary tools for the structural analysis, in particular of the disordered powders investigated in chapter 3. Starting with elementary scattering of X-rays by electrons, an expression for the intensity scattered by a stack of layers with faults was derived. By applying strain and random faults to the intra-layer structure and the approximation of the tangent cylinder to the powder averaging process, the intensity, as it would be measured on a powder diffractometer, could be evaluated with only one numerical integration. Chapter 2 gives an example of the scenario where tools are available in the literature, and the objective lies in combining the appropriate ones.

The application of the results of chapter 2 was the main focus of the structural investigation presented in chapter 3, which applied the model of the ramsdellite/pyrolusite intergrowth to measured powder X-ray diffraction patterns of a chemically and an electrolytically prepared manganese dioxide. The intergrowth was described as a stochastic, parallel stacking of four distinct layers that possess two-dimensional periodicities perpendicular to the stacking direction. To characterize the intergrowth, an order parameter, p, was defined, which was 0 for the pure ramsdellite case and 1 for pure pyrolusite. These limiting structures could be fit reasonably well.

Fits to the chemically prepared manganese dioxide and its heat-treated derivatives revealed that p increased during heating and the structure converted almost, but not quite, to pure pyrolusite, as p remained slightly less than one. On the other hand, the structure of electrolytically prepared manganese dioxide was not well described by the ramsdellite/pyrolusite intergrowth, although heat-treated derivatives could be fit by this model, if the temperature of the heat-treatment was sufficiently high (above 300 °C or so).

In further efforts to describe the structure of electrolytically prepared manganese dioxides, I suggested that there may be water-containing galleries between some of the oxygen layers. Investigation with a transmission electron microscope, or re-investigation of such data, may give confirmation to this hypothesis. Powder X-ray

diffraction could only hint at the existence of such galleries by showing some broad diffraction peaks. The possibility of an intergrowth with an α-MnO_2-type structure was ruled out as unlikely, since a phase separation was observed for some samples.

A brief discussion of the microtwinning model for manganese dioxide led to an extension of the same that included both microtwinning and ramsdellite/pyrolusite intergrowth, although the model of the latter was slightly altered from its previous description. Detailed calculations and fits need to follow here. To obtain a more general structure calculation based on a fixed oxygen lattice with manganese atoms occupying half of the available octahedral sites, I proposed the use of the Debye formula in connection with the histogram method. Such a calculation would then form the basis for fits utilizing a modified Reverse-Monte-Carlo algorithm.

Thermogravimetric analysis confirmed the large water content of manganese dioxides, in particular the electrolytically prepared ones, whereas differential scanning calorimetry showed that the increase in order parameter, p, is not associated with a large release of energy. I also found that there seem to be two types of transitions from the dioxide to the sesquioxides as some materials show doublets for the associated endothermic transition peaks.

Powder X-ray diffraction of an electrolytic manganese dioxide discharged in a 9 molar potassium hydroxide solution revealed that structural changes occured due to the co-insertion of potassium, which was even more pronounced for a chemically prepared manganese dioxide. However, the same chemically prepared manganese dioxide did not show any indication of potassium co-insertion in a 1 molar potassium hydroxide solution. In fact, the structure, after discharge to the hydrogen-evolution potential, could be fit by a groutite/manganite intergrowth with a groutite-to-manganite ratio similar to the ramsdellite-to-pyrolusite ratio of the initial material.

In chapter 4, the focus shifted away from manganese dioxides for alkaline cells towards the spinel-type manganese dioxide for lithium-ion cells. Here, I shed light on some aspects of the capacity fade that is experienced with this material during repeated charging and discharging. In particular, I revisited the question of whether or not the thermodynamic metastability of the de-lithiated spinel may be responsible for the fade. I found that this was not the case, as the transition to the more stable

pyrolusite would take a hundred years or more at practical operating temperatures.

It turned out, however, that the transition from the spinel manganese dioxide with its cubic close packed oxygen lattice to pyrolusite proceeded in two steps: (1) conversion of the cubic close packing of oxygen to hexagonal close packing, (2) ordering of the manganese atoms. These two steps overlapped somewhat, but the first was completed when manganese atoms in part of the material were still in disordered position. From differential scanning calorimetry data, I found that most of the heat released during the spinel-to-pyrolusite transition was associated with the conversion of the cubic close packed oxygen sublattice to a hexagonal close packed sublattice.

Analysis of electrochemical data of spinel cathodes suggested that the main contributor to the fade was most likely the dissolution of manganese atoms into the electrolyte. This dissolution may have occurred at high potentials when the possibility of a spinel-electrolyte reaction could lead to oxygen loss from the electrode, or during charge as manganese is extracted from the structure instead of lithium. More investigation will be necessary here, in particular one that addresses the question of why excess-lithium spinels behave differently from stoichiometric spinels.

In chapter 1, I started my thesis by pointing out that batteries and battery materials are topics that could be categorized under the heading "energy management", a subject that becomes more and more pressing, as traditional resources of energy (mainly fossil fuels) are running out and environmental concerns are increasing. My hope is, that this thesis may become a small gear in the large clockwork that is ticking to avoid the foreseeable energy crises.

Appendix A

Experimental Details

A.1 Glass Cell and Hg/HgO Electrode

A glass cell is a primitive realization of either the two-electrode or three-electrode design shown in figures 1.1 and 1.2. Such cells are of limited use for systems with non-aqueous electrolytes because the electrode materials change as they are charged or discharged so that the material may become unstable in the presence of air or moisture. Since these contaminants would most certainly be absorbed from the surrounding lab air, unless the whole cell was kept in a controlled atmosphere, the cell would not measure the true electrochemical properties of the electrodes of interest, but of the moisture- or air-modified electrode. On the other hand, when investigating the electrochemical behaviour of aqueous systems, a glass cell is a simple, but adequate, tool to perform the measurements.

The reference electrode can be chosen from a wide variety of chemistries, a common one being the so-called calomel electrode, which utilizes the (pH-independent) Hg/HgCl equilibrium. Unfortunately, the calomel electrode is not stable in strong alkaline solution; it converts to a Hg/HgO system so that it is most sensible to start with this chemistry.

On the left in figure A.1 a complete Hg/HgO electrode is depicted. The main electrode chamber contains the electrolyte solution, for instance 1 M KOH and is connected to the electrolyte of the glass cell through a glass frit. The actual electrode

part is shown enlarged on the right hand side. It is prepared by fusing a piece of platinum wire into the closed end of a short glass tube. Through the open end, one introduces a few drops of mercury metal and then adds a mixture of mercury, red mercury oxide and some 1 molar KOH solution. A little bit of glass wool keeps the solid particles in place and allows for the free exchange of electrolyte solution.

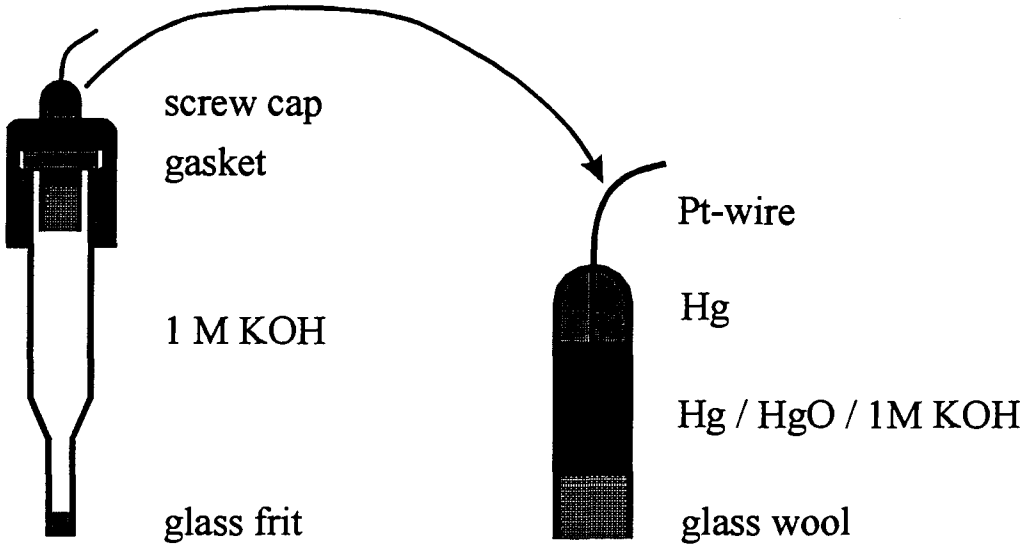

Figure A.1: An Hg/HgO Electrode.

For the alkaline manganese dioxides investigated in this thesis, I used pieces of stainless steel as counter electrodes and as current collectors of the working electrodes. During the discharge of the working electrode the counter electrode supplies electrons that come from the dissociation of water according to

$$6\ H_2O \longrightarrow\ O_2 + 4\ H_3O^+ + 4\ e^-. \qquad \text{(A.1)}$$

In a 1 M KOH solution, this dissociation occurs at a potential of +0.4 V and would almost make a good reference on its own as long as the direction of the current is not switched. Should the current direction change, as when re-charging the working electrode, the reaction at the stainless steel counter electrode changes so as to produce hydrogen gas at a potential that is 1.23 V lower, if all is in equilibrium.

The working electrode was typically prepared by mixing the active material (90%

by weight) with carbon black (Super S; Chemetals Inc., Baltimore, MD, USA; 5% by weight) to enhance the electronic conductivity of the electrode material and some rubber binder (EPDM — ethylene propylene diene monomer; 5% by weight) to prevent mechanical disintegration during handling. After most of the binder solvent (cyclohexane) had evaporated, the mixture was pressed into small pellets of about 100 mg in weight and about 8 mm in diameter.

The pellets were then immersed in electrolyte solution that was kept under partial vacuum so as to replace air trapped inside the pellets with electrolyte. This vacuum treatment also allowed the de-aeration of the electrolyte, which limits the possibility of re-oxidation of the discharged working electrode by oxygen. However, no precautions were taken to avoid re-dissolution of air in the electrolyte afterwards.

With the help of a plastic frame, the wet pellets were mounted between two pieces of stainless steel mesh. One of the mesh pieces was spot welded to a strip of stainless steel foil that acted as the current lead.

A.2 Coin Cell Design

Working electrodes for non-aqueous lithium cells were prepared by mixing the active materials with carbon black (Super S, Chemetals, Baltimore, MD, USA) and a binder in weight fractions of typically 90%, 5%, and 5%. The binder was EPDM (ethylene propylene diene monomer), initially dissolved in cyclohexane, which evaporated at room temperature — ideal for the investigation of thermally unstable compounds.

The mixture was then spread onto aluminum foil as I am investigating materials whose voltage *vs.* Li/Li^+ is more than 3 V so that alloying of lithium with aluminum is not favoured over the lithium insertion into the working electrode. Typically, the coating led a coverage of 5–15 mg/cm^2. From these coated foils, disk shape electrodes of 1/2-inch diameter were cut.

The assembly of the complete electrochemical cell, which used 2320 coin-type casing (23 mm diameter and 2.0 mm height), was performed inside an argon-filled glove box. An exploded view of such a cell is shown in figure A.2. The working electrode was placed into the bottom of the casing and electrolyte was added until the

electrode appeared sufficiently wet. In order to keep the working electrode electrically insulated from the counter electrode, a microporous polypropylene separator was utilized, either two pieces of Celgard 2500 or one piece of Celgard 2502 (Hoechst Celanese) leading to a total thickness of 50 μm in both cases. In some instances, extra electrolyte was added at this stage so that the separator was wet as well. Since I used 1 molar solution of $LiBF_4$ in a mixture of ethylene carbonate/diethyl carbonate (30:70), the wetting of working electrode and separator occurred readily under atmospheric pressure.

Since the coin cell has only two contacts, all measurements have to be performed in the two-electrode design. For electrochemical testing, one therefore prefers to choose as counter electrode a material that can act as a proper reference at the same time. Lithium metal is the obvious choice and was used in form of 5/8-inch diameter disks of 125 μm thickness. Although changes in the morphology of the lithium as counter electrode due to dendrite formation or reaction with the electrolyte, for instance, will not change the potential of the lithium as reference electrode, the internal resistance of the cell may be affected leading to possible changes of the IR-drop in the cell.

The empty space inside the coin cell was filled with a stainless steel spacer and a disk spring, which also maintained a stack pressure on the working electrode so that the electrical contact to the metal foil current collector remained good. The casing top, electrically insulated from the bottom by a polypropylene gasket, was then mechanically crimped to the bottom. The gasket also acted a seal that prevented electrolyte from evaporating and air from entering.

A.3 Differential Scanning Calorimeter

Much of this section is based on a review in reference [101], which should also be consulted for further details and more background information. I only excerpted those parts that are crucial for the understanding of the operation of a differential scanning calorimeter.

With a differential scanning calorimeter, one is interested in measuring calorimetric data of a substance (*i.e.* its enthalpy or its heat capacity) with respect to

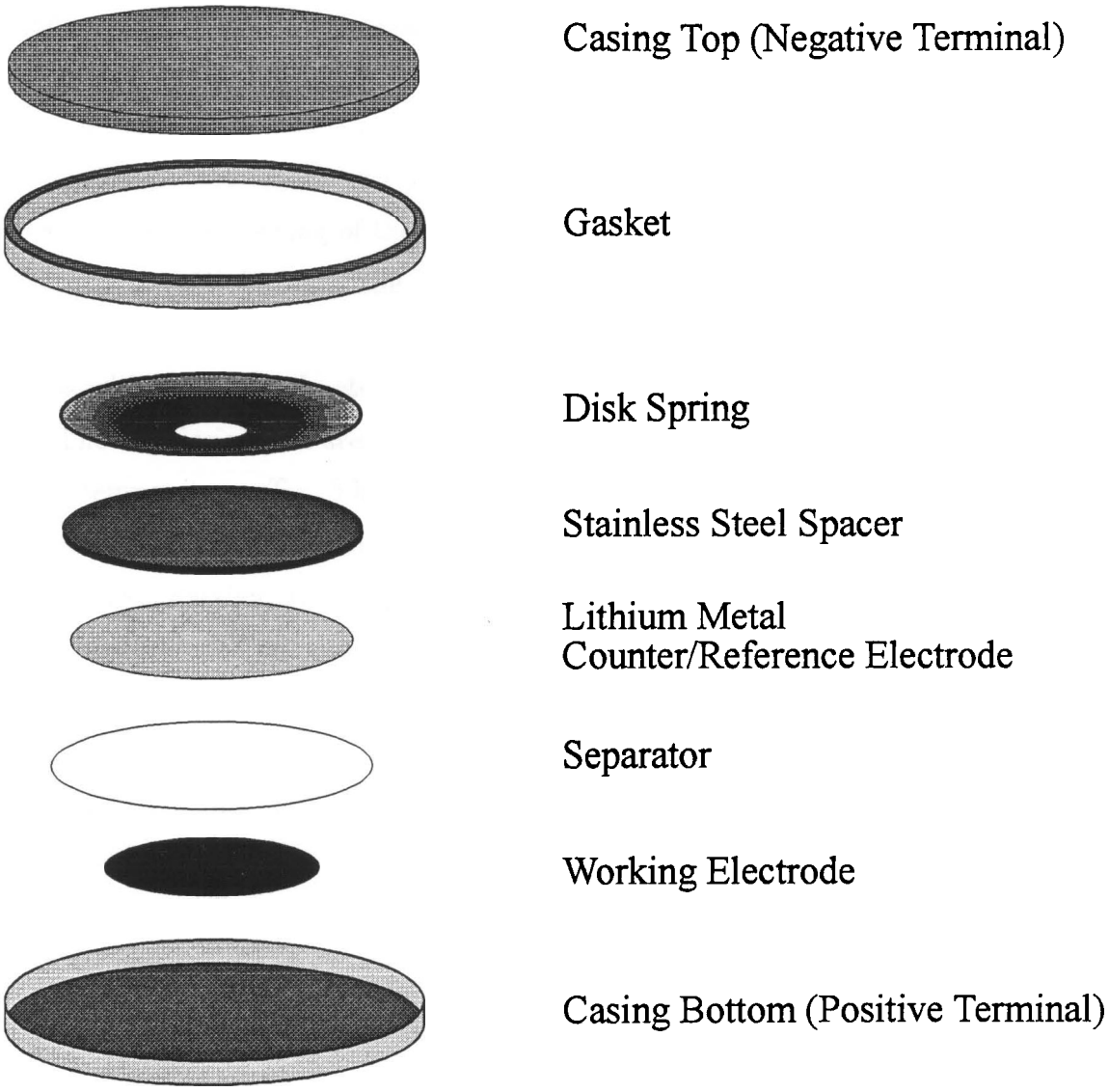

Figure A.2: Exploded View of a Coin Cell.

a reference, while the temperature is continuously ramped at a rate of $\mathrm{d}T/\mathrm{d}t$. The primarily measured signal is the electromotive force that develops in a differential thermocouple due to a temperature difference between the sample of interest and the reference. The electromotive force can, with proper calibration, be converted into a temperature difference, ΔT_{meas}.

In order to interpret this temperature difference appropriately, one needs to take a closer look at the set-up. Typically, the sample is placed in an aluminum pan of about 6.5 mm diameter and 1.5 mm height, onto which a lid with similar dimensions is crimped. The squeezing of the sample powder between the pan and the lid improves thermal contact between the powder and the pan. As a reference, one utilizes a similar, but empty, pan/lid assembly. These two cans are then placed onto designated areas within the calorimeter.

The two designated areas lie on a thermally well-conducting plate which is heated to a temperature, T_{h}. The particular temperatures of the sample, T_{s}, and of the reference, T_{r}, may be different from T_{h} due to finite thermal resistances and heat capacities. Further, the temperatures of the thermocouple junctions, T_{sm} and T_{rm}, may be different from each other and from T_{h} as well. Figure A.3 shows the relevant quantities. Note that the thermal resistances, R and R', are symmetric for the sample and the reference because of the assumed identical construction.

There are two fundamental thermal relations that one needs to exploit. On the one hand the change in heat of a material is equal to its heat capacity times the change in temperature, or

$$\frac{\mathrm{d}q_{\mathrm{s}}}{\mathrm{d}t} = C_{\mathrm{s}} \frac{\mathrm{d}T_{\mathrm{s}}}{\mathrm{d}t}, \tag{A.2}$$

and similar for the reference pan. On the other hand a temperature gradient leads to transport of heat

$$\frac{\mathrm{d}q_{\mathrm{s}}}{\mathrm{d}t} = \frac{1}{R}\left(T_{\mathrm{h}} - T_{\mathrm{sm}}\right), \tag{A.3}$$

and, again, similar for the reference side. Here it is assumed that the rates at which heat flows into the sample and reference thermocouples are identical so that these terms cancel when evaluating the difference between T_{rm} and T_{sm}.

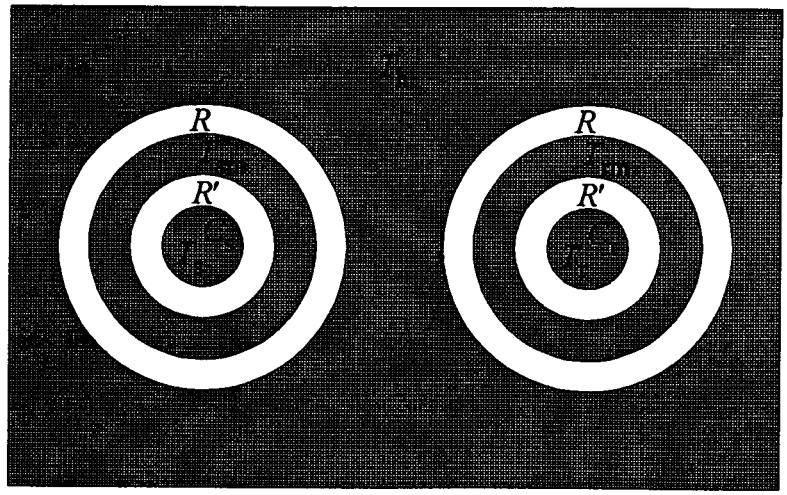

Figure A.3: The two areas for sample and reference in a differential scanning calorimeter, characterized by the respective heat capacities, C_s and C_r. The thermal resistance between the heating block of temperature T_h and the two thermocouple junction of temperatures T_{sm} and T_{rm} are assumed to be identical and equal to R. Also the thermal resistance between these two junctions and the two pans of temperature T_s and T_r are assumed to identical and equal to R'.

The signal, $\Delta T_{meas} = T_{rm} - T_{sm}$, is the then given by

$$\Delta T_{meas} = R\frac{dT}{dt}\Delta C \tag{A.4}$$

and is directly proportional to the difference ΔC of the heat capacities of the sample and the reference, $\Delta C = C_s - C_r$. The thermal resistance, R, does not depend on the exact placement of the thermocouples with respect to the sample, as long as the assumption of symmetry between the reference and sample sides is justified. The constant R is easily calibrated, for instance, with the known heat of melting of indium metal.

The signal recorded by the calorimeter is $\Delta T_{meas}/R$, which has units of power. The data that I present in my thesis are corrected for the heating rate and for the sample size (mass, m_s), so that I will show $\Delta C/m_s$ in units of J/gK. The heat capacities of the reference as well as of the sample container are assumed to vary smoothly. If the sample undergoes an endothermic or exothermic reaction or phase transition, then it takes up or releases heat at constant temperature. This will show up as a peak in the heat capacity of the sample and, since C_r does not vary strongly, as a peak in

$\Delta C/m_s$. Positive peaks correspond to a release of heat by the sample (exotherm), negative peaks correspond to heat uptakes (endotherm).

Bibliography

[1] Carl Friedrich von Weizsäcker. *Aufbau der Physik.* Deutscher Taschenbuch Verlag, München, 1988.

[2] David Linden (ed.). *Handbook of Batteries — 2nd edition.* McGraw-Hill, Inc., New York, 1995.

[3] Hans-Rudolf Christen. *Grundlagen der allgemeinen und anorganische Chemie. 6. Auflage.* Salle + Sauerländer, Frankfurt am Main und Aarau, 1980.

[4] Y. Chabre and J. Pannetier. Structural and electrochemical properties of the proton/γ-MnO_2 system. *Progress in Solid State Chemistry*, 23:1–135, 1995.

[5] Yuan Gao, K. Myrtle, Meijie Zhang, J.N. Reimers, and J.R. Dahn. Valence band of $LiNi_xMn_{2-x}O_4$ and its effects on the voltage profiles of $LiNi_xMn_{2-x}O_4$/Li electrochemical cells. *Physical Review B*, 54:16670–16675, 1996.

[6] Qiming Zhong, Arman Bonakdarpour, Meijie Zhang, Yuan Gao, and J.R. Dahn. Synthesis and electrochemistry of $LiNi_xMn_{2-x}O_4$. *Journal of the Electrochemical Society*, 144:205–213, 1997.

[7] S.T. Coleman, W.R. McKinnon, and J.R. Dahn. Lithium intercalation in $Li_xMo_6Se_8$: A model mean-field lattice gas. *Physical Review B*, 29:4147–4149, 1984.

[8] Z.Y. Wu, G. Ouvrard, S. Lemauz, P. Moreau, P. Gressier, F. Lemoigno, and J. Rouxel. Sulfur K-edge X-ray absortption study of the charge transferr upon lithium intercalation into titanium disulfide. *Physical Review Letters*, 77:2101–2104, 1996.

[9] Guy Ouvrard and Z. Wu. Importance of sulfur in the charge transfer upon lithium intercalation into titanium dioxides. 190th Meeting of the Electrochemical Society, Inc. Paper No. 852. San Antonio, Texas, 1996.

[10] G.G. Amatucci, J.M. Tarascon, and L.C. Klein. CoO_2, the end member of the Li_xCoO_2 solid solution. *Journal of the Electrochemical Society*, 143:1114–1123, 1996.

[11] D. Glover, B. Schumm, and A. Kozawa (eds.). *Handbook of Manganese Dioxides Battery Grade.* Int'l Battery Material Ass'n (IBA, Inc.), pp. 25–32 without place, 1989.

[12] Michael J. Root (Rayovac Corp.). private communication, 1996.

[13] R. Williams, R. Fredlein, G. Lawrance, D. Swinkels, and C. Ward. Effect of deposition conditions on structural, chemical, physical and electrochemical properties of EMD. *Progress in Battery & Battery Materials*, 13:102–112, 1994.

[14] P.M. de Wolff. Interpretation of some γ-MnO_2 diffraction patterns. *Acta Crystallographica*, 12:341–345, 1959.

[15] James C. Hunter. Preparation of a new crystal form of manganese dioxide: λ-MnO_2. *Journal of Solid State Chemistry*, 29:142–147, 1981.

[16] Monique Richard. The behaviour of lithium and sodium iron oxides as cathode materials for lithium batteries. M.Sc. thesis, Simon Fraser University, Burnaby, B.C., Canada, 1996.

[17] Kenneth Kurani, Daniel Sperling, and Thomas Turrentine. The marketability of electric vehicles: battery performance and consumer demand for driving range. *Annu. Battery Conf. Appl. Adv. 11th, IEEE*, pages 153–158, 1996.

[18] Hidden solids revealed. New York Times. 16 January, 1896.

[19] W.C. Röntgen. Ueber eine neue Art von Strahlen (Erste Mittheilung). *Annalen der Physik und Chemie. Neue Folge. (reprinted from: Sitzungsbericht der Würzburger physikalisch-medicinischen Gesellschaft, Dec. 1895)*, 64:1–11, 1898.

[20] W. Friedrich, P. Knipping, and M. Laue. Interferenzerscheinungen bei Röntgenstrahlen. *Annalen der Physik (reprinted from: K.Bayer.Akad. Münchener Sitzungsberichte 1912, 303)*, 41:971–988, 1913.

[21] J.A. Bearden. X-ray wavelengths. *Review of Modern Physics*, 39:78–124, 1967.

[22] William C. Sauder, James R. Huddle, J. D. Wilson, and Robert E. Lavilla. Detection of multiplet structure in $CuK\alpha_{1,2}$ by means of a monolithic double crystal spectrometer. *Physics Letters*, 63A:313–315, 1977.

[23] Leslie E. Ballentine. *Quantum Mechanics.* Prentice Hall, Englewood Cliffs, New Jersey, 1990.

[24] A. Gibaud, J.S. Xue, and J.R. Dahn. A small-angle X-ray scattering study of carbon made from pyrolyzed sugar. *Carbon*, 34:499–505, 1996.

[25] Ivars Henins and J.A. Bearden. Silicon-crystal determination of the absolute scale of X-ray wavelengths. *Physical Review*, 135:A890–A898, 1964.

[26] John David Jackson. *Classical Electrodynamics.* John Wiley & Sons, Inc., New York, 1975.

[27] James A. Ibers and Walter C. Hamilton (eds.). *International Tables for X-ray Crystallography, Vol. 4.* The Kynoch Press, Birmingham, England, 1974.

[28] Masayasu Tokonami. Atomic scattering factor of O^{2-}. *Acta Crystallographica*, 19:486, 965.

[29] B. E. Warren. *X-ray Diffraction.* Addison-Wesley Publishing Company, Reading, Massachusetts, 1969.

[30] B.D. Cullity. *X-ray Diffraction.* Addison-Wesley Publishing Company, Inc., Reading, Massachusetts, 1967.

[31] J.J. Sakurai and San Fu Tuan (ed.). *Modern Quantum Mechanics.* Addison-Wesley Publishing, Reading, Massachusetts, 1994, rev. ed.

[32] Sterling Hendricks and Edward Teller. X-ray interference in partially ordered layer lattices. *The Journal of Chemical Physics*, 10:147–167, 1942.

[33] Victor A. Drits and Cyril Tchoubar. *X-ray Diffraction by Disordered Lamellar Structures.* Springer-Verlag, Berlin Heidelberg New York, 1990.

[34] M.M.J. Treacy, J.M. Newsam, and M.W. Deem. A general recursion method for calculating diffracted intensities from crystals containing planar faults. *Proceedings of the Royal Society London A*, 433:499–520, 1991.

[35] S. Ergun. Analysis of coherence, strain, thermal vibration and preferred orientation in carbons by X-ray diffraction. *Carbon*, 14:139–150, 1976.

[36] Sabri Ergun. X-ray scattering by very defective lattices. *Physical Review B*, 1:3371–3380, 1970.

[37] B.E. Warren. X-ray diffraction in random layer lattices. *The Physical Review*, 59:693–698, 1941.

[38] R.A. Young (ed.). *The Rietveld Method.* Oxford University Press, Oxford, New York, 1993.

[39] Ann Marie Byström. The crystal structure of ramsdellite, an orthorhombic modification of MnO_2. *Acta Chemica Scandinavica*, 3:163–173, 1949.

[40] Alfred Schmier. Process of producing ramsdellit [sic], a type of manganese dioxide. *United States Patent Office*, 3427128, 1969.

[41] Margaretha H. Rossouw, Annemare de Kock, David C. Liles, Rosalind J. Gummow, and Michael M. Thackeray. Synthesis of highly crystalline ramsdellite MnO_2 and its lithiated derivative $Li_{0.9}MnO_2$. *Journal of Materials Chemistry*, 2:1211–1211, 1992.

[42] M.M. Thackeray, M.H. Rossouw, R.J. Gummow, D.C. Liles, K. Pearce, A. de Kock, W.I.F. David, and S. Hull. Ramsdellite-MnO_2 for lithium batteries: The ramsdellite to spinel transformation. *Electrochimica Acta*, 38:1259–1267, 1993.

[43] Ralph W. G. Wyckoff. *Crystal Structures, second edition, Volume 1.* Robert E. Krieger Publishing Company, Malabar, Florida, 1963, reprint 1982.

[44] Pieter M. de Wolff, Jan W. Visser, Rudolf Giovanoli, and Rudolf Brütsch. Über ϵ-Mangandioxid. *Chimia*, 32:257–259, 1978.

[45] G. Sterr and A. Schmier. Zur Kenntnis des "δ"-Mangandioxids. *Zeitschrift für anorganische und allgemeine Chemie*, 368:225–230, 1967.

[46] Pierre Strobel. Dehydration and lithium insertion studies in phyllomanganates. *Material Research Symposium Proceedings*, 293:63–68, 1993.

[47] Pierre Strobel and Christian Mouget. Electrochemical lithium insertion into layered manganates. *Materials Research Bulletin*, 28:93–100, 1993.

[48] R. Giovanoli, W. Feitknecht, and E. Fischer. Über Oxidhydroxide des vierwertigen Mangans mit Schichtgitter. 3. Mitteilung: Reduktion von Mangan(III)-manganat(IV) mit Zimtalkohol. *Helvetica Chemica Acta*, 54:1112–1124, 1971.

[49] Jeffrey E. Post and David R. Veblen. Crystal structure determination of synthetic sodium magnesium and potassium birnessite using TEM and the Rietveld method. *American Mineralogist*, 75:477–489, 1990.

[50] A.R. Armstrong and P.G. Bruce. Synthesis of layered $LiMnO_2$ as an electrode for rechargeable lithium batteries. *Nature*, 381:499–500, 1996.

[51] H.-A. Lehmann and K. Teske. Zum Verhalten von Manganoxiden in Kaliumhydroxidschmelzen. *Zeitschrift für anorganische und allgemeine Chemie*, 336:197–199, 1965.

[52] Anders Byström and Ann Marie Byström. The crystal structure of hollandite, the related manganese oxide minerals, and α-MnO_2. *Acta Crystallographica*, 3:146–154, 1950.

[53] M. H. Rossouw, D. C. Liles, M. M. Thackeray, W. I. F. David, and S. Hull. Alpha manganese dioxide for lithium batteries: A structural and electrochemical study. *Materials Research Bulletin*, 27:221–230, 1992.

[54] Jeffrey E. Post, Robert B. von Dreele, and Peter R. Buseck. Symmetry and cation displacements in hollandite: structure refinement of hollandite, cryptomelane and priderite. *Acta Crystallographica*, B 38:1056–1065, 1982.

[55] W.H. Press, S.A. Teukolsky, W.T. Vetlering, and B.P. Flannery. *Numerical Recipes in Fortran. The Art of Scientific Computing.* Cambridge University Press, Cambridge, 1989.

[56] D.B. Wiles and R.A. Young. A new program for rietveld analysis of X-ray powder diffraction patterns. *Journal of Applied Crystallography*, 14:149–151, 1981.

[57] C.J. Howard and R.J. Hill. Report No. M112. Technical report, Australian Atomic Energy Commission, 1986.

[58] Paul Ruetschi. Cation-vacancy model for MnO_2. *Journal of the Electrochemical Society*, 131:2737–2744, 1984.

[59] Paul Ruetschi. Influence of cation vacancies on the electrode potential of MnO_2. *Journal of the Electrochemical Society*, 135:2657–2662, 1988.

[60] Paul Ruetschi and R. Giovanoli. Cation vacancies in MnO_2 and their influence on electrochemical reactivity. *Journal of the Electrochemical Society*, 135:2663–2669, 1988.

[61] T. N. Andersen and R. G. Moody. N_2 BET surface area of MnO_2. Third IBA inter-laboratory test. *JEC Battery Newsletter*, pages 68–77, 1994.

[62] F. Fillaux, H. Ouboumour, J. Tomkinson, and C. T. Yu. An inelastic neutron scattering study of the proton dynamics in γ-MnO_2. *Chemical Physics*, 149:459–469, 1992.

[63] F. Fillaux, H. Ouboumour, C. Cachet, J. Tomkinson, and L.T. Yu. Proton dynamics in manganese dioxides. *Physica B*, 180 & 181:680–682, 1992.

[64] F. Fillaux, C.H. Cachet, H. Ouboumour, J. Tomkinson, C. Lévy-Clément, and L.T. Yu. Inelastic neutron scattering study of the proton dynamics in manganese oxides. I. γ-MnO_2 and manganite. *Journal of the Electrochemical Society*, 140:585–591, 1993.

[65] F. Fillaux, H. Ouboumour, C.H. Cachet, J. Tomkinson, C. Lévy-Clément, and L.T. Yu. Inelastic neutron scattering study of the proton dynamics in manganese dioxide. II. Proton insertion in electrodeposited MnO_2. *Journal of the Electrochemical Society*, 140:592–598, 1993.

[66] F. Fillaux, S.M. Bennington, J. Tomkinson, and L.T. Yu. Inelastic neutron-scattering study of free proton dynamics in γ-MnO_2. *Chemical Physics*, 209:111–125, 1996.

[67] M. Ripert, C. Poinsignon, Y. Chabre, and J. Pannetier. Structural study of proton electrochemical intercalation in manganese dioxide. *Phase Transitions*, 1991:205–209, 32.

[68] J. Pannetier. A comprehensive structural model of EMD and CMD based on de Wolff disorder and microtwinning. *Progress in Batteries and Battery Materials*, 11:51–55, 192.

[69] J. Pannetier. Characterization of manganese dioxides by X-ray diffraction. *Progress in Batteries & Battery Materials*, 13:132–135, 1994.

[70] Wen-Hong Kao, Victor J. Weibel, and Michael J. Root. The influence of potassium ion on the electrodepostion and electrochemistry of electrolytic manganese dioxide. *Journal of the Electrochemical Society*, 139:1223–1226, 1992.

[71] R. L. McGreevy and M. A. Howe. RMC: modelling disordered structures. *Annual Review of Materials Science*, 22:217–242, 1992.

[72] R. L. McGreevy. Reverse Monte Carlo: fact and fiction. *Journal of Non-Crystalline Solids*, 156-158:949–955, 1993.

[73] B.D. Hall and R. Monot. Calculating the Debye-Scherrer diffraction pattern for large clusters. *Computers in Physics*, 5:414–417, 1991.

[74] J.P. Gabano, B. Morignat, E. Fialdes, B. Emery, and J.F. Laurent. Étude de la réduction chimique du bioxyde de manganèse γ. *Zeitschrift für physikalische Chemie Neue Folge*, 46:359–372, 1965.

[75] W.C. Maskell, J.E.A. Shaw, and F.L Tye. Manganese dioxide electrode — IV. Chemical and electrochemical reduction of an electrolytic γ-MnO_2. *Electrochimica Acta*, 26:1403–1410, 1981.

[76] Christian Mondoloni, Marc Laborde, Jacques Rioux, Edouard Andoni, and Claude-Levy Clement. Rechargeable alkaline manganese dioxide batteries. I. *in situ* X-ray diffraction investigation of the H^+/γ-MnO_2 (EMD-type) insertion system. *Journal of the Electrochemical Society*, 139:954–959, 1992.

[77] L.S. Dent Glasser and Lorna Ingram. Refinement of the crystal structure of groutite, α-MnOOH. *Acta Crystallographica*, B24:1233, 1968.

[78] D. Aurbach, I. Weissman, E. Zinigrad, P. Dan, Y. Herzel, and E. Mengeritsky. Presentation of a new Li-MnO_2 battery technology from Tadiran. 190th Meeting of the Electrochemical Society, Inc. Paper No. 115. San Antonio, Texas, 1996.

[79] Rolf Norrestam. α-Manganese(III) oxide — a C-type sesquioxide of orthorhombic symmetry. *Acta Chemica Scandinavica*, 21:2871–2884, 1967.

[80] S. Geller. Structures of α-Mn_2O_3, $(Mn_{0.983}Fe_{0.017})_2O_3$ and $(Mn_{0.37}Fe_{0.63})_2O_3$ and relation to magnetic ordering. *Acta Crystallographica*, B27:821–828, 1971.

[81] Ralph W. G. Wyckoff. *Crystal Structures, second edition, Volume 3.* Robert E. Krieger Publishing Company, Malabar, Florida, 1963, reprint 1982.

[82] R. J. Gummow, A. De Kock, and M. M. Thackeray. Improved capacity retention in rechargeable 4 V lithium/lithium-manganese oxide (spinel) cells. *Solid State Ionics*, 69:59–67, 1994.

[83] J.N. Reimers, Eric W. Fuller, Erik Rossen, and J.R. Dahn. Synthesis and electrochemical studies of $LiMnO_2$ prepared at low temperatures. *Journal of the Electrochemical Society*, 140:3396–3401, 1993.

[84] Immo Koetschau. In-situ X-ray study of Orthorhombic Lithium Manganese Oxide. M.Sc. thesis, Simon Fraser University, Burnaby, B.C., Canada, 1997 (in preparation).

[85] Oliver Schilling, E.W. Fuller, Monique Richard, W. Li, J.N. Reimers, and J.R. Dahn. Methods to increase the available lithium in Li-Mn-O compounds. In *Seventh International Meeting on Lithium Batteries. Extended Abstracts.*, pages 426–428, 1994.

[86] Dominique Guyomard and Jean-Marie Tarascon. High-voltage-stable electrolytes for $Li_{1+x}Mn_2O_4$/carbon secondary batteries. *United States Patent*, 5192629, 1993.

[87] Monique N. Richard, E.W. Fuller, and J.R. Dahn. The effect of ammonia reduction on the spinel electrolyte materials $LiMn_2O_4$ and $Li(Li_{1/3}Mn_{5/3})O_4$. *Solid State Ionics*, 73:81–91, 1994.

[88] D. Guyomard and J. M. Tarascon. Li-metal-free $LiMn_2O_4$/carbon cells: Their understanding and optimization. *Journal of the Electrochemical Society*, 139:937–948, 1992.

[89] Yuan Gao and J.R. Dahn. The high temperature phase diagram of $Li_{1+x}Mn_{2-x}O_4$ and its implications. *Journal of the Electrochemical Society*, 143:1783–1788, 1996.

[90] Jean-Marie Tarascon. Method for synthesis of high capacity $LiMn_2O_4$ secondary battery electrode compounds. International Patent Application. No. PCT/US94/04776, 1994.

[91] Yuan Gao and J.R. Dahn. Synthesis and characterization of $Li_{1+x}Mn_{2-x}O_4$ for Li-ion battery applications. *Journal of the Electrochemical Society*, 143:100–114, 1996.

[92] Yuan Gao and J.R. Dahn. Correlation between the growth of the 3.3 V discharge plateau and capacity fading in $Li_{1+x}Mn_{2-x}O_4$ materials. *Solid State Ionics*, 84:33–40, 1996.

[93] G.G. Amatucci, C.F. Schmutz, A. Blyr, and J.M. Tarascon. Enhanced high temperature performance of $LiMn_2O_4$ based Li-ion batteries through the use of surface treatments. 190th Meeting of the Electrochemical Society, Inc. Paper No. 870. San Antonio, Texas, 1996.

[94] J.M. Tarascon and D. Guyomard. The $Li_{1+x}Mn_2O_4/C$ rocking-chair system: A review. *Electrochimica Acta*, 38:1221–1231, 1993.

[95] Yongyao Xia and Masaki Yoshio. An investigation of lihtium ion insertion into spinel structure Li-Mn-O compounds. *Journal of the Electrochemical Society*, 143:825–833, 1996.

[96] Qi Feng, Yoshitaka Miyai, Hirofumi Kanoh, and Kenta Ooi. Li^+ extraction/insertion with spinel-type lithium manganese oxides. Characterization of redox-type and ion-exchange-type sites. *Langmuir*, 8:1861–1867, 1992.

[97] Yuan Gao and J.R. Dahn. Thermogravimetric analysis to determine the lithium to manganese atomic ration in $Li_{1+x}Mn_{2-x}O_4$. *Applied Physics Letters*, 66:2487–2489, 1995.

[98] Yuan Gao, J.N. Reimers, and J.R. Dahn. Changes in the voltage profile of $Li/Li_{1+x}Mn_{2-x}O_4$ cells as a function of x. *Physical Review B*, 54:3878–3883, 1996.

[99] M. Yoshio and Y. Xia. Electrochemical behavior of $Li/LiMn_2O_4$ at a low and high operating temperature. 190th Meeting of the Electrochemical Society, Inc. Paper No. 869. San Antonio, Texas, 1996.

[100] G.G. Amatucci, D. Larcher, A.S. Gozdz, F.K. Shokoohi, and J.M. Tarascon. Investigation of oxygen stoichiometry, electrochemical features, and failure mechanisms of $LiMn_2O_4$ spinel with the aid of $Li_xMn_2O_{4-y}F_y$ solid solution. 190th Meeting of the Electrochemical Society, Inc. Paper No. 820. San Antonio, Texas, 1996.

[101] Ared Cezairliyan and S.C. Mraw. Differential scanning calorimetry. In C.Y. Ho, editor, *Specific Heat of Solids. CINDAS Data Series on Material Properties. Volume I-2*, chapter 11, pages 395–435. Hemisphere Publishing Corporation, New York, 1988.